

**DEVELOPMENT AND APPLICATIONS OF A MULTI-
USER POLYMER MEMS TECHNOLOGY**

by

Dan Sameoto
M.A.Sc, Dalhousie University, 2004
B.A.Sc., Dalhousie University, 2002

THESIS SUBMITTED IN PARTIAL FULFILLMENT OF
THE REQUIREMENTS FOR THE DEGREE OF

DOCTOR OF PHILOSOPHY

In the
School of Engineering Science

© Dan Sameoto 2008

SIMON FRASER UNIVERSITY

Summer 2008

All rights reserved. This work may not be
reproduced in whole or in part, by photocopy
or other means, without permission of the author.

APPROVAL

Name: Dan Sameoto
Degree: Doctor of Philosophy
Title of Thesis: Development and Applications of a Multi-User Polymer MEMS Technology

Examining Committee:

Chair: **Dr. Kamal Gupta**
Professor, School of Engineering Science

Dr. M. Parameswaran (Ash)
Senior Supervisor
Professor, School of Engineering Science

Dr. Albert M. Leung
Supervisor
Professor, School of Engineering Science

Dr. Bonnie L. Gray
Supervisor
Assistant Professor, School of Engineering Science

Dr. Zou-Guang Ye
Internal Examiner
Professor, Department of Chemistry

Dr. Luke Lee
External Examiner
Professor, Department of Bioengineering
University of California, Berkeley

Date Defended/Approved: _____

ABSTRACT

This thesis covers the development and characterization of an all polymer micromachining process designed for multi-user applications. This thesis describes the first MEMS process designed to provide multi-user functionality using polymers as structural and sacrificial layers, and offers new fabrication abilities not previously available with silicon micromachining. The structural material for this MEMS process is the negative tone photoresist SU-8, which is excellent for low temperature permanent applications. This work has developed a very reliable method of producing compliant SU-8 microstructures and has characterized it for a new class of structures and actuators.

The use of SU-8 offers many advantages with respect to processing, but also introduces many processing challenges that were solved in this work. The polymer MEMS process developed for this work has a multi-thickness structural layer separated from the substrate by a single sacrificial layer. The sacrificial layer includes dimple features to reduce stiction and allow structures in excess of $5000 \times 5000 \mu\text{m}^2$ to release without problems. The list of working devices fabricated in this process includes low and high aspect ratio compliant mechanisms, micro-optical components, thermal and electrostatic actuators, micro antennas and compliant grippers.

The many processing advances introduced through this work include elimination of adhesion failure of polymers during multiple processing steps, alignment of two polymers with similar indices of refraction, development of an anti-stiction substrate with high adhesion anchor areas, characterization of stress gradient in SU-8 with processing conditions, and successful gold wirebonding onto SU-8 devices.

Keywords: MEMS; polymer; SU-8; multi-user; polystyrene; actuator

DEDICATION

To the memory of Anne Veronica Sameoto, October 2nd, 1916 – February 19th,
2008. You will be missed.

ACKNOWLEDGEMENTS

Thank you to my senior supervisor, Dr. M. Parameswaran (Ash). This work might not have been possible without his financial and academic support for a topic that I felt strongly about. He took a chance on me with my research direction and allowed me the necessary flexibility and direction to complete this work. I owe much of my success to him. I would also like to thank my other internal supervisors, Dr. Bonnie Gray and Dr. Albert Leung for their many suggestions about applications, and improvements to this research.

I would like to acknowledge the contributions of my lab mates at SFU, as every one of them helped me in some way. I have been honoured to work with such a dynamic, interesting and supporting lab group. Special thanks are extended to Robert Johnstone, who took all the scanning electron microscope images used for this thesis.

I would like to thank both Bill Woods and Eva Czyzewska for all of their assistance in fabrication and cleanroom advice. Their help was vital and greatly appreciated.

Finally, thank you to my family, friends and girlfriend. Your love and support made the difficult times bearable, and the good times better. I will always appreciate your presence over the last three years. I would not be here without you.

Parts of this thesis have been previously published and are acknowledged in the credits.

TABLE OF CONTENTS

Approval	ii
Abstract	iii
Dedication	iv
Acknowledgements	v
Table of Contents	vi
List of Figures	ix
List of Tables	xvi
Glossary	xvii
1 Introduction	1
1.1 What is MEMS?	1
1.2 Mechanical properties of silicon	4
1.3 Uses for silicon	5
1.4 Important concepts in MEMS	6
1.5 Multi-user MEMS processes	8
1.5.1 PolyMUMPs.....	9
1.5.2 Silicon-on-Insulator (SOI) processes	13
1.6 Polymers for micromachining	15
1.7 Motivation and scope of research.....	16
2 Fabrication Facilities and Equipment	18
2.1 Introduction to cleanroom facilities.....	18
2.2 Cleanroom overview	18
2.3 Class 100 cleanroom equipment.....	20
2.3.1 Spin-coater	20
2.3.2 Hot-plates/ovens.....	21
2.3.3 UV aligner	24
2.3.4 PECVD/RIE	27
2.3.5 Acid/Base wet bench.....	28
2.3.6 Solvent wet bench	28
2.4 Class 1000 Cleanroom Equipment.....	28
2.4.1 Microscopes	29
2.4.2 Profilometer.....	29
2.4.3 Wafer scribe.....	30
2.4.4 Wirebonders	30
2.4.5 Micro-probe station	31

2.5	Mini-cleanroom equipment and design tools	31
3	SU-8 for MEMS applications	34
3.1	Introduction	34
3.2	Physical properties of SU-8	35
3.3	History of SU-8 applications and uses	37
3.4	Potential sacrificial materials for SU-8	39
3.4.1	Use of photoresist as a sacrificial layer for SU-8	44
3.4.2	Uncrosslinked SU-8 as a sacrificial layer	46
3.4.3	Polystyrene as a sacrificial layer	49
3.4.4	Producing and characterizing polystyrene solutions	50
3.4.5	Patterning of polystyrene	51
3.5	Polymer MEMS process steps	56
3.6	Fabrication challenges and process design rules	67
3.6.1	Minimum feature sizes	67
3.6.2	Negative sidewalls	69
3.6.3	Tensile stress	73
3.7	Polymer MEMS design rules	74
3.7.1	Anchors	75
3.7.2	Release holes	79
3.7.3	Dimples	81
3.7.4	Double thickness structures	82
3.7.5	Very large structures and tethering	83
3.7.6	Alignment	85
4	Modification of SU-8 processing for improved reliability and packaging	86
4.1	Introduction	86
4.2	Control of out-of-plane curvature in SU-8 compliant structures	87
4.3	Theory of SU-8 curvature	96
4.4	Robust electrical connections to SU-8 structures and actuators by gold wirebonding	107
4.4.1	Past work on powering SU-8 structures	108
4.4.2	Gold wirebonding to SU-8	109
4.4.3	Metal thickness and its effect on Bond yield	114
4.4.4	Bond yield with hardbaking parameters	116
4.4.5	Measuring bond strength and improving it using surface activation	119
4.4.6	Improving bond strength to SU-8 using surface activation	124
5	Polymer MEMS structures, actuators, and applications	135
5.1	Introduction	135
5.2	Experimental setup	136
5.3	Mechanical structures for process optimization	136
5.4	Thermal actuators	145
5.4.1	Background	145
5.4.2	SU-8 hot/cold arm thermal actuators	146
5.4.3	SU-8 chevron thermal actuators	149
5.4.4	SU-8 hybrid thermal actuators	154
5.4.5	SU-8 thermal actuator force output	160

5.5	Untethered polymer scratch drive actuators	163
5.5.1	Robocup nanogram competition	163
6	Contributions	174
	Conclusions.....	180
	Appendices.....	184
A.	A solvent free lift-off method to pattern metal on SU-8	184
B.	Process recipe for three level SU-8 nanobots.....	190
	Reference List.....	193

LIST OF FIGURES

Figure 1.1:	Basic lithography steps: a) start with a material layer to pattern on a substrate, b) add photoresist layer, c) expose photoresist layer through a mask, d) develop exposed photoresist, e) etch exposed material, f) strip remaining photoresist.	2
Figure 1.2:	Basic fabrication steps of a conformal MEMS process (left), and a planarized process (right).	3
Figure 1.3:	Process layers and thicknesses of the PolyMUMPs process.	10
Figure 1.4:	Examples of SFU MEMS designs fabricated in PolyMUMPs technology. SEMs are courtesy of Robert Johnstone.	12
Figure 1.5:	MEMS designs fabricated in two different SOI technologies.	14
Figure 2.1	Full view and close up of the spin coater used for coating all polymers in this work.	20
Figure 2.2:	Isothermal ovens (left) and digital ramping hotplates (right) used for baking of polymer MEMS wafers.	23
Figure 2.3	Temperature distribution on an HP30 digital hotplate held at an average temperature of 100 °C. The area is 18x18 cm.	24
Figure 2.4	Quintel UV aligner.	25
Figure 2.5:	Process of securing a Mylar mask in position with a glass cover plate and powerful magnets. The magnets are attracted to the ferromagnetic material in the corners of the mask holder. Stronger magnets are required for thicker glass plates.	27
Figure 2.6:	Photograph of mini-cleanroom setup with the probe station (a), camera (b), function generator (c), and computer (d). Polymer MEMS can be inspected and tested as either a full wafer, or as individual die under the microscope.	32
Figure 3.1:	Behaviour of positive and negative tone photoresists after exposure and development.	35
Figure 3.2:	Images of several process stages while using photoresist as a sacrificial layer for compliant SU-8 structures.	45
Figure 3.3:	Aluminum deposition on uncrosslinked SU-8. Scotch tape easily pulls aluminum off the SU-8 surface (a), and uncrosslinked SU-8 can be developed (b). If the SU-8 is baked after metal deposition, crosslinking can occur, and all areas of SU-8 that have been coated with metal become insoluble in SU-8 developer.	47

Figure 3.4:	Development depth of dimple features with exposure dose. Wafer is coated with Cr/Au followed by 6 μm of PS and 6.7 μm of thick photoresist. Photoresist bake time was 15 minutes at 100 $^{\circ}\text{C}$ and was exposed through a chrome mask.....	54
Figure 3.5:	Images of underexposed photoresist features after development and profilometer data of dimples produced in photoresist through a Chrome (left) and Mylar emulsion mask.	55
Figure 3.6:	Basic steps of the polymer MEMS process.....	62
Figure 3.7:	Compliant SU-8 structures: a) thick SU-8 fixed-fixed bridge arrays, b) close-up of cantilever anchors demonstrating the two SU-8 thicknesses and planarization of the polystyrene topology.	63
Figure 3.8:	a) Electrostatic SU-8 linear combdrive structure and b) close-up of combdrive fingers. The poor edge quality of features on the emulsion masks results in rough sidewalls on the SU-8 structures.....	64
Figure 3.9:	SU-8 thermal actuators coated in Cr/Au: a) hot/cold arm thermal actuators, b) chevron thermal actuators showing raster scanning effects (arrow) of the mask writing process.	64
Figure 3.10:	Out-of-plane pop-up structures reported in [37], demonstrating dimples (a) and multi-thickness thermal isolation platform designed by myself (b) [89].....	65
Figure 3.11:	The visual effect of polystyrene RIE on SU-8 optical properties [89]. The polystyrene surface roughness is transferred to the underside of SU-8 membranes, resulting in a cloudy appearance when the underlying polystyrene is removed. The dashed line separates the areas of O ₂ RIE exposure.	66
Figure 3.12:	Feature size swelling and alignment errors due to emulsion mask contact problems. Structures on the left were fabricated near the wafer center, while those on the right were near the wafer edge. Minimum and maximum SU-8 thicknesses are 5 and 15 μm	69
Figure 3.13	Rough edges on an emulsion mask feature. The arrows indicate the greyscale region.....	70
Figure 3.14	Two side views of SU-8 microstructures fabricated using a low quality emulsion mask. Significant negative sidewalls exist for both double exposed (left) [89] and single exposed (right) 40 μm thick SU-8 layers.....	71
Figure 3.15	Photomicrograph of the effect of thin features in 150 μm thick SU-8 exposed through an emulsion mask. Beams on the left do not transfer all the way to the bottom but stop at the dashed lines showing the bottom and the reflected image of the bottom.	72
Figure 3.16	Photographs of the effect of deliberate greyscale effects introduced by mask design. Significant variation in sidewall profile can be achieved with a single exposure dose. Features with large negative sidewalls (and their reflections) are circled.....	73

Figure 3.17	Potential configurations of anchors and dimples. This diagram assumes two exposures that are individually not enough to fully expose the photoresist. The anchor exposure in this case is longer than the dimple exposure.....	76
Figure 3.18	L-Edit layout of a typical anchor structure in the polymer MEMS process.....	77
Figure 3.19	L-Edit layout of a cantilever array designed to be electrically connected to the substrate after a blanket metal deposition.....	78
Figure 3.20:	Release hole failure due to overexposure of POLY1+POLY2 in a single thickness SU-8 structure. Polystyrene remains undeveloped in the centre of the structure. The dashed line indicates the POLY2 feature.....	81
Figure 3.21	L-Edit layouts of two potential dimple arrangements: a) fully enclosed dimples on a large plate, b) large dimples to release an array of thin cantilevers.....	82
Figure 3.22	Cross-sectional view of perfectly aligned and misaligned POLY1 and POLY2 exposures defining a double thickness structure.....	83
Figure 3.23	L-Edit layout of a cantilever array held on the substrate by a series of breakable tethers on a 1x1 cm die. This whole array can be removed from the substrate after breaking tethers using the method described in [82].....	84
Figure 3.24	Layout of a large pop-up structure held with four tethers. Tethers are compliant in two axes to allow tensile stress to be relieved after release.....	85
Figure 4.1:	L-Edit layout of removable cantilever test structures for observing out-of-plane curvature. The longest cantilever in the array is 6400 μm long [102].....	88
Figure 4.2:	Exposure times at 10 mW/cm^2 for cantilever arrays on curvature test wafers.....	91
Figure 4.3:	Cantilever arrays taped to glass slides for under exposed and over exposed conditions [102].	92
Figure 4.4:	Photomicrographs of SU-8 cantilevers used for curvature trials.....	93
Figure 4.5:	Geometry used for determining the radius of curvature of SU-8 cantilevers [102].....	93
Figure 4.6:	Curvature versus exposure dose for short baking times.....	94
Figure 4.7:	Curvature versus exposure dose for long baking times.....	95
Figure 4.8:	Calculated dose received at different depths within SU-8, for an exposure dose of 450 mJ/cm^2 . Two SU-8 film thicknesses of 20 and 40 μm are modelled in this case.....	100
Figure 4.9:	Calculated dose received at different depths within SU-8, for an exposure dose of 450 mJ/cm^2 . SU-8 film thicknesses of 40, 160 and 400 μm are modelled in this case.....	100

Figure 4.10: Experimental data on T _g of SU-8 taken from figure 11 of Feng [44], and fit to different reaction rate orders. T _g is assumed to be proportional to conversion percentage.	103
Figure 4.11: Bonding steps for ball-wedge bonders: (1) spark from electric flame-off (EFO) wand melts wire tip and forms ball, (2) ball positioned over bond pad, (3) bonder tip is pressed against the heated bond pad and ultrasonic energy is applied to deform the ball and weld the metal surfaces, (4) bond tip pulls away, leaving welded ball bond and forming loop, (5) bonder tip moves to package pad, (6) wedge bond is created, (7) bonder tip pulls away and breaks wire, leaving a completed bond.	111
Figure 4.12: Close up of wirebonder and chip to be bonded.	113
Figure 4.13: Ball bond yield on 1 μm thick SU-8 structures with different metal compositions [110]. Yield data is based on at least 30 attempted bonds.	115
Figure 4.14: SU-8 cantilevers without gold before (left) and after hardbaking without restraints.	117
Figure 4.15: Wirebond yield versus hardbake temperature on different SU-8 thicknesses. Chuck temperature was set to 114 °C, which was the highest setting that avoided plastic deformation of SU-8 structures. Yield data is based on 30 attempted bonds.	118
Figure 4.16: Schematic of ball bond and bond pull setup. Dimensions are not to scale.	120
Figure 4.17: Linear stages and force probe used for bond pull tests.	122
Figure 4.18: Close-up view of the force probe used to measure bond failure forces. The spring loaded probe moves the needle which remains in the position of the highest measured force after the bond breaks.	122
Figure 4.19: Average bond pull failure forces for gold wirebonds onto a silicon substrate. Different bonder tip temperatures were used to determine if the wire was weakened at higher temperatures. All bonds failed by wire fracture directly above the ball bond.	123
Figure 4.20: Average bond strength and one standard deviation of failure force on SU-8 for different activation times and chuck temperatures [110].	126
Figure 4.21: Failure force and modes of bonds made at 104 °C for different activation times. The distribution of wire failures is represented by area percentage of the bars.	127
Figure 4.22: Failure force and modes of bonds made at 123 °C for different activation times.	127
Figure 4.23: Failure force and modes of bonds made at 151 °C for different activation times.	128
Figure 4.24: Optical micrographs of bond failures with low activation times (left), and high activation times (right). Observations of the bond	

	failures at high activation times through an optical microscope are difficult due to extremely rough SU-8 surfaces.	129
Figure 4.25:	SEM images (a and b) and photographs (c and d) of bonds to SU-8 with smooth (a and c) and rough (b and d) surfaces.	130
Figure 4.26:	Photographs of SU-8 posts coated in Cr/Au that had been activated for 10 minutes on top of bare silicon (a), and a gold coated substrate (b), prior to metal deposition.	131
Figure 4.27:	Average failure force and one standard deviation for wirebonds on hardbaked SU-8 posts on a silicon wafer activated for 10 minutes with standard activation recipe. Shaded section represents the relative percentage of wire failures. Between 25 and 30 bonds are tested for each trial.	132
Figure 4.28:	Average bonded area, failure force, and calculated SU-8/metal adhesion strength based on wirebond pull tests (arrows indicate the relevant y-axis). The number of samples was 19 and 16 for the 5.0 and 8.0 power setting trials respectively.	133
Figure 5.1:	Material property and process control test die layout. The die is 1x1 cm ²	138
Figure 5.2:	Fabricated structures for the polymer MEMS test die.	140
Figure 5.3:	Schematic of the mechanical characterization die test system. This image is used with permission from [120]. The resonating test structures are observed through the microscope and each image corresponds to a specific input frequency.	142
Figure 5.4:	Fixed-fixed bars resonating at approximately 25 kHz.	143
Figure 5.5:	Hot/cold thermal actuator layout in L-Edit showing geometric properties.	147
Figure 5.6:	Performance of a wirebonded SU-8 hot/cold arm thermal actuator as deflection versus input power. Actuator is 1 mm long and 40 μm thick with a 20 μm wide hot arm [110].	148
Figure 5.7:	SEM images of chevron thermal actuators fabricated in an early version of the polymer MEMS process [89]. Raster scanning effects from the low quality masks can be seen on the arms in a) and b). The actuators have very little electrical resistance due to the large number of wide arms in parallel.	149
Figure 5.8:	Chevron thermal actuator layout in L-Edit and geometric properties.	150
Figure 5.9:	Displacement versus power for an SU-8 chevron thermal actuator. Hysteresis occurs after plastic deformation of the SU-8 due to overpowering, resulting in a negative deflection.	151
Figure 5.10:	Time response of the chevron thermal actuator design described in Figure 5.9. A time constant of 13 ms has been fit to the raw data [89].	153
Figure 5.11:	Frequency response of the chevron thermal actuator design described in Figure 5.9 [89].	153

Figure 5.12: Under exposed and highly stressed chevron thermal actuators fabricated in a 180 μm thick SU-8 layer. Tensile stress is amplified by the actuator geometry and results in a negative initial deflection compared to the designed position (shown in outline).....	155
Figure 5.13: L-Edit layouts and images of hybrid thermal actuators fabricated in 180 μm thick SU-8. The folded suspension shrinks with the hot-arms, but constrains the hot arms during actuation. Full shrinkage compensation is not achieved with these actuators due to the anchor spacing.....	156
Figure 5.14: Deflection versus input power for chevron and hybrid thermal actuators that are 120 μm thick with 1 mm long hot arms and a designed geometric advantage of 10.	158
Figure 5.15: Hybrid thermal actuator performance with identical designs fabricated with different thicknesses on the same wafer.....	159
Figure 5.16: Force versus displacement of two different hot/cold thermal actuator designs with different hot arm widths [122]. Input power is 69.4 and 64.35 mW for the 20 and 40 μm wide designs, respectively.	161
Figure 5.17: Force versus displacement of a chevron thermal actuator at different input powers. The actuator is 40 μm thick with two 40 μm wide hot arms, each 1 mm long with a designed geometric advantage of 10.....	161
Figure 5.18: Force versus displacement of a hybrid thermal actuator with an input power of 33.24 mW [122]. The actuator is 180 μm thick with two 20 μm wide hot arms, each 1 mm long with a designed geometric advantage of 10.	162
Figure 5.19 Schematic of scratch drive actuator motion.	164
Figure 5.20: Basic untethered polymer scratchdrive robot structure. Structural thicknesses are designed to be 5, 10 and 15 μm	166
Figure 5.21: Photograph of the underside of a chrome coated polymer scratch drive actuator that has broken off after metal deposition. Waviness of the bottom surface is up to 200 nm.	167
Figure 5.22: Removal and flipping procedure of SU-8 nanobots. Acupuncture needles attached to microprobes remove (b), and manipulate robots. Spinning the needle (d), rotates the robots out-of-plane, where they can be transferred to another needle (e), prior to being rotated into the upside down position (g), and placed on the substrate (h).	168
Figure 5.23: Optical image of an SU-8 nanobot on a playing field, demonstrating curvature away from the field due to the compressively stressed aluminum coating.....	169
Figure 5.24: Exaggerated schematic of tripod balancing of upside down nanobot design. Areas of contact are circled.	170
Figure 5.25: Buckled beam nanobot design. This particular structure operates with the SU-8 in contact with the substrate and the top aluminum surface causes negative curvature.	171

Figure 5.26: Selection of special topics course nanobot designs.....	172
Figure A.1: Basic process steps for using a positive tone photoresist on patterned (but undeveloped) SU-8 structures. a) SU-8 is exposed and baked, but not developed; b)-c) a highly absorbing photoresist like Shipley 1827 is deposited on top of the SU-8 and exposed and developed; d) metal is deposited on photoresist layer; e) Photoresist is removed with TMAH, lifting off metal.....	185
Figure A.2: Basic process steps to convert a liquid photoresist into a dry, laminatable layer.	186
Figure A.3: Schematic of laminating pouch and image of HeatSeal laminator with a 4” wafer for scale. Laminating pouch is made of acetate or Mylar.	188
Figure A.4: Sequence of metal deposition, lift-off, encapsulation and development of embedded gold electrode in SU-8.	189

LIST OF TABLES

Table 1.1:	Published physical properties of single crystal and polycrystalline silicon.	5
Table 1.2:	Scaling laws for selected MEMS properties [18].....	7
Table 3.1:	Published physical properties of SU-8	37
Table 3.2:	Potential sacrificial materials for SU-8 with advantages and drawbacks.....	43
Table 3.3	Suggested minimum features and spacing for the polymer MEMS process assuming a 15 μm thick first SU-8 layer and 40 μm thick total SU-8 layer.	75
Table 5.1:	MEMS material property testing techniques adapted from [116].....	137
Table 5.2	Governing equations used to find several mechanical properties of polymers based on the test structures shown in Figure 5.1. These equations assume rectangular cross-sections.	140

GLOSSARY

A	Area
AC	Alternating Current
A_c	Cross-sectional area
BCB	Benzocyclobutene
CAD	Computer Aided Design
CMC	Canadian Micro-Electronics Corporation
CMOS	Complementary Metal Oxide Semiconductor
C_p	Specific heat
CTE	Coefficient of thermal expansion
CVD	Chemical Vapour Deposition
d	Deflection
DC	Direct Current
DIP	Dual In-line Package
DMM	Digital Multi-Meter
DRIE	Deep Reactive Ion Etch
E	Young's modulus
F	Force
f	Frequency;
FEA	Finite Element Analysis
FEM	Finite Element Model
g	Gap, gravitational force
G.A.	Geometric advantage
GBL	Gamma-butyrolactone
h	Convection heat transfer coefficient
h_r	Radiation heat transfer coefficient
I	Moment of inertia (second moment of area)
IPA	Isopropyl Alcohol
k	Thermal conductivity
K	Boltzmann constant
L	Length
L_c	Characteristic length
LIGA	L ithographie, G alvanoformung, A bformung (German acronym for lithography, electroforming and molding)
LCD	Linear Comb Drive

M	Moment
m	Mass
MEMS	Micro-Electro-Mechanical-Systems
micron	1 μm or 1×10^{-6} m
MUMPs	Multi User MEMS Process
Nu	Nusselt number
n	Number of comb fingers
P	power, perimeter
PDMS	Polydimethylsiloxane
PECVD	Plasma Enhanced Chemical Vapour Deposition
PGMEA	Propylene Glycol Monomethyl Ether Acetate
PMMA	Polymethylmethacrylate
Poly	Polysilicon
PR	Photoresist
PS	Polystyrene
R	Electrical resistance
r	Resistivity; hot arm - cold arm spacing in STAs
Ra	Rayleigh number
RIE	Reactive Ion Etch
SDA	Scratch Drive Actuator
SEM	Scanning Electron Microscope
SiO ₂	Silicon Dioxide
SMA	Shape Memory Alloy
STA	Standard thermal actuator (hot/cold arm thermal actuator)
SU-8	Negative acting, epoxy based photoresist
T	Temperature
t	Time or thickness
TA	Thermal Actuator
T _f	Film temperature
t _r	Response time
T _s	Surface temperature
U	Heat transfer coefficient
UV	Ultra violet
V	Voltage
w	Width
x, y, z	Rectangular coordinates
ZIF	Zero Input Force

1 INTRODUCTION

This chapter introduces the field of Micro-Electro-Mechanical-Systems (MEMS) with an overview of materials, processes, and devices. Information about existing silicon micromachining technologies for multi-user applications is provided, along with the evolution of newer materials for micromachining technology. This work demonstrates that although researchers have a wide selection of commercially available silicon based processes for MEMS prototyping, polymer MEMS processing is missing the generalized process technologies that allow for rapid testing of new designs. The motivation behind the development of the first multi-user polymer MEMS process is described, along with details on how this development has produced new insights into polymer micromachining.

1.1 What is MEMS?

Micro-Electro-Mechanical-Systems (MEMS) are small structures and devices that combine mechanical and electrical components with sizes from 1-100's of μm . MEMS technology can produce thousands of passive and active components on a single chip using batch fabrication technologies adapted from the integrated circuits (IC) industry, making the cost of individual MEMS devices very low. The field of MEMS grew out of the processing work and technologies originally developed for the IC industry, which involve the deposition, patterning and removal of various materials on rigid substrates of silicon or glass. The fundamental processing step in the fabrication of MEMS and ICs is

called lithography: a sequence of depositions, exposures, developments, and stripping of a photosensitive layer that protects other materials from chemical or physical etching. An example of a complete lithography step is shown in Figure 1.1.

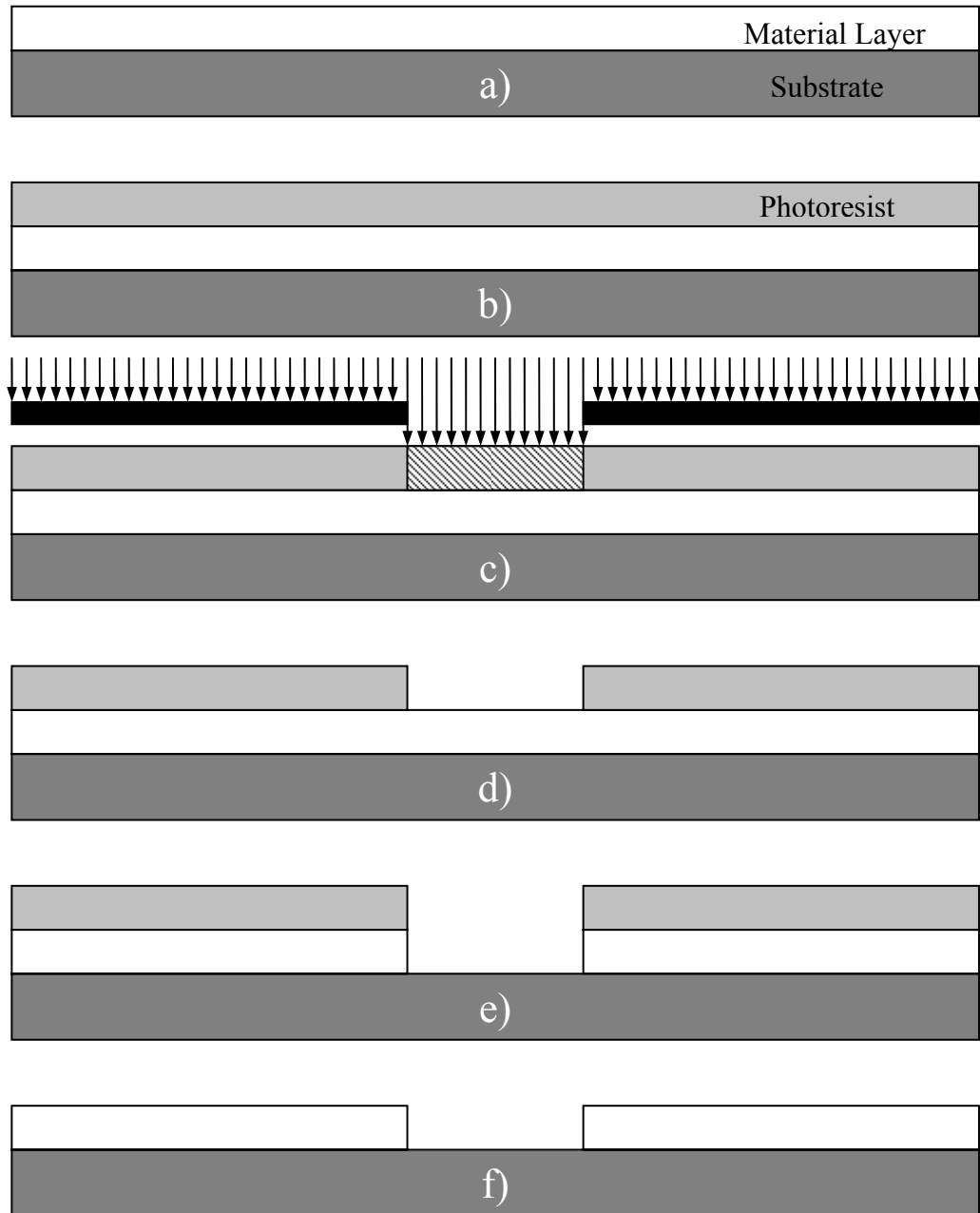


Figure 1.1: Basic lithography steps: a) start with a material layer to pattern on a substrate, b) add photoresist layer, c) expose photoresist layer through a mask, d) develop exposed photoresist, e) etch exposed material, f) strip remaining photoresist.

Lithography works best when substrates are flat, with thin photoresist layers. Most IC processing involves dozens of patterned layers, but all these layers are very thin (10's-100 of nm). MEMS processes typically have fewer patterned layers, but these are much thicker, usually more than one micrometer (μm). As the number of layers increase, the topological effect of previous layers can become important and ultimately limits the thicknesses and number of layers in a MEMS process. For a MEMS process like PolyMUMPs [1], all layers conform to the shape of the substrate and previously defined structures; therefore, this type of process exhibits conformal layers. Other processes, like SUMMiT [2], can deposit material in the same manner, but use a special step to polish away the height differences, making these types of processes planarized. A sample process flow for creating cantilevers in either conformal or planarized processes is shown in Figure 1.2.

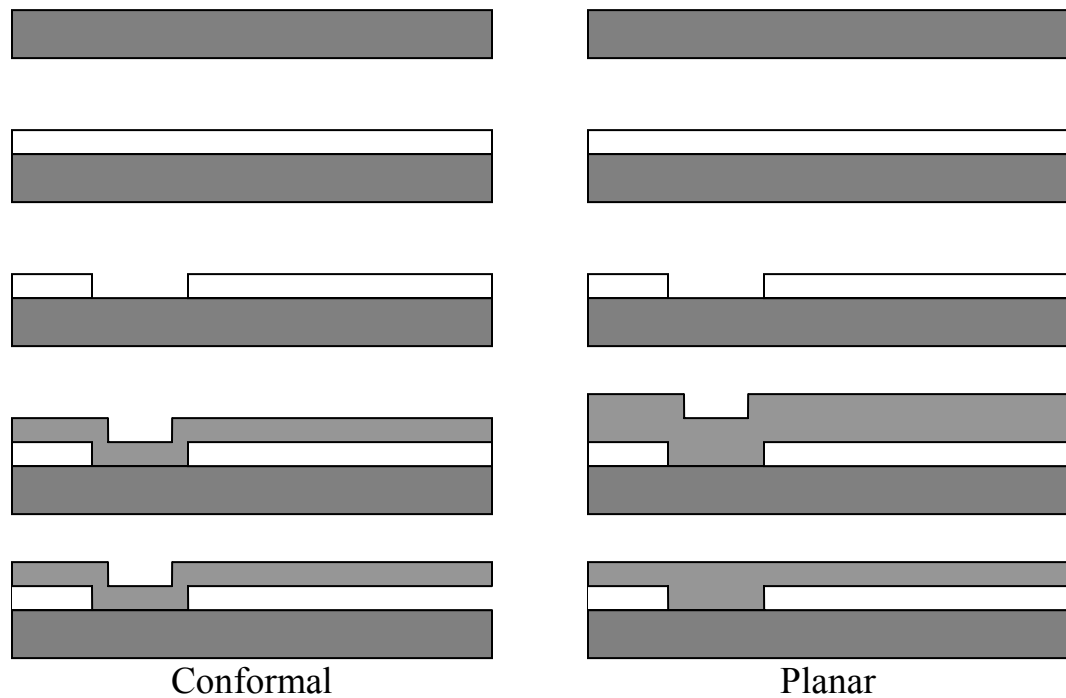


Figure 1.2: Basic fabrication steps of a conformal MEMS process (left), and a planarized process (right).

To date, the vast majority of MEMS devices and processes use silicon as a structural layer [3]. The use of silicon as the basis for the first MEMS processes was mostly a matter of convenience because the equipment and knowledge necessary to process it with a high degree of accuracy and reliability already existed for the fabrication of ICs. Manufacturing of MEMS occurs in very clean environments, known as cleanrooms, due to the high sensitivity of the manufacturing processes to contaminants like dust. The construction and maintenance of these cleanrooms can be very expensive, and, therefore, they are typically only found in larger universities and at specialized companies. Large institutions often offer standardized processes designed to be useful for multiple users as prototyping services for MEMS devices. Although commercial processes based on silicon, metals, and glass are available, silicon has been the most widely used material for MEMS applications for over 20 years.

1.2 Mechanical properties of silicon

Two types of silicon are widely used for the manufacturing of MEMS devices: single crystal silicon (SCS) and polycrystalline silicon (polysilicon). The properties of each type of silicon are very different, as are their intended uses. Single crystal silicon is grown from a tiny seed crystal into large ingots using various processes to form the basis for most silicon wafers. Every atom of silicon in SCS is contained within one giant lattice making the mechanical and electrical properties very ordered and predicable [3].

This crystalline form of silicon is most often used for substrates or large thickness mechanical components, and it usually exhibits little to no residual stress after manufacturing. While the mechanical properties of SCS are predictable, they are not necessarily the same in all directions, due to the anisotropic nature of the material.

Polysilicon is a form of silicon that is widely used for many small mechanical components and surface micromachining technologies. Common deposition methods for polysilicon are chemical vapour deposition (CVD) processes or sputtering, which usually result in thin layers ($\sim 1 \mu\text{m}$). After deposition, an annealing step reduces stress and produces many tiny non-aligned silicon crystals with distinct grain boundaries. Polycrystalline silicon has isotropic material properties in general, but often has residual stress and stress gradients which makes its physical properties more dependent on process parameters than SCS. Table 1.1 summarizes a few mechanical properties of SCS and polysilicon. Polysilicon properties can vary significantly based on the specific deposition conditions [4].

Table 1.1: Published physical properties of single crystal and polycrystalline silicon.

	SCS	Polysilicon
Young's Modulus (GPa)	130.2-187.5 theory [5] 125-180 experimental [6] (orientation dependent)	169 [7], 161 [4]
Poisson's ratio	0.279 [5] $0.048 < \nu < 0.403$ [8] (orientation dependent)	0.22 [7], 0.226 [4]
Yield Strength (GPa)	7.0 [9]	1.20 [7]
Coefficient of Thermal Expansion (K^{-1})	2.33×10^{-6} [9]	3.5×10^{-6} [10] 3×10^{-6} [11]
Thermal Conductivity ($\text{W}\cdot\mu\text{m}^{-1}\cdot\text{K}^{-1}$)	157 [9]	41×10^{-6} [10] 50×10^{-6} [11]

1.3 Uses for silicon

Silicon is an excellent material for a variety of electrical and mechanical applications. Silicon is a semi-conductor, which means that introducing impurities into the crystal lattice (doping) can significantly change its electrical properties. Silicon substrates can be fabricated with variable conductivities depending on doping, and this

ability exists for polysilicon as well. These characteristics allow a large variety of circuits, sensors, and actuators to be fabricated using silicon for many applications. Silicon has been used in the fabrication of devices ranging from micro-manipulators [12], accelerometers [13], pumps [14], and micro-optical components [15], making it an extremely versatile material for MEMS. Mechanically, silicon is also excellent for long-term applications because it has a low coefficient of thermal expansion, a high melting point, and very few fatigue issues when operated within its elastic limits.

Despite the wide application of silicon in MEMS devices and structures, it does have some significant drawbacks. Deposition or annealing temperatures of polycrystalline silicon can be quite high ($>600\text{ }^{\circ}\text{C}$) [16], which can result in damage to previously processed ICs [17]. This issue prevents easy integration of polysilicon MEMS with CMOS processes, and it has been a large limitation on complete microsystems. Other drawbacks include the very high stiffness of silicon, and its low thermal expansion coefficient, which limits silicon electrostatic or thermal actuators to relatively low force, or low displacement operation. For biological MEMS applications, like micro-fluidics, silicon is difficult to work with because it is not electrically insulating, or optically transparent, both of which are required for techniques like electrophoresis or fluorescence microscopy. Despite the weakness of silicon for bioMEMS and low temperature applications, it will remain the dominant material for most MEMS applications for the near future.

1.4 Important concepts in MEMS

When designing devices on the microscale, engineers cannot simply reduce macroscale devices in size and obtain the same results. The materials available are

different, the processing techniques are different, the engineering tolerances are different, but most importantly, the types of forces experienced by MEMS are very different than their macroscale counterparts. The behaviour of structures and devices changes according to scaling laws. These laws describe how the importance or effectiveness of certain physical properties change with characteristic dimensions. Some of these effects are beneficial to MEMS, while others can be detrimental. To understand why MEMS are designed the way they are, it is important to understand scaling laws. A sample of important scaling laws adapted from [18] is listed in Table 1.2.

Table 1.2: Scaling laws for selected MEMS properties [18].

Parameter	Scaling	Comments
Length (L)	L^1	Fundamental
Area (A)	L^2	Fundamental
Volume (V)	L^3	Fundamental
Surface area/Volume (A/V)	L^{-1}	Fundamental
Mass (M)	L^3	Assumes scale-independent density
Inertial Force (F)	L^3	Scales with mass
Power (W)	L^2	Assumes scale-independent density
Power/Volume (W/V)	L^{-1}	Assumes scale-independent density and scale-independent power/mass
Structural natural frequency (ω)	L^{-1}	Assumes scale-independent density and scale-independent Young's modulus
Surface tension	L^1	Assumes scale independence

Table 1.2 demonstrates that some properties are much more dependent on scaling than others. For example, forces that act on the surface of an object, like drag or friction, increase in importance relative to body forces like inertia as the size of an object is reduced. This fact implies that when objects are very small, body forces like gravity can be virtually ignored while surface forces like friction and electrostatic attraction become dominant. The scaling laws also explain why many MEMS devices are attractive for sensing applications, as their response times are inversely proportional to their size. For

applications where MEMS structures or sensors are not in direct contact with other surfaces, reliability and sensitivity can be very high.

For applications where MEMS are in contact with other surfaces, large friction forces can occur that result in device failure. This extreme static friction is a major source of MEMS design failure and is known in the field as stiction. Other potential failure modes for MEMS include electrostatic charging, or contamination from dust or humidity. Most MEMS fabricated in silicon require special packaging technologies to prevent contamination in order to maintain acceptable operation for long-term applications. Even with good process control and sealed packaging, many of the mechanisms in wide use for macro scale devices such as joints, hinges and gears, show significant wear and adhesion failure when fabricated on the microscale due to the lack of lubrication. For this reason, outside of academic articles, hinges and gears have no practical applications in MEMS, and successful devices are primarily based on compliant mechanisms, that approximate the behaviour of joints [19].

1.5 Multi-user MEMS processes

Many different organizations are involved with MEMS research in industry and academia, but the capacity to fabricate devices is limited to organizations that have access to micromachining foundries and cleanrooms. Smaller companies and universities often cannot fabricate MEMS prototypes at their facilities, and they must make use of commercial MEMS foundries. To reduce costs for users wishing to test out MEMS designs, many of these foundries have developed generalized processes for multiple users. By making these processes relatively unspecialized, many designs for different applications can be produced on the same wafer, achieving economies of scale.

Prototyping MEMS devices using these processes allows much lower costs compared to custom processing, and greatly speeds the research process. Many companies offer processes based on CMOS, polysilicon, electro-plated metal, glass, or silicon-on-insulator technologies [20]. Two different multi-user MEMS processes are described below as examples of available process types and capabilities for silicon based MEMS.

1.5.1 PolyMUMPs

PolyMUMPs is possibly the most widely used surface micromachining MEMS process for researchers [1]. MUMPs® stands for Multi-User-MEMS-Process and PolyMUMPs has been available to researchers for over a decade, making this process one of the best understood and popular tools for MEMS prototyping. Despite the economies of scale with PolyMUMPs, an academic price for designs is over \$3000 USD for fifteen 1x1 cm die [1].

The PolyMUMPs process uses two moving structural layers of polysilicon, which are separated from the substrate and each other using a sacrificial layer of phosphosilicate glass (PSG). A layer of gold is added to the second polysilicon layer to make wires on each die. The PSG layers are selectively removed at the end of the process using hydrofluoric acid (HF), leaving the silicon and gold layers behind. The first structural polysilicon layer is only 2 μm thick, and the second is 1.5 μm thick. The minimum feature size that can be reliably fabricated in PolyMUMPs is 2 μm , meaning that the maximum aspect ratio (height to width) of a double thickness structure (POLY1+POLY2) is 3.5:2 or 1.75:1. Processes with generally low aspect ratios are known as highly planar and limit the functionality of many mechanical devices, because structures are typically more compliant out-of-plane than in-plane. The first silicon oxide

layer is patterned with both anchors to the substrate and dimples. These dimples are shallow holes in the glass sacrificial layer that will result in bumps on the underside of the POLY1 layer. These dimples are designed to minimize the area in contact with the substrate for compliant polysilicon structures after release and help to reduce stiction problems. Although this process is relatively simple and has been available commercially for over a decade, it is still a technology widely used by researchers and designers who do not have access to their own foundries or fabrication labs. Figure 1.3 shows a representation of the layer order and thicknesses in the PolyMUMPs process.

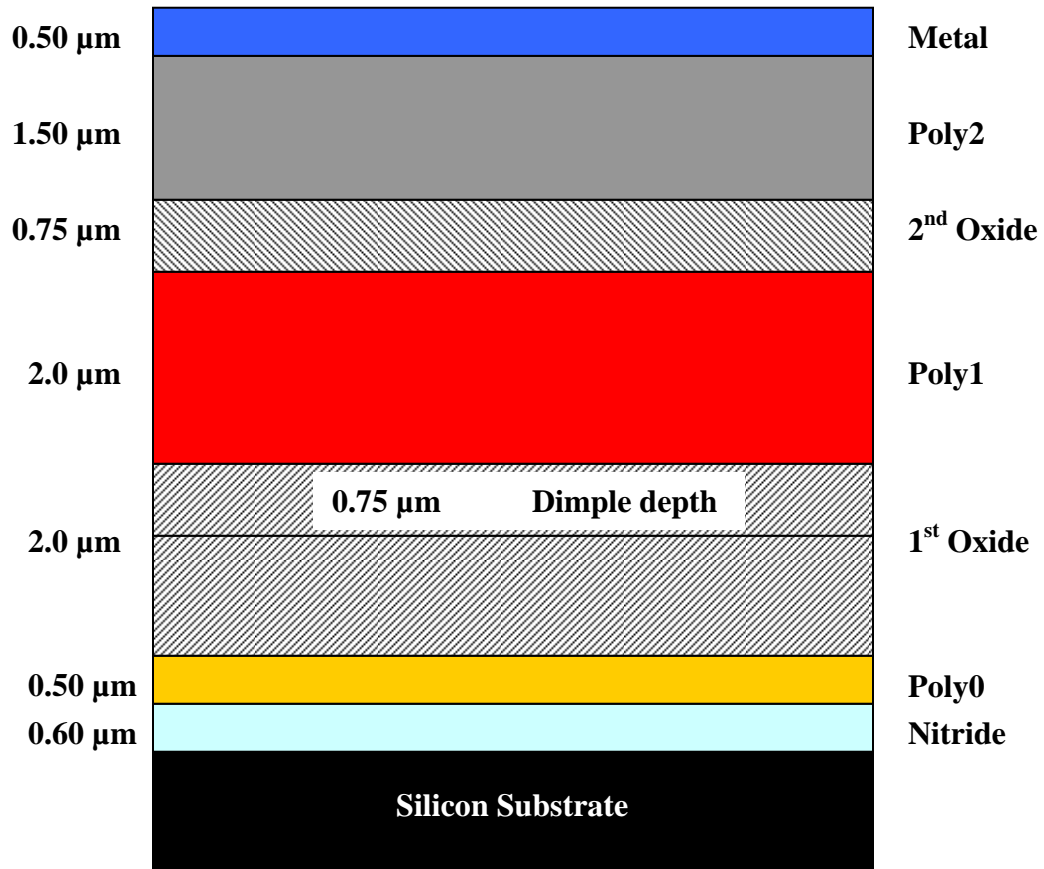


Figure 1.3: Process layers and thicknesses of the PolyMUMPs process.

Processes like PolyMUMPs that have independent structural layers allow for the fabrication of devices like gears, hinges, and multi-thickness structures. Multi-thickness

structures can also allow the assembly of structures using the deformation caused by non-uniform residual stresses [21]; they also permit a range of structural stiffnesses out-of-plane. With only two moving structural layers, PolyMUMPs cannot fabricate true gear chains, but more advanced processes like SUMMiT [2] can permit gears on different levels, for conversion of high speed, low torque motors to produce high forces. These capabilities allow the creation of structures that can replicate the basic functions of many macroscale structures or allow the assembly of complex mechanisms on the chip's surface. Figure 1.4 shows examples of gears, hinges, and multi-level assembled self-assembled structures fabricated in the PolyMUMPs process.

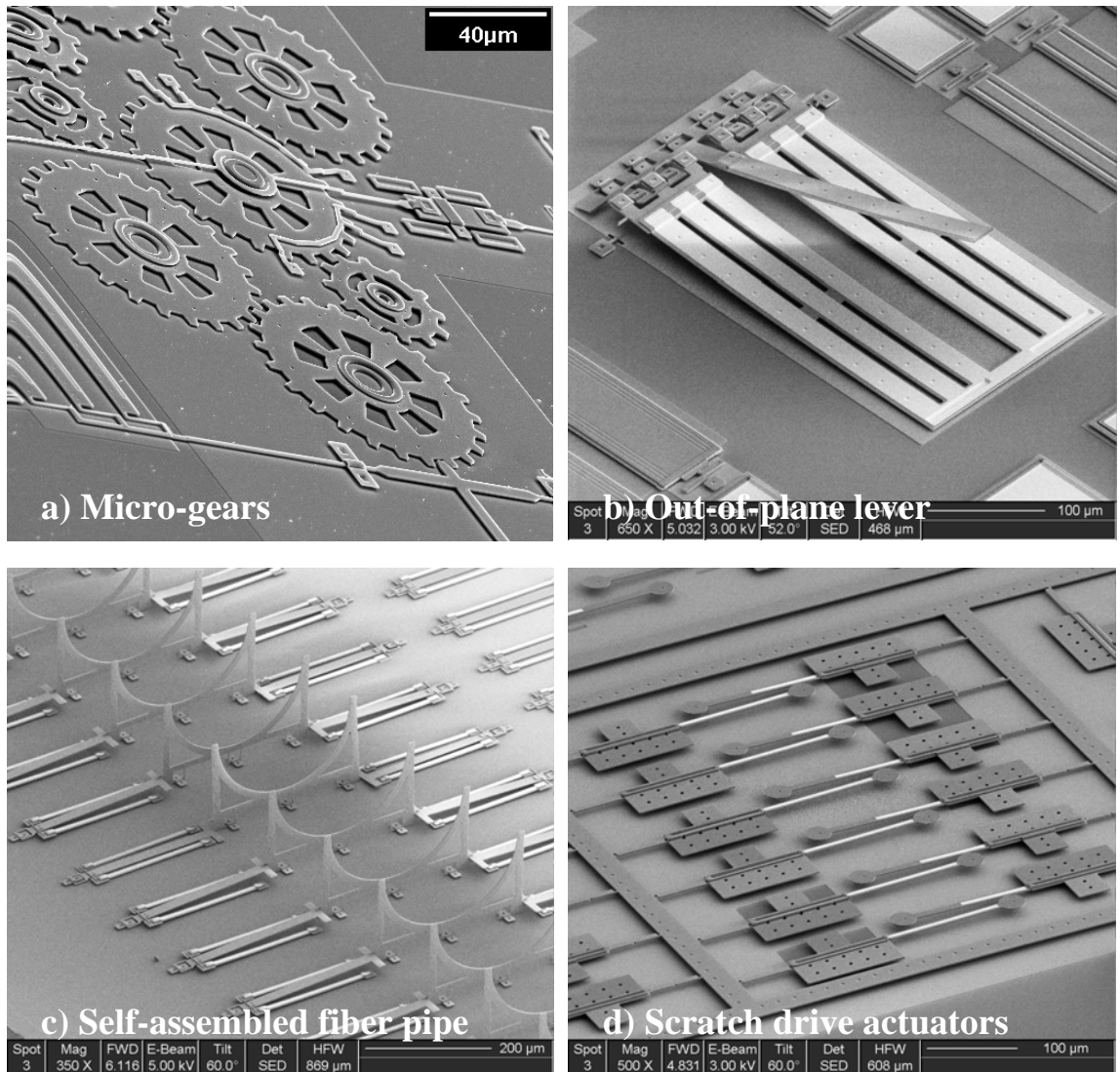


Figure 1.4: Examples of SFU MEMS designs fabricated in PolyMUMPs technology. SEMs are courtesy of Robert Johnstone.

The disadvantages of hinges and gears on the microscale is that they have very poor tolerances and wear out extremely quickly. As a result, although PolyMUMPs can readily fabricate hinged structures, only compliant mechanisms demonstrate significant reliability and yield for long-term operations. In addition, the low aspect ratios of most surface micromachining structures mean that compliance out-of-plane can be much greater than in-plane for large structures, causing many of these structures to fail due to stiction. Besides gears and hinges, PolyMUMPs has been used to fabricate a large

variety of devices including thermal and electrostatic actuators [22], micro-optical components [15], and electrodes for dielectrophoresis [23].

1.5.2 Silicon-on-Insulator (SOI) processes

Surface micromachining processes can be used for many interesting applications, but their surface topographies, internal stresses, and low aspect ratios have been a limitation since their introduction. In contrast, silicon-on-insulator (SOI) processing was developed to make use of more advanced dry etching techniques, such as deep reactive ion etching (DRIE) [24]. This type of etching has allowed thick ($>10\ \mu\text{m}$) SCS sheets to be patterned with aspect ratios greater than 10:1 which results in selective in-plane compliance when released with a sacrificial layer. SOI processing is primarily used for applications where very flat surfaces are desirable, like micro-optics [25]. It has also been used for large displacement linear combdrive actuators [26] because the effectiveness of these actuator designs improves with increasing thickness and aspect ratio. Many commercially available technologies are based on SOI processing, including SOIMUMPs [27] and MicraGEM™ [28]. While the technologies have minor differences, their main advantages are; high aspect ratios, low stress structures, and very flat surfaces.

In general, the fabrication complexity and cost for SOI technologies can be greater than standard surface micromachining, which is primarily due to the cost of SOI wafers and the DRIE equipment. Despite these increased costs, the desirability of high aspect ratio MEMS has made SOI processing a very popular technology. The images in Figure 1.5 show MEMS structures fabricated in both SOIMUMPs and MicraGEM™.

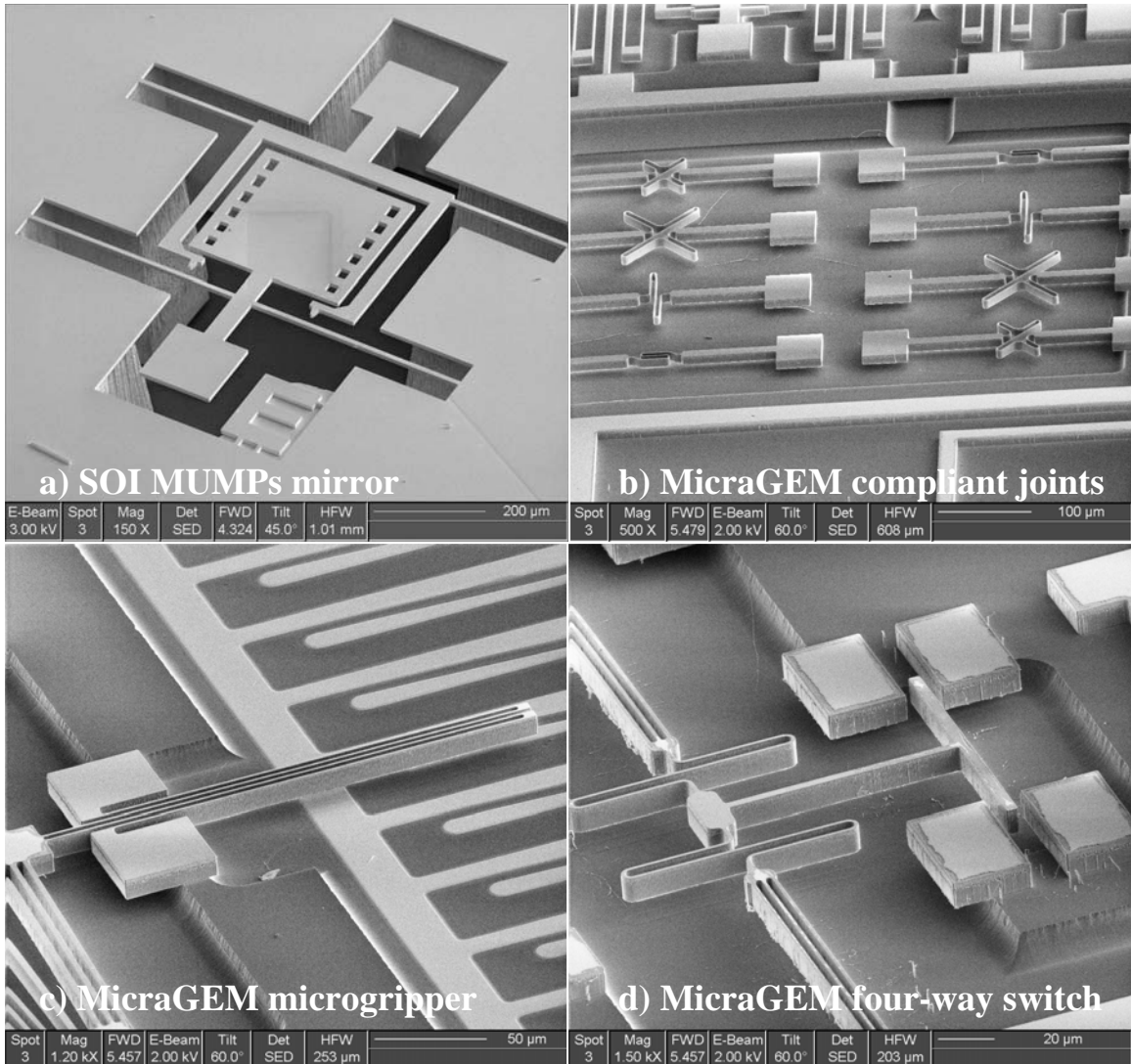


Figure 1.5: MEMS designs fabricated in two different SOI technologies.

With SOIMUMPs, SCS structures are suspended over DRIE etched holes that continue all the way through the substrate. A buried oxide etch stop prevents the structural layer from being etched at the same time as the trench. With MicraGEM™, the SCS structures are suspended over trenches up to 10 μ m deep that are etched in Pyrex. Clearly, both technologies require etching in order to pattern both the structural and sacrificial layers. Because most SOI processes use only a single structural layer, creating hinged structures is not possible; therefore, all devices must be compliant mechanisms.

The second limitation of SOI processes is that, in general, only a single structural thickness is available. As a result, most multi-user SOI processes have been limited to in-plane applications.

1.6 Polymers for micromachining

The availability of multi-user processes has been beneficial for many researchers without access to fabrication facilities of their own. As mentioned earlier, the commercially available multi-user processes use silicon, metal, glass, CMOS technology, and a few other materials; however, no processes use polymers as the basic structural and sacrificial layers.

This lack of polymers is a problem, as the number of polymers that have been used in MEMS has increased over the last ten years. Many of the applications for polymer micromachining have been for low-cost, low temperature microfluidics, or for highly compliant structures. Given that polymer stiffnesses are often several orders of magnitude less than silicon or metals, larger displacements can be achieved using polymers with the same forces, which is beneficial considering the very poor performance of many MEMS actuators with respect to output forces [29].

Perhaps the most important breakthrough for polymer MEMS has been the development of thick film photoresists for permanent applications, the most widely used being SU-8 [30]. Since its introduction a decade ago, SU-8 has become widely used in the MEMS community for its ease of processing, wide selection of possible thicknesses ($< 1\mu\text{m}$ to $> 200\mu\text{m}$ in a single coat [31]), and its ability to be patterned directly with near UV light in thicknesses up to 1 mm. With optimized processing conditions, aspect ratios

of up to 20:1 can be directly patterned using only organic solvents to remove unwanted material. Once exposed to UV light, SU-8 is thermally, mechanically, and chemically stable, making it very difficult to remove as it is a crosslinked epoxy. This ability to rapidly produce permanent high aspect ratio structures with minimum fabrication complexity and cost has made SU-8 very popular for MEMS applications.

To date, SU-8 has primarily been used for specific applications, with processing steps and requirements tailored for the research being published or device being manufactured. The benefits obtained from access to multiple silicon multi-user processes should be extended to a polymer MEMS process that provides access to researchers without fabrication facilities of their own. Given that SU-8 is a commonly used microfabrication material, with reasonably low cost and fabrication complexity, it is an ideal candidate to form the basis of a multi-user polymer MEMS process.

1.7 Motivation and scope of research

The primary purpose of this thesis is to develop an all polymer MEMS process that has similar capabilities to SOI processes with respect to structure thicknesses and aspect ratios. Creating a multi-user polymer MEMS process could significantly reduce the cost and time involved in prototyping MEMS structures, while also providing insights into the reliability of polymers for compliant microstructures. The negative photoresist SU-8 was chosen to be the structural material for this polymer MEMS process due to its unique processing characteristics and wide acceptance as a structural MEMS material. Polystyrene is shown to be a reliable and inexpensive sacrificial layer for SU-8 in this work, and the basic patterning and processing steps for this polymer may be modified for other sacrificial layers.

Successfully designing a multi-user polymer MEMS process required determining suitable sacrificial layers and processing techniques, and characterizing several common MEMS devices fabricated in this process. The process is designed to require minimum processing time, while offering various layer thicknesses and device sizes without significantly altering processing parameters. A new multi-level patterning technique was developed for sacrificial polymers that only requires a single reactive ion etch step and can be adapted for other organic sacrificial materials. After developing the standard processing steps, the compliant SU-8 microstructures and actuators were characterized. Our results produced a new thermal actuator design optimized for linear displacement using SU-8, and the first reported SU-8 based untethered electrostatic actuator. All temperatures required in this process are below 200°C, making it one of the lowest temperature MEMS processes available. This low temperature may allow for the direct fabrication of polymer MEMS devices on previously processed electronics wafers. Advances have been made with respect to packaging technologies that make this thesis the first published work describing the integration of SU-8 with commercially used wirebonding technologies, which greatly improves the commercial applications for polymer MEMS in general, and the use of SU-8 for MEMS specifically.

2 FABRICATION FACILITIES AND EQUIPMENT

2.1 Introduction to cleanroom facilities

All development of the polymer MEMS process described in this work was completed in the School of Engineering Sciences cleanroom at Simon Fraser University. To understand why certain materials and process steps were used, it is necessary to understand the available equipment and technologies. As much as possible, processing was simplified to avoid using equipment that was in heavy use or techniques that could not be easily replicated by other researchers. Access to metal deposition and dry etching were limited in the early stages of experiments, leading to a process that minimized their use. The use of low-cost, flexible emulsion masks, rather than standard glass/chrome masks for nearly all work for this thesis required innovations with respect to alignment and exposures, but significantly increased the speed at which new designs could be fabricated.

The equipment and techniques involved in fabrication and testing of polymer MEMS is described in this section. Fabrication was completed in the engineering science cleanroom, while the majority of tests were conducted within a mini-cleanroom module built specifically for this purpose [32].

2.2 Cleanroom overview

The engineering science cleanroom is divided into two distinct areas; a relatively high particle count class 1000 cleanroom, and a more highly filtered cleanroom that is

approximately class 100. These class numbers give an upper value of the number of particles $>0.5\mu\text{m}$ in size within a cubic foot of air, where lower numbers correspond to a higher cleanliness level. For microelectronics, the cleanliness requirements for manufacturing are very high, due to the high sensitivity of electronics to tiny contaminants during manufacturing. With MEMS, larger features are slightly less sensitive to contaminants, but still require a great deal of care during manufacturing.

The bulk of the sensitive fabrication equipment is located within the class 100 cleanroom at SFU. In addition, because UV sensitive photoresists are used for all patterning steps, this class 100 cleanroom is illuminated only with fluorescent lights that have the blue end of the spectrum filtered out, resulting in a yellow appearance of the room. Within this yellow room are located the 7 major pieces of equipment used in MEMS manufacturing: a spin-coater, ovens/hotplates for baking, a UV aligner, a combined plasma-enhanced chemical vapour deposition/reactive ion etcher (Axic Benchmark 800 PECVD/RIE), a sputterer, a wet bench/fume hood for acids and bases, and a wet bench for solvent processing. All of these items, with the exception of the PECVD, are used during processing of polymer MEMS.

Within the class 1000 room is equipment used for packaging, characterization, and measurements, including microscopes, a profilometer, a wafer scribe, wirebonders, and a micro-probe station. All of this equipment is used to test polymer MEMS devices once they have been fabricated and released, and they are important for determining the effects of different processing steps. The microscopes and profilometer are used often during the processing to provide feedback on process quality.

2.3 Class 100 cleanroom equipment

The class 100 cleanroom houses the equipment most often used during the manufacturing of polymer MEMS, so detailed descriptions of the equipment are provided below. Any special techniques for using these items are noted, as the operator's actions can have significant effects on the overall process quality.

2.3.1 Spin-coater

A spin coater is designed to spread a liquid on the surface of a flat wafer quickly and evenly. The thickness of this layer is a function of liquid viscosity, solids content, and spin speed. These coaters are most commonly used to spread a photoresist film over a wafer for patterning, and therefore need to be accurate in spin-speed and time. The specific model of spin-coater available in our lab is a relatively old model manufactured by Headway Research Inc. and is shown in Figure 2.1.



Figure 2.1 Full view and close up of the spin coater used for coating all polymers in this work.

The wafer is held in place on a spinning chuck by applying a vacuum, while spin time and speed can be set independently. No control is provided over acceleration up to the set spin-speed, nor is there any control over deceleration after completing the cycle. The spin-coater, in general, reaches full speed within a second and also decelerates within

a second when finished. For most films, spin-speed is set between 1000-4000 rpm, although the spin coater can operate at higher speeds. A faster spin-speed will typically provide a more even coating, but where thicker layers are required, operating at low speeds is necessary. A line of aluminum foil around the wafer chuck is used to catch any material that has been thrown off the wafer. This liner can be disposed of with other hazardous materials, leaving the underlying spin coater clean. This method is an excellent way to reduce cleaning time, and prevents excess polymers from clogging internal parts within the spin coater after extended use. Although this particular model is very basic, it reliably coats wafers with minimal problems.

2.3.2 Hot-plates/ovens

After spin-coating photoresists or polymers onto wafers, a baking step is usually required to drive off remaining solvents in the film, or to relax and/or densify the polymer on the wafer. For standard photoresists and some polymers, two actively controlled isothermal ovens are used for this baking step. These ovens are held at either 100 °C or 120 °C because these temperatures commonly used for standard photoresists in cleanroom lithography. Baking times within these ovens range from 5-30 minutes depending on the photoresist thickness used. These ovens have effectively no ramping of temperatures, so their use is not recommended if the spun material is vulnerable to thermal shocks. In general, these ovens are used in polymer MEMS processing only for sacrificial layers and standard photoresists.

SU-8 is baked on HP30 digitally controlled ramping hotplates, from Torrey Pines Scientific [33], shown in Figure 2.2. These hotplates provide highly repeatable baking temperatures with programmable temperatures and ramping rates. Through front panel

access, a desired baking temperature, a linear temperature ramp rate, and an auto-off feature after a selected baking time may all be controlled. These hot-plates can only bake one 4" wafer at a time. The hot plates can be set to temperatures up to 450 °C, and with temperature ramps as great as 450 °C/hr. For this work, most bakes for SU-8 layers were set to 95 °C, with a 300 °C/hr ramp up. For a typical ambient temperature of 20 °C, this means that a ramp to 95 °C can be achieved by setting a ramping time of 15 minutes on the hotplate timer in addition to the total baking time required at 95 °C. Temperature ramp rates set to 450 °C/hr often result in an overshoot of as much as 10 °C over the desired final temperature before stabilizing. For this reason, most bakes on these hotplates ramp at no more than 300 °C/hr, which result in a overshoot of only 2 °C. The auto-off feature turns off the heater when the timer finishes and effectively cools the hotplate and wafer with a first-order response. Cooling of the hotplate between 95 °C and 50 °C takes approximately 15 minutes with this option, and is referred to as a 'natural cool' step in the lab notes. Cooling in this manner is typically slow enough to avoid thermal shock for the temperatures used and will not negatively affect process quality. Natural cooling to below 50 °C was used in all SU-8 baking steps unless specifically noted.



Figure 2.2: Isothermal ovens (left) and digital ramping hotplates (right) used for baking of polymer MEMS wafers.

Hotplates were calibrated when received, but because the top surface is ceramic, there can be several degrees difference across the plate when baking. A thermocouple is used to test the hotplate temperature at different locations while held at a defined temperature. The average measured value is used to correct the digital output on the hotplate and keep relatively consistent results between hotplates. Despite these calibrations, there are still small differences between hotplates, so where possible, all baking steps for a single wafer are completed on the same hotplate. Figure 2.3 shows a temperature distribution across a hotplate before and after a silicon wafer is placed in the centre.

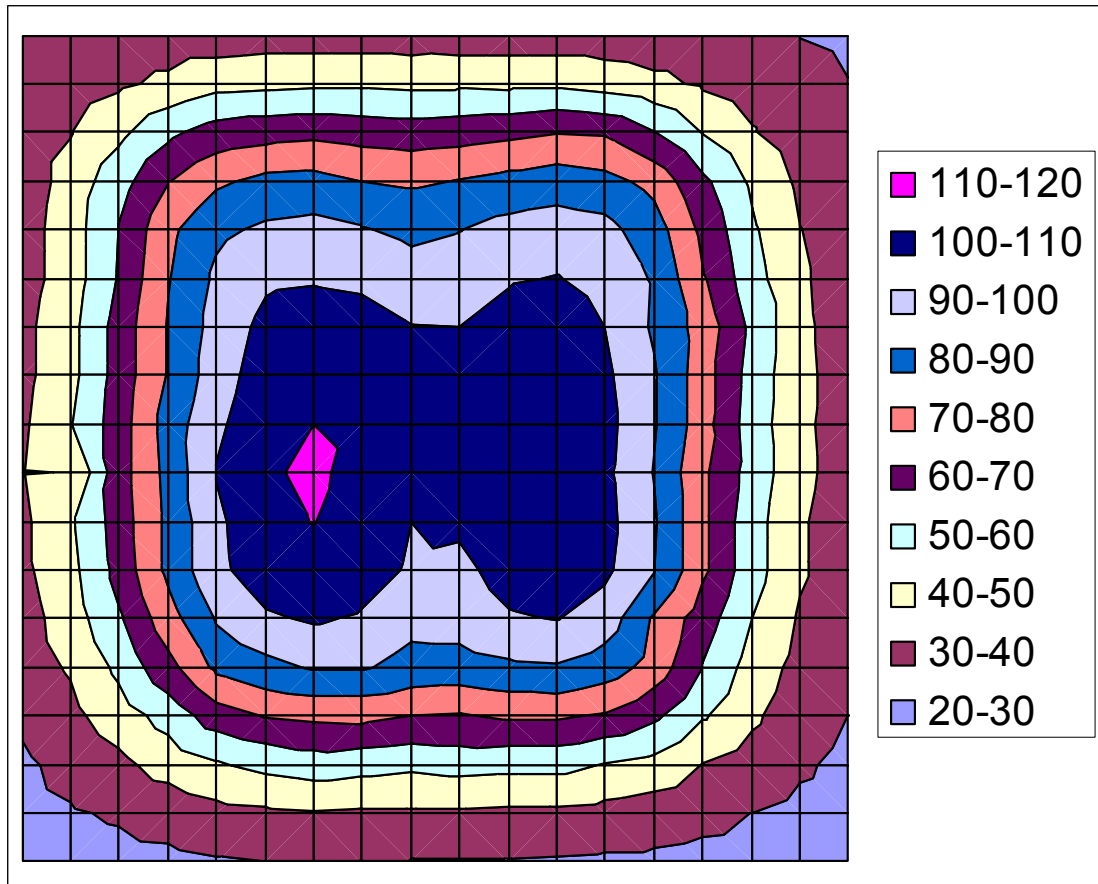


Figure 2.3 Temperature distribution on an HP30 digital hotplate held at an average temperature of 100 °C. The area is 18x18 cm.

2.3.3 UV aligner

An ultra violet (UV) aligner is one of the most critical pieces of equipment for all MEMS processing. It provides a collimated UV light source for exposure of photosensitive materials, and the ability to align one layer to the next with a high degree of accuracy. The Quintel aligner used in our cleanroom is shown in Figure 2.4.

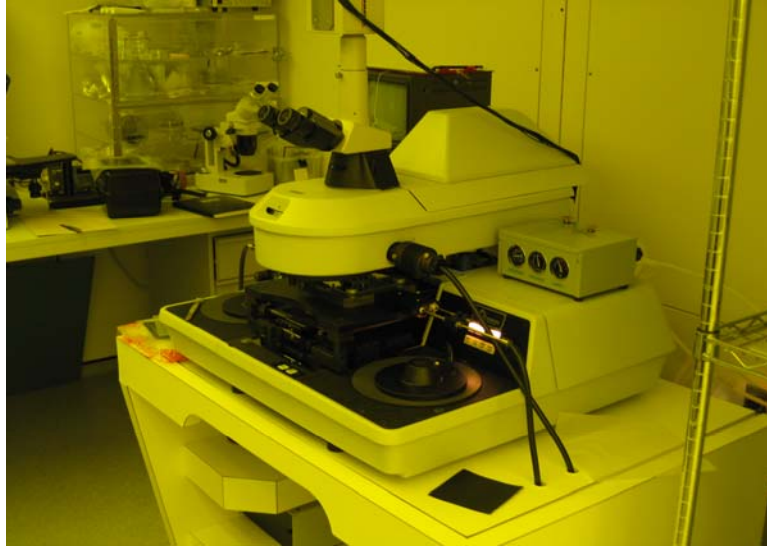


Figure 2.4 Quintel UV aligner.

This particular aligner uses an i-line source, which emits strongly at 365 nm. Measured emission at this wavelength is in units of mW/cm^2 ; multiplying this power density by the total exposure time provides the total dose in mJ/cm^2 . During early experiments, the power output of the UV aligner was $10 \text{ mW}/\text{cm}^2$, but during later work has been either 8 or $6 \text{ mW}/\text{cm}^2$. For reasons that are explained later in this thesis, these values are very important for the polymer MEMS process.

The UV aligner is connected to a vacuum line that is designed to hold the wafer on the chuck and a mask securely in position over the wafer. The wafer is firmly pressed against the mask to ensure full contact in order to minimize any gaps between the wafer and the mask. Good contact between the mask and the wafer is the most critical parameter to achieving the desired feature sizes when exposing sensitive photoresists like SU-8. When both the wafer and the mask are rigid, the vacuum holds both wafer and mask in place; however, if a flexible emulsion mask is used, significant problems can occur.

Part of the attraction to polymer MEMS processing is low cost and rapid turnaround times. Unfortunately, fabrication of novel structures can only be completed with the creation of new masks for each MEMS layer. Typically, this can require weeks between submission, writing, and shipping, with a cost of hundreds of dollars per mask when the masks are defined with a chrome layer on glass plates. Alternatives, in the form of emulsion printing on acetate or Mylar sheets, can be produced within days for less than \$20 per mask with minimum features as small as 5 μm [34]. The cost and time advantage is great enough that virtually all masks used in this work were printed on Mylar sheets. However, this method has drawbacks and it poses significant challenges for creation of polymer MEMS. Unlike chrome masks, the Mylar masks are flexible and buckle when held by vacuum or pressed by the wafer. This buckling results in features being stretched or compressed across the wafer and is unsatisfactory if good contact and alignment is required.

To compensate for this vacuum induced buckling, a new method of holding the Mylar masks in position during alignment and exposure was developed. It requires the use of neodymium rare earth magnets and a glass cover plate to keep the Mylar mask in position over the wafer during exposure. Rather than pulling down on the Mylar, the magnets press down on the glass cover plate over the Mylar, creating enough friction to hold the mask in place while also providing a rigid backing after the wafer is brought up in contact to the mask. Previous to this work, mylar masks had been taped to glass plates at SFU prior to exposures, but the use of magnets is superior because it does not contaminate the mask with adhesives, introduce any extra thickness to the bottom part of the glass plate, or require that a flexible mask be trimmed and secured to glass for each

exposure. Using magnets to secure a flexible mask is a simple solution that has yielded great dividends for integration of low cost mask materials. Figure 2.5 shows an example of securing a Mylar mask through magnets.

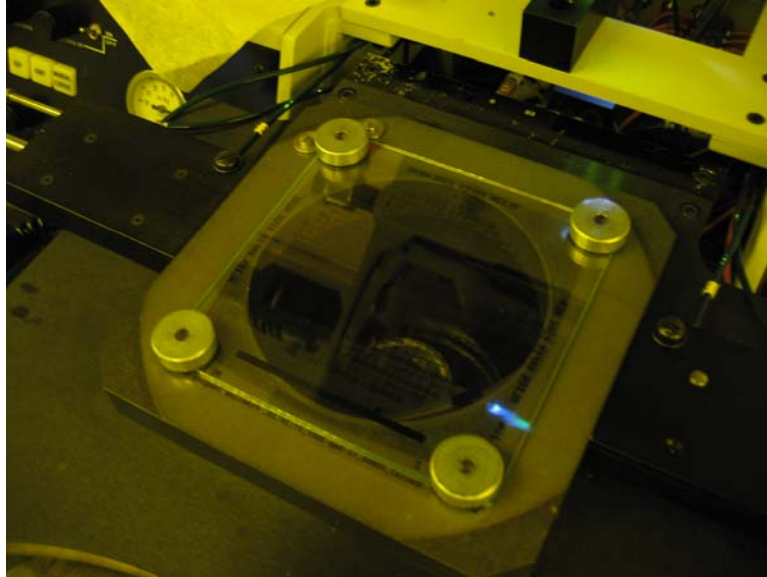


Figure 2.5: Process of securing a Mylar mask in position with a glass cover plate and powerful magnets. The magnets are attracted to the ferro-magnetic material in the corners of the mask holder. Stronger magnets are required for thicker glass plates.

2.3.4 PECVD/RIE

The reactive ion etch (RIE) machine is used for two main purposes for polymer MEMS processing. It dry etches polymers that otherwise cannot be developed cleanly to produce good features, and it can activate surfaces to enhance adhesion between layers. Three gases are commonly used for reactive ion etching in this work: nitrogen, oxygen, and carbon tetrafluoride (CF_4). Nitrogen is an inert gas used mainly for venting the chamber and diluting any hazardous gases prior to opening the RIE chamber. Oxygen is the primary gas used for etching of polymers, and will remove nearly any organic material in a process step also referred to as ashing. The CF_4 is used to change the etching characteristics, potentially resulting in smoother layers [35], and will remove

most inorganic materials using fluorine chemistry that may be mixed with the polymer layer. In general, an oxygen rich RIE is required for all polymer etches and surface activations.

2.3.5 Acid/Base wet bench

The acid/base wet bench is located under a fume hood within the class 100 cleanroom, and is used when working with all liquids and highly volatile solvents to protect users from fumes. Almost all developments using organic solvents are completed in this area, as was all early work that used corrosive liquids for inorganic patterning. Pre-cleaning of silicon wafers prior to metal deposition also occurs in this area, making it the main location for all wet processing when creating polymer MEMS structures.

2.3.6 Solvent wet bench

The solvent wet bench is an open area with laminar air flow to trap solvent fumes. A DI water source, hotplates, spin-dryer, dry N₂ gas source, and an ultrasonic bath are all part of this area, which is easier to work at than the acid wetbench. Drying of wafers and developing of most photoresists is completed in this area. The ultrasonic cleaner is moved to the fume hood when high agitation development in volatile organic solvents is required.

2.4 Class 1000 Cleanroom Equipment

The equipment in the class 1000 cleanroom is seldomly used for manufacturing, but is important for characterizing the quality of the process and determining the manufactured dimensions. The microscopes and profilometer in this area are used extensively during the processing in order to determine layer thicknesses and quality of feature transfers,

while the wafer scriber, wirebonders, and micro-probe station are used to create, package, and test die from a polymer MEMS wafer.

2.4.1 Microscopes

Two microscopes are located within the class 1000 cleanroom: one is a long focal length microscope attached to a micro-probe station that is necessary when manipulating moving parts on the wafer after fabrication; the other is a short focal length design that is mainly used to examine very small features and capture them with an attached camera system. Due to the relatively thick structures produced in the polymer MEMS process, the long focal length microscope is more useful for device inspection after release.

2.4.2 Profilometer

The profilometer is a piece of equipment that drags a stylus across a wafer, while recording the topographical change on a line. This piece of equipment is very important for characterizing the thickness of layers greater than a few μm . Other equipment, such as, elipsometers, are appropriate to characterize layers that have relatively well known thicknesses and refractive indices, but are not suitable for thicker layers with variable surface morphologies and refractive indexes.

When fabricating multi-thickness layers for polymer micromachining, the profilometer is an invaluable tool to measure the thickness variations across a wafer. The profilometer is used after every thick photoresist development to determine the total thickness which is used to estimate the etch time of the subsequent step. Feedback on the layer thickness, prior to and after etching, also helps characterize the etching quality, speed, and repeatability.

2.4.3 Wafer scriber

The wafer scriber is used to break a fabricated wafer into multiple individual die. The minimum size of the final die using this equipment is partly determined by operator skill, but can be as small as several mm². The scriber works by scratching a small line in the surface of the silicon wafer in line with a crystal plane. The silicon crystal will cleave easily along its crystal planes; the scribe lines are required to direct the breaks at the desired locations. Because only <100> orientation silicon wafers were used for this work, these crystal planes are both parallel and perpendicular to the major flat of the wafer, allowing orthogonal fractures that result in square or rectangular die lined up with the fabricated structures. If silicon wafers of different orientations are used, a wafer saw is required to cut the die into the desired shape. The use of a scriber to create die also allows the release of MEMS structures to be completed on the wafer level, rather than as individual die after cutting on a wafer saw because spraying lubricant and coolant is not required during the dicing process.

2.4.4 Wirebonders

The class 1000 cleanroom has two different wirebonders: a semi-automatic aluminum wedge-wedge ultrasonic bonder, and a Mech-EI NU-829 semi-automatic ball-wedge gold wire bonder. Wirebonding is the most used packaging technology for electrical connection of microchips today, and gold bonding is the most common wirebonding technique [36]. The aluminum ultrasonic bonder was acquired relatively recently, and was not used for this work. The gold wirebonder is a much older piece of equipment and was used for all packaging of polymer MEMS structures. Packaging of MEMS is a frequently overlooked aspect of academic research, but for this work the

ability to package polymer MEMS using commercially available equipment was necessary to demonstrate the feasibility of a polymer MEMS process for multiple users. Experiments with these packaging technologies were completed after most other process aspects had been characterized.

2.4.5 Micro-probe station

The micro-probe station was used to test released structures for mechanical and electrical properties without having to package devices first. A stage with a vacuum source holds a full wafer in place while micro-probes manipulate mechanical structures or provide power to electrical systems on the chip. Primarily, this setup was used to test the polymer MEMS structures were properly released properly from the substrate, would not plastically deform under normal deflections, and test for a variety of mechanical failure modes. Where possible, these tests were also conducted within the mini-cleanroom facility [32] fabricated outside the main cleanroom area, so as to not monopolize time on the probe station. Experiments on thermal and electrostatic actuators, and mechanical trials on compliant assembly mechanisms [37, 38] were all first completed on this probe station.

2.5 Mini-cleanroom equipment and design tools

The mini-cleanroom is a small semi-clean environment designed and built for the testing of MEMS devices. Many polymer MEMS structures are relatively insensitive to contamination by dust or other particulates once processing is complete, so the cleanliness standards for the test area are less stringent. The fabrication and use of the cleanroom module are described in [32], and will not be covered in detail in this thesis.

Within this module is a probe station, AC and DC power supplies, AC and DC high voltage amplifiers, and a computer. The computer can record pictures through a camera attached to the probe station microscope and it controls various electronic equipment through data acquisition cards. Figure 2.6 shows the interior of the mini-cleanroom.

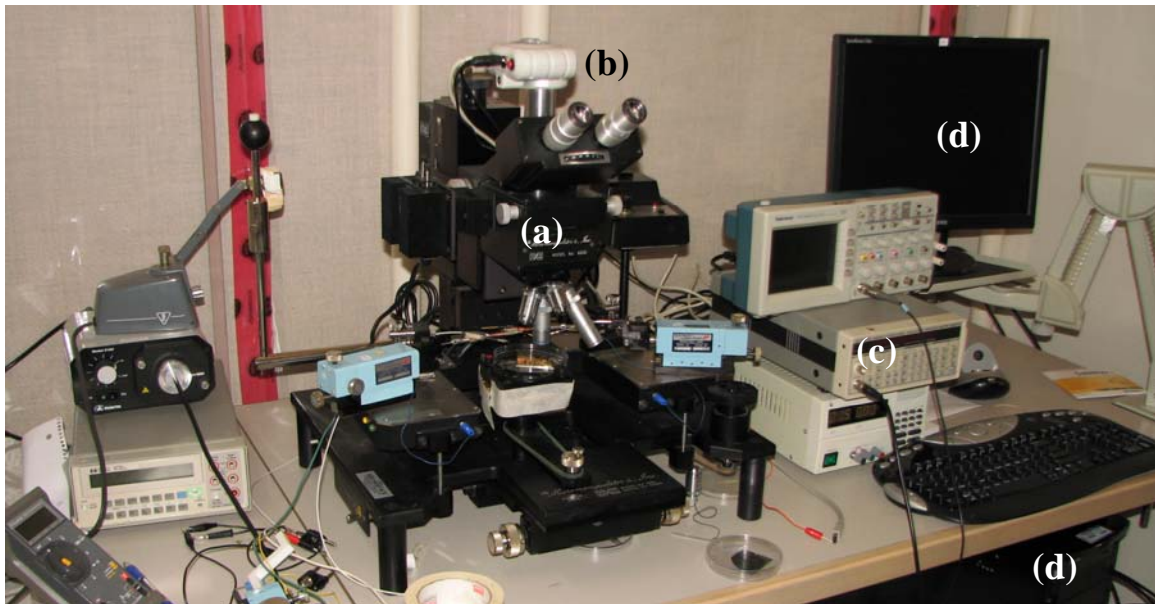


Figure 2.6: Photograph of mini-cleanroom setup with the probe station (a), camera (b), function generator (c), and computer (d). Polymer MEMS can be inspected and tested as either a full wafer, or as individual die under the microscope.

This setup is used for all experiments to measure device motion, or material properties. For instance, a typical experiment on a thermal actuator will involve taking pictures of the actuator for various input powers, and using National Instruments Vision Builder software for Automated Inspection [39] to compare deflections to the unpowered condition. This Vision Builder software is a powerful tool for measuring a wide variety of device geometries or motions through calibrated pictures, and has been extensively used in this thesis to measure fabricated dimensions, actuator deflections, and material properties.

Outside of this mini-cleanroom were computers with CAD tools used for designing masks used for this work. The CAD program used most often by the author is L-Edit. It is a less common tool in industry, but it is more user friendly and it much better at defining non-Manhattan geometries. Masks were generated using the PolyMUMPs design file, which was used primarily because most previous MEMS designs submitted through commercial foundries used this process and the design file was chosen for aesthetic reasons. Masks were typically 5x5 inches in size, with individual die set as either 1x1 cm or 5x5 mm. In this configuration, over 50 1x1 cm die could be produced on a single 4" wafer. Mask designs were submitted to Fine-line imaging to be printed on Mylar sheets and costs approximately \$30 per mask with a 5 μm minimum feature size.

3 SU-8 FOR MEMS APPLICATIONS

3.1 Introduction

Creating a new MEMS process with polymers was selected partly out of interest, and partly out of necessity. Very little access to the equipment necessary to create high aspect ratio MEMS in silicon, like deep reactive ion etching, was available at SFU. Commercially fabricated MEMS is available through the Canadian Microelectronics Corporation [20], but this option is time consuming and expensive. Many times a MEMS designer simply wants to test whether an idea is practical or not, without needing a large investment of resources or long times between fabrication runs.

Designing a process that could be easily duplicated at other facilities that required minimal equipment time and costs, and could be of use to multiple users was a significant challenge, but one that would be of great value to many researchers at SFU and elsewhere. Developing a polymer MEMS process could potentially reduce the cost of failure in terms of money and time, and would encourage more aggressive designs by researchers and reduce the time between design iterations. The use of polymers for MEMS and microfluidics was introduced during an early course taken at SFU, and the possibility of creating an all polymer, multi-aspect ratio MEMS process for novel applications became apparent. The backbone of this process would be the use of SU-8 as a structural material.

3.2 Physical properties of SU-8

SU-8 is an epoxy based negative tone photoresist optimized for i-line (365 nm) exposures. A negative photoresist becomes insoluble in developer once it is exposed to light, unlike positive acting resists, which are insoluble unless exposed. Figure 3.1 shows examples of the behaviour of positive and negative resists behave when exposed to light.

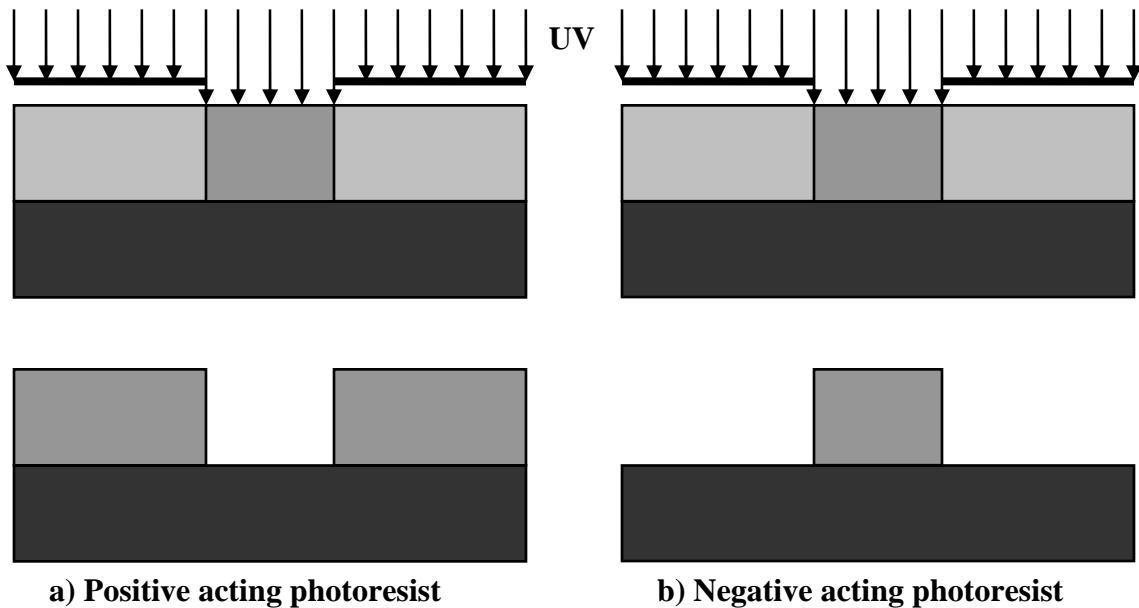


Figure 3.1: Behaviour of positive and negative tone photoresists after exposure and development.

SU-8 is sensitive to light at wavelengths below 400 nm, but does not absorb light strongly until the wavelength is below 360 nm [40]. Because light can penetrate deeply into SU-8, layers several hundred μm thick can be exposed in a single step [40], resulting in nearly vertical sidewalls. For thicker layers, aspect ratios up to 20:1 are possible using standard lithography techniques and greater still when alternate techniques are used [41]. The main components of SU-8 photoresist are an epoxy base, a photoinitiator and a solvent. When exposed to UV light, the photoinitiator decomposes into an acid, which initiates a crosslinking reaction between SU-8 monomers, into a large epoxy network.

SU-8 must be post exposure baked to accelerate this reaction, and the degree of total crosslinking depends on the input exposure dose, and the time and temperature of the post exposure bake. The solids content suspended in the solvent determines the viscosity of the mixture and the ultimate layer thickness for a given spin speed. To choose an appropriate SU-8 formulation for a specific application, the desired layer thickness is chosen, and examining the data sheets on thickness versus formulation and spin speeds will allow an appropriate SU-8 formulation to be selected. Nearly all the SU-8 used in this work are part of the SU-8 2000 series provided by the MicroChem Corporation [31], with SU-8 2010 being the most common formulation used. In this series, the solvent is cyclopentanone, which dries faster and adheres better to most substrates than the basic SU-8 formulations, which uses GBL as the solvent. The mechanical, electrical, and thermal properties of SU-8 have been thoroughly investigated by other researchers [42-44]. The electrical properties are relatively well understood, but mechanical and thermal properties have been found to vary significantly with processing conditions [44]. The most important variable for material properties appears to be the degree of crosslinking [44], but there is very little published data on the exact correlation between crosslink density and specific material properties. Table 3.1 shows a selection of the physical properties of SU-8 taken from various published sources.

Table 3.1: Published physical properties of SU-8

Property	Value	Comments
Young's Modulus: E	4 GPa [42], 1.6-2.7 GPa [44], 3.8-5.4 GPa [45]	Process dependent, degree of crosslinking not given
Yield strength (tensile)	33.4-73.1 MPa [44]	Process dependent, degree of crosslinking not given
Poisson's ratio	0.22 [45]	Assumed value
Glass transition temperature (T_g)	~50 °C (uncrosslinked) 238 °C (fully crosslinked) [44]	Increases with increased crosslink density
Coefficient of thermal expansion (CTE)	$52 \pm 5 \times 10^{-6} \text{ K}^{-1}$ [30, 46]	Temperature dependence not known
Thermal conductivity (k)	$0.3 \text{ W}\cdot\text{m}^{-1}\cdot\text{K}^{-1}$ [30]	Temperature dependence not known
Refractive index (n)	1.67 @ 365 nm [47] 1.59 @ 633 nm [48]	Uncrosslinked at 365 nm Crosslinked at 633 nm
Relative dielectric constant (ϵ_r)	3.2 @ 10 MHz [30], 2.9 @ 1 THz [49]	Processing conditions not given

SU-8 in its normal form is nearly transparent to visible light, and is an electrical insulator. Although adding nanoparticles can change its electrical [50] and mechanical [51] properties, this thesis work only used unmodified formulations available through commercial manufacturers. Using an unmodified formulation of SU-8 allows this work to be of greater use to engineers working with polymer micromachining and reduces the variables required to characterize the process.

3.3 History of SU-8 applications and uses

Since its introduction to the MEMS community a decade ago [42], SU-8 has become one of the most popular polymers for micromachining in the academic community. Its original use was as a replacement for Polymethylmethacrylate (PMMA) in high aspect ratio micromoulding and electroplating in LIGA processing [52]. PMMA requires high energy X-rays [52], or deep UV light to pattern, and requires very large doses of X-ray energy ($\sim 3500 \text{ J/cm}^3$) to successfully develop high aspect ratio structures [53]. SU-8 on the other hand can produce structures with aspect ratios up to 20:1 with a near UV light source and with significantly lower doses. SU-8's disadvantage as a mould

for electroplating is that it cannot be removed in organic solvents once crosslinked and, therefore, requires time-consuming plasma ashing, or complicated lift-off systems. Other researchers realized that SU-8 could form microchannels and reservoirs with much greater control than other materials such as glass, leading to a number of papers on its use in microfluidic devices directly [54], or as a negative for the soft lithography of PDMS channels [55].

After several more years, SU-8 was used as a compliant material for microvalves and microgrippers [56, 57], demonstrating that the material had potential for structures that were not fixed in place on the substrate. These efforts marked the first steps in demonstrating that SU-8 is a truly functional material. Actuators fabricated using SU-8 were first powered either pneumatically [58] or with a shape-memory alloy (SMA) [59]. While these examples demonstrated that SU-8 could be part of an actuator, the material itself was still passive, acting only as a compliant mechanism that would amplify existing displacements. In 2003, the first actuator that used SU-8 as an active material was reported by Kim *et al.* [60]. This design was a bi-morph actuator that used the different coefficients of thermal expansion between polysilicon and SU-8 to make an out-of-plane actuator for the eventual purpose of probing living cells [60]. The actuator used a metal resistor in contact with the SU-8 to heat the polymer and produced significant vertical deflection ($>10\ \mu\text{m}$). Other thermal actuators using SU-8 with integrated resistors quickly followed. Nguyen *et al.* fabricated and tested an in-plane microgripper powered by a patterned metal layer on top of the structure [61], while Chronis and Lee demonstrated a much smaller SU-8/gold microgripper operating in air and under water [62]. In both these cases, however, the processing of the actuators was quite complex.

The gripper described in [61] was over 6000 μm long and used a shadow mask to define the metal layer on top of the gripper after the SU-8 was developed. The silicon substrate itself was a sacrificial material, meaning that this structure cannot be fabricated in large quantities or be used for on-chip manipulation. In the device described by [62], a thin polysilicon sacrificial layer was removed by Xenon difluoride (XeF_2) gas, but a blind cut of the underlying substrate was required to make the gripper hang off the silicon. This release method is not practical if the SU-8 actuator is to be integrated with other silicon components, as the XeF_2 gas would attack the silicon indiscriminately. Despite the weaknesses of each individual design from a processing standpoint, they are all excellent examples of how SU-8 can be a potentially useful mechanical material for active applications.

Besides compliant mechanisms and actuators, SU-8 has also been gaining popularity as a component for many sensors. Because it is a good thermal and electrical insulator, SU-8 has been used for many devices for integration with sensing electrodes [63, 64] and has also been used as a proof mass for micro-accelerometers [65]. As the applications using SU-8 as a structural or active material have increased, so has the demand for an acceptable material for a sacrificial layer. Despite the nearly 10 years of SU-8 processing, a cheap, effective, and easily processed sacrificial layer for SU-8 has been difficult to find.

3.4 Potential sacrificial materials for SU-8

When choosing a material for a sacrificial layer in a MEMS process, several key criteria need consideration:

- Compatibility with structural material;
- Etch selectivity to the structural material;
- Ease of deposition, patterning, and removal;
- Compatible temperature tolerances;
- Adhesion to substrate/structural material;
- Cost of material.

With most silicon processing technologies, the sacrificial layer is a doped silicon dioxide (glass). This layer of glass can be grown thermally, deposited by CVD, or in some cases, spun-on in liquid form before curing. Glass is an ideal sacrificial material for silicon because it meets all the criteria listed above. Silicon and glass are similar enough that very few problems with adhesion or compatibility arise during processing, and the temperatures that they can withstand are similar. Reactive ion etching can define very small features in glass for anchors, dimples, or vias. When the final release of silicon structures is required, hydrofluoric (HF) acid will rapidly remove all glass structures while leaving silicon nearly untouched. The creation, patterning, and removal of thin glass layers is very controllable and low cost. Because glass meets the above criteria so well, it is usually the sacrificial material of choice when releasing silicon structures.

With polymer micromachining, selecting a sacrificial material is not as simple. The above criteria doesn't yield a clear choice, so a large number of materials have been used as sacrificial layers for SU-8 compliant structures in previous studies with varying degrees of success. Metals, glass, silicon, and other polymers are the main options for sacrificial materials. The drawback to most metals as a sacrificial material is that only very thin layers (100's of nm) can be deposited without resorting to long sputtering or

evaporation times, or electroplating. These thin layers can have significant mass transport issues when releasing very large SU-8 structures off the substrate, and thicker metal layers are often required for releasing large SU-8 parts [57]. A second problem with using metal layers is that SU-8 adheres well to only a few metals [66]. When multiple baking steps are involved, delamination of SU-8 off the substrate can be a very large problem while using a sacrificial metal with poor SU-8 adhesion [66]. For large structures requiring a thick metal sacrificial layer, electroplated copper appears to be the best choice [56], while for smaller structures, a Cr/Au/Cr layer has been suggested [67].

Glass appears to be a good sacrificial layer with SU-8 for certain applications. It is unaffected by SU-8 developer, and crosslinked SU-8 is not affected by the HF release. Glass can be easily patterned to make anchors and dimples using standard reactive ion etching recipes, and its behaviour is very well characterized. Unfortunately, SU-8's adhesion to glass can be poor under certain processing conditions, and removing glass with HF acid can damage or destroy existing metals like aluminum or titanium.

Polysilicon has excellent adhesion to both SU-8 and most underlying substrates. It can be removed with a dry XeF_2 etch which does not affect SU-8 [62] and can minimize or eliminate many stiction problems. Unfortunately, controlling the timing of XeF_2 etching is difficult [68], and the deposition of polysilicon requires CVD equipment. If polysilicon is used as a sacrificial layer, the processing equipment required would remove some of the cost and time advantages of using a polymer structural layer. In addition, a XeF_2 etch would be problematic if polymer MEMS was to be integrated with silicon based micro-electronic components.

Polymers are a more interesting choice for sacrificial layers with SU-8. In general, polymers can be spun-on the wafer in a similar manner to SU-8, allowing multiple thicknesses of material to be selected with different spin speeds and viscosities. Using polymer sacrificial layers maintains the advantages of SU-8, in which multiple thicknesses can be produced with minor changes to processing steps. Polymers typically also have similar coefficients of thermal expansion to SU-8, making adhesion failures between SU-8 and sacrificial polymers less likely. One final benefit of polymers as sacrificial layers is that many can be directly photo-patterned or moulded, eliminating the requirements for multiple deposition, patterning, and etch steps.

An ideal polymer will have excellent adhesion to the substrate and SU-8, can be directly patterned with near UV light, is unaffected by SU-8 solvent, and is dissolved in solutions that do not affect crosslinked SU-8 or metal layers. This polymer should also be capable of producing layers from 1-20 μm without significant internal stress and require minimal processing times to reduce cost. A suitable sacrificial polymer should allow low cost processing of compliant SU-8 MEMS structures to be completed quickly and reliably. To examine the possible list of sacrificial materials for SU-8, the list in Table 3.2 is compiled from various sources. This list is not exhaustive, as new materials and processes are constantly being published.

Table 3.2: Potential sacrificial materials for SU-8 with advantages and drawbacks.

Material	Deposition	Thickness	Etchants	SU-8 Adhesion	Compatibility with SU-8	Comments
Silicon [61]	NA	100's μm	KOH, XeF ₂ TMAH	Excellent	Unaffected by SU-8 developer or solvent.	Bulk etching is time consuming and wasteful
Polysilicon [62]	CVD	1-2 μm	KOH, XeF ₂ TMAH	Excellent	Unaffected by SU-8 developer or solvent.	Very good for low stiction releases if XeF ₂ is used as an etchant
SiO ₂ [69]	Thermal CVD Spin-on	<1 μm 1-2 μm <1 μm	HF HF Vapor BOE	Unknown	Unaffected by SU-8 developer or solvent.	SU-8 adhesion to glass is not well characterized. HF acid is dangerous.
Copper [56]	Sputtered Electroplated	nm's- μm 's	Na ₂ S ₂ O ₈	Poor	Unaffected by SU-8 developer or solvent.	Thick (>5 μm) copper layers are required to release large SU-8 areas.
Au [42, 70]	Sputtered Evaporator	10s – 100s nm	KI, Aqua Reagia, SU-8 delamination	Very Poor/Good	Unaffected by SU-8 developer or solvent.	SU-8 adhesion to gold appears to be very processing dependent [71].
Cr/Au/Cr [67]	Sputtered Evaporator	0.05 -0.5 μm	Chrome etchant	Good	Unaffected by SU-8 developer or solvent.	Electrochemical reaction between gold and chrome speeds the removal of this sacrificial layer.
Photoresist [72]	Spin-on	0.5-10 μm	Acetone SU-8 Developer	Good	Dissolves in SU-8 developer and solvent.	Typical photoresist (Shipley 1827) is not compatible with SU-8.
Uncrosslinked SU-8 [54, 73-75]	Spin-on	100's μm	SU-8 Developer	Excellent	Dissolves in SU-8 developer and solvent.	Results are highly variable and difficult to control.
Polystyrene [76, 77]	Spin-on	1-20 μm	Toluene Anisole	Excellent	Swells in SU-8 solvent and developer.	SU-8 developer removes polystyrene with agitation.
Poly(ethylene) Carbonate(PEC) [78]	Spin-on	5-25 μm	Heat depolymerisable	Good (when roughened)	Unaffected by SU-8 developer or solvent.	Requires high temperatures (>200 °C) to depolymerise.
Poly(acrylic) acid [79]	Spin-on	1-10 μm	water	Excellent	Unaffected by SU-8 developer or solvent.	It is very difficult to pattern using standard photoresists due to water solubility.

The list of materials summarized in Table 3.2 was the result of an extensive literature search on potential materials for a sacrificial layer for SU-8. Although inorganic materials would usually provide an acceptable sacrificial layer for SU-8, the difficulty of depositing relatively thick layers of metal, silicon, or glass, as well as the limitations on equipment and material availability made this option impractical for the development of a multi-user MEMS process. Ideally, a low temperature, directly patternable spin-on layer would be used as a sacrificial material because it could be easily processed with the tools available. To accomplish this process, two near UV patternable sacrificial layers for SU-8 were tested during early work: a positive tone photoresist, and uncrosslinked SU-8.

3.4.1 Use of photoresist as a sacrificial layer for SU-8

The first potential sacrificial material attempted with SU-8 was Shipley 1827 photoresist. Positive tone photoresists, like Shipley 1827, are easily patterned with near UV light, with well defined processing conditions in layers from 1-5 μm . They develop in alkaline-based developers and are stripped by many organic solvents. If a photoresist could be found that would not dissolve in SU-8 solvent, but could be removed by other developers, it would make an excellent sacrificial layer. Several early trials to produce compliant SU-8 structures were based on the work by Song and Ajmera [72] who used a hard baked layer of photoresist as a sacrificial layer for SU-8 moulds. The photoresist that was used in [72] was very similar to the Shipley 1827 formulation used in our case, but it was baked at much higher temperatures (175 °C) than recommended by the manufacturer's guidelines (~115 °C). The very high baking temperature was required to toughen the resist against the SU-8 solvent so that it would not dissolve during SU-8 spin

coating. The work reported by [72] did not keep the SU-8 structures for the final device, but stripped them off the substrate using a combination of heated solvents and O₂ plasma ashing. Because this mechanism of removal in [72] is incompatible with fabricating permanent SU-8 structures, a combination of lower temperature hard bakes were attempted with Shipley 1827 to fabricate compliant SU-8 devices. Our early work proved that SU-8 compliant microstructures could be fabricated using a photoresist sacrificial layer, but the results were unreproducible and the yield was extremely poor. Figure 3.2 shows a series of pictures from one of the more successful attempts at using a Shipley 1827 sacrificial layer for SU-8 compliant microstructures.

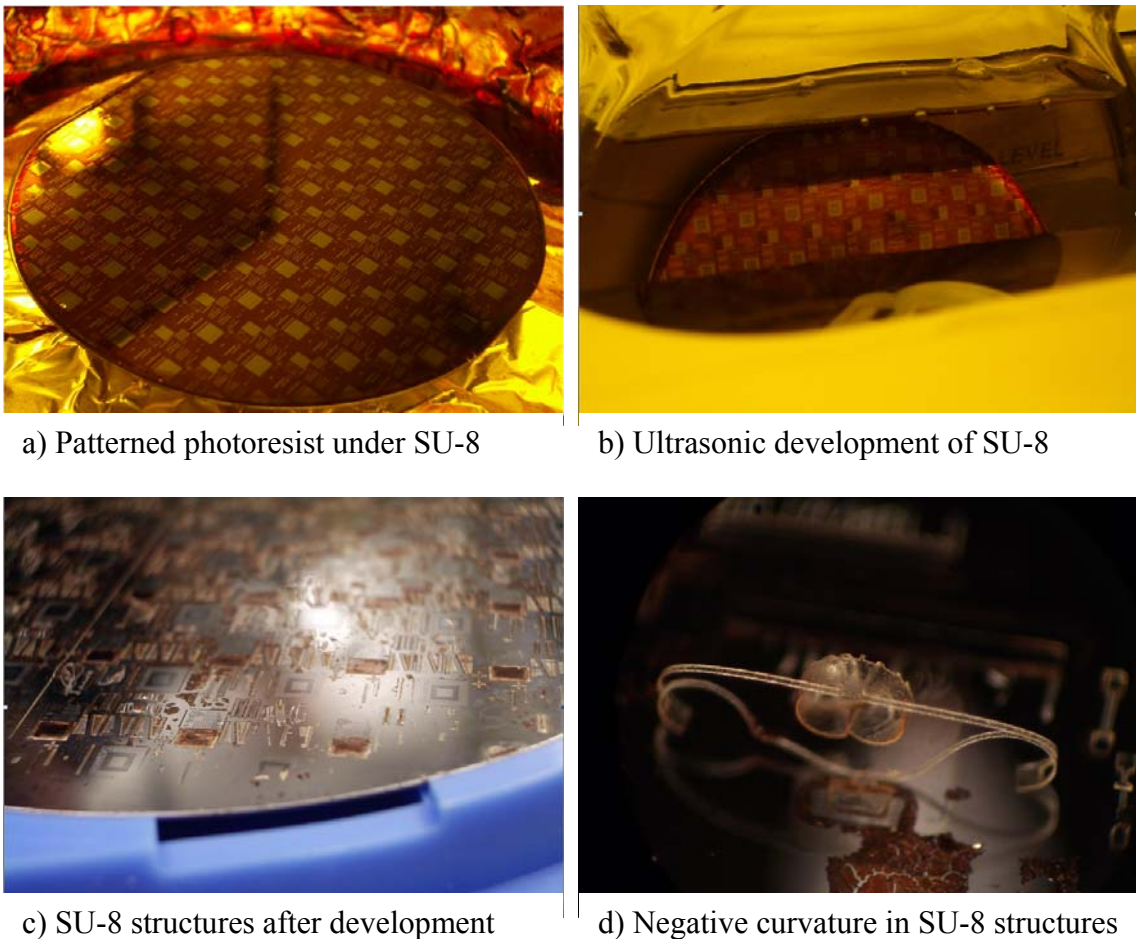


Figure 3.2: Images of several process stages while using photoresist as a sacrificial layer for compliant SU-8 structures.

As evident from Figure 3.2, the photoresist does not clear completely and the released SU-8 structures demonstrate extreme out-of-plane curvature. After attempting a variety of processing conditions for the photoresist, a baking combination that allowed photoresist features to resist SU-8 solvent while still being soluble in SU-8 developer could not be found. Further, efforts to directly use Shipley photoresist as a sacrificial layer were abandoned as impractical.

3.4.2 Uncrosslinked SU-8 as a sacrificial layer

Using uncrosslinked SU-8 as a sacrificial material appears to an ideal option at first glance: it develops quickly, can be spun in layers up to several hundred μm 's, and will show no adhesion problems to other SU-8 layers. In fact, the promise of uncrosslinked SU-8 as a sacrificial material to form microchannels was described in some of the earliest papers using it for MEMS applications [54]. Two primary methods use uncrosslinked SU-8 as a sacrificial material. The first involves blocking UV from penetrating past a certain depth by using blocking layers, such as a thin metal [54, 73] or highly absorbing polymers [80], while the second method controls the exposure dose to crosslink only the top portion of the SU-8 film. The first method is theoretically the simplest, as the depth of SU-8 crosslinking will be well defined and repeatable for many applications. The second method requires precise UV dosage control, either of the standard 365 nm light source [75], or of more energetic deep UV rays [74] to expose SU-8 to a pre-determined depth.

Using a metal UV blocking mask on unexposed SU-8 was proposed in some of the earliest SU-8 work [54], but it is a much more challenging process than described in most papers. The main problem is that the radiation and heat generated during a typical

metal deposition can be more than enough to cause crosslinking reactions to occur in the SU-8. If deposition rates are too high, the temperature at the SU-8 surface can be greater than the glass transition temperature of uncrosslinked SU-8 (~50 °C), resulting in severe reticulation of the surface [81]. In addition to this effect, many metal etchants are acidic and can initiate SU-8 crosslinking reactions at the surface, even in the absence of a significant exposure dose. Figure 3.3 shows an example of SU-8 reticulation from high temperatures and reflow due to sputtering aluminum on uncrosslinked SU-8.

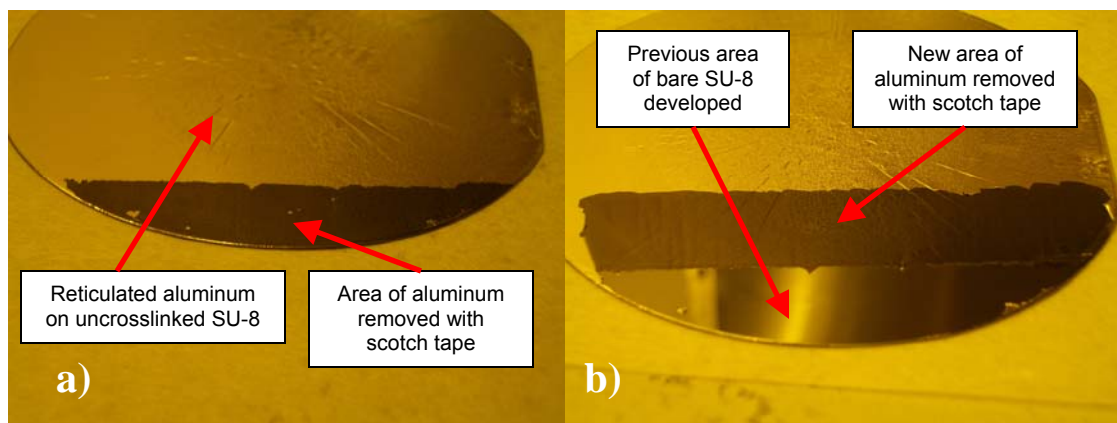


Figure 3.3: Aluminum deposition on uncrosslinked SU-8. Scotch tape easily pulls aluminum off the SU-8 surface (a), and uncrosslinked SU-8 can be developed (b). If the SU-8 is baked after metal deposition, crosslinking can occur, and all areas of SU-8 that have been coated with metal become insoluble in SU-8 developer.

The processing window for acceptable metal deposition and development without crosslinking SU-8 is very small, and, as a result, this method is impractical for robust processing. Using a UV absorbing polymer layer can also pose problems. Intermixing of SU-8 and other polymers can be a significant issue depending on the solvents used, resulting in unknown mechanical properties and severe internal stresses [80]. In addition, the exact thickness of crosslinked SU-8 depends strongly on the total exposure and other processing parameters, introducing significant process variations from run to run.

Controlling exposure dose conceptually simple, and for thick SU-8 layers can be a useful method of creating channels. Gaudet *et al.* [75] modelled the crosslinking depth with exposure dose assuming a 365 nm source; they were able to fabricate SU-8 bridges using a dual exposure method. This mechanism can be repeated by most equipment setup for i-line lithography, but has significant disadvantages. The actual thickness of crosslinked SU-8 shows significant variation across the beam length, mainly due to interactions between the two exposed areas. The second disadvantage is that this method cannot produce very thin beams, because the transmittance of SU-8 at 365 nm is close to 50% [30]. SU-8 layers were required to be approximately 100 μm thick to use this method successfully [75]. To fabricate thinner beams of SU-8 using exposure dose control, a more highly absorbed UV wavelength is required. Fu *et al.* [74] describe using a 254 nm source on a typical mask aligner to expose SU-8 beams and bridges in much thinner layers than are possible with 365 nm exposures. Unfortunately, this method requires the use of masks that transmit a significant percentage of 254 nm light. Many regular glass or plastic plates heavily attenuate light at this wavelength making them inappropriate for deep UV masks. The final problem with both types of exposure depth control for SU-8 compliant structures is that the stress gradients and resulting curvature of the SU-8 will be quite high [82]. The SU-8 at the bottom of these beams is barely crosslinked, as demonstrated by other work [82]. Under exposed SU-8 can show a great deal more of out-of-plane stress than when it is fully exposed.

After several attempts to use positive tone photoresists and uncrosslinked SU-8 as a sacrificial material for compliant SU-8 structures, the efforts were abandoned as

unfeasible for reliable processing. The focus then turned to alternative polymers as a sacrificial layer.

3.4.3 Polystyrene as a sacrificial layer

Polystyrene is a commonly used industrial polymer, with a wide variety of uses and applications. A large body of work in the literature characterizes the spin coating of polystyrene in thin layers on silicon [83]. Moreover, it can be purchased from chemical suppliers with high purity and with well defined molecular compositions. The use of polystyrene as a sacrificial layer was reported by Luo *et al.* for the lift-off of complete SU-8 structures off a substrate [76]. In their work, the objective was to remove SU-8 structures and membranes completely off of a substrate. Luo *et al.* observed little to no intermixing of SU-8 and polystyrene after SU-8 spin coating, and claimed that the toluene used to dissolve the polystyrene did not affect crosslinked SU-8. The use of polystyrene appears to be close to ideal as a sacrificial layer because it can be spun on top of substrates in a variety of thicknesses. Furthermore, SU-8 solvents minimally affect it, it dissolves in solvent that does not affect crosslinked SU-8, and it is inexpensive. Its biggest weakness from a processing perspective is that it is not photopatternable with standard i-line lithography. Luo *et al.* did not attempt to pattern the polystyrene sacrificial layer according to their paper, so the work contained here is, to the author's knowledge, the first use of polystyrene as a patterned sacrificial layer for MEMS applications.

After examining available materials for use with SU-8, polystyrene was chosen as the sacrificial layer for a multi-user polymer MEMS process. This decision was made for four main reasons: it has been very well characterized as a spin on layer in thicknesses

from a few nm to 20 μm [83]; it can be patterned with nanometer scale features using techniques like nano-imprint lithography [84]; it was available in our lab in large quantities; and it is extremely low cost. While polystyrene does not conform exactly to the sacrificial layer requirements outlined in section 3.4 (it is damaged by SU-8 developer), it is acceptable for basic research and prototyping. The SU-8 developer damages the polystyrene surface and reduces its solubility in toluene, requiring that at least 10 seconds of ultrasonic agitation be applied to break up this layer and speed the release process. In addition, many of the techniques that are developed in this work for patterning and removing polystyrene can be adapted for nearly any spin-on polymer, making future work with other sacrificial polymers much easier. After selecting polystyrene as a sacrificial material, work began on creating polystyrene solutions and determining optimal processing conditions.

3.4.4 Producing and characterizing polystyrene solutions

In earlier work with spin-on polystyrene solutions, the solvent of choice has been toluene [76, 83]. It is relatively inexpensive, dissolves polystyrene readily, and can produce viscosities high enough to spin-coat polystyrene in layers up to 20 μm thick. Toluene was therefore, selected as the solvent for all polystyrene solutions in this work.

Multiple solutions were made with varying concentrations of polystyrene. Polystyrene concentration is measured by weight percentage, which is typical of previous studies [83]. The polystyrene used for this work had been purchased by the engineering cleanroom prior to the start of this work, and was in the form of small pellets. These pellets were dissolved in toluene to form several concentrations by weight. The average

molar masses of the polystyrene solution used for this work was calculated using gel permeation chromatography by the chemistry department at SFU.

The number average, weight average and z average values for the molecular weight of the polystyrene used are $M_n = 65182$ g/mol, $M_w = 139991$ g/mol and $M_z = 203676$ g/mol as defined below [85]:

$$M_n = \frac{\sum (M_i N_i)}{\sum N_i} \quad (1)$$

$$M_w = \frac{\sum (M_i^2 N_i)}{\sum (M_i N_i)} \quad (2)$$

$$M_z = \frac{\sum (M_i^3 N_i)}{\sum (M_i^2 N_i)} \quad (3)$$

Two concentrations used for the majority of this work were 15% wt. polystyrene and 20% wt. polystyrene. These concentrations were sufficient to spin coat layers up to 6 μm thick. The characterization of spin-coating polystyrene films on silicon has been covered extensively in other work [83], and no significant differences from published behaviour were discovered in this work.

All polystyrene layers for this process were spun-on for 30 seconds at the desired spin speed with maximum acceleration. For all but the thickest layers (15-20 μm thick), the toluene had evaporated while the wafer was spinning.

3.4.5 Patterning of polystyrene

Unlike many inorganic materials, polystyrene cannot be easily patterned by the use of wet etchants. Many organic solvents that dissolve polystyrene can also damage common photoresists used for masking. Toluene, in general, is not harmful to Shipley

photoresists, but it is absorbed by the photoresist and will affect the polystyrene underneath if given enough time. If an inorganic mask on polystyrene is used, this problem is avoided, but the lack of proper developers for polystyrene can cause significant redeposition problems. Organic solvents will first swell the polystyrene film, then detach molecules from the surface of polystyrene films. In between the solid polystyrene film and the bulk solvent, a gel like layer exists with a very high concentration of dissolved polystyrene. The existence of this gel layer makes cleanly stopping the development impossible, as the polystyrene will redeposit over the wafer once the wafer is removed from the toluene. Rinsing with fresh toluene reduces this problem, but the repeatability and quality of wet etching polystyrene is very poor.

Because of the problems encountered with wet etching polystyrene, a dry process was used to define polystyrene features. Most work patterning small polystyrene features uses a combination of nano-imprint lithography [86] and oxygen plasma to etch polystyrene features. Nano-imprint lithography is excellent for producing very small, high aspect ratio structures, but it is not practical for rapid prototyping due to the specialized equipment and mould requirements. The size of structures fabricated in this process do not require high aspect ratio features in the polystyrene sacrificial layer, so a direct RIE step can be used to pattern the layer. Traditionally, RIE of polymer layers uses an inorganic material as a mask for high selectivity. To do so, however, required a separate metal deposition and patterning step and introduced significant extra complexity to the process. To avoid the metal deposition step, a thick layer of photoresist can be directly spun-on and patterned to mask the polystyrene. Most photoresists will be etched quickly by the same gases that remove polystyrene, so high selectivity cannot be

achieved and the photoresist thickness must be equal to or greater than the polystyrene layer. Given the wide variety of photoresist thicknesses that can be spun-on, this requirement is not difficult and provides an opportunity to add extra features to the polymer MEMS process.

The photoresist chosen for this work was Shipley 1827, which was readily available in our lab at the time of this work. Shipley 1827 photoresist is designed to be used in layers up to a few microns thick, and absorbs UV light at very high rates. A deliberate underexposure of thicker layers will result in the removal of only a percentage of the total resist thickness after development. These techniques have been used in the past for grayscale lithography [87], but, for patterning of polystyrene in this process, only two exposure doses are required. A long exposure allows complete development of anchor features in the photoresist, while shorter doses can define dimple features on the photoresist film. If the polystyrene and photoresist etch at the same rate in the RIE, the exact topology, as defined by the photoresist patterning, can be directly transferred to the polystyrene film. Using this method greatly speeds up the processing, as only a single layer of photoresist is required for two feature masks and the RIE is only required once to transfer all features to the polystyrene.

To effectively create dimple features, a photoresist layer greater than 2 μm is required. The developed depth of Shipley 1827 features is non-linear with exposure dose, and is very difficult to control in depths less than one μm . The development depth of features in 6.7 μm thick Shipley 1827 photoresist film over polystyrene on a gold coated substrate with varying exposure dose is shown below in Figure 3.4. A

development for 3 minutes in MF-319 developer is followed by a de-ionized water rinse and nitrogen dry.

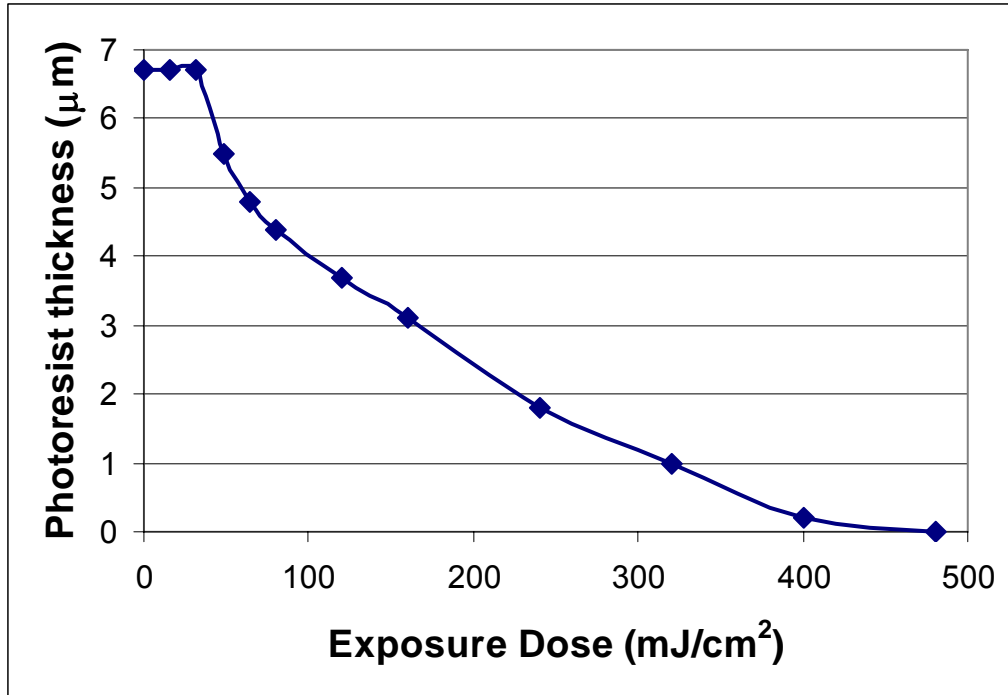


Figure 3.4: Development depth of dimple features with exposure dose. Wafer is coated with Cr/Au followed by 6 μm of PS and 6.7 μm of thick photoresist. Photoresist bake time was 15 minutes at 100 °C and was exposed through a chrome mask.

Using chrome masks produces a very smooth surface at the bottom of all dimple features, but the use of Mylar or acetate emulsion masks can create far more variability in dimple depth. This variability in developed depth enhances the effectiveness of the dimple features, but predicting the exact depth is more difficult. Figure 3.5 shows images and profilometer data for underexposed photoresist features produced using chrome masks and Mylar emulsion masks.

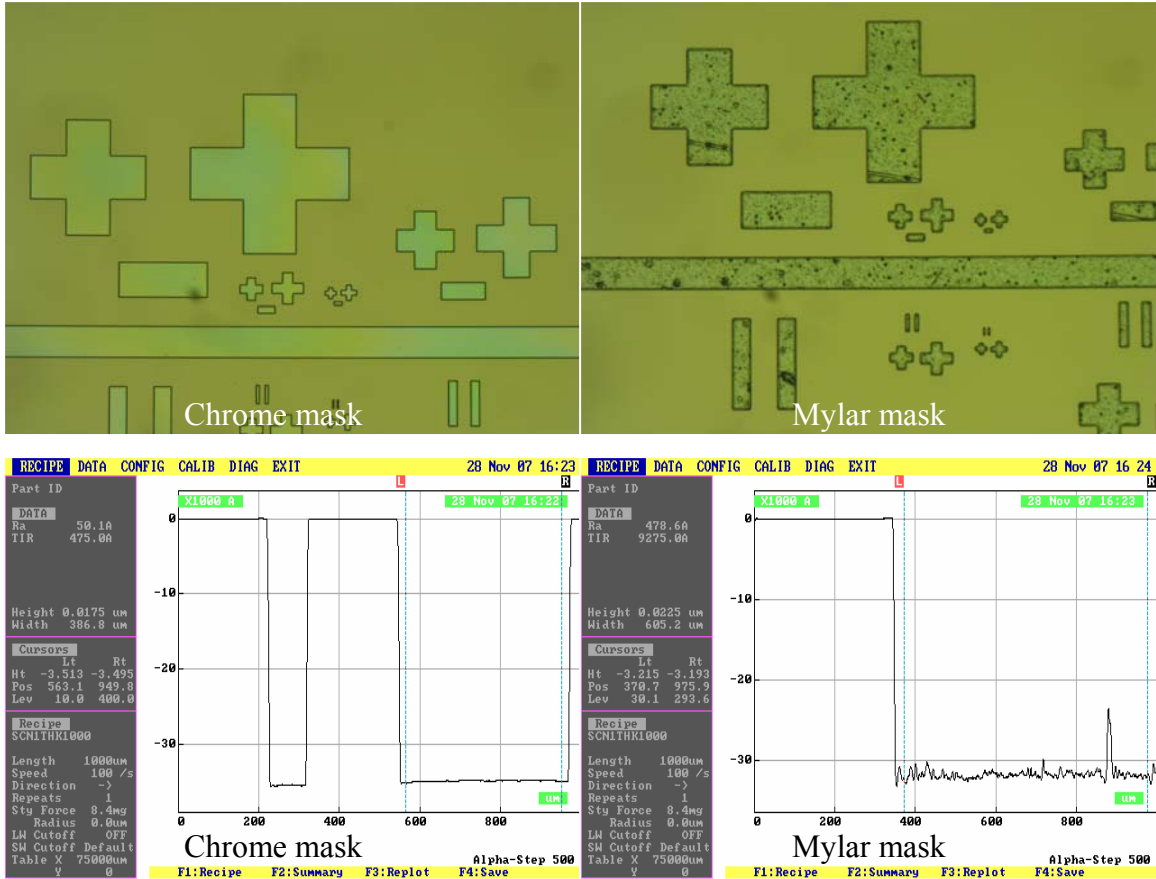


Figure 3.5: Images of underexposed photoresist features after development and profilometer data of dimples produced in photoresist through a Chrome (left) and Mylar emulsion mask.

Clearly, from the visual appearance, the dimples fabricated using Mylar masks are significantly rougher than those that used chrome masks, and profilometer data shows that these dimples defined through Mylar can vary several hundred nanometres in depth. The cause of the much greater variability of dimple depths fabricated with Mylar masks is the imperfections in the mask material that cause localized amplification and attenuation of exposure dose. The resulting peaks and valleys in the underexposed dimple areas can be several hundred nanometres high. If the total photoresist or polystyrene layer is too thin, this roughness can cause micro-anchors and, potentially, cause SU-8 to adhere to the substrate in undesirable locations.

3.5 Polymer MEMS process steps

Early work with polystyrene as a sacrificial material used silicon as a substrate with chrome alignment markers. Alignment markers are required on the substrate because the closely matched indices of refraction of SU-8 and polystyrene, combined with the planarization of the SU-8 film, make the patterned polystyrene features impossible to distinguish under an SU-8 layer when observed through the aligner microscope. This basic system of chrome alignment markers on silicon works, but it showed significant reliability issues. A bare silicon surface can quickly oxidize after cleaning, and polystyrene has very poor adhesion to glass. As a result, many silicon wafers suffered from polystyrene delamination if a significant time passed between wafer cleaning and polymer processing. A solution was found in previous research demonstrating that polystyrene has preferential wetting to gold over silicon or glass [88] so a chrome/gold bi-layer was deposited on silicon wafers to ensure strong polystyrene adhesion after spin-coating. The surface of a gold layer changes very little over time, so the adhesion of polystyrene to a gold surface can be very good without requiring cleaning prior to spinning. Most previously published work indicates that SU-8 has poor adhesion to gold [70], so an etch step is required to remove gold from all anchor areas. In doing so, this step can simultaneously create high contrast alignment markers, avoiding the requirement for a separate patterning step.

Aqueous potassium iodide as a gold etchant was used successfully in earlier work and acts quickly at room temperature with a very high selectivity to other materials used in this process. Creating a process flow for a polystyrene layer that showed no adhesion issues between the substrate or the SU-8 layers, that also allowed for easy alignment, and

successful removal with minimal damage to SU-8 or stiction issues required significant trial and error. After several process variations, the following basic steps for a multi-user polymer MEMS process were developed:

Step 1: RCA clean silicon or pyrex wafers and sputter Cr/Au onto the wafers. The amount of metal can be altered for various applications, but, for the majority of this work, this metal bi-layer was selected to be 50 nm Cr/50 nm Au.

Step 2: Spin coat a layer of polystyrene onto the Cr/Au coated wafers from the polystyrene/toluene solutions. The thickness of this layer can be selected by process parameters, but it has typically been chosen to be greater than 5 μm . Spinning 20% wt. polystyrene at 1500 rpm for 30 seconds results in an average thickness across the wafer of $6.2 \mu\text{m} \pm 0.3 \mu\text{m}$. This layer can be baked for 10 minutes at 100 °C to relax the layer, or simply left for a few minutes to dry. On a gold surface, no adhesion problems have been observed when the relaxation bake is skipped.

Step 3: Spin coat a layer of Shipely 1827 photoresist on top of the polystyrene with approximately the same thickness as the polystyrene. For spinning on a polystyrene surface, spin coating at 1500 rpm for 30 seconds typically results in a photoresist thickness of $6.5 \mu\text{m} \pm 0.5 \mu\text{m}$, which is approximately 20% thicker than when spinning onto gold. This resulting thickness allows the same spinner settings to be used for both polystyrene and photoresist when using 20% wt. polystyrene solutions. The wafer is baked at 100 °C for 15 minutes in an oven to drive off photoresist solvents.

Step 4: An anchor level mask is aligned to the wafer's major flat and exposed for at least 80 seconds. This long exposure time is required to completely expose small anchors in a 6 μm thick photoresist layer. The wafer is developed in either MF-319 or

MF-322 for at least two minutes with agitation, but most developments are continued for three minutes to ensure completion. The wafer is rinsed in DI water and dried with N₂ gas.

Step 5: The dimple level mask is aligned to the anchor features and exposed for 10-15 seconds. The exposure in this step is designed to result in 1-2 μm deep holes. Anchor areas are typically re-exposed with this mask layer to ensure that any remaining photoresist from an anchor under-exposure or under-development is removed. Another 3 minute development in MF-319 or MF-322 is used to clear dimple areas prior to a DI rinse and dry. Because this step is not designed to completely develop areas, keeping the development time equal for all runs is necessary to achieve consistent results. A profilometer is used after this step to determine photoresist thickness and dimple depth across the wafer as well as to check for uniformity.

Step 6: A reactive ion etch (RIE) is used to ash both the polystyrene and the photoresist. These two materials are removed at approximately the same rate for the RIE parameters used. The RIE can either be pure O₂ gas, or a mixture of O₂ and CF₄. A pure O₂ RIE was used for most early work, but it tends to leave more scum behind from any residual inorganic material and results in a much rougher surface at the end of the etch. A small amount of CF₄ in the gas mixture smoothes the final surface and is better at removing scum from anchor areas. The specific RIE recipe used most often in later work uses 40 sccm (standard cubic centimetres) O₂, 5 sccm CF₄ at 100 mtorr and 150W with an electrode height of 1". This recipe removes the photoresist/polystyrene at a rate of approximately 160 nm/minute. The etch is timed to finish just after the anchors clear of polystyrene, and is estimated from the previous measurements of polystyrene and

photoresist thicknesses. The clearing of anchors can be observed as a visible change in the colour of the anchor areas during the RIE from light to dark grey as the smooth substrate is revealed. Profilometer measurements across the wafer determine the final layer thicknesses and uniformity.

Step 7: A 30 second gold etch with aqueous potassium iodide (KI) is used to remove gold from all exposed anchor areas. This etch simultaneously provides areas of good adhesion for SU-8 and creates high contrast alignment markers that can be used for all subsequent process steps. After the gold etch is complete, the wafers are rinsed with DI water, dried with N₂ gas, and dehydration baked for 5 minutes at 120 °C.

Step 8: SU-8 is spun on in the desired thickness and baked to drive off solvents. Parameters for SU-8 processing can be roughly determined from SU-8 data sheets [30, 40], but must be optimized through experimental means. The first SU-8 feature mask is aligned and exposed and then the wafer is post exposure baked (PEB) to complete the crosslinking reaction. At this point, the wafer can be developed or another layer of SU-8 can be added. For most of this work, a multi-level SU-8 structural layer is used to increase the mechanical device variations. If the first layer of SU-8 is greater than 20 μm, very little sacrificial layer topology is transferred to the final structures. A general rule of thumb, based on many trials and fabricated wafers, is to use a structural layer at least three times thicker than the maximum sacrificial layer topology to prevent significant radial streaks and uneven surfaces after spin coating the structural layer.

Step 9: Additional layers of SU-8 are spun on, pre-baked, aligned, exposed, and post exposure baked. Most devices created in this work used two structural thicknesses, but in principle, any number of additional non-overhanging layers may be spun on and

patterned prior to development. All SU-8 baking steps begin below 50 °C and are ramped up at 300 °C/hr and naturally cooled to prevent thermal shocks to compliant microstructures. Cooling to below the glass transition temperature of SU-8 occurs before the wafers are removed from hotplates.

Step 10: Development and release of the SU-8 structures uses a dual solvent step, with ultrasonic agitation first in SU-8 developer, followed by a brief ultrasonic agitation in toluene. Ultrasonic agitation in SU-8 developer is completed until polystyrene begins to separate from the substrate as a skin-like film, then the wafer is transferred to toluene for 10-15 seconds of ultrasonic agitation, followed by gentle agitation by hand for a few minutes. The exposure of polystyrene to SU-8 developer appears to chemically alter its surface and prevents easy dissolution in toluene if agitation is not used. Once the partial break up of the film is finished in SU-8 developer and toluene, gentle agitation is sufficient to remove the remainder of PS. The wafer is rinsed in fresh toluene, followed by IPA. After rinsing in IPA, the wafer is dried carefully with N₂ gas, and is then left for several hours to evaporate any remaining solvent. During the development process, ensuring that the wafer does not dry out until the end is critical, otherwise polystyrene will redeposit across the wafer and leave a scum that is very difficult to remove. Most developments result in a very clean surface with little to no scum.

Step 11: After all solvent has evaporated from the SU-8 structures, a blanket metal deposition is used for electrical connectivity. A highly directional metal deposition technique, such as evaporation can place metal primarily on the top surfaces of SU-8 structures with low levels of sidewall coverage, eliminating electrical connection between levels. Most metal deposition by our lab uses a sputterer, which coats sidewalls with

significant metal thickness. Depending on the application, SU-8 structures can be designed with overhanging anchors to electrically isolate individual devices from the substrate and each other. Using this ability, multiple electrically conductive MEMS devices can be tailored for a variety of applications. Figure 3.6 is a graphical representation of the basic process steps described.

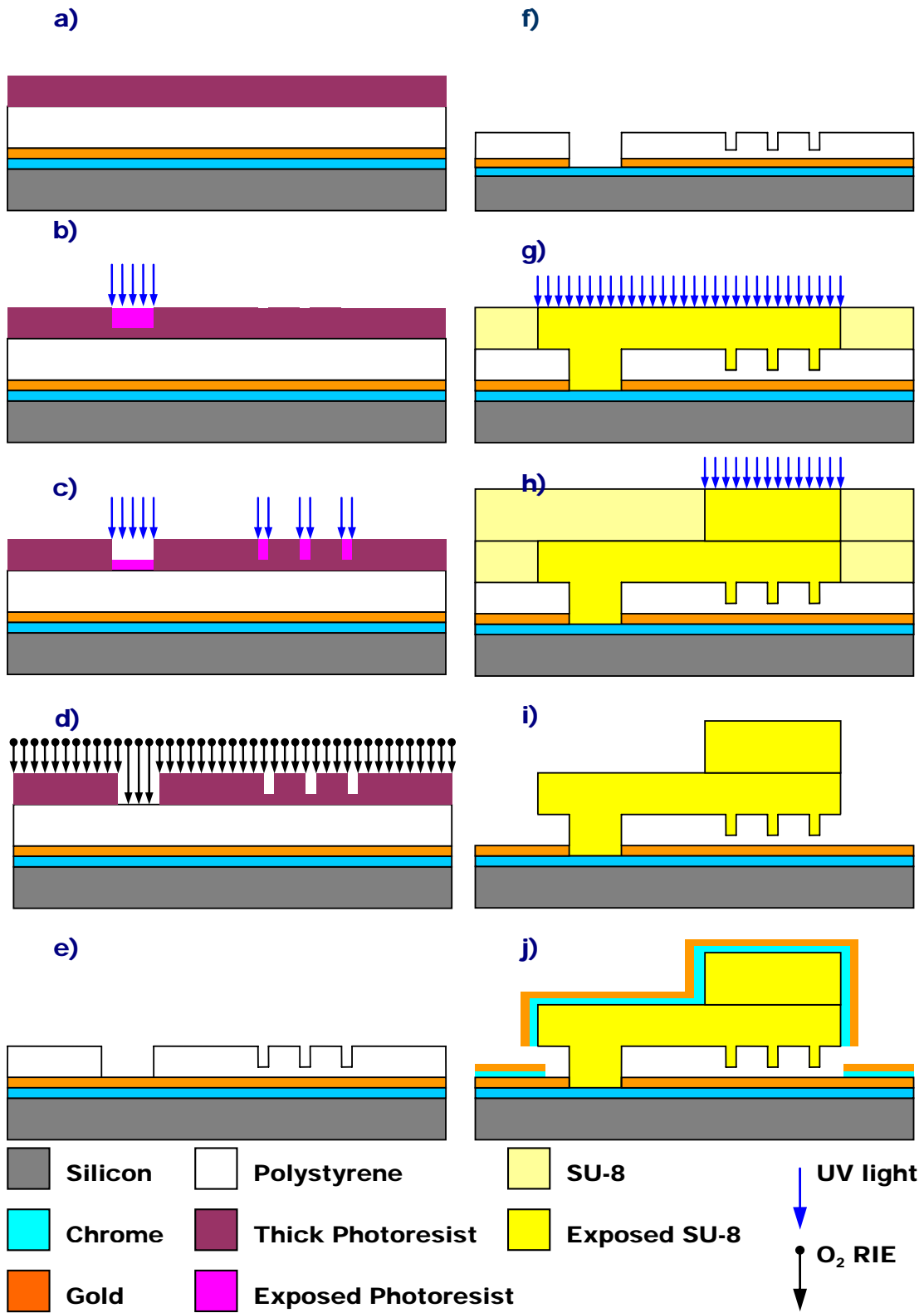
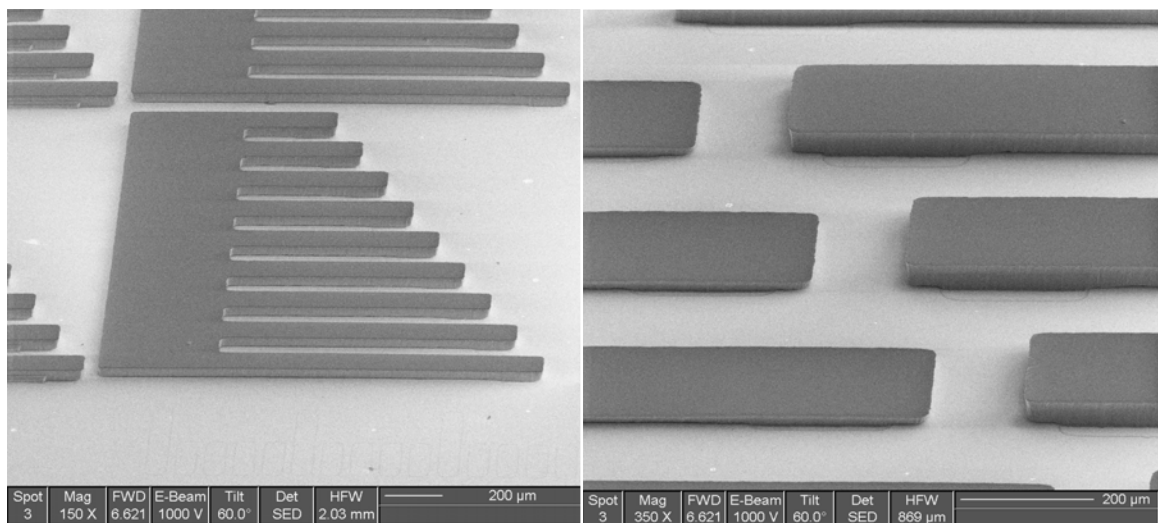


Figure 3.6: Basic steps of the polymer MEMS process

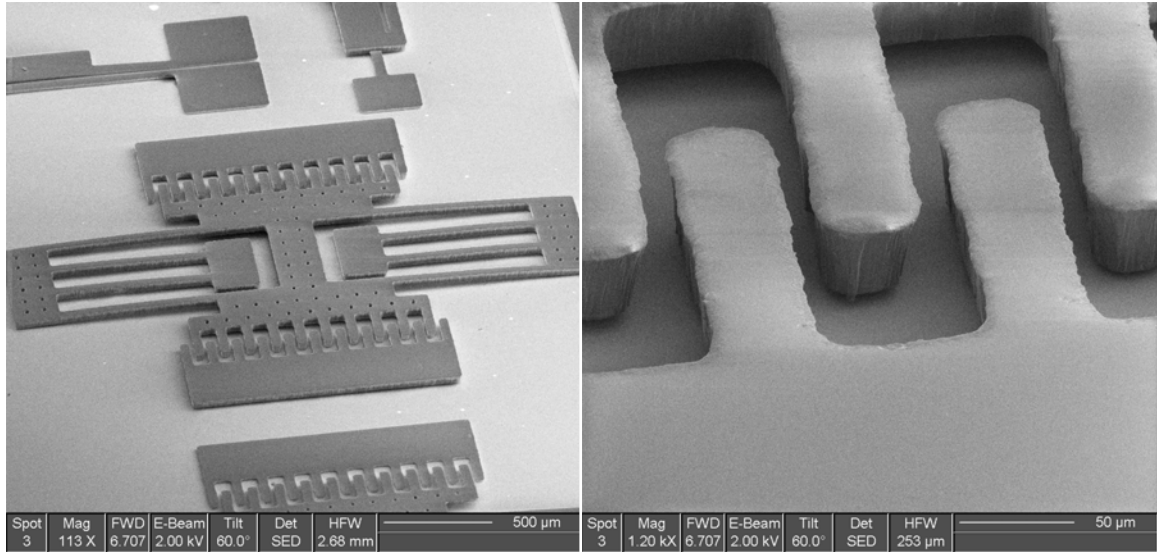
The process steps described above and shown in Figure 3.6 have allowed the development of a highly repeatable and reliable process using SU-8. The development of such a process lead to an enormous number of compliant SU-8 microstructures that were designed and tested. Over 20 wafers were processed without major failures. To reduce costs, all early work used inexpensive emulsion masks that were locally printed. Although the minimum features of structures were relatively large (30 μm), proof of concept devices for actuators, sensors, and mechanical structures were successfully fabricated and tested. The following devices are a small selection of the structures and actuators tested during early trials; shown in Figure 3.7, Figure 3.8, Figure 3.9 and Figure 3.10.



a) Multi-length bridges

b) Close-up of bridges

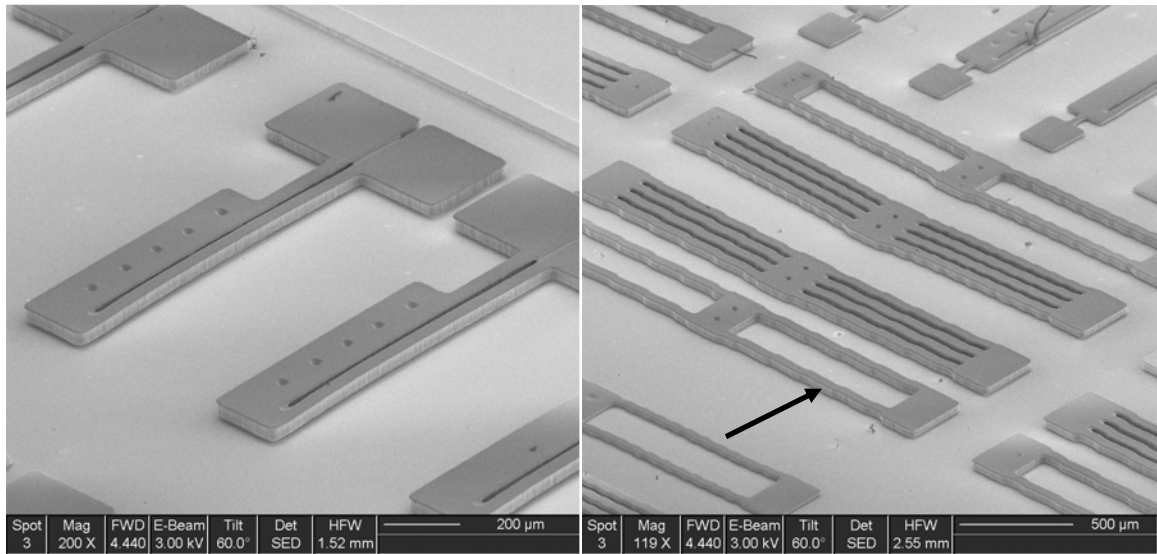
Figure 3.7: Compliant SU-8 structures: a) thick SU-8 fixed-fixed bridge arrays, b) close-up of cantilever anchors demonstrating the two SU-8 thicknesses and planarization of the polystyrene topology.



a) SU-8 combdrive structure

b) Combdrive fingers

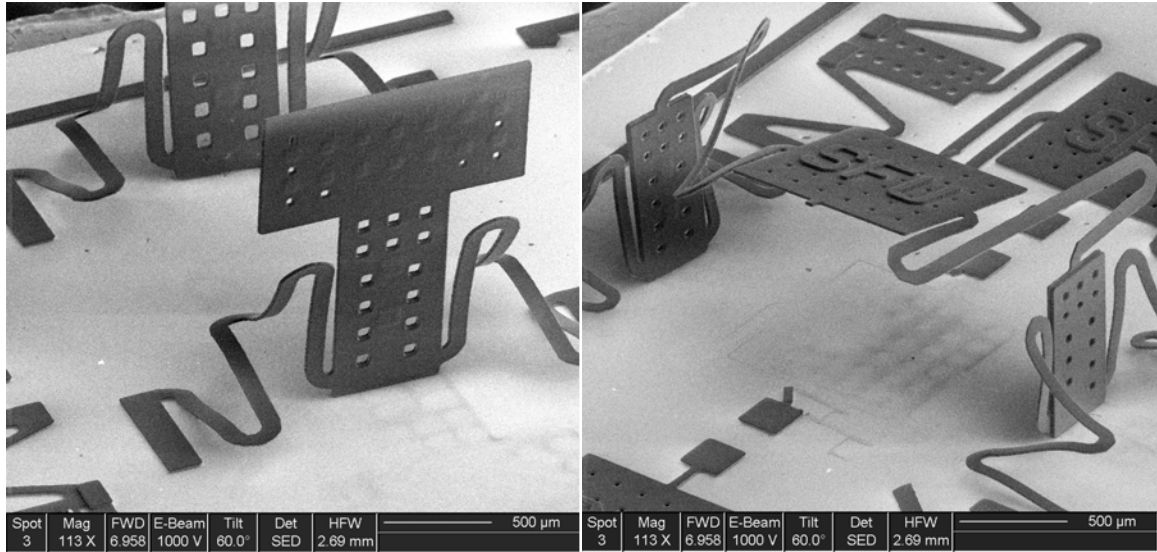
Figure 3.8: a) Electrostatic SU-8 linear combdrive structure and b) close-up of combdrive fingers. The poor edge quality of features on the emulsion masks results in rough sidewalls on the SU-8 structures.



a) Hot/cold thermal actuators

b) Chevron thermal actuators

Figure 3.9: SU-8 thermal actuators coated in Cr/Au: a) hot/cold arm thermal actuators, b) chevron thermal actuators showing raster scanning effects (arrow) of the mask writing process.



a) Out-of-plane spring structure b) Thermal isolation platform

Figure 3.10: Out-of-plane pop-up structures reported in [37], demonstrating dimples (a) and multi-thickness thermal isolation platform designed by myself (b) [89].

The SEM images do not show everything of interest with respect to the fabrication of SU-8 structures. One of the more interesting characteristics of the devices fabricated is that the SU-8 looks cloudy prior to metal deposition rather than transparent as demonstrated in earlier work with polystyrene [76]. The cause of this change was determined experimentally to be the surface roughness of the underside of SU-8 caused by the reactive ion etching of polystyrene. The long etching time of photoresist can cause significant roughness due to small variations in etch rate across the wafer, with higher roughness at the wafer edge. The result is the transfer of this rough polystyrene surface to the underside of SU-8 structures, leading to a cloudy appearance after release.

To demonstrate this change, and to eliminate all other variables from the processing steps, a polystyrene-coated wafer was exposed to an O₂ RIE on one-half only and then spin-coated with SU-8. Large areas were exposed and the whole wafer was partially developed to observe the changes in appearance of the SU-8. As shown in

Figure 3.11, the side of the wafer exposed to RIE prior to coating with SU-8 shows significantly greater cloudiness.

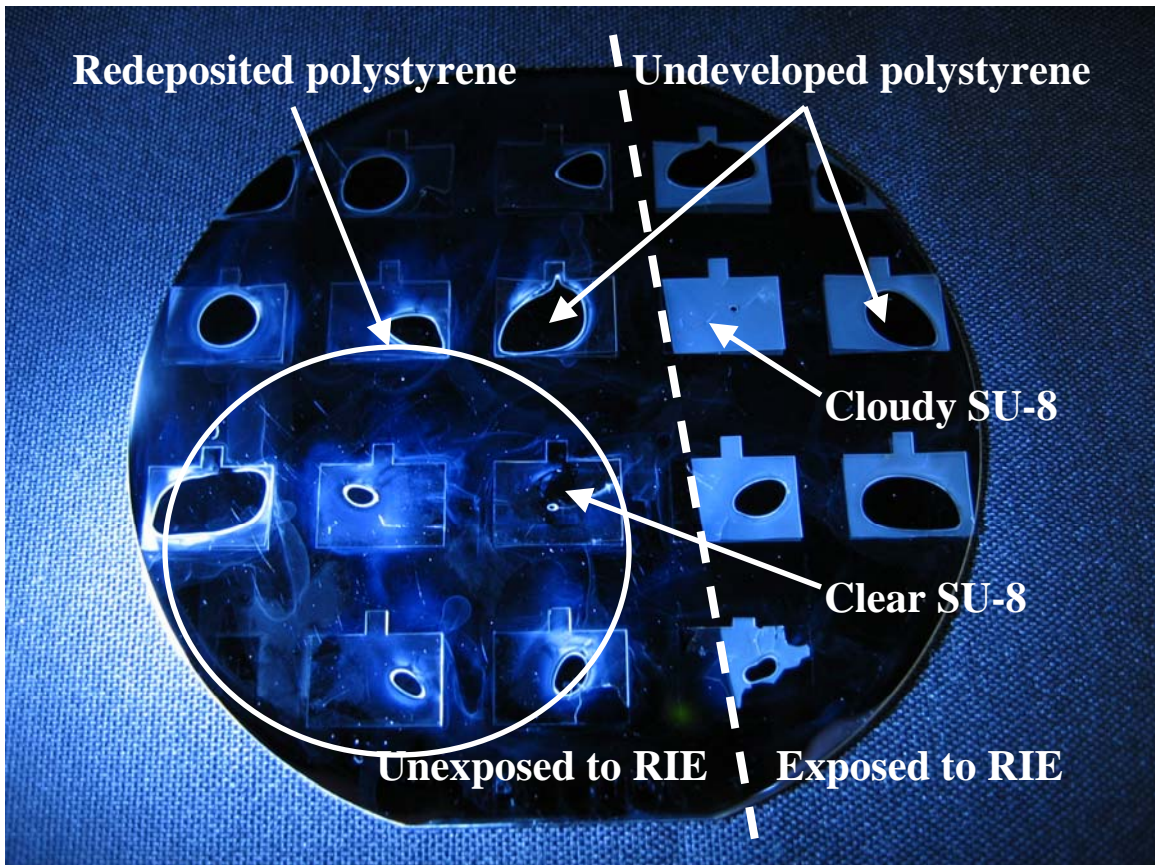


Figure 3.11: The visual effect of polystyrene RIE on SU-8 optical properties [89]. The polystyrene surface roughness is transferred to the underside of SU-8 membranes, resulting in a cloudy appearance when the underlying polystyrene is removed. The dashed line separates the areas of O_2 RIE exposure.

An unexpected side effect of this transfer of surface roughness to the bottom of SU-8 structures is that stiction after release is decreased. The increased roughness of the polystyrene due to RIE effects leads to dimples a few 10's of nanometers deep on the underside of SU-8. While not deliberately designed into this process, this rough bottom surface significantly improves device yield and allows many smaller structures to be released without requiring a dimple mask. If this rough surface is not desired, then the use of a thicker photoresist layer can be used to pattern the polystyrene. If the

polystyrene anchor features are cleared prior to complete photoresist removal, then a blanket exposure and development can remove the remaining rough photoresist and leave a smooth polystyrene layer behind. For the majority of applications using this process, this step is not required.

3.6 Fabrication challenges and process design rules

The process as designed is robust enough to allow fabrication of SU-8 structures for a variety of applications and prototypes, but many factors can cause yield problems. The use of Mylar emulsion masks and the quality of available lab equipment can partly explain the primary processing problems encountered in this work. These process problems include: large out-of-plane stresses, poor feature definitions, negative sidewalls, and significant tensile stress. Some of these issues, like tensile stress, are inherent due to the physical properties of SU-8 and cannot be avoided. Other problems, like poor features or negative sidewalls, can be avoided with the use of higher quality emulsion masks or chrome masks. Still, other problems like the out-of-plane stresses, have been thoroughly characterized in this process and was the topic of a journal article published by the author [82]. This work is further described in Chapter 4, while descriptions of general process problems and design rule suggestions to minimize these issues are listed here.

3.6.1 Minimum feature sizes

A great deal of work has been published with respect to optimizing SU-8 feature sizes and aspect ratios. Most of this work involves changing baking parameters and exposure doses to achieve good results [90, 91]. When using a high quality mask in good

contact with the SU-8, the combination of appropriate baking times and exposure doses has the greatest effect on achievable feature quality. If the mask is not in good contact with the SU-8 surface, in addition to the processing conditions, the achievable feature sizes and sidewall profile of SU-8 structures is dependent on the gap size between the SU-8 and the mask [41, 92]. For very thick SU-8 layers, this gap can be caused by a large edge bead on the wafer after spin-coating. Most modern spin-coaters have dispensing mechanisms for solvents that will remove this edge bead automatically, but this option was not available on the spin coater used. In extreme cases, the edge bead can be removed manually, but this method is unreliable. Consequently, problems arising from large edge beads on very thick SU-8 layers were not fully resolved with the available equipment.

Despite the edge beads on thick layers, these beads still had a relatively minor contribution to the problem of poor feature sizes. Even features defined in relatively thin SU-8 layers can be swollen near the edge of wafers using Mylar masks, indicating that the problems with feature sizes were primarily due to flexing of the masks, rather than the edge bead, SU-8 thickness, or processing conditions (see Figure 3.12). As a result, the minimum achievable feature size for SU-8 was often significantly larger than the smallest definable feature in the emulsion masks. Due to this contact problem, no significant studies were completed on optimizing minimum feature sizes in this process, but significant improvements could be achieved by the use of chrome masks and proper edge bead removal.



Figure 3.12: Feature size swelling and alignment errors due to emulsion mask contact problems. Structures on the left were fabricated near the wafer center, while those on the right were near the wafer edge. Minimum and maximum SU-8 thicknesses are 5 and 15 μm.

3.6.2 Negative sidewalls

SU-8 is designed to provide nearly vertical sidewalls when processed with optimal conditions [40], but if the processing is not optimal, SU-8 structures will typically have a negative sidewall profile, in which the top of the SU-8 feature is larger than the bottom. This effect can be due to under-exposure, too much deep-UV exposure in a wide spectrum source, or a large gap between the SU-8 and the mask [92]. The emulsion masks that were used in this work cause negative sidewalls in almost all SU-8 structures primarily because they have rough edges on all their features (see Figure 3.13).

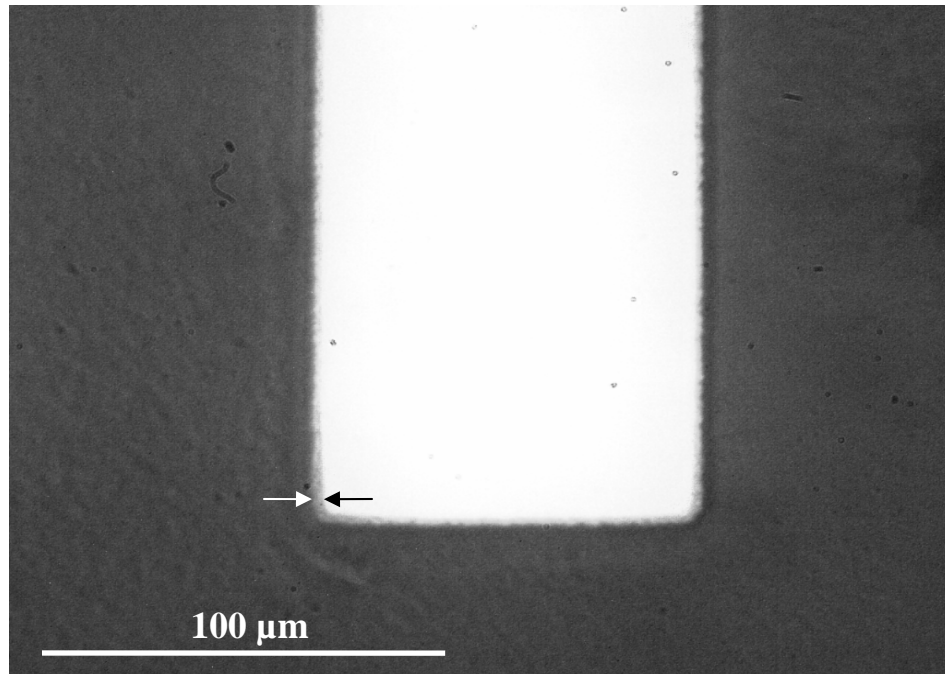


Figure 3.13 Rough edges on an emulsion mask feature. The arrows indicate the greyscale region.

Unlike chrome masks which have very high contrast between their transparent and opaque regions, the emulsion masks have a small gradient of transmission between transparent and opaque regions. This effect is basically a very small region of greyscale lithography, where a significant gradient of exposure dose can occur across the feature, even with very good mask contact. For the high quality Mylar masks used in later work, this region is less than one μm across, but on early masks, this greyscale region has been as great as several μm across. The result is that many SU-8 features are underexposed at the edges, which will result in a negative sidewall profile. The lower the quality of printing and minimum feature size, the more pronounced this effect. Figure 3.14 shows a side view of two cantilevers fabricated using emulsion masks with 30 μm minimum features sizes that demonstrate significant negative sidewalls.

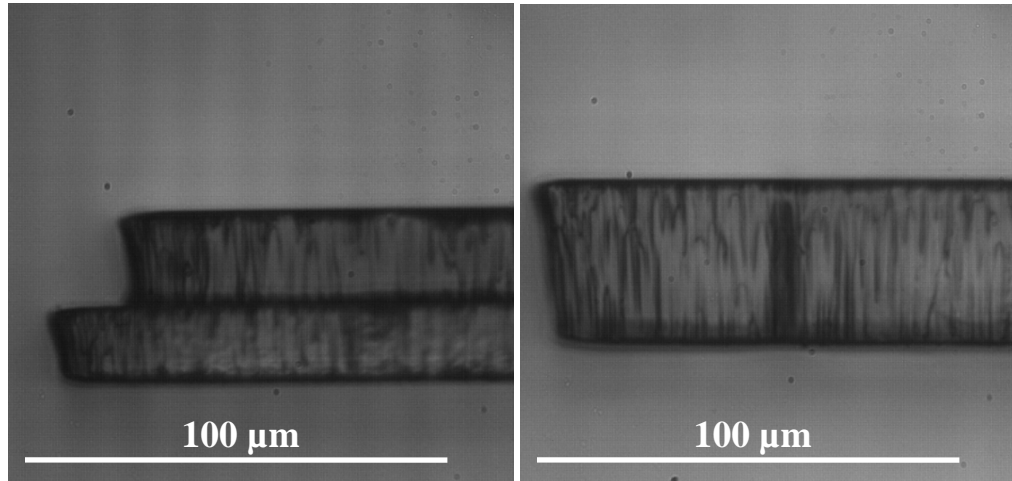


Figure 3.14 Two side views of SU-8 microstructures fabricated using a low quality emulsion mask. Significant negative sidewalls exist for both double exposed (left) [89] and single exposed (right) 40 μm thick SU-8 layers.

This greyscale effect on SU-8 exposed through emulsion masks is most pronounced on narrower structures, where the greyscale effects of the structure perimeter dominate the exposure. As seen in Figure 3.15, in extreme cases, thin structures do not crosslink the full thickness of the SU-8 film.

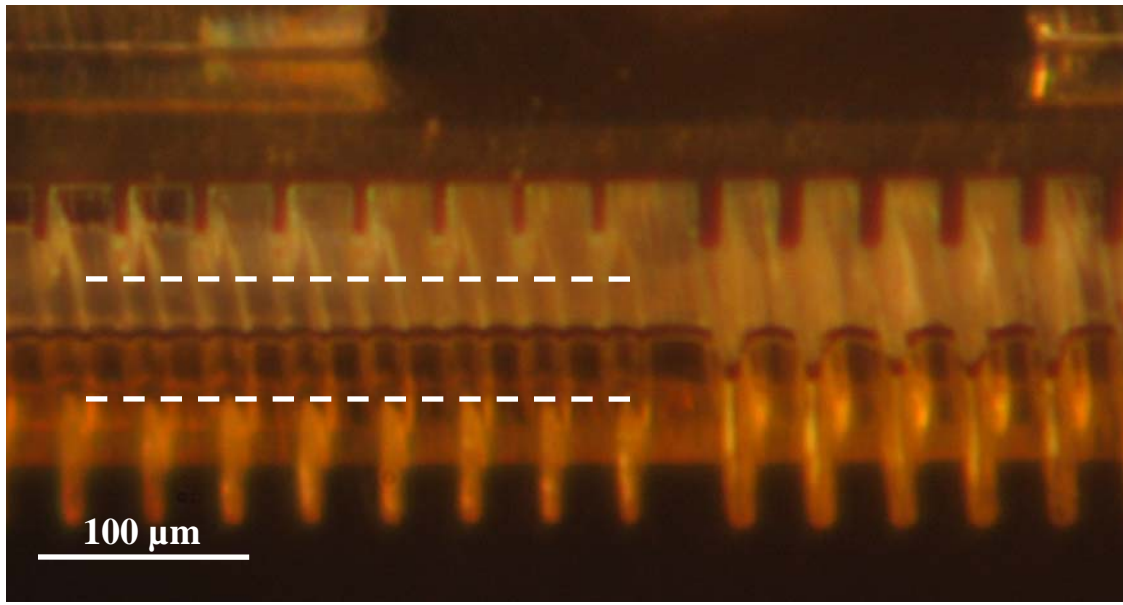


Figure 3.15 Photomicrograph of the effect of thin features in 150 μm thick SU-8 exposed through an emulsion mask. Beams on the left do not transfer all the way to the bottom but stop at the dashed lines showing the bottom and the reflected image of the bottom.

Despite the problems that can arise from the greyscale edges of the emulsion masks, in certain circumstances, these effects can be deliberately introduced for interesting future applications. If electrical isolation between SU-8 layers is desired after a blanket metal deposition, defining an extreme negative sidewall is possible in order to produce a lift-off profile in the SU-8. This lift-off method will not work as well if the metal is sputter deposited, due to the significant sidewall metal coverage that sputtering causes; however, if a more directional deposition technique, like evaporation, is used, a crude method of metal patterning on monolithic objects can be achieved. Figure 3.16 shows the effect of creating a deliberate greyscale region through a fine pitch pattern of lines or squares of minimum feature size [93] around solid beams of SU-8. Significant changes in sidewall profile, depending on the size of the greyscale area, are seen clearly in the reflection of the underside of the beams. In this instance, a single exposure can

result in dramatically different structure profiles, but requires a relatively thick ($> 50 \mu\text{m}$) SU-8 layer to work properly.

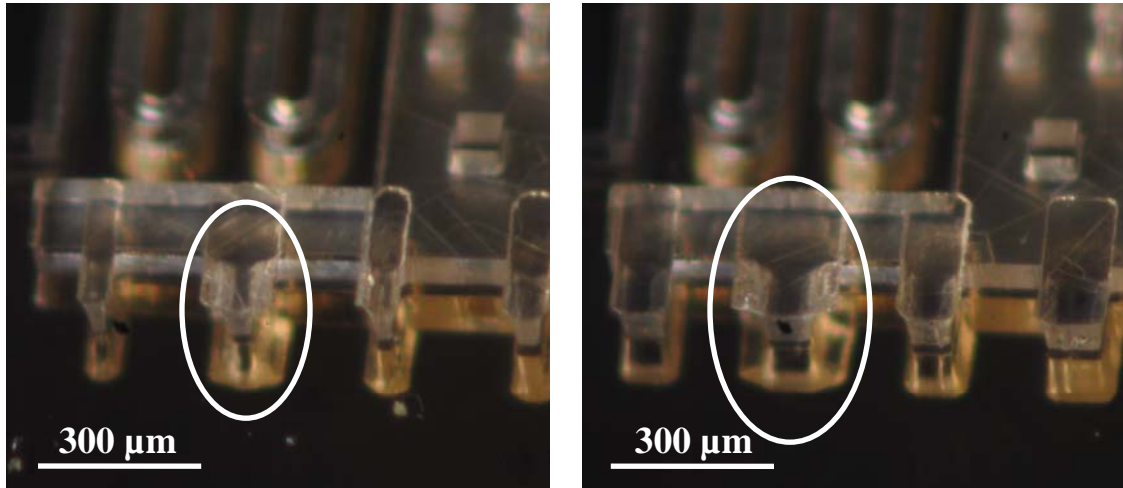


Figure 3.16 Photographs of the effect of deliberate greyscale effects introduced by mask design. Significant variation in sidewall profile can be achieved with a single exposure dose. Features with large negative sidewalls (and their reflections) are circled.

3.6.3 Tensile stress

The crosslinking reactions in SU-8 that occur after exposure and baking will always result in a residual tensile stress in fabricated structures. The shrinkage of SU-8 after crosslinking has been measured to be between 2-8%, depending on processing conditions [44], which is a very large dimensional change compared with inorganic MEMS materials, and requires care in designs to compensate for this effect. Some researchers have reported that thin SU-8 layers can be made compressively stressed with exposure to an $\text{SF}_6/\text{N}_2/\text{O}_2$ plasma [94], but whether this technique could be modified to affect thicker layers is not known. The severity of SU-8 shrinkage depends on the maximum baking temperature, with increased baking temperatures resulting in larger shrinkage. Because the temperature stability and material strength also increases with increased baking time, the optimal processing conditions for SU-8 depend greatly on the

expected application. For the majority of rapid prototyping applications, a baking temperature of 95 °C is sufficient for good results.

3.7 Polymer MEMS design rules

To ensure maximum yield of fabricated devices, a general set of design rules was identified for this process. The rules discussed below assume the standard processing technology with a 5 µm thick sacrificial layer and two structural layers of approximately 20 and 40 µm using SU-8 2010 [30]. The design rules provide users with an excellent basis on which to produce high yield structures using this MEMS process. It is not a comprehensive list of all things that can successfully be fabricated or be modified to work, nor does it absolutely guarantee success for all devices. These rules were originally written for use with emulsion masks with a minimum feature size of 30 µm. The rules are mainly designed to produce large, relatively low aspect ratio structures. The acquisition of higher quality emulsion masks has allowed a reduction in minimum feature sizes and increased aspect ratios, but the structures should be designed no smaller than absolutely necessary to ensure maximum device yield.

The naming conventions for many layers are taken from the PolyMUMPs design rules file. This layer convention was chosen because most MEMS designers are familiar with the PolyMUMPs process, and the same technology file was originally used when designing the first polymer MEMS masks. The author used L-Edit to create the dimple design in the POLY0 layer because it is easier to see visually in this particular CAD software. Table 3.3 outlines the SU-8 layer names, potential thicknesses and corresponding layer name in the PolyMUMPs technology file.

Table 3.3 Suggested minimum features and spacing for the polymer MEMS process assuming a 15 μm thick first SU-8 layer and 40 μm thick total SU-8 layer.

Feature	Min. Feature	Min. Spacing	Drawn with:
Anchor	10 μm	10 μm	ANCHOR1
Dimple	10 μm	10 μm	POLY0
Thin SU-8	10 μm	15 μm	POLY1
Thick SU-8	10 μm	15 μm	POLY2

These minimum features and spaces all assume an emulsion mask is used that is capable of defining a 10 μm feature. Producing structures with arbitrary sizes greater than 10 μm may be possible, but in general, keeping features with integer multiples of this minimum size is recommended. Minimum spaces are selected to be larger than the minimum features because the SU-8 features tend to swell if they are overexposed or if the mask is in poor contact. The result is that small gaps are more difficult than small structures to fabricate properly, and an extra margin of error is built into these design rules for this reason.

Because this process has no separate metal patterning step for depositing metal on top of SU-8 so no mask is used in the basic process to define the metal areas. A novel method of lift-off metal processing on a partially uncrosslinked SU-8 wafer is described in the Appendix, but was not the primary focus of this work.

3.7.1 Anchors

The method by which anchors are formed in this process offers the possibility of multiple anchor profiles. All anchors and dimples are defined by patterning the thick photoresist layer and transferring this topology to the polystyrene layer. Figure 3.17

shows a profile of anchor and dimple structures that can be defined with a combination of two mask levels.

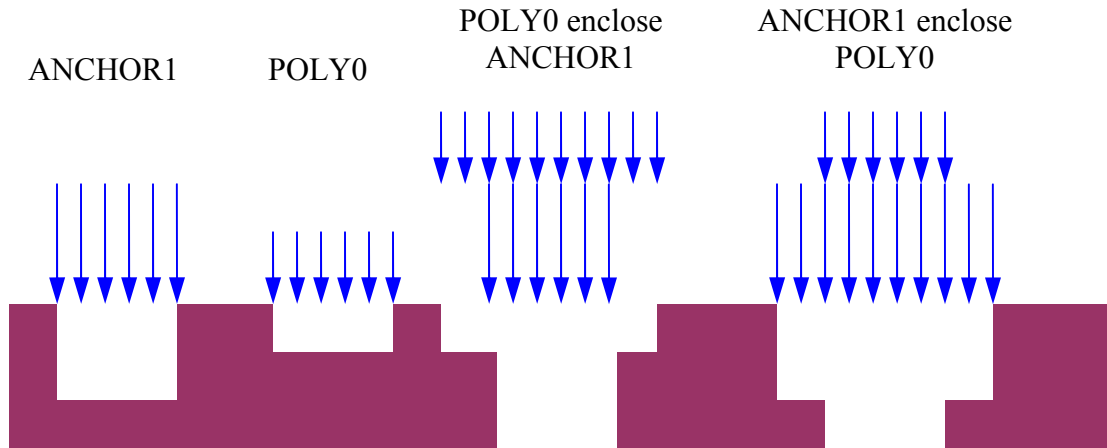


Figure 3.17 Potential configurations of anchors and dimples. This diagram assumes two exposures that are individually not enough to fully expose the photoresist. The anchor exposure in this case is longer than the dimple exposure.

This particular configuration assumes a relatively high degree of control of exposure depth, which is more difficult with emulsion masks. When exposed through chrome masks, underexposed photoresist will develop to a very repeatable depth, but using emulsion masks can introduce significant variations due to non-uniform optical properties. To achieve the different profiles shown in Figure 3.17, a 20 and 30-second exposure may be used for POLY0 and ANCHOR1 respectively. For the majority of work, a single dimple depth is sufficient, and a long anchor exposure that removes all photoresist in a single step is used. The default configuration produces dimples that are between 1-2 μm deep and enclosing all ANCHOR1 features by POLY0 is encouraged. This procedure produces an over exposure of all anchor layers which should ensure maximum anchor reliability. Although the minimum feature size for anchors is 10 μm in these design rules, the smallest recommended dimension for a robust anchor is 60 μm .

Smaller anchors can work, but device yield is reduced significantly at smaller dimensions.

Most anchors in this process are designed to provide the most reliable mechanical connection to the substrate without being electrically connected after a blanket metal deposition. Figure 3.18 shows an example layout in L-Edit of an anchor structure designed to be electrically isolated from the substrate.



Figure 3.18 L-Edit layout of a typical anchor structure in the polymer MEMS process.

In this example, the POLY0 encloses ANCHOR1 to ensure the anchor clears, and the encompassing dimple structure reduces each step height, which can minimize radial streaking during the spin-coating of SU-8. The requirement for POLY1 to enclose POLY0 is not an absolute requirement but is highly recommended. When alignment is good, having POLY1 features the same size as POLY0 will not affect the design in a significant manner. However, if alignment is poor, structures fixed to the anchor might

have an unwanted step difference in thickness at their base, possibly affecting the mechanical properties of a cantilever for example.

If an anchor is required to be electrically connected to the substrate, then the ANCHOR1 and POLY0 features should both be larger than the SU-8 structure on at least one side of the structure. This avoids the overhanging SU-8 features that would normally cause electrical isolation after the blanket metal deposition. An example of an anchor that is electrically connected to the substrate while not mechanically affecting cantilever structures is shown in Figure 3.19.

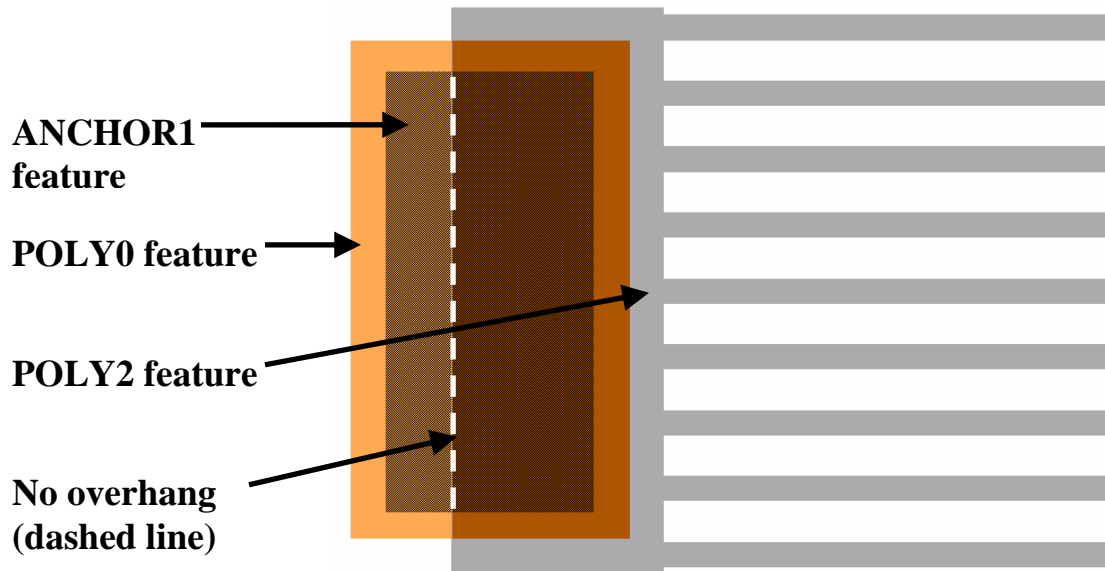


Figure 3.19 L-Edit layout of a cantilever array designed to be electrically connected to the substrate after a blanket metal deposition.

If anchors are designed to be several thousand μm^2 , the chance of SU-8 delamination from the substrate decreases because the ratio of device to anchor size decreases, which lowers the peeling chances during ultrasonic release. As a result, unless it is necessary to have electrical isolation is necessary between two parts in very close proximity, having one large anchor with many compliant structures attached is

recommended, rather than multiple minimum feature size anchors. The cantilever array in Figure 3.19 is an excellent example of using one large anchor to hold multiple parts.

Very large anchors that enclose multiple parts can be used with this process to produce SU-8 structures that are directly anchored to the substrate in a manner similar to processes without sacrificial layers but this configuration can change the processing characteristics. The effect of very large anchors is that they alter the SU-8 thickness relative to surrounding structures. For small to medium sized anchors, the planarization of the spin-on processing creates a total SU-8 anchor thickness that is equal to the regular SU-8 thickness plus the thickness of the sacrificial layer ($\sim 5 \mu\text{m}$). The topographical effect of the missing sacrificial layer can be transferred to the SU-8 thickness when these anchors become much larger (several 100's of μm). In this case, the SU-8 areas close to the anchor edge can be highly variable in thickness due to streaks and waviness in the layers caused by spinning over relatively large step heights. For thinner layers, these streaks are not completely removed by the softbaking steps. If redesigning the structural and sacrificial layer thicknesses in this process, a good rule of thumb is to have the first structural SU-8 layer at least 3-4 times thicker than the sacrificial layer, which minimizes radial streaks and waviness after spin coating and results in much more repeatable processing.

3.7.2 Release holes

For the polymer MEMS process, the successful release of the compliant structures requires that SU-8 not break or remain stuck to the substrate after development.

Removing the polystyrene with toluene is extremely rapid compared with alternative

sacrificial layers, but given the size of the structures that are possible to produce in this process, the introduction of release holes can significantly reduce development times. A typical release will remove polystyrene from under a 200 μm wide structure in less than a minute. However, etch rates for sacrificial layers eventually decrease with increasing structure size as mass transport and diffusion rates become limiting. To avoid excessive time in the ultrasonic bath which will eventually damage compliant structures, all devices larger than 250X250 μm^2 should include holes through which polystyrene can be dissolved by the toluene. The etch hole size recommended for large structures is 50x50 μm^2 and should be spaced no more than 200 μm apart. This release hole dimension will work fine for both emulsion masks and chrome masks and is large enough to work for nearly all layer thicknesses and exposure doses. Smaller holes can also be used, but at greater risk of filling in the hole due to feature swelling. A minor swelling problem that reduces the size of the release holes can cause major issues with unreleased structures, so designs should always err on the side of caution when placing and designing the holes. Unlike the PolyMUMPs process which defines holes in separate mask layers [1], no Boolean operations are calculated automatically when generating masks; therefore, etch holes should be drawn as HOLE1 or HOLE2 then subtracted using the L-Edit Boolean function. If these holes are drawn improperly, or fabricated incorrectly, release failures, like those shown in Figure 3.20, can occur.

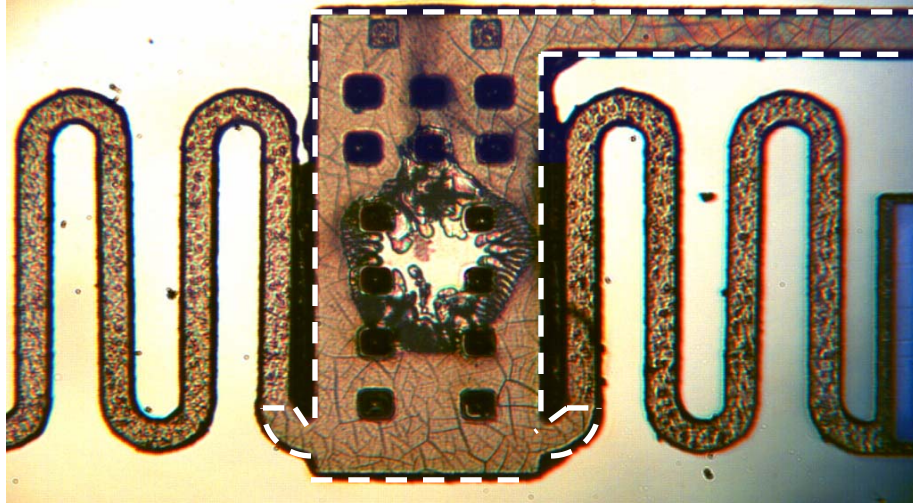


Figure 3.20: Release hole failure due to overexposure of POLY1+POLY2 in a single thickness SU-8 structure. Polystyrene remains undeveloped in the centre of the structure. The dashed line indicates the POLY2 feature.

3.7.3 Dimples

The purpose of the dimples is to reduce the stiction force between the SU-8 and the substrate after release. SU-8 has lower incidence of stiction than silicon due to its low surface energy ($\sim 30 \text{ mJ/cm}^2$) [95] combined with the RIE roughening of the polystyrene surface. The effect of the rough underside of SU-8 combined with its low surface attraction to gold allows many small structures to be successfully released without adding dimples, but for larger structures, dimples are critical for acceptable yield. The number and placement of these dimples depends on the size of the structure, and the requirements for electrical isolation. Dimple spacing is recommended to be $100 \mu\text{m}$ at most, but designers are free to use as many or as little dimples as they wish. A dimple that completely encloses a compliant structure can also be effective if acetate or Mylar masks are used, due to the micro-roughening from uneven transmission through these materials.

To prevent electrical shorting of SU-8 structures to the substrate after the blanket metal deposition, dimples should be enclosed completely by SU-8 structures. If there is no metal coverage or no need to keep the SU-8 and substrate electrically isolated, then dimples can be defined arbitrarily. Figure 3.21 shows L-Edit layouts of two dimple designs, one with enclosed dimples and the other as a dimple field over which devices have been fabricated. The minimum size a dimple can be fabricated is $10 \times 10 \mu\text{m}^2$, but $20 \times 20 \mu\text{m}^2$ is the smallest recommended size when using emulsion masks.

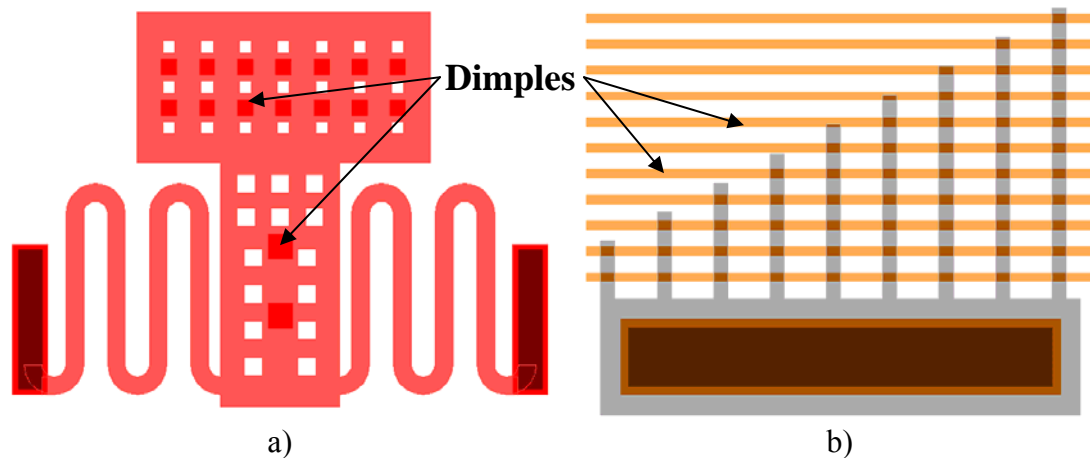


Figure 3.21 L-Edit layouts of two potential dimple arrangements: a) fully enclosed dimples on a large plate, b) large dimples to release an array of thin cantilevers.

3.7.4 Double thickness structures

Unlike the PolyMUMPs process, to produce thick structures, both POLY1 and POLY2 need not be drawn. Although POLY1 and POLY2 can be drawn on the same area to produce a nearly identical structure as POLY2, small differences occur in the final device fabrication. If the two layers are misaligned, a small step appears on some sections of a structure that is defined with both POLY1 and POLY2.

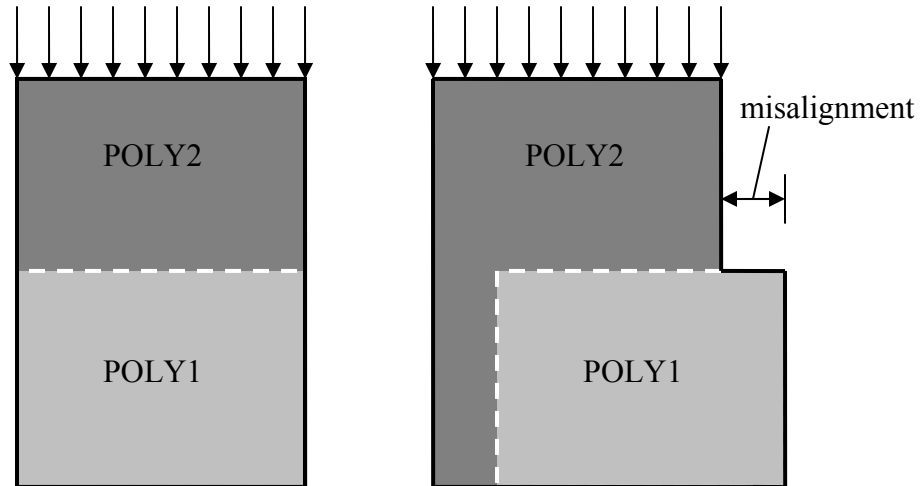


Figure 3.22 Cross-sectional view of perfectly aligned and misaligned POLY1 and POLY2 exposures defining a double thickness structure.

A second difference is that the total exposure dose given to a structure defined with both POLY1 and POLY2 layers is greater than that defined by only POLY2; therefore, the thermal history of the crosslinked SU-8 is different. The material properties of such a structure are then slightly different due to the greater amount of crosslinking, and the change can be very dramatic for thicker structures. The exposure doses should be optimized for a single mask defining a feature, so a double exposed structure will be overexposed in general. These issues mean that in most cases, if a thick SU-8 structure is desired with good feature sizes, only a POLY2 layer should be defined.

3.7.5 Very large structures and tethering

The polymer MEMS process is capable of producing structures with areas from a few hundred μm^2 to several mm^2 . When designing very large structures, designing for minimum release times and maximum yield is important. Very long, thin structures tend to have the greatest yield problems. Where possible, they should be reinforced with tethers that can be broken later. These tethers prevent large structures from fracturing

during the ultrasonic release. In extreme cases, some very large structures, like microgrippers, may be designed for removal from the substrate after release and appropriate tether designs will ensure device survival until removal. Figure 3.23 and Figure 3.24 show potential tether configurations for different applications.

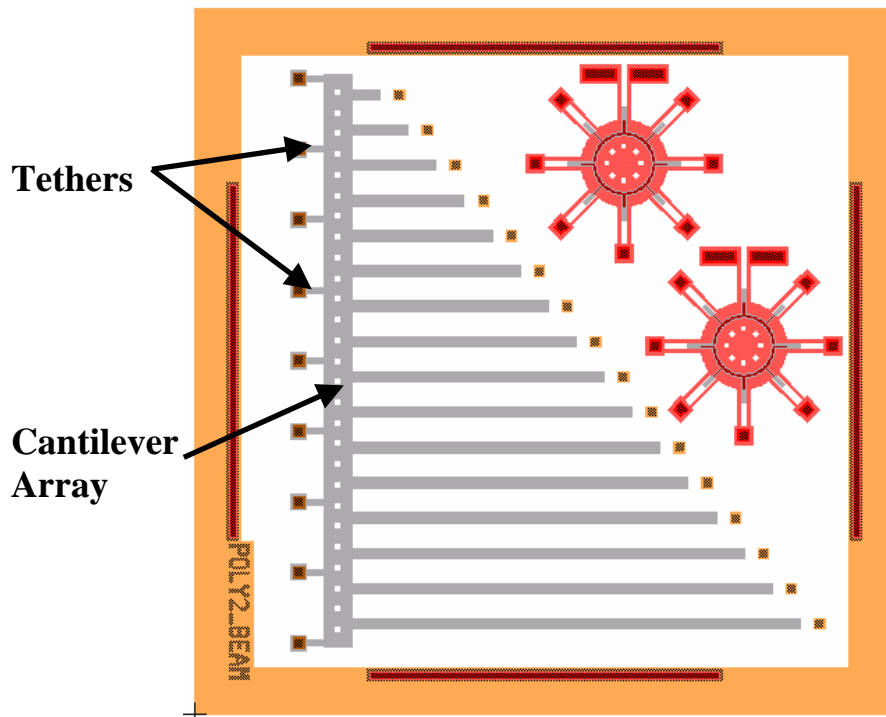


Figure 3.23 L-Edit layout of a cantilever array held on the substrate by a series of breakable tethers on a 1x1 cm die. This whole array can be removed from the substrate after breaking tethers using the method described in [82].

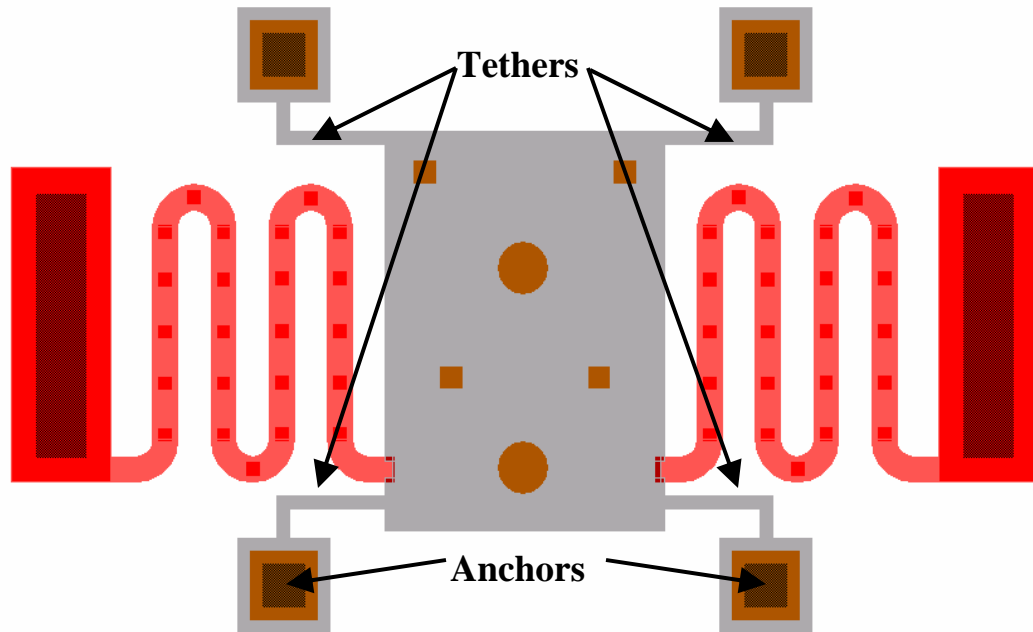


Figure 3.24 Layout of a large pop-up structure held with four tethers. Tethers are compliant in two axes to allow tensile stress to be relieved after release.

3.7.6 Alignment

The different masks used in this process all have to be aligned to the first anchor layer. As the layers become thicker, ensuring proper alignment to the substrate becomes more difficult. Alignment between ANCHOR1, POLY0, and POLY1 is typically very good, but POLY2 can be misaligned by 5-10 μm when very thick layers are being used. In addition, there is always the possibility of run-out error in Mylar emulsion masks that can cause alignment problems at the edge of wafers. As a result, if possible, structures should enclose anchors by 30 μm to avoid electrical shorts to the substrate. Very tight spacing between POLY1 and POLY2 features should also be avoided as this might result in merged features which cannot separate structures.

4 MODIFICATION OF SU-8 PROCESSING FOR IMPROVED RELIABILITY AND PACKAGING

4.1 Introduction

During the development of the SU-8 process, the primary focus was on mechanical stability and yield of compliant SU-8 structures. In addition to these experiments, work was also completed with respect to electrical connection of SU-8 based MEMS actuators to commercially available packages. Both mechanical optimization and packaging technologies are aspects of SU-8 processing that have not been adequately addressed prior to this work, but are detailed in this chapter.

Previous researchers have optimized SU-8 with respect to feature sizes and aspect ratios [90, 91, 96], demonstrating how these properties can change with altered processing conditions. While important, these parameters are not as critical for mechanical applications. In fact, the processing parameters that allow fabrication of very high aspect ratio structures frequently result in highly stressed SU-8 films or mechanical failures during release in this process. Once the basic process was developed, a large number of compliant SU-8 structures were fabricated and observed. One of the most common variations observed in long compliant SU-8 structures was the different stress gradients across individual wafers, and the different stresses between different wafers that had been processed at different conditions. The curvature of compliant SU-8 structures (anchored structures that are free to move relative to the substrate) has been reported previously [97-100] under a variety of processing conditions and device types, but no

researchers has systematically investigated this phenomenon in order to explain it.

Observing the behaviour of many SU-8 cantilevers revealed that curvature could be either negative or positive; indicating that optimization of curvature was possible to provide flat structures. The research results regarding this topic was the subject of a paper published in the Journal of Micromechanics and Microengineering [82].

4.2 Control of out-of-plane curvature in SU-8 compliant structures

During early trials with wafers fabricated in the finalized general process, most SU-8 structures appeared relatively flat and stable. Later efforts to determine the maximum length of SU-8 structures that could be successfully released revealed that SU-8 frequently demonstrated out-of-plane curvatures that were visible to the naked eye and occasionally severe enough to interfere with device function. The fact that identical structures on different wafers processed at different conditions showed significantly different curvatures indicated that this behaviour was not random. Consequently, this behaviour needed to be explained and optimized. A set of experiments were conducted to determine how the curvature of SU-8 compliant structures could be controlled.

The curvatures in SU-8 cantilevers appeared most severe at lower baking times and exposure doses; these conditions always resulted in SU-8 structures that would curl towards the substrate. Thinner structures processed with the same parameters were flat, or occasionally curled upward. To determine the exact behaviour, a series of wafers were fabricated that included multiple structures designed to test out-of-plane curvature. These structures included a cantilever array that could be removed from the substrate for direct observation, and cantilevers that can be assembled out-of-plane for observation based on

the out-of-plane mechanism described by Tsang *et al.* [37, 101]. An L-Edit layout of the removable cantilever array is shown in Figure 4.1.

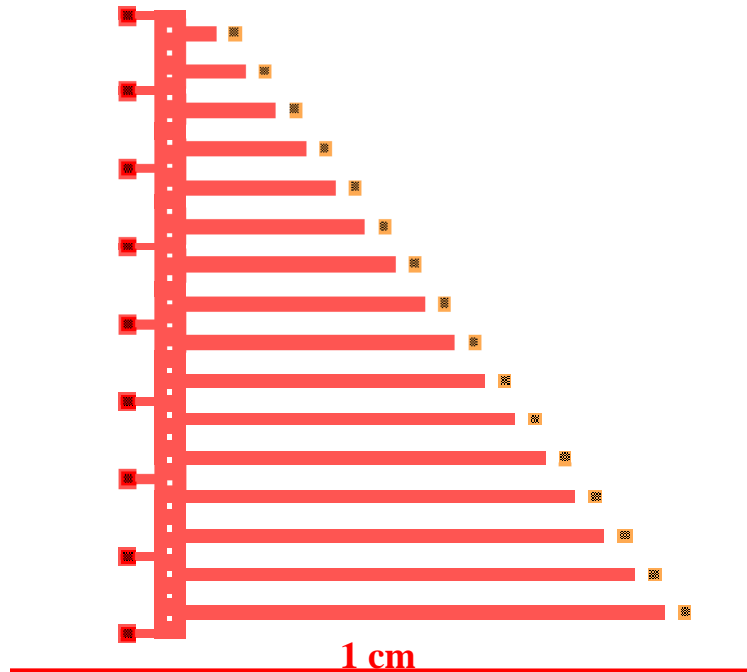


Figure 4.1: L-Edit layout of removable cantilever test structures for observing out-of-plane curvature. The longest cantilever in the array is 6400 μm long [102].

For thicker structures ($>40 \mu\text{m}$), the out-of-plane mechanism described in [37, 101] failed prior to being assembled, so the majority of tests were completed on the array of cantilevers shown in Figure 4.1, which were the subject of the paper listed in [82].

The following processing steps are summarized from [82]:

- a) Four silicon wafers were RCA cleaned and sputtered with 50 nm Cr/50 nm Au for alignment and adhesion purposes.
- b) An 8 μm thick layer of polystyrene (PS) was spin coated onto the wafers and baked for 10 minutes at 100 $^{\circ}\text{C}$ to dry and relax the film. A 6 μm thick layer of Shipley 1827 photoresist was spun onto the PS and baked for 15 minutes at 100 $^{\circ}\text{C}$.

- c) The wafers were aligned and exposed with an anchor mask, and then developed.
- d) A timed O₂ reactive ion etch etched the photoresist and PS at the same rate, transferring the anchors to the PS. A final PS thickness of 5 μm was achieved.
- e) A flood exposure and development removed any residual photoresist.
- f) A 30 second gold etch removed gold from all anchor areas, revealing chrome. A DI water rinse for 1 minute was followed by an N₂ dry and a 5 minute dehydration bake at 120 °C, providing high contrast alignment markers and areas with strong adhesion to SU-8.
- g) SU-8 2010 from Microchem Corp. [30] was spun onto the wafer at 1500 rpm for 30 seconds. Then, in order to remove solvents, a softbake on a ramping hotplate follows that ramps up to 95 °C from room temperature at 300 °C/hr. The wafer is held at 95 °C for 30 minutes before being naturally cooled on the hotplate to room temperature. The softbaking time in this work greatly exceeds the manufacturers recommended times for the thicknesses used [30], but it ensures better repeatability of results by minimizing solvent content. Reducing solvent content with longer pre-bake times has also been reported to reduce stress in developed SU-8 structures [103]. The SU-8 thickness of non-anchor areas after this step is approximately 15 μm.

- h) A second layer of SU-8 2010 is spun onto the wafer at 1500 rpm for 30 seconds. The softbake ramps from room temperature at 300 °C/hr and is held at 95 °C for 45 minutes before being cooled to room temperature. The resulting total thickness is approximately 40 μm.
- i) A structural mask is aligned to the wafer, and cantilevers are exposed with different energies across the wafer; between 300 and 900 mJ/cm². Each wafer is exposed with 13 different doses. A post exposure bake (PEB) is performed on each wafer, ramping up from room temperature at 300 °C/hr to 95 °C which is held for a different time for each wafer (either 0, 10, 20 or 30 minutes) before being naturally cooled on the hot plate. The ramping bakes and slow cooling helps minimize the transient thermal gradients within the SU-8 film.
- j) Development is completed using a 2 minute ultrasonic bath of SU-8 developer followed by a 1 minute ultrasonic bath of toluene before being rinsed with fresh toluene and isopropyl alcohol. The wafers are dried with N₂ and left for at least a day to ensure remaining solvent evaporation, as residual solvents can swell minimally crosslinked SU-8 and affect the measured curvature. After one day, no further changes in cantilever curvature are observed. The resulting cantilever thickness is approximately 40 μm.

The absorption of toluene and IPA by underexposed SU-8 typically leaves all cantilevers curled up immediately after development, but as they dry, underexposed cantilevers will begin to curl downward, while the over exposed cantilevers remain at

approximately the same curvature. The majority of curvature change occurs within 24 hours. When exposing the wafer, an emulsion mask was used with 8 rows of 1x1 cm die. The mask was placed in tight contact between a glass plate and the wafer, while an opaque sheet to block UV light was placed on top of the glass plate. Exposure dose was provided across the wafer by moving the opaque sheet between short exposures. Exposures were timed manually to keep the wafer from disengaging from the aligner after the auto-exposure step, which avoided having to realign the wafer each time. The position of each exposed die and their total exposed time is illustrated in Figure 4.2. The measured output power of the aligner for this experiment was 10 mW/cm² for this experiment.

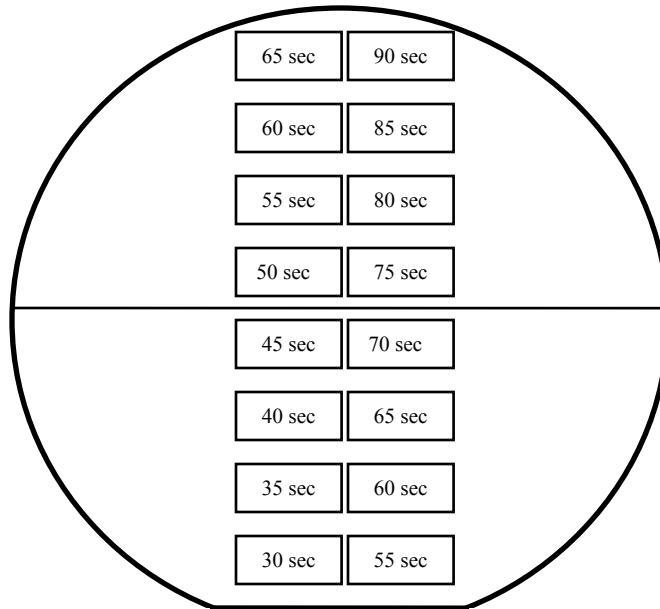


Figure 4.2: Exposure times at 10 mW/cm² for cantilever arrays on curvature test wafers.

After the cantilever curvatures stabilized, the cantilever arrays were removed from the substrate with a piece of double sided tape. The base anchor was large enough to align to by hand, and tweezers were used to position tape across the whole base of the

cantilever array and smooth the tape across the chip. This technique provides an even adhesion and prevents fracturing of the cantilever base. Peeling the tape off the gold coated substrate removes the cantilever array intact, and the tape is still tacky enough to secure the cantilever array to a glass slide which can then be mounted under a microscope (see Figure 4.3).

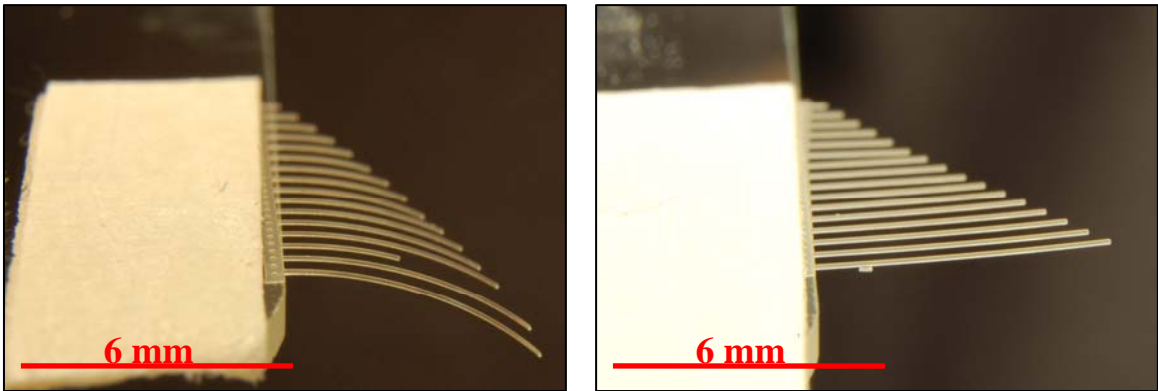


Figure 4.3: Cantilever arrays taped to glass slides for under exposed and over exposed conditions [102].

When the slides are mounted at 90° to the microscope's field of view, the curvature of each cantilever is clearly visible. As shown in Figure 4.4, to obtain a good image of individual cantilevers, the longest cantilevers were bent downward at the base to observe them independently from the rest of the array. Images were analyzed with National Instruments Vision Builder for Automated Inspection [39]. The system was calibrated to the correct dimensions with an object of known size at the same magnification. Using the geometry shown in Figure 4.5 and equations (4)-(7), the radius of curvature, R , can be determined from the distance D between two tangent points on the curve, a and b , and the angle between these tangents, τ .

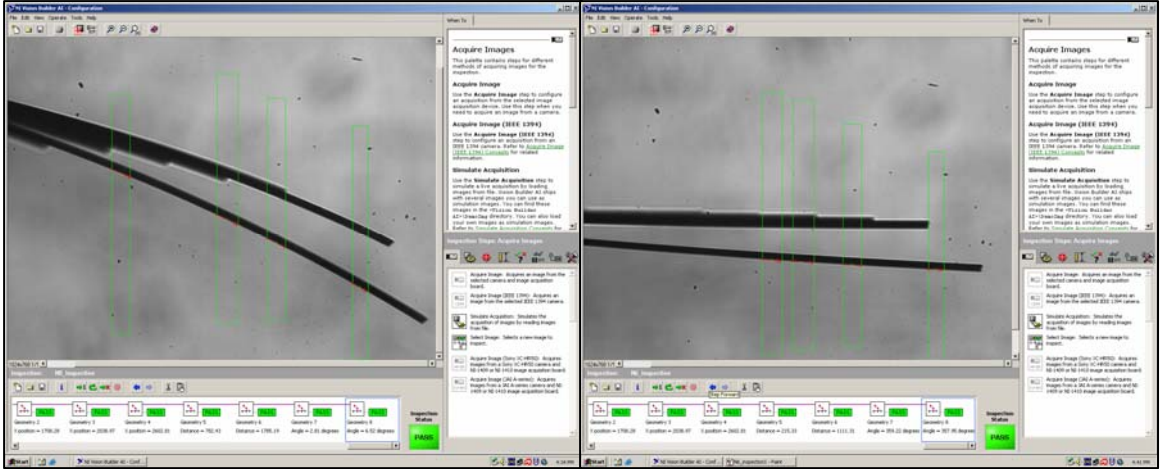


Figure 4.4: Photomicrographs of SU-8 cantilevers used for curvature trials.

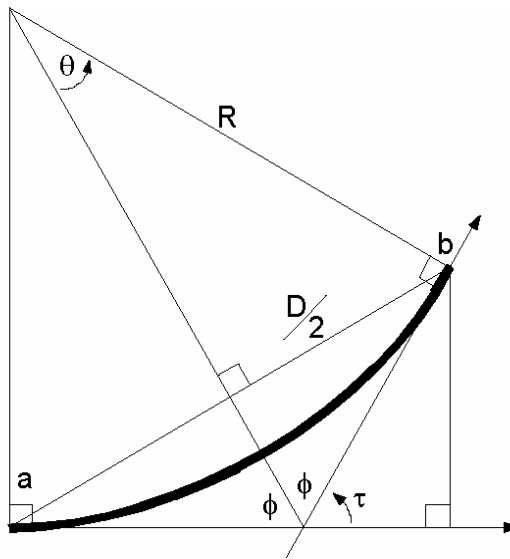


Figure 4.5: Geometry used for determining the radius of curvature of SU-8 cantilevers [102].

The relationship for R , D , a , b and τ are as follows:

$$R = \frac{D/2}{\sin \theta} \quad (4)$$

$$\theta = \frac{\pi}{2} - \phi \quad (5)$$

$$\phi = \frac{\pi - \tau}{2} \quad (6)$$

$$\theta = \frac{\pi}{2} - \left(\frac{\pi - \tau}{2} \right) = \frac{\tau}{2} \quad (7)$$

The plot of radius of curvature versus exposure dose is difficult to interpret, because the radius of curvature becomes infinite at a crossover value, therefore, the data collected in the National Instruments software is plotted against curvature, which is the inverse of the radius of curvature. Figure 4.6 and Figure 4.7 provide the cantilever curvature versus exposure dose for different baking times.

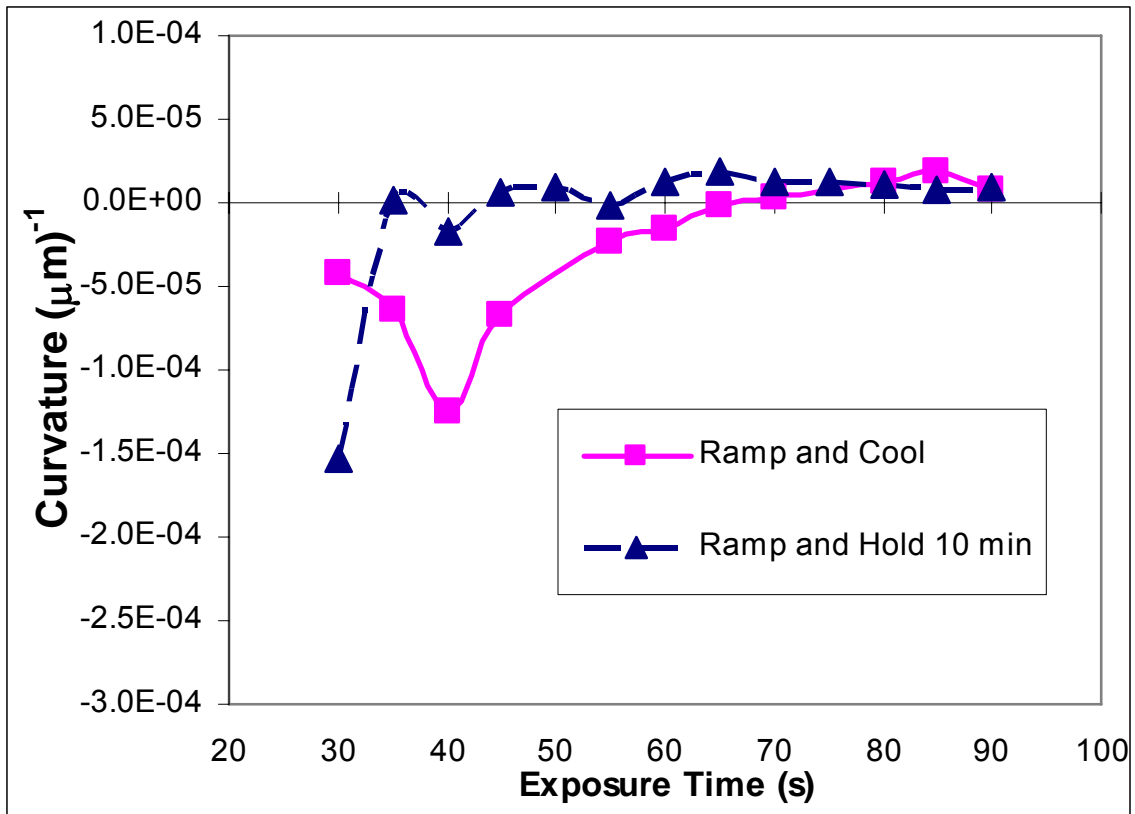


Figure 4.6: Curvature versus exposure dose for short baking times.

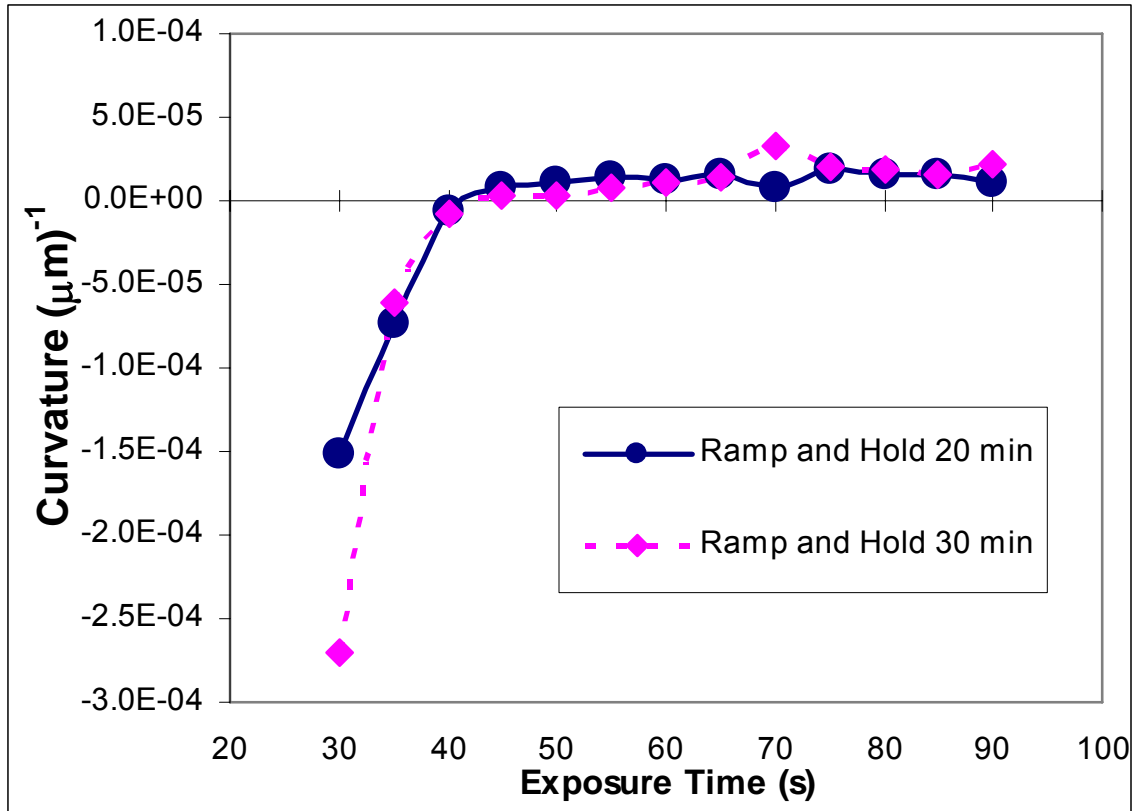


Figure 4.7: Curvature versus exposure dose for long baking times.

From Figure 4.6 and Figure 4.7, two observations can be made: at low exposure doses, the cantilevers will exhibit a negative curvature (curvature towards the substrate) for all baking times and this curvature becomes positive for higher exposure doses. A secondary effect is that the behaviour of curvature versus exposure dose becomes far more stable for the longer baking times, with a generally predictable curve after 20 minutes of baking. It appears that for all post exposure baking times at 95 °C there exists an optimal exposure dose that will provide zero curvature parts. For the thicknesses and processing conditions used in this experiment, this optimal dose ranges from 400 mJ/cm² for a 30 minute baking time, to as large as 700 mJ/cm² for the shortest baking time. This finding is important because it leads to the prediction that the curvature of compliant SU-8 structures can be controlled. In order to properly control the curvature, the exact

mechanism behind the curvature behaviour must be identified. Very little information was previously published on this specific topic, but other research has been completed into the general behaviour of SU-8 with different exposure doses and baking parameters by Feng and Farris [44]. In this work, they identified that the thermal coefficient of expansion of SU-8 can change with increased baking temperatures. The original work in [44] assumed constant material properties throughout the film, but they used very high exposure doses in their processing. This information, combined with a general understanding of epoxy crosslinking reactions, provides a possible mechanism for the curvature behaviour with varying doses. Based on the observed data, the curvature of SU-8 microstructures is primarily a function of the crosslink density throughout the film thickness, as well as the corresponding differences in material properties.

4.3 Theory of SU-8 curvature

Based on the observations of the SU-8 behaviour, the cause of the variable curvatures in SU-8 complaint structures is hypothesized to be due to gradients in crosslink density. Crosslinking density in SU-8 is a function of the baking temperature, and as identified by Feng [44], the coefficient of thermal expansion is greater for SU-8 that has been baked at lower temperatures. While the entire SU-8 film has a tensile stress induced by the crosslinking reaction, the differences in the thermal expansion coefficient due to crosslinking density produce a stress gradient after cooling. If crosslinking density was only a function of temperature, then SU-8 would always curl in the same direction, but this was not the observed behaviour. The mechanism of crosslinking needs to be better understood and modelled to explain the behaviour observed in Figure 4.6 and Figure 4.7.

A large number of publications have been written on the cure kinetics of epoxy resins, and the general crosslinking behaviour of many epoxies is well understood. The total crosslinking density, as it is frequently referred to in publications on epoxies, is known as conversion [104]. A condition of total conversion (100% crosslinked) occurs when the epoxy is baked at its full cure temperature, and the rate at which this occurs is related to the temperature, time, and the addition of any catalysts to accelerate the rate of reaction. For the baking of an epoxy, the rate of reaction can be summarised in certain cases with the following equation [104]:

$$\dot{\alpha} = \frac{d\alpha}{dt} = A \exp(-E_a / RT)(1 - \alpha)^n \quad (8)$$

where $\dot{\alpha}$ is the rate of reaction, E_a is the activation energy, A is the frequency factor, R is the gas constant, T is the temperature, and n is the order of the reaction. The activation energy, frequency factor, and order of the reaction cannot be found analytically, but must be determined from experimental data. In this work, there was no way to measure the exact rate of crosslinking reactions within SU-8 films, but predictions of general behaviour can be made based on equations such as these.

In the case of SU-8 crosslinking, the only variables under direct control are the temperature and the activation energy. The control of temperature during processing is self evident, but the control of activation energy comes from the exposure dose provided to the SU-8. A catalyst produced in response to UV radiation chemically amplifies the polymerization of the SU-8 photoresist by reducing the activation energy of the photoresist. This lower activation energy greatly reduces the temperature at which SU-8 crosslinks. The concentration of catalyst is not uniform throughout the thickness of the

SU-8 film, however, and this non-uniformity results in the curvature behaviours seen in compliant SU-8 structures.

For all SU-8 structures fabricated for this work, the exposure dose is delivered from the top of the film through a standard UV aligner. The absorbed energy is always greater in the top of the film, which results in a gradient of generated catalyst through the film thickness. This gradient of catalyst causes a gradient of reaction rates, with the top of the film reacting at a faster rate than the bottom. However, this effect is offset by the countering temperature gradient caused by baking on a hotplate. If the energy released during the crosslinking reaction is ignored, the thermal gradient during baking is linear with a maximum temperature at the bottom of the SU-8 film. These two countering gradients of catalyst concentration and baking temperature lead to a total crosslinking reaction that can produce either positive or negative curvature.

In order to observe the general effect of crosslinking gradients, a model of exposure dose was borrowed from the work of Gaudet et al. [75]. In their work, this model was used to find the minimum exposure dose necessary to cause SU-8 to become insoluble in developer. Their work included values for minimum exposure dose and values for the changing UV absorption of the SU-8 film with increasing dose. Most of the parameters used in this model are specific to the processing steps and experimental setup found in that specific paper, but as a means to observe the general exposure dose behaviour, the model is still valid for this work. This model uses several simplifications. The first simplification is that it ignores all pre-baking effects. The solvent content of SU-8 films prior to being exposed has been identified as a means to reduce stress induced by crosslinking [103], while the pre-bake temperature has been observed to affect

minimum resolution and stress of SU-8 structures [105]. In the designed process, virtually all baking times are far in excess of the manufacturer's recommendations, which should keep solvent content very low. Additionally, for consistency, the pre-bake temperature is maintained at 95° in all cases. The energy released by the crosslinking reaction is ignored in this model. The additional heat caused by chemical reactions is assumed to be small relative to the temperature of the hotplate. Moreover, this energy is reduced as time progresses, leaving a steady state temperature that depends solely on the thermal conductivity of the SU-8 and the temperature on the top and bottom of the film. Finally, any effects on the UV dose from the presence of the polystyrene layer are ignored, and the reflection of UV off the underlying gold layer is taken to be the same as silicon, so that the same values for reflected light may be used. In reality, based on the recommended doses from the SU-8 datasheets [30], the reflection off the gold layer is expected to be much lower than that of silicon.

The dose, D , provided at a particular depth of SU-8 and time of exposure through the top surface is given by [75]:

$$D(d, t_{\text{exp}}) = \frac{(1 - R_1)I_0 t_{\text{exp}} (1 + R_2 e^{-2\alpha_{\text{Unexp}}(d_{\text{total}} - d)})(e^{-\alpha_{\text{Unexp}}d} - e^{-\alpha_{\text{Exp}}d})}{(\alpha_{\text{Exp}} - \alpha_{\text{Unexp}})d} \quad (9)$$

where R_1 and R_2 are the reflection coefficients at the air/SU-8 interface and the SU-8/substrate interface, respectively, α_{Unexp} and α_{Exp} are the absorption coefficients of the unexposed and exposed SU-8, and I_0 is the input exposure power. Gaudet *et al.* measured the values of α_{Unexp} and α_{Exp} to be $38 \pm 1 \text{ cm}^{-1}$ and $49 \pm 1 \text{ cm}^{-1}$, respectively, with the value for α_{Exp} chosen at the maximum value of linearly increasing α with dose. The maximum α continues to increase at a slower rate with increasing dose for over

exposures, but this effect is not used in the model. This basic formula was used in an Excel spreadsheet to simulate the delivered dose at different levels in an SU-8 film with time. Simulated values for received dose at different depths of SU-8 are plotted in Figure 4.8 and Figure 4.9.

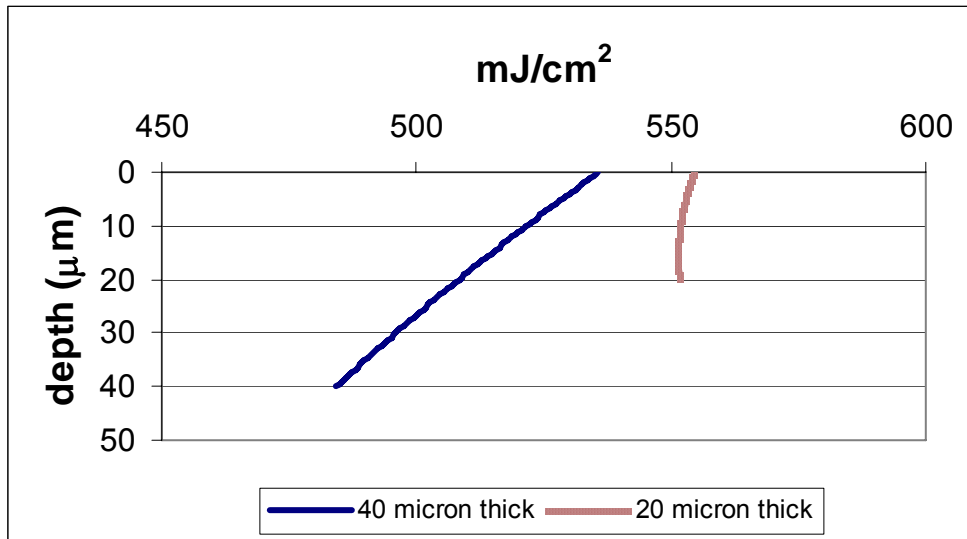


Figure 4.8: Calculated dose received at different depths within SU-8, for an exposure dose of 450 mJ/cm². Two SU-8 film thicknesses of 20 and 40 µm are modelled in this case.

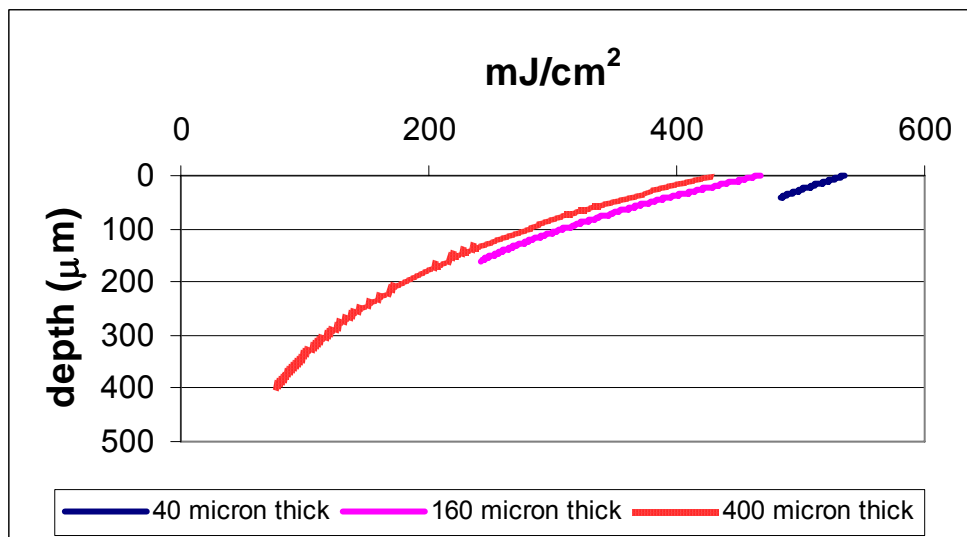


Figure 4.9: Calculated dose received at different depths within SU-8, for an exposure dose of 450 mJ/cm². SU-8 film thicknesses of 40, 160 and 400 µm are modelled in this case.

The reflection of the incident UV light off the substrate makes a significant difference in the dose received for thinner SU-8 layers. Due to the double exposure from the reflected light, the maximum dose received at certain depths in thin SU-8 layers is actually greater than the maximum input dose. For very thin SU-8 layers, this reflection effect can actually cause a minimum dose to occur at a point above the substrate, rather than the bottom of the SU-8 film. If this reflection off the substrate were zero, all curves for exposure dose versus depth would be independent of SU-8 film thickness. In the model presented, the reflection coefficient between SU-8 and the substrate was approximately 0.37 (estimated from the interface between SU-8 and silicon) [75]. The gradients in received dose through the film thickness will produce variations for catalyst created by the photo initiator. This variation will affect the material properties of the SU-8 after crosslinking, which depends on the baking temperature and time. Note that this model presently does not account for the saturation effect after all the photoinitiator has been reacted within the SU-8 film. After very long exposures, a maximum catalyst concentration will exist at all depths within the SU-8 film, and only thermal gradients will affect the curvature of SU-8 compliant structures. The exact dose required to maximize catalyst concentration is not known for SU-8, but it can be estimated by the exposure dose that results in positive curvature parts with minimum baking times.

Because all post exposure baking of SU-8 in this work was completed on the ramping hotplates, a thermal gradient always existed within SU-8 films during this baking step. To simplify the effect of baking, an isothermal model was used, ignoring the effects of ramping up or down. If the concentration of catalyst is constant in the SU-8 film, the hottest parts of the SU-8 will have a higher crosslinking density after the

reaction is complete and the steady state thermal gradient will be linear between the top and bottom SU-8 surfaces. The magnitude of this gradient depends on the temperature difference between the surroundings and the hotplate, as well as the heat transfer coefficient of the surrounding environment.

In addition to temperature and catalyst concentration, the rate of crosslinking within the SU-8 film progresses depending on the overall reaction order, n .

$$\dot{\alpha} = -\frac{d\alpha}{dt} = k\alpha^n \quad (10)$$

When integrated, this rate for 1st, 2nd and n^{th} order reactions is as follows:

$$\alpha = \alpha_o e^{-kt} \quad \text{1st order} \quad (11)$$

$$\frac{1}{\alpha} = \frac{1}{\alpha_o} + kt \quad \text{2nd order} \quad (12)$$

$$\frac{1}{\alpha^{n-1}} = \frac{1}{\alpha_o^{n-1}} + (n-1)kt \quad \text{nth order (except for 1st order)} \quad (13)$$

This reaction order is impossible to know with certainty due the lack of empirical data, but that of fully exposed SU-8 can be estimated from earlier published data. The reaction order is estimated based on the isothermal baking data from Feng [44], who claimed that the glass transition temperature (T_g) of SU-8 is proportional to the crosslinking density. The glass transition temperatures of fully exposed SU-8 were estimated from that paper and fit to different reaction rates. The results of three different best fits with different assumed reaction orders are shown below in Figure 4.10.

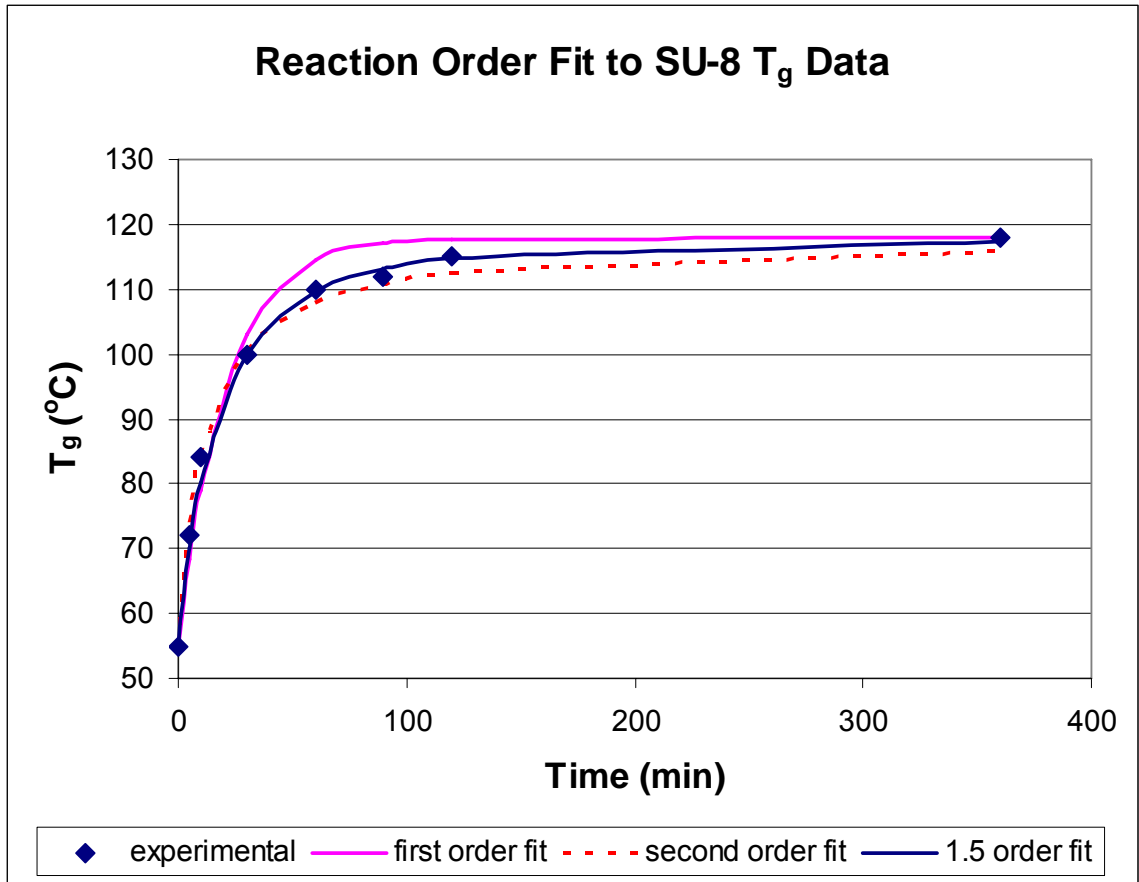


Figure 4.10: Experimental data on T_g of SU-8 taken from figure 11 of Feng [44], and fit to different reaction rate orders. T_g is assumed to be proportional to conversion percentage.

When the experimental data is fit to three different reaction orders, it appears that the reaction rate of fully exposed SU-8 is very close to a 1.5 order reaction ($n = 1.5$), which is in the range of typical epoxy reactions [104]. With future work, an exact reaction rate may be determined for different exposures and baking conditions, allowing prediction of SU-8 curvature values for any processing conditions. This work is beyond the scope of this thesis, as it will be a complex modelling problem, and require a much greater understanding of the exact properties of SU-8 at different crosslinking densities. It is important to note however, that standard processing times and temperatures will not result in a completely crosslinked condition. Only by baking SU-8 at temperatures

greater than 200°C is the crosslinking reaction expected to be complete, with T_g reaching ~238°C [44].

The effect of the counteracting gradients of catalyst concentration and temperature leads to SU-8 curvatures that can change with processing conditions. Three cases are possible: underexposed conditions, where the SU-8 parts will always curl downward for any baking times; moderately exposed conditions, where SU-8 can curl upwards or downwards depending on baking conditions; and overexposed conditions, where SU-8 demonstrates positive curvature for all baking times. In the underexposed case, the gradient of catalyst concentration within the SU-8 film is dominant, and the temperature differences that occur during baking can never fully compensate for this effect. In this instance, the bottom SU-8 surface will have a larger tensile stress after cooling, resulting in structures that will always curl towards the substrate. In moderately exposed conditions, the gradient of catalyst concentration can be countered by thermal gradients, but the reaction rates of the top and bottom surfaces are different. A fast reaction in the top part of the SU-8 film due to higher catalyst concentration will eventually be overcome by the slower reaction at the bottom of the film. The higher temperature at the bottom of the film will eventually result in a higher total conversion than the top of the film. By this mechanism, maximum crosslink density may be at the top or bottom of the film, with a corresponding change in curvature due to the thermal expansion coefficient. In these moderately exposed conditions, there will always exist a baking time and temperature that will result in zero curvature parts. In overexposed conditions, the catalyst concentration through the SU-8 film is at, or close to, a maximum due to saturation; and only the thermal gradient effects will be important. In this

condition, the SU-8 curvature will always be positive when baking on a hotplate, and maximum curvature will be related to the thermal gradient within the film during baking.

Several predictions of SU-8 behaviour can be made based on the models and assumptions listed above, which include:

Thinner SU-8 layers will have lower gradients, but will curl more for the same gradient. From the plots in Figure 4.8 and Figure 4.9, thinner layers have a much lower gradient in received exposure dose, which will result in a lower gradient of catalyst within the film. Because the stiffness of rectangular beams is proportional to the cube of their thickness, an equal gradient in a thin beam will result in much higher curvature. Practically, however, because of material weakness throughout the beam thickness, thinner beams will usually fail mechanically if underexposed enough to result in negative curvature.

A higher baking temperature will result in a larger positive curvature for over exposed SU-8 structures. If the ambient conditions surrounding the hotplate remain the same, a higher hotplate temperature will result in a greater thermal gradient across the SU-8 film, which will reduce the exposure dose required for zero curvature parts and make the maximum positive curvature more severe.

Post exposure baking in an oven may reduce curvature caused by thermal gradients. If the hotplate is responsible for positive curvatures due to thermal gradients, then it should be possible to reduce them by baking with an isothermal ambient temperature in an oven. In this case, however, a long exposure dose is required to minimize the catalyst gradient within the SU-8 before being baked, as no counteracting linear thermal gradient will be present. A slow ramp of the oven to the PEB temperature

and back down again may be necessary to minimize transient thermal gradients that would make results less predictable.

Very thick structures are much more difficult to optimize for curvature. A significant non-linear gradient in absorbed energy exists between the top and bottom surfaces for very thick layers. As a result, the majority of structures fabricated in thicknesses of 100 μm or above have had negative curvature. Solutions to this problem are to dramatically increase exposure dose (which results in bloated features and poor repeatability), increase baking temperature (which will increase the thermal gradient, but also reduces resolution), or use a UV wavelength that is absorbed at a lower rate in SU-8. Using a UV wavelength with lower absorption will reduce the exposure gradient, but the time required to deliver an appropriate dose will be very high [41] and new optimization tests will be required based on these different wavelengths.

A final problem that must be addressed in future designs is the effect that poor mask contact, or emulsion edge greyscale effects, will have on narrow compliant structures defined using standard UV wavelengths. The cantilevers tested in this work were still relatively low aspect ratio ($\sim 1:3$) and had a high area to perimeter ratio. As the width of these structures is diminished, the gradient across the beams in-plane becomes more important, until in extreme cases, very thin structures will always be under exposed relative to wider areas for the same exposure dose. One dimensional modelling of exposure dose and thermal gradients will no longer be sufficient to predict the general behaviour of curvature, and more detailed models, like those described by Yang and Wang [41] would be required to accurately determine absorbed dose in two dimensions. A final method of controlling the curvature in thicker SU-8 structures is the subject of a

forthcoming article by Sae-Won Lee and the author, which requires multiple doses at different layers in this process. The general behaviour of this effect was discovered accidentally while examining SU-8 sidewalls on pop-up structures during earlier work on this thesis. Biographical information on this work should be available by the time this thesis is completed.

Ultimately, the degree of control over SU-8 curvature depends on the process control, and repeatability of the equipment used. The variability of curvature in overexposed SU-8 baked for 30 minutes is approximately $\pm 7.5e-6 \mu\text{m}^{-1}$. The test die design described in section 5.3 for feedback of process quality will provide better data on curvature variability across future process runs.

4.4 Robust electrical connections to SU-8 structures and actuators by gold wirebonding

The development of a multi-user polymer MEMS process has been very useful for determining polymer material properties and behaviour. The mechanical structures fabricated in SU-8 have been used to great effect in the prototyping of many novel compliant microstructures. The use of SU-8 as an actuator material has already been described in earlier work, and the specific use as a material for chevron thermal actuators was first described in [77]. Unfortunately, for nearly all actuators fabricated in SU-8, electrical interconnection has been a problem. Without a reliable method of wiring SU-8 sensors and actuators to external signals, this process is limited to the prototyping of individual devices, rather than full systems. In the field of polymer MEMS, the issues of reliable electrical interconnection between external signals and electrodes on, or within, SU-8 structures had been virtually ignored, despite the fact that integrating MEMS with

commercial packaging technologies with reliable yield is consistently one of the greatest barriers to developing useful devices and potential future products. To demonstrate that polymers may be integrated with existing commercial packaging technologies, a method was developed to reliably wirebond onto active SU-8 MEMS structures. The results are the topic of a conference paper presented at TRANSDUCERS 2007 [106].

4.4.1 Past work on powering SU-8 structures

Over the last few years, an increasing number of publications have focused on active SU-8 structures – defined in this work as SU-8 with integrated electrodes for sensors or actuators. Early publications focused on electrodes attached to SU-8 for Joule heating of thermal actuators [60, 61, 77, 107], while more recently, other groups have integrated electrodes for sensing deflection, or chemical reactions [63, 67]. In the work described for the actuators, electrodes were initially connected to a rigid silicon substrate [60, 62] which could be either bonded, electrically connected with conductive glue [61], or directly powered with microprobes [77]. Directly connecting electrodes to the substrate allows any traditional bonding method, like gold or aluminum wirebonding, to be achieved easily. However, it can cause problems when trying to electrically connect over a significant step height of several μm [63], which limits the size of the sacrificial layer that can be used, and potentially reduces the effectiveness of thermal actuation due to the proximity of resistors to the substrate [11]. When metal is deposited on the top surface of SU-8 actuators [61, 77], the direct electrical connection of these electrodes to the substrate is nearly impossible. Conductive glues have been used for powering individual devices fabricated in SU-8 [61, 108]. This method works reasonably well because the glues can be placed over large step heights and do not require high

temperatures during bonding. This method, unfortunately, is inappropriate for large scale bonding and is not compatible with existing commercial packaging techniques. More recently, investigations into electrically connecting an SU-8 cantilever chip for bio-sensing applications used flip-chip bump bonding, which revealed that bond yields up to 80% can be achieved using a process that is gradually gaining acceptance for commercial applications [108]. Unfortunately, the maximum yield for flip-chip bump bonding is still not high enough for reliable applications using SU-8, and using this method for rapid prototyping is difficult, due to the specialized equipment and procedures that are necessary. The same work that described flip-chip bonding also revealed that good wirebonding yields (close to 100%) could be achieved on SU-8 if a thick (13 μm) electroplated bond pad was used on top of the SU-8 [108]. Apparently, yield is very poor if this thick pad is not used, but no failure modes were given. Other reports on wirebonding onto polymers, like benzocyclobutene (BCB), detail how gold wirebonds onto polymers up to 20 μm thick can be as strong as those onto silicon, but only with sufficiently thick electroplated metal ($> 5\mu\text{m}$ total thickness of copper, nickel and gold) that mechanically reinforce the pads [109].

4.4.2 Gold wirebonding to SU-8

Wirebonding is presently the most popular method for connecting microelectronics die to ceramic packages for commercial applications [36]. Several different styles of wirebonders are used with different materials in bonding applications. Types of wirebonders include thermocompression, thermosonic, and ultrasonic bonders, each with a different operating principle. Thermocompression bonders typically heat a metal wire to very high temperatures and then apply pressure to form a bond.

Thermocompression bonders are less common because they require relatively high temperatures ($>300\text{ }^{\circ}\text{C}$) which can damage many non-ceramic packaging materials [36]. In contrast, thermosonic bonders operate in a lower temperature region, and apply ultrasonic energy to the bonder tip to provide the extra energy necessary for welding to occur between metal layers. These bonders are flexible with respect to the operating temperatures and input energies, and are the most common bonder type used in industry. Typically, thermosonic bonders use gold wire, and produce what is known as a ball-wedge bond. First, a ball bond is completed to the device to be electrically connected, followed by a wedge bond to the package. After the wedge bond is completed, a spark melts the end of the gold wire left in the bonder tip to create a new ball, allowing the next bond to begin.

For ultrasonic bonders, bonding can occur at room temperature, and a separate ball creating step is not necessary. In this case, a wedge-wedge bond is made, where a wire is placed parallel to the substrate, and ultrasonic energy is used to create a paddle shaped wedge bond. The wire is then directed towards another location where the second wedge is made before the wire is broken off, and the machine is ready to start a new bond.

Thermosonic ball-wedge bonders are the most common in industry because they can move the wire at any angle after ball bonding, which increases the speed of bonding. In contrast, wedge-wedge bonds must be aligned prior to bonding because changing wire direction after the first wedge bond places large stress on the wire [36]. Figure 4.11 shows the basic bonding steps of the Mech-EI NU-829 gold ball bonder used for this work.

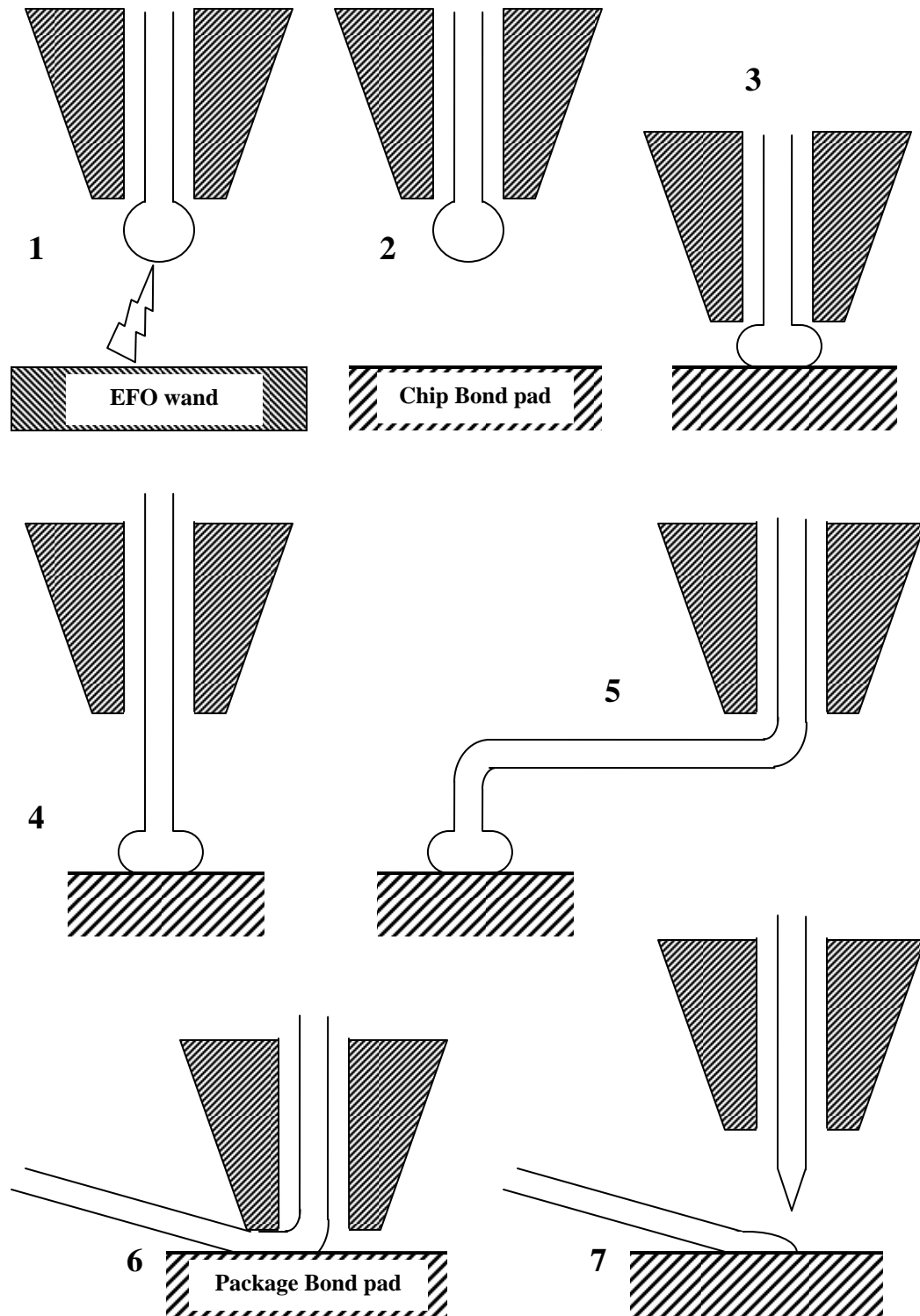


Figure 4.11: Bonding steps for ball-wedge bonders: (1) spark from electric flame-off (EFO) wand melts wire tip and forms ball, (2) ball positioned over bond pad, (3) bonder tip is pressed against the heated bond pad and ultrasonic energy is applied to deform the ball and weld the metal surfaces, (4) bond tip pulls away, leaving welded ball bond and forming loop, (5) bonder tip moves to package pad, (6) wedge bond is created, (7) bonder tip pulls away and breaks wire, leaving a completed bond.

The Mech-EI NU-829 wirebonder was the only one available when first attempts to bond to SU-8 were made (an ultrasonic bonder was purchased and commissioned later). The Mech-EI wirebonder uses a 25 μm diameter gold wire and has independent settings for power and time for both ball and wedge bonds, as well as temperature control over the heated chuck and the bonder tip. The chuck temperature is set with a dial and has feedback in the form of an LED display. Setting the chuck temperature requires some fine adjustments, as the actual temperature is never the same as the set temperature, due to calibration errors in the wirebonder. When temperature values are listed in this work, they are for the actual chuck temperature as read by the LED display. No correction is made for any temperature difference between the chuck and the top surface of the chip being bonded. The wirebonder tip temperature is set by a dial with settings from 0 to 10. No direct feedback is available on the bonder for the actual tip temperature, so this value is determined using a thermocouple and digital multi-meter (DMM) calibrated for reading temperature. Tip temperature measurements are taken 10 minutes after any setting changes because the tip has a relatively long time constant, resulting in some overshoot in temperature. Measurements of tip temperature are taken at the screw which holds the ceramic tip onto the bonder arm (the closest area that can be reliably measured with the thermocouple); the actual temperature at the gold wire is assumed to be the same as that measured at the screw. Figure 4.12 shows a close up view of an SU-8 chip for bonding and the location of the tip temperature measurements.

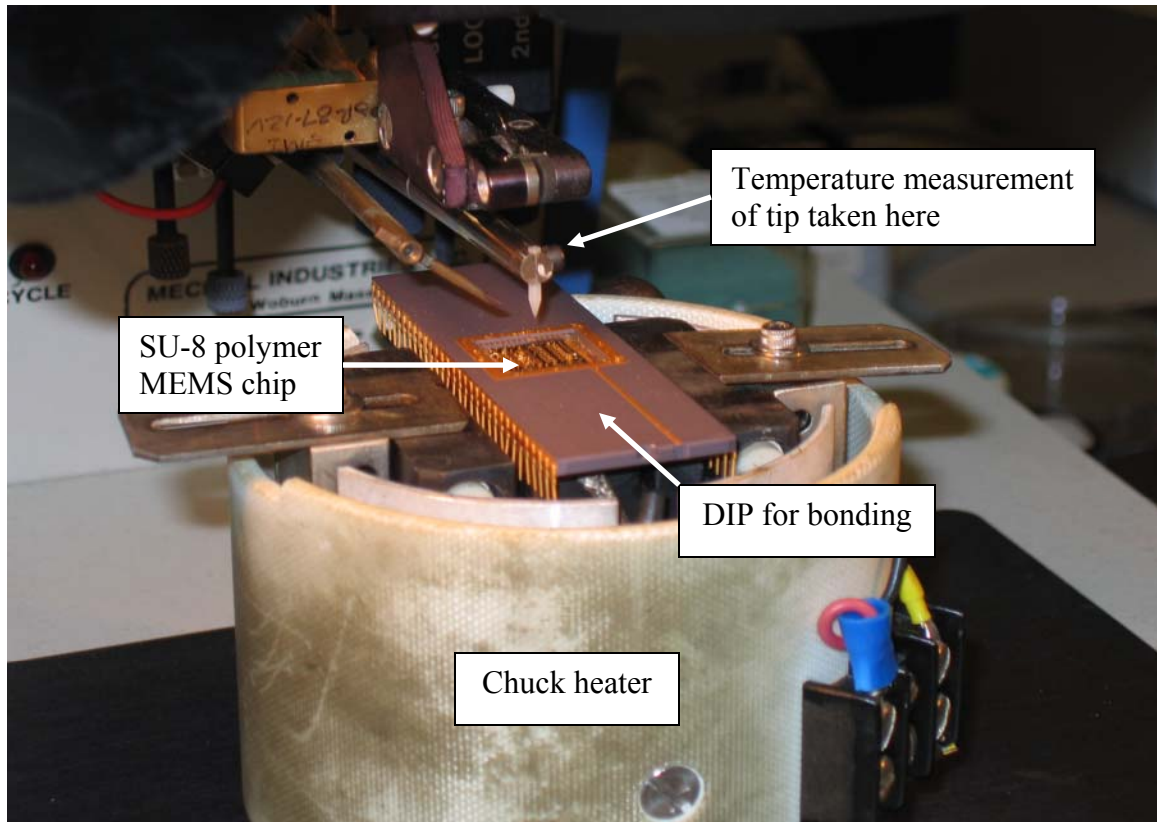


Figure 4.12: Close up of wirebonder and chip to be bonded.

Power and time settings for the wirebonder are listed as arbitrary units on two different dials, measuring from 0.0 to 10.0. The bonder manual does not mention the relationship between these values and the resulting power or times, therefore, the optimal values for bonding on different machines cannot be directly determined. In the experiments, bonding attempts were made to relatively thin layers of metal on SU-8 structures in order to remove any potential electroplating issues from failure modes as well as to examine specific failures related to SU-8. Wirebonding to thicker electroplated bond pads is a well known method to improve bonding yield and strength to soft substrates [36], but this method was not investigated for this work.

4.4.3 Metal thickness and its effect on Bond yield

Early experiments with bonding onto SU-8 were completed on very thin SU-8 layers with different metal compositions. This work was designed to minimize the effects of SU-8 stiffness on ball bond yield, and to determine the metal layers/thicknesses that result in the highest bond yields. The SU-8 formulation used was SU-8 2002 [30], which was spun on a scrap silicon wafer at maximum speed, resulting in a layer approximately 1 μm thick. This SU-8 was exposed, developed, and hardbaked for 30 minutes at 200 °C to increase the glass transition temperature and Young's modulus of the SU-8 [44]. No sacrificial layer was used in this early experiment, and only Cr/Au was used for coating the SU-8 structures. Chrome was selected because it had been used exclusively as an adhesion layer for gold until this point, and it has a very high Young's modulus, which has been identified as a useful feature for stiffening soft bond pads [36]. Gold was used as the top metal surface because it was used for all previous active devices in this work, and it also shows the greatest reliability with gold wirebonds [36]. Bonding tests were completed using a variety of bonding parameters until reasonable results were achieved; these settings were then used for all wirebond yield tests. Wirebond yield was measured as the percentage of successful ball bonds relative to the total number of bonds attempted. If the ball bond remained attached to the SU-8 until after the wedge bond was completed, the bond was considered a success for these early trials. As shown in Figure 4.13, the metal thickness has a large effect on the ball bond yields.

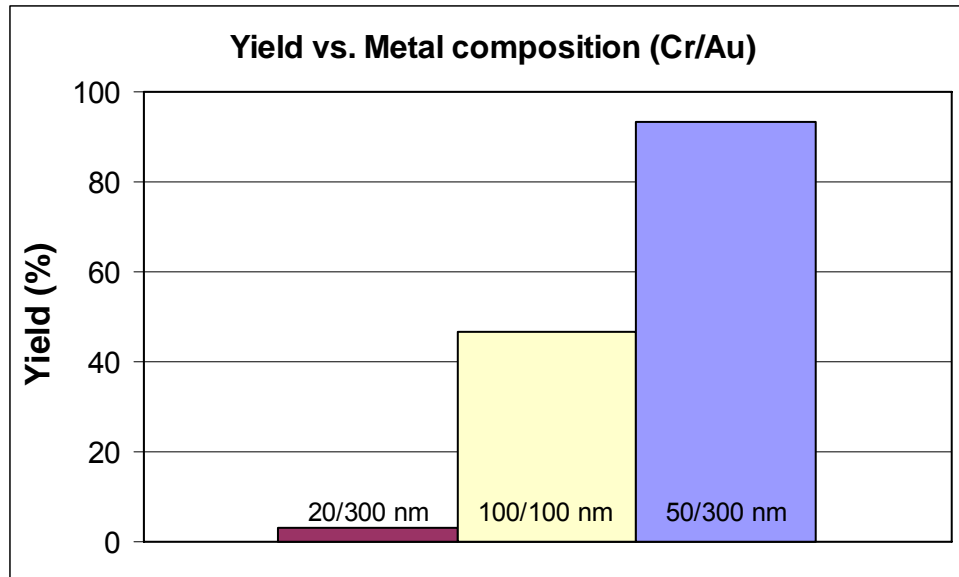


Figure 4.13: Ball bond yield on 1 μm thick SU-8 structures with different metal compositions [110]. Yield data is based on at least 30 attempted bonds.

Obviously, from Figure 4.13, the yield of ball bonds to SU-8 depends highly on both the chrome and gold thicknesses, with yield increasing with increasing metal thicknesses. Many trials that used thinner metal layers had negligible yields, and were, therefore, not included in this graph. The chrome thickness appeared to have the greatest effect on the ball bond yield, with a 30 nm increase resulting in a nearly 25 fold increase in yield. Increasing gold thicknesses also improved yield, but had a smaller effect than chrome thickness. Failure modes on these early trials were exclusively between the chrome layer and the SU-8 surface, which will be referred to as metal delamination for this thesis. This metal delamination is the primary source of bonding failure for all SU-8 structures that have been hardbaked. For all future wirebonding tests, the 50/300 nm Cr/Au metal thicknesses were used, due to their high yields in this early trial.

4.4.4 Bond yield with hardbaking parameters

Hardbaking SU-8 can result in a great deal of tensile stress [44], and keeping this polymer shrinkage to a minimum after processing is preferable. To determine the lowest acceptable hard bake temperature that still provides good yields onto SU-8, a series of thicker SU-8 structures were fabricated using the polymer MEMS process developed for this work, followed by a hardbake after development. According to the procedure outlined in section 4.2, compliant structures were fabricated to achieve as little out-of-plane curvature as possible. After the compliant structures were developed and dried, 15% polystyrene solution was poured over top of all the structures and left to dry for 24 hours. This step filled in all gaps under the compliant structures, encapsulating all SU-8 structures in a thick polystyrene film. This polystyrene casting held all SU-8 structures in place during a hardbaking step, but after baking at temperatures up to 200 °C, could be removed very easily in toluene after baking at temperatures up to 200 °C. The SU-8 structures needed to be relatively flat prior to casting or else any curvature or warping would become permanent. The polystyrene could reflow slightly after exceeding its glass transition temperature, but its viscosity and high surface tension prevented any out-of-plane motion by SU-8 structures. Encapsulating SU-8 within another polymer with similar thermal conductivity also keeps temperatures within the SU-8 structures more uniform than if they were baked on a hot-plate in open air. In fact, as shown in Figure 4.14, if SU-8 compliant structures were baked on a hot plate without constraints, the gradient in thermal expansion coefficients through the SU-8 film would cause out-of-plane motion and subsequent plastic deformation.

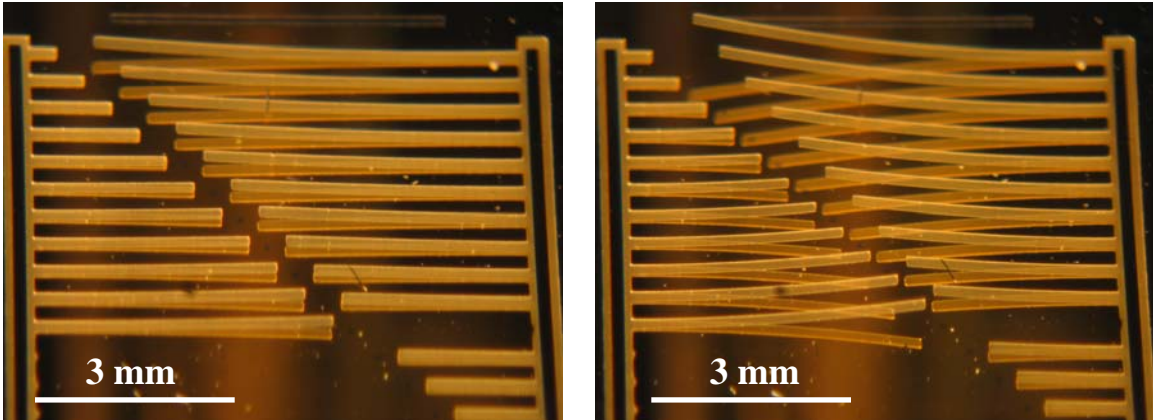


Figure 4.14: SU-8 cantilevers without gold before (left) and after hardbaking without restraints.

For all compliant SU-8 structures, hardbaking was performed on the ramping hot plates starting at 50 °C and ramping at 300 °C/hr to the desired hardbake temperature. The hotplate was held at the hardbake temperature for 30 minutes before being cooled at 300 °C/hr to 50 °C. At this point, the hotplate was turned off and the wafer was naturally cooled to ambient temperatures. The polystyrene cast was removed in toluene and IPA and the wafer was ready for metal deposition after drying.

Three different thicknesses of SU-8 were hardbaked at different temperatures, and coated with 50/300 nm Cr/Au with the same deposition parameters. Wirebonding parameters were the same for the same thicknesses, and yield was measured using the same criteria as before. The results are summarized in Figure 4.15.

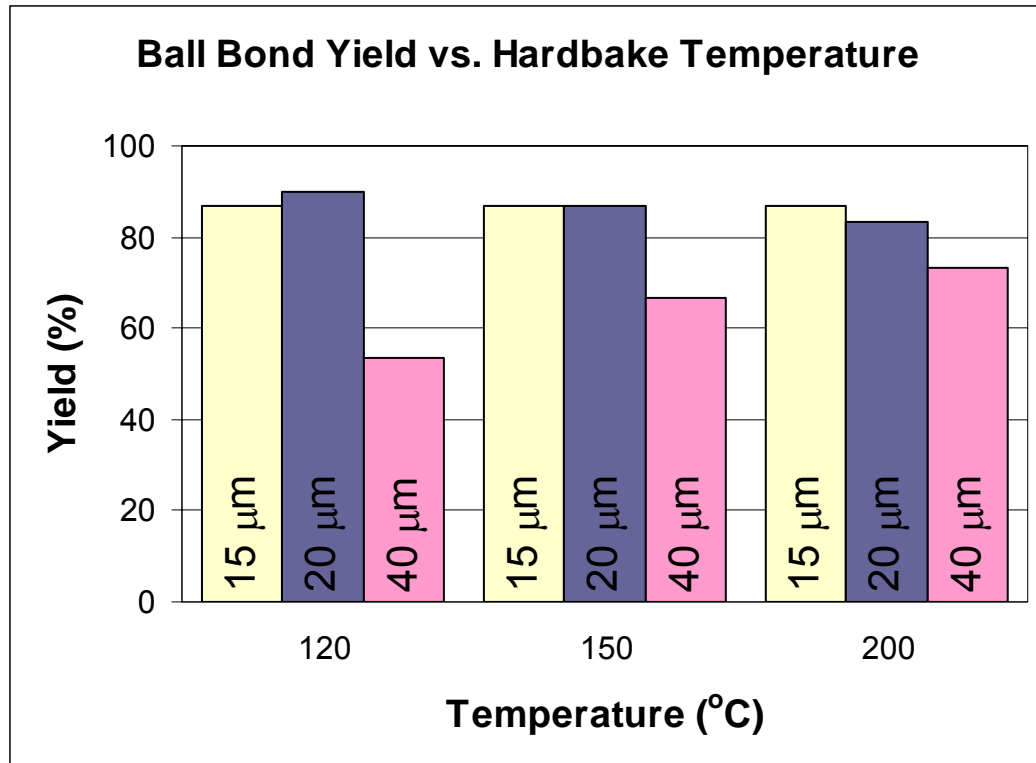


Figure 4.15: Wirebond yield versus hardbake temperature on different SU-8 thicknesses. Chuck temperature was set to 114 °C, which was the highest setting that avoided plastic deformation of SU-8 structures. Yield data is based on 30 attempted bonds.

The yield data reveal that the wirebond yield to thin SU-8 structures (< 20 μm) is not affected significantly by increasing hardbake temperature beyond 120 °C, but that thicker SU-8 structures demonstrate improved yield with increased hardbaking. These results demonstrate that the improved stiffness and temperature tolerance created by hardbaking the SU-8 only becomes significant when the thickness of the SU-8 bondpads creates significant softening during the bonding processes. In all these trials, the primary failure mode remained metal delamination from the SU-8 surface, with only a few obvious bond pad collapses, demonstrating mechanical deformation due to SU-8 weakness or plastic deformation. The continued problem of metal delamination during bonding meant that improving the adhesion between chrome and SU-8 was critical to achieving good bond yields.

4.4.5 Measuring bond strength and improving it using surface activation

The measurements of bond yields were useful in early tests to generally understand the likely effects of different metal and SU-8 thicknesses and hardbaking temperatures. Unfortunately, the yield values are not a very good quantitative measure of the overall bond strength. In industry, wirebonds are carefully tested by several different procedures to determine their resilience and longevity. One of the common tests used in industry is the bond pull test [36]. In this particular test, a hook is placed under the wire loop connecting two bonds, and the loop is pulled until one bond fails. The force required to break the loop must meet minimum requirements to be acceptable for industry, and it depends on a number of factors, including metal composition, bonder settings, and substrate material. In modern industry, this bond pull test is being replaced by different non-destructive tests, or bond shear tests, [36] which are designed to provide more accurate data on ball bond strength. Unfortunately, the test equipment required for shear tests, or non-destructive tests, cannot be found in small research cleanrooms like that at SFU, and little equipment was on hand to produce a substitute. Fabricating a ball pull test setup is relatively easy however, and this was accomplished using equipment in the lab.

The ball pull test requires a hook, a force measurement system, and a means of accurately positioning the hook and pulling it in a vertical direction. Figure 4.16 shows a diagram of this basic setup.

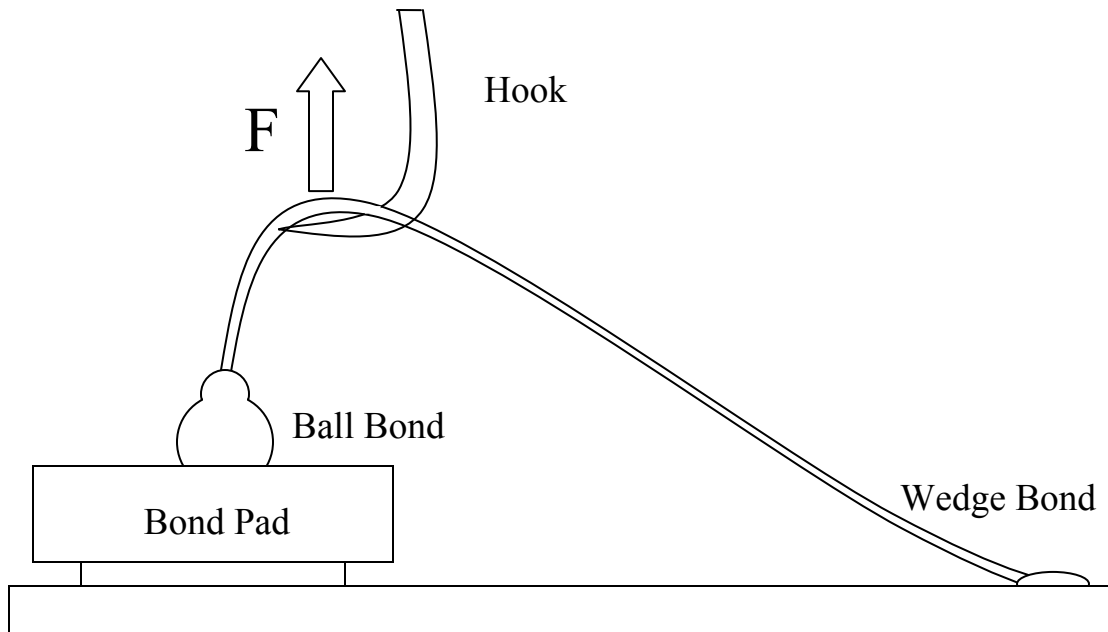


Figure 4.16: Schematic of ball bond and bond pull setup. Dimensions are not to scale.

For the bond pull test, the measured force of the hook is distributed between the two bonds, and the amount of force applied to each bond is dependent on geometry. The weakest bond of most ball-wedge bonds is typically the wedge bond, due to the greater deformation of the wire at that point. For this reason, most bond pull tests try to carefully control the position of the hook such that the distribution of forces in each bond is relatively well known and is not distributed too unequally in order to ensure that the weaker bond will fail first [36]. In the case of bonding to SU-8, the weakest bond is consistently the ball bond, so all bond pull tests applied most of the force to this bond. Because the wirebonder cannot be set with an automatic trajectory, the loop shape depends greatly on the individual operator, resulting in geometry that may be difficult to repeat. To minimize this problem, a relatively long wire is used with a maximum loop height set as close to the ball bond as possible. This geometry should result in most of the force being applied to the ball bond when the hook is placed at the top of the loop,

and minimize the effect of minor differences in loop length. For this reason, the pull force is assumed to be equal to the force applied to the ball bond.

The equipment used to conduct bond pull tests was fabricated out of three manual linear translation stages that were arranged to provide accurate displacement in three axes. A long metal beam was attached to the three stages that allowed the force probe to be placed in close proximity to the tested wires. The force probe consisted of a spring gage which measured the maximum force applied prior to bond failure. Double sided tape was required to hold the force probe in place on the metal beam, and wires were used to ensure the probe did not fall if the adhesive force of the tape diminished. Pull forces on the bonds were measured in grams-force (gf) (a single gram-force is equal to 9.8 mN). The gram-force unit is the one used most often in describing bond strength [36], so it is used in this work to be consistent with the literature. Pictures of the full linear stages and a close-up of the force probe are shown in Figure 4.17 and Figure 4.18.

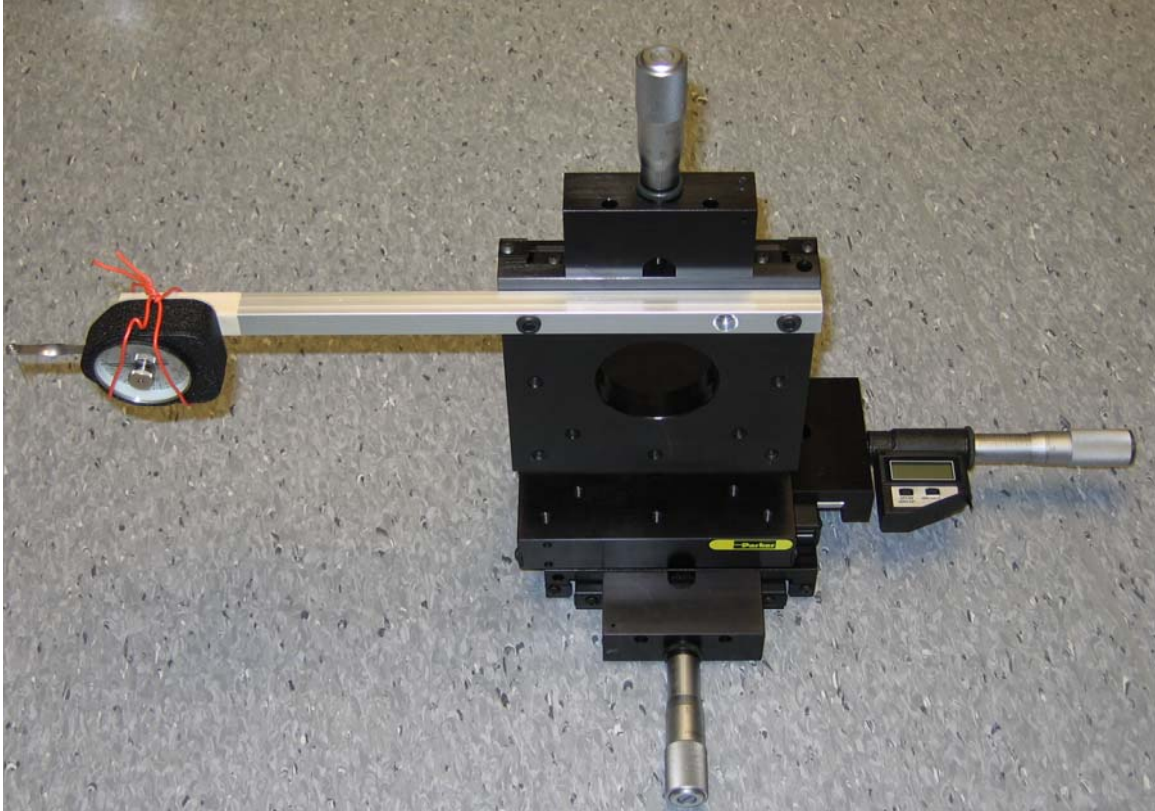


Figure 4.17: Linear stages and force probe used for bond pull tests.

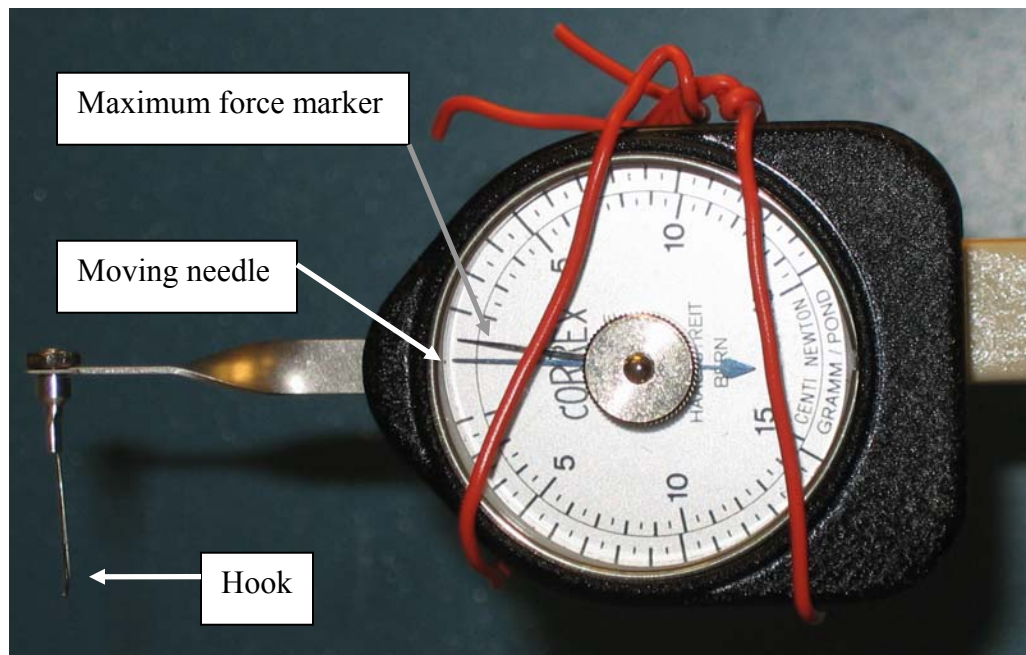


Figure 4.18: Close-up view of the force probe used to measure bond failure forces. The spring loaded probe moves the needle which remains in the position of the highest measured force after the bond breaks.

The hook for the probe was fabricated using a 300 μm diameter stainless steel acupuncture needle that was bent at the tip. The needle was sufficiently small and stiff enough to pull all bonds without difficulty. When pulling the bonds, the whole setup was placed on the wirebonder chuck at room temperature. The wirebonder was the only piece of equipment with sufficient magnification at an oblique angle to accurately place the hook under the wire loops. Once the hook was placed under the wire loop as close to the ball bond as possible, the Z-stage was pulled up slowly until the bond failed. For each bond, the failure mode and maximum measured force was noted. To determine the average failure force of bonds to a silicon surface with this setup, pull tests were performed on wirebonds made with different tip temperatures. An average failure force of 6 gf was found with standard deviations smaller than 0.5 gf as shown in Figure 4.19.

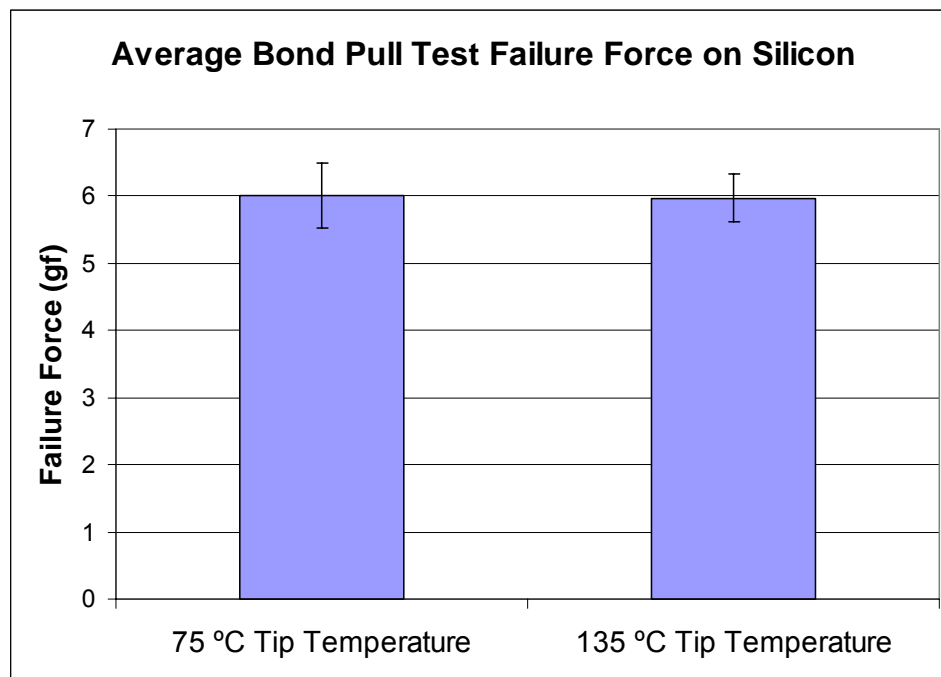


Figure 4.19: Average bond pull failure forces for gold wirebonds onto a silicon substrate. Different bonder tip temperatures were used to determine if the wire was weakened at higher temperatures. All bonds failed by wire fracture directly above the ball bond.

From the data in Figure 4.19, the bond pull setup appears to provide reasonable repeatability, given that the accuracy of the analogue force probe is approximately ± 0.3 gf. The ultimate strength of the gold wire above the ball bond is approximately 6 gf, which represents the upper limit on expected bond strength using this test.

4.4.6 Improving bond strength to SU-8 using surface activation

The high percentage of failures by delamination of metal from SU-8 during yield trials revealed that poor metal adhesion to the SU-8 surface was the most critical parameter to improve bond yields. Fortunately, a literature search revealed that improving the adhesion strength of chrome to SU-8 had already been investigated by Ge and Kivilahti [35]. In their work, multiple surface treatments of SU-8 were examined to determine the best way to improve adhesion between SU-8 and copper, and SU-8 and chrome. The results in [35] indicated that a reactive ion etch of 75% O₂ and 25% CF₄ was highly effective at improving the adhesion strength between SU-8 and chrome. The optimal activation parameters for gas flow rates, power, pressure and time were found by Ge and Kivilahti to be 15 sccm O₂, 5 sccm CF₄, 80W, 4 Pa (~30 mTorr) and 20 minutes respectively [35]. Excessive RIE would actually cause a reduction in adhesive force due to the creation of a weak boundary layer at the SU-8 surface [35]. The maximum adhesive strength between SU-8 and chrome was found by Ge and Kivilahti to be approximately 6 N/mm² after which SU-8 itself fractured prior to metal delamination. No adhesive strength between unactivated SU-8 and chrome was reported, but this interface was said to fail a tape test [35]. This behaviour was observed in these wirebonding experiments as well. To test the effect of surface activation on ball bond

strength, test structures were created in the multi-user polymer MEMS process, and they were hardbaked at 200 °C prior to being activated by a similar reactive ion etching step.

Because the average yields of bonds were so poor, the mechanical strength of ball bonds to the SU-8 surface had not been measured prior to this experiment. After surface activations on thin (< 20 μm) SU-8 structures, bonding yields routinely exceeded 90%, so bond pull tests were used to quantify the effect of surface activation. To determine the effect of surface activation on SU-8 structures that had been hardbaked, a series of die were taken from the same wafer and activated for different times using the following etching parameters: 15 sccm O₂, 5 sccm CF₄, 80 W, and 68 mtorr. The exact pressure used by Ge and Kivilahti in the previous activation tests could not be reached by the lab's RIE equipment for the flow rates used. The actual pressure setting was 60 mtorr, but 68 was the lowest actual pressure at a 20 sccm total flow rate. Figure 4.20 lists the measured failure forces of bonds onto 16 μm thick SU-8 structures bonded with different chuck temperatures. All bonder settings, with the exception of chuck temperature, were kept constant in these trials and the minimum sample size was 15 bonds.

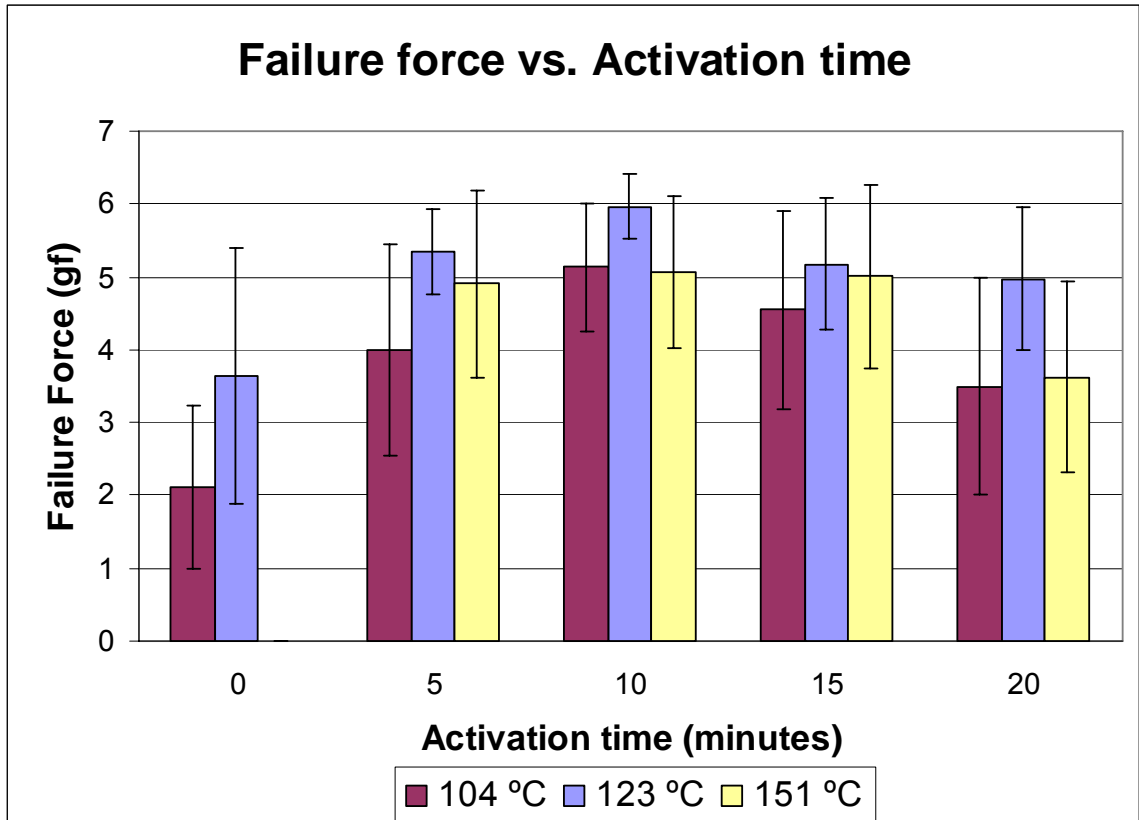


Figure 4.20: Average bond strength and one standard deviation of failure force on SU-8 for different activation times and chuck temperatures [110].

These results reveal that the activation step creates significant difference in bond strength onto SU-8. In addition, an optimum chuck temperature during bonding results in higher strengths. With respect to the temperature effect, higher temperatures likely allow the gold ball to deform more and create a greater area of contact between the ball and the bond pad. At very high temperatures, however, the SU-8 softens significantly [111], and visco-elastic effects reduce the energy available to deform the gold ball. This deformation likely reduces the bonded area and results in the lowered failure forces. The detailed results on the three trials shown in Figure 4.20 are shown in Figure 4.21, Figure 4.22, and Figure 4.23.

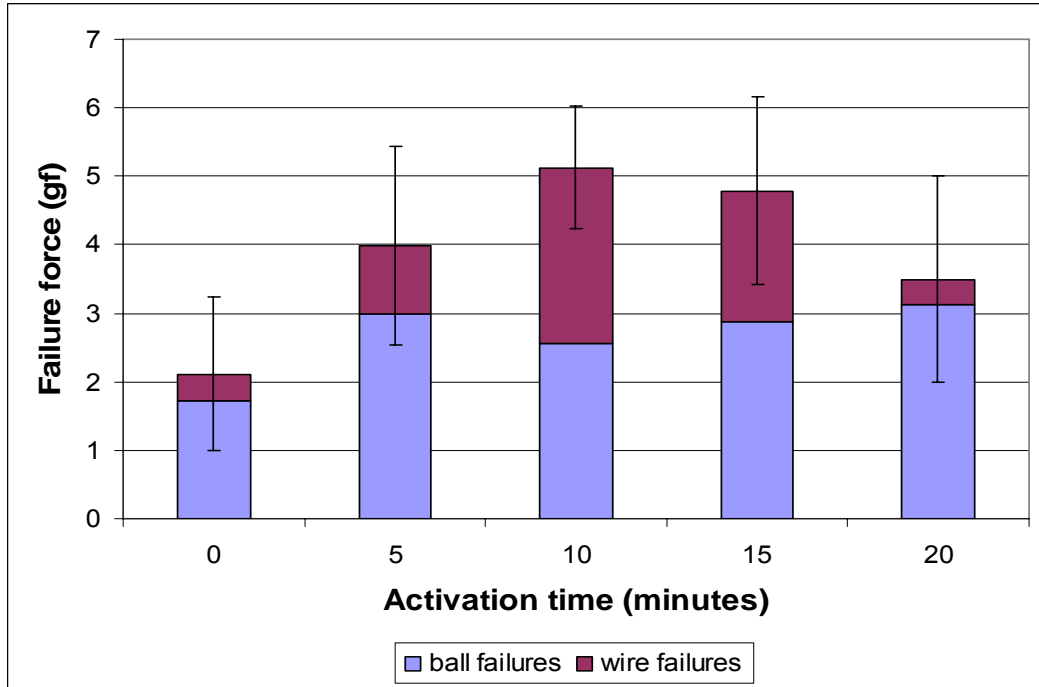


Figure 4.21: Failure force and modes of bonds made at 104 °C for different activation times. The distribution of wire failures is represented by area percentage of the bars.

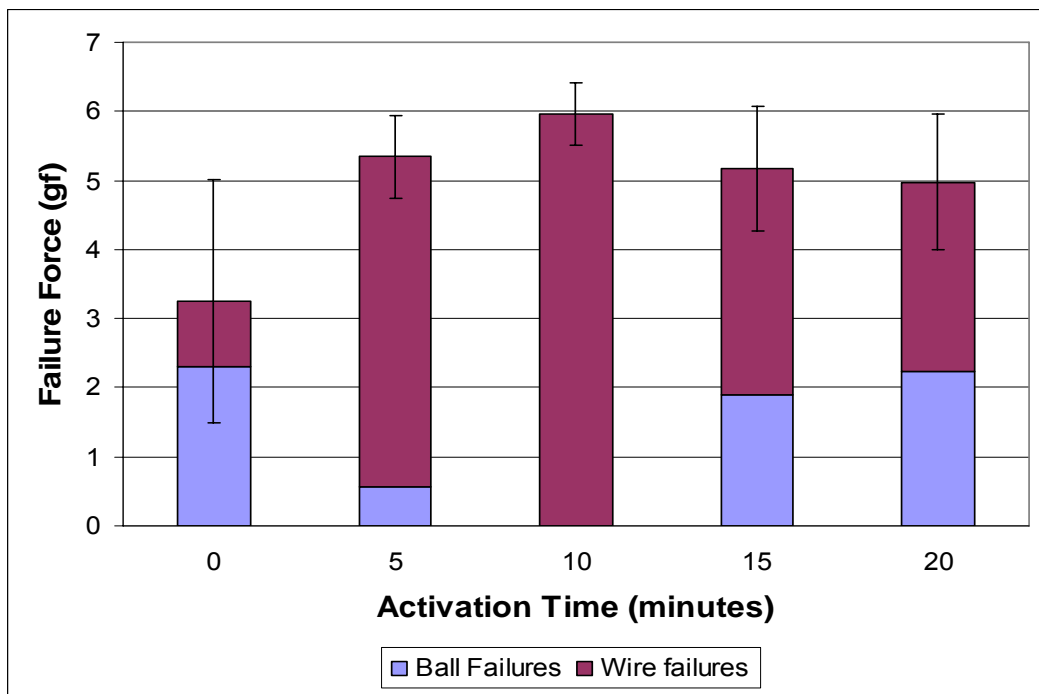


Figure 4.22: Failure force and modes of bonds made at 123 °C for different activation times.

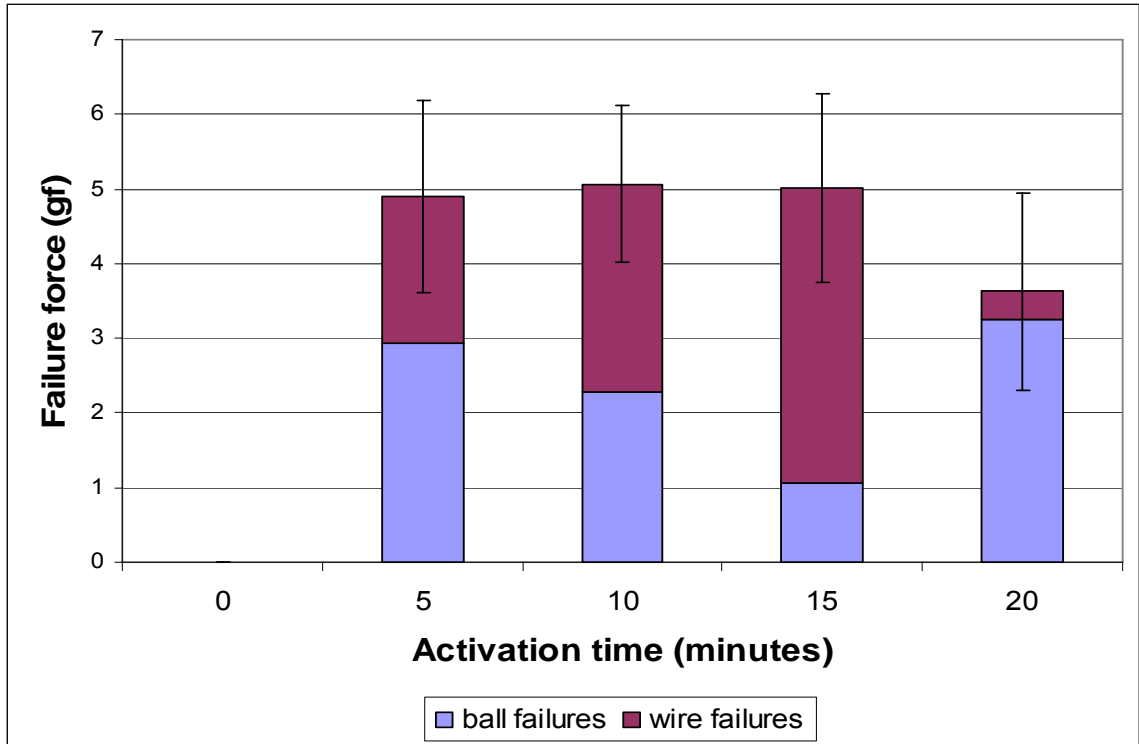


Figure 4.23: Failure force and modes of bonds made at 151 °C for different activation times.

The maximum adhesive strength occurred in the bonding trials at 123 °C for the SU-8 structures given a 10 minute activation. In this particular instance, a 100% wire failure was achieved, showing that the bonds are adequate, and the average force was identical to that found for bonds to silicon. The average failure force decreases as the percentage of bond failures increases, which is expected, but the mechanism of bond failures changes as the activation time increases.

For short activation times, the bond failures appear exactly as those for unactivated SU-8, with Cr/Au peeling off the SU-8 surface. As the activation time increases, however, more bond failures occur between the ball and the gold surface. Photographs of both types of failure modes are shown in Figure 4.24.

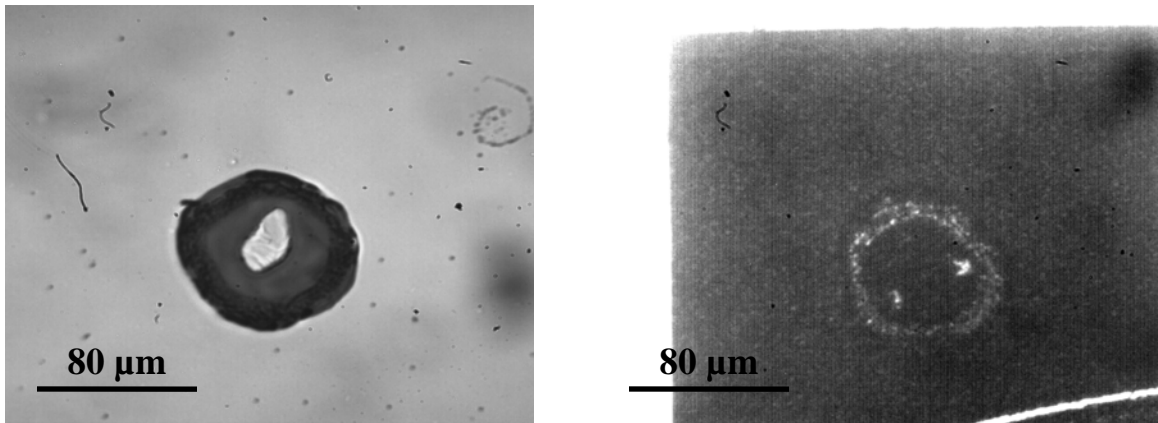


Figure 4.24: Optical micrographs of bond failures with low activation times (left), and high activation times (right). Observations of the bond failures at high activation times through an optical microscope are difficult due to extremely rough SU-8 surfaces.

The cause of this change in failure mode is the rapid increase in roughness observed in the SU-8 surface as the activation progresses. This effect was not seen in earlier work [35], and it was unknown early in the experiments if this roughening effect on our SU-8 was related to the relatively small areas of SU-8 being etched, or the higher pressure in our RIE. SEM and optical images of gold bonds to roughened and non-roughened SU-8 are shown in Figure 4.25 to demonstrate this effect.

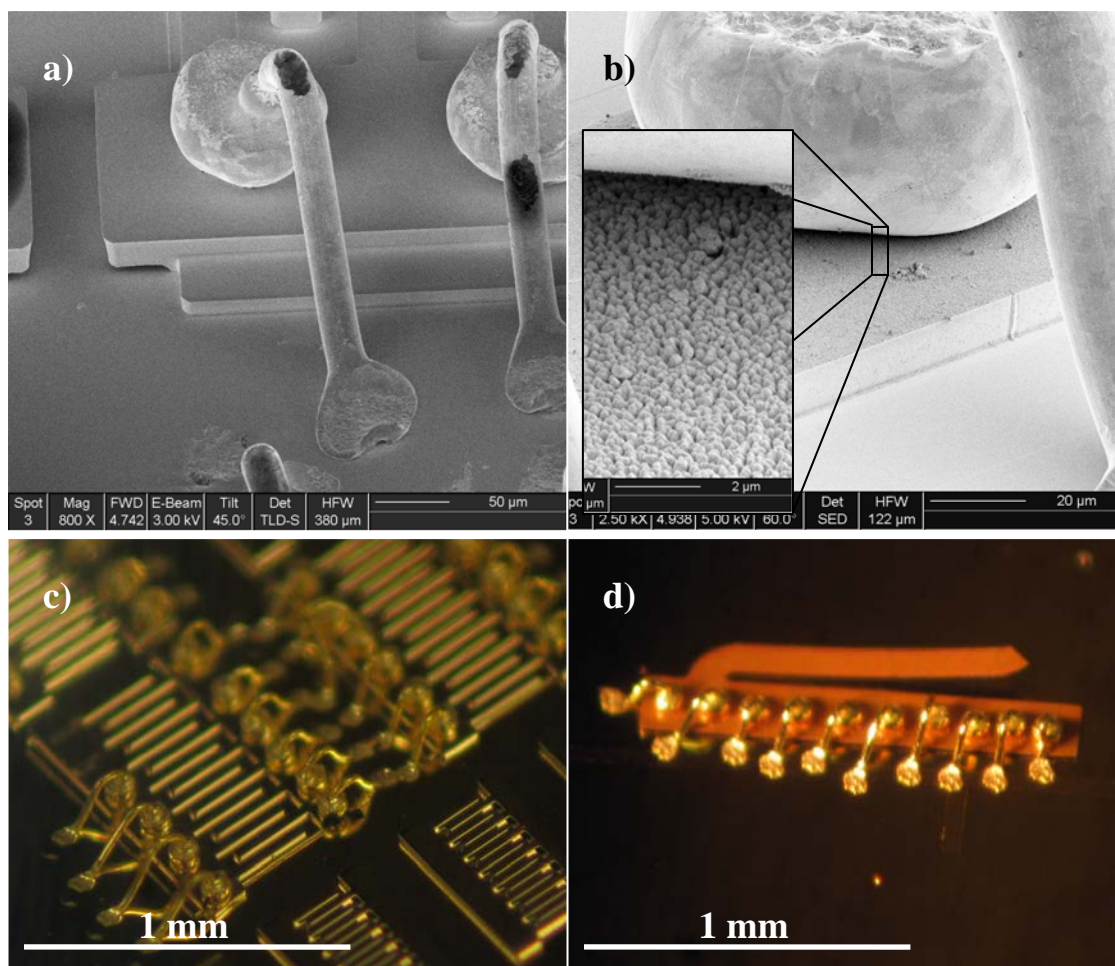


Figure 4.25: SEM images (a and b) and photographs (c and d) of bonds to SU-8 with smooth (a and c) and rough (b and d) surfaces.

The significant roughening of the SU-8 surface results in a relatively porous metal layer. For activations in excess of 20 minutes, electrical conductivity on this rough SU-8 can be lowered to as little as 1/2 to 1/3 of its normal values for smooth surfaces. Also, the maximum bonding yield on SU-8 is maximized under these conditions after 10 minutes. While loading effects may be partially responsible for this accelerated activation and early creation of a weak boundary layer [35], the porosity of the metal layer on roughened SU-8 is more likely responsible for the failure of bonds to the gold surface. Not until after the majority of bonding experiments were completed that was an explanation found as to the cause of this surface roughening during SU-8 activation.

A review of the literature on polymer surface activation did not explain why SU-8 would show such significant roughness, but a paper presented at TRANSDUCERS 2007 provided an explanation as to the possible cause [112]. This particular paper describes how nano-scale polymer pillars can be created by a low pressure RIE in the presence of aluminum, which is sputtered by the bombardment of gas ions. This aluminum redeposits on the polymer film, producing tiny masked areas which result in polymer pillars with increased etching times. This general effect is described as RIE grass or micromasking [113]. Gold has been identified as the material which produces the greatest amount of micro-masking [113], and it likely accounted for all the increased roughness observed in our surface activation experiments. To test this hypothesis, several wafers were fabricated with 16 μm thick SU-8 pillars on bare silicon wafers or gold coated wafers. No sacrificial layers were used in either case, in order to avoid additional variables. Ten minutes of the activation recipe were used for both SU-8 on silicon and SU-8 on gold followed by a 50/300 nm Cr/Au deposition. Visual results were dramatic, the SU-8 pillars on gold showed significantly rougher surfaces than those on silicon, which appeared smooth, as seen in Figure 4.26.

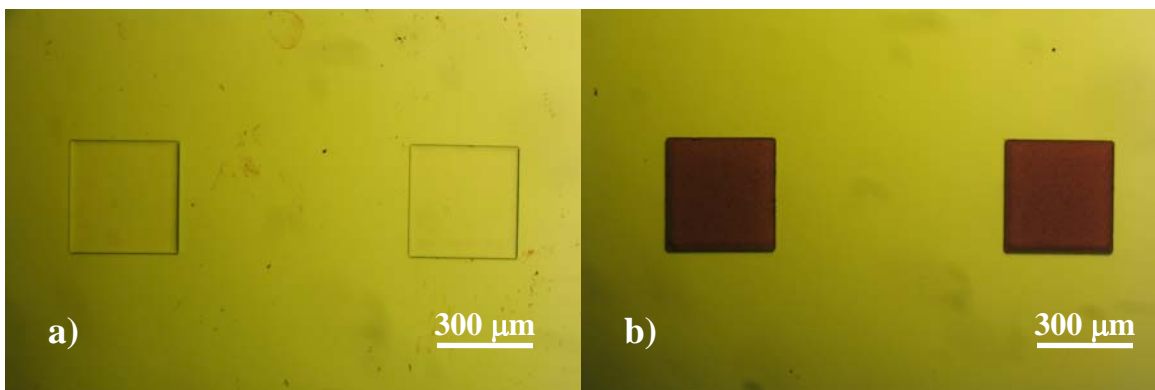


Figure 4.26: Photographs of SU-8 posts coated in Cr/Au that had been activated for 10 minutes on top of bare silicon (a), and a gold coated substrate (b), prior to metal deposition.

To test the effect of this difference on wirebonding strength with the previously optimized activation time and chuck temperature from Figure 4.20, a series of wirebonds onto SU-8 activated on silicon were completed at different bonding parameters and tested. The results are summarized in Figure 4.27.

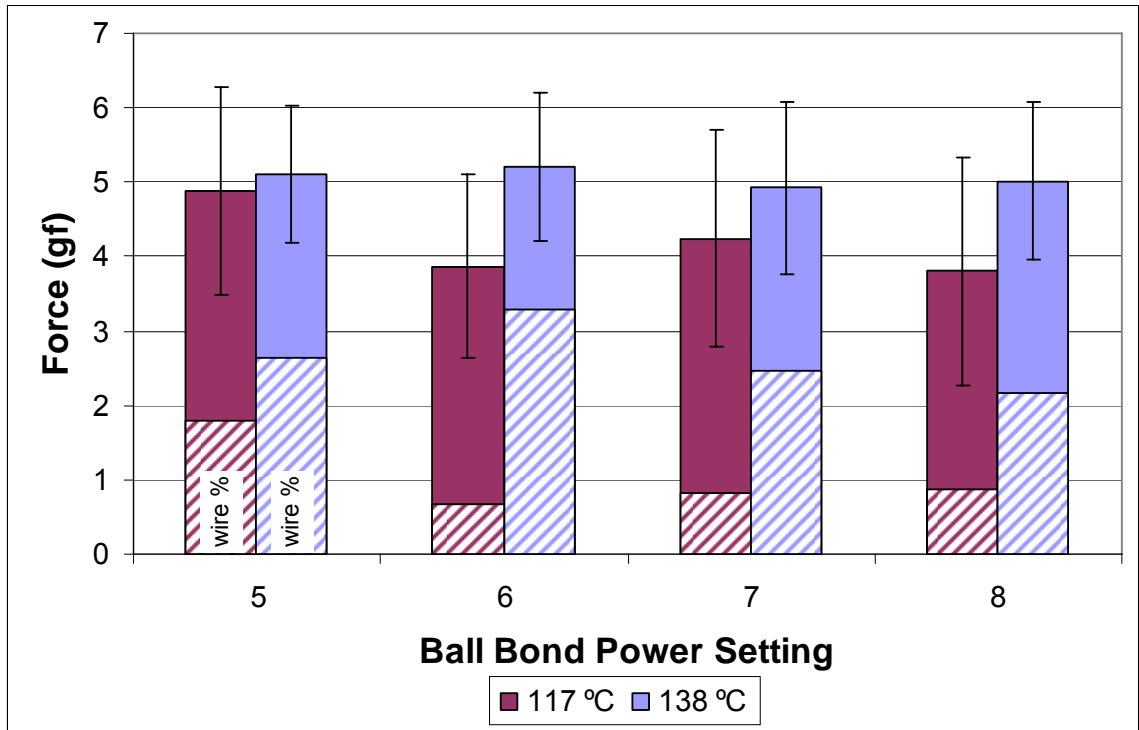


Figure 4.27: Average failure force and one standard deviation for wirebonds on hardbaked SU-8 posts on a silicon wafer activated for 10 minutes with standard activation recipe. Shaded section represents the relative percentage of wire failures. Between 25 and 30 bonds are tested for each trial.

A very large number of wire bonder parameters were tested in an attempt to achieve good bonding, but the maximum strength in this instance was never as great as the maximum that was achieved during earlier bonding test on roughened SU-8. From this experiment, it is likely that minor SU-8 roughening from micromasking improves metal adhesion significantly due to mechanical interlocking effects; however, at longer etch times, the roughening is too great to allow proper welding between the gold ball and the gold surfaces. The ball failures on activated, smooth SU-8 were examined optically

after two pull test trials to determine the area that delaminated from the SU-8. These failures were compared with the force required to break the bond, which provides an estimate of the surface adhesion force achieved during this experiment. The two trials with the extreme ends of the bonder setting were used to determine whether bonder settings have any effect on this adhesion. These results are summarised in Figure 4.28.

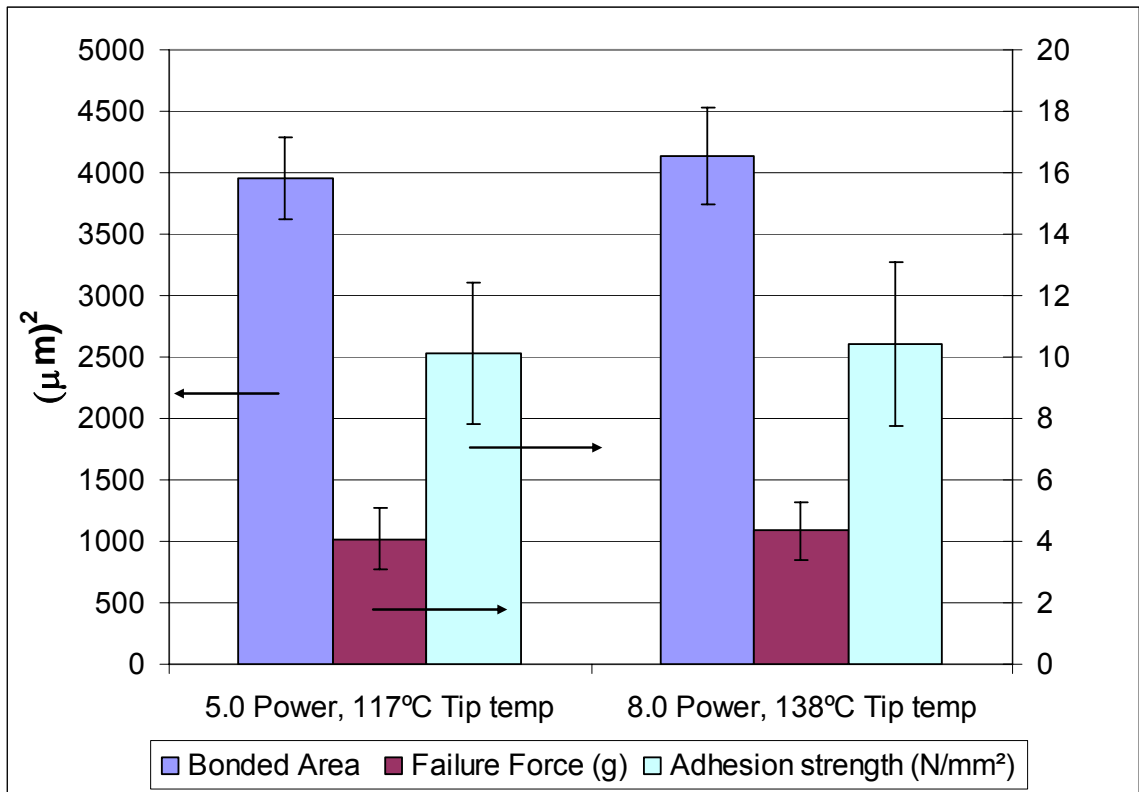


Figure 4.28: Average bonded area, failure force, and calculated SU-8/metal adhesion strength based on wirebond pull tests (arrows indicate the relevant y-axis). The number of samples was 19 and 16 for the 5.0 and 8.0 power setting trials respectively.

Because this trials only consider ball failures, the average failure force in this data is lower than that for the same trials listed in Figure 4.27. From this data, clearly, the bonded area in these two trials did not change significantly, although significant variations in failure forces for each bond occurred. The failure force for each individual bond was matched to the area of delaminated metal in order to estimate the adhesion

force for each bond using correlation. The variability in these values was quite high, but was still found, on average, to be approximately 10 N/mm^2 . This value is over 50% greater than the maximum reported by Ge and Kivilahti [35], but it is attributed to the increased strength of SU-8 due to hardbaking. Ge and Kivilahti had identified the failure mechanism of SU-8/chrome bonds as mechanical failure within the SU-8 after optimal activation, but the increased yield strength of SU-8 with hardbaking [44] makes this failure mode much more unlikely. This estimate of adhesion force is only approximate, but, given the relatively constant size of bonded area onto SU-8, it seems likely that the average adhesion force in these trials is greater than 10 N/mm^2 when the wire failures are taken into account. This finding is important, as it indicates that with proper optimization, SU-8 can be reliably wire bonded using commercial packaging technologies.

Future work on this topic should be pursued with automatic wirebonders and calibrated test equipment to gather more detailed data for a larger variety of processing conditions, but this work demonstrates for the first time that relatively minor processing steps can dramatically improve the packaging yield of SU-8 MEMS structures. Increasing the glass transition temperature through higher baking temperatures, and improving metal adhesion through surface activations can both be accomplished relatively simply, which suggests that future SU-8 processing should include both these techniques as standard processing procedures.

5 POLYMER MEMS STRUCTURES, ACTUATORS, AND APPLICATIONS

5.1 Introduction

Throughout the development of this process, structures and devices commonly found in other MEMS processes were fabricated to determine their performance as well as gain insight into the applicability of SU-8 as an effective structural layer for different applications. Using different test structures, the process was varied with different SU-8 thicknesses and aspect ratios in order to investigate the flexibility of the basic processing steps to adapt to new applications. At the extreme range of the process capabilities, SU-8 cantilevers as long as 3 cm, and untethered MEMS robots that are less than 300 μm across, were fabricated using variations on the basic process. Device thicknesses have ranged from 3 μm to almost 200 μm with few alterations to the basic steps. Optimization of each process variation was not always completed, but due to the general understanding of processing issues with SU-8 as a structural layer, the extensive practical knowledge gained during the work on this thesis allowed acceptable results in fabrication during most first attempts.

This chapter outlines a selection of the individual devices and structures fabricated using the basic process technology and its variations. This chapter also provides metrics for performance of several individual devices. The wide variety of devices fabricated using this process is proof of its applicability as a rapid prototyping system.

5.2 Experimental setup

The majority of experiments on fabricated devices were completed in the mini-cleanroom built in our lab [32]. A micro-probe station was available, with a camera, power supplies, and high voltage amplifiers that could power devices and record information regarding their behaviour. Force measurements were taken of different structures were performed using a modified version of the micro-force probe described by Lai et al. [114], but with a similar experimental setup. For early frequency and time response measurements of SU-8 thermal actuators, the optical measurement system described by Fettig [19] and Hickey [11] at the Dalhousie MEMS lab was used with the assistance of Dr. Ted Hubbard. Displacement and dimension measurements of SU-8 structures were made using National Instruments Vision Builder for Automated Inspection software [39] from images taken with a Moticam 1300 camera .

5.3 Mechanical structures for process optimization

Purely mechanical structures, such as cantilevers, spring systems, and membranes, were the first fabricated structures using SU-8, with their primary use to test the mechanical behaviour of SU-8 and evaluate process reliability. The most important parameter to optimize for SU-8 was the curvature of compliant structures, which used the information covered in the previous section. The optimization of one property in SU-8 is often not optimal for other parameters. For example, the mechanical resilience of SU-8 increases dramatically with increased baking temperatures, but this will result in swollen features and poorer minimum resolution. For the majority of processing, layers and thicknesses were kept constant, so few changes were made in the processing steps once acceptable results were obtained. As more researchers used the process and wished to

create different thicknesses, a system was developed for rapid process optimization. To do so, a new methodology was required that would rapidly measure material properties, feature sizes, curvature, and residual stresses in the processes. Because manually testing individual structures is too time consuming, this system needed to be as automatic as possible. A complete test system, comprising of a test die and an external vibration source, was developed near the end of this thesis for use with future process iterations. The information on the basic system was presented at Texpo 2007 as a poster [115], and is covered briefly here.

The rapid optimization of future process modifications requires feedback on several properties, including structure curvature, minimum feature size, Young's modulus, and tensile stress. A review of the literature on MEMS material property testing revealed many potential techniques, listed below in Table 5.1. The highlighted techniques are adopted in this work for measurements of polymer MEMS properties.

Table 5.1: MEMS material property testing techniques adapted from [116].

Capabilities of microscale testing techniques						Test structures compatible with test techniques				
Test	E	σ_y	σ_f	σ_r	$\nabla\sigma_r$	Thin	Thick	Free	Constrained	Integrated
Tension	√	√	√			√	√	√		No
Plate bend			√				√	√		No
Microbeam bend	√	√	√			√	√	√		No
Bulge test	√			√		√		√		No
M-test	√			√		√		√		Yes
Wafer curvature				√		√	√		√	No
Resonance	√			√		√	√	√		Yes
Strain gages				√	√	√	√	√		Yes

The most important properties to measure in the polymer MEMS process are Young's modulus, residual stress, curvature/stress gradient, and minimum feature size as these properties have the greatest effect on the mechanical properties of fabricated devices. Also, any test system must be integrated, which is defined as a system that allows material properties to be determined without removing parts from the wafer, or requiring direct manipulation of devices. Based on the information summarized in Table 5.1, a combination of resonance tests and strain gauges were designed that could be integrated on a test die. Figure 5.1 shows an L-Edit layout of this die.

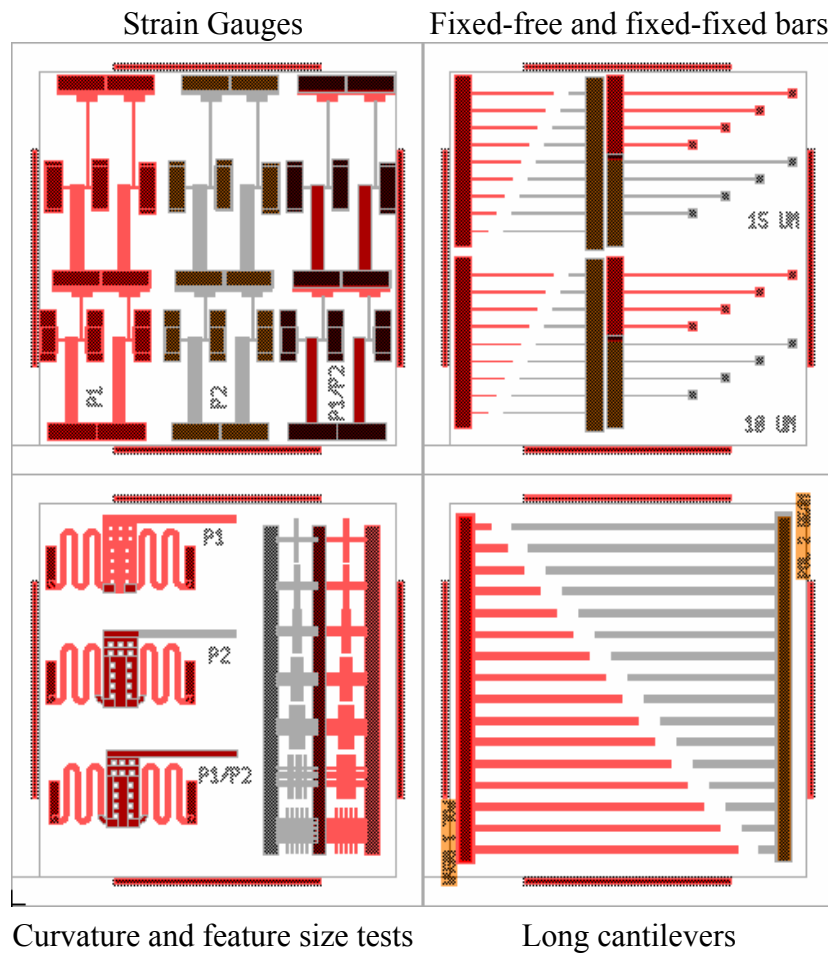


Figure 5.1: Material property and process control test die layout. The die is 1x1 cm².

From the upper left in Figure 5.1 moving clockwise are quarter die with strain gauges, fixed-free and fixed-fixed bars, long cantilevers, and out-of-plane curvature measurement structures and feature size tests. Strain gauges have been described by [117] and a version of these structures is used to determine the residual strain in the material. Unfortunately, determining values for residual stress using these structures is only possible when other material properties like Young's modulus, and Poisson's ratio, are known. Young's modulus can be found from resonating cantilevers, and residual stress may be found from the resonant frequency of fixed-fixed structures if Young's modulus is known [116]. The minimum fabricated structures and gaps can be directly observed using optical methods and calibrated images. Finally, curvature can be directly observed by propping structures out of plane and observing them edge on [82]. The pop-up structure designed by Tsang *et al.* [37], allows for measurement without removing anything from the substrate. Figure 5.2 shows images of several fabricated test tie structures.

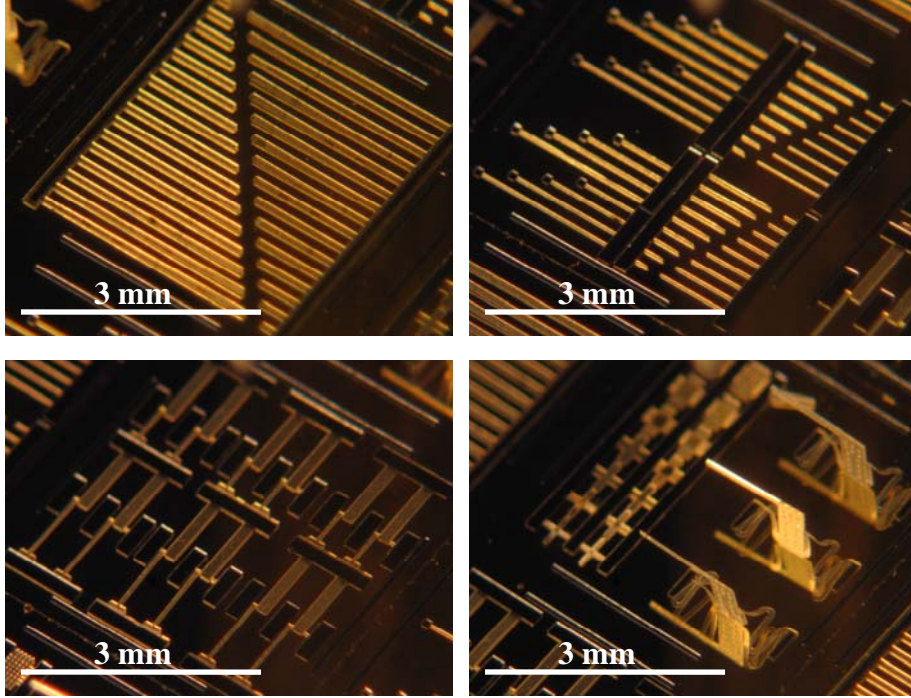


Figure 5.2: Fabricated structures for the polymer MEMS test die.

The equations that allow material properties to be extracted are taken from [116], and are listed below in equations (14)-(17) within Table 5.2.

Table 5.2 Governing equations used to find several mechanical properties of polymers based on the test structures shown in Figure 5.1. These equations assume rectangular cross-sections.

Resonant frequency of a cantilever assuming no damping. While vibrating in-plane, h is beam width, and ρ is density. Beam thickness does not affect in-plane resonant frequency.	$f = 0.1618 \frac{h}{L^2} \sqrt{\frac{E}{\rho}}$	(14)
Resonant frequency of a fixed-fixed beam with a residual stress σ_r and assuming no damping. Beam thickness is unimportant.	$f = \frac{\pi}{2\sqrt{12}} \frac{h}{L^2} \sqrt{\frac{E}{\rho}} \left[\sqrt{1 + \frac{12\sigma_r L^2}{\pi^2 E h^2}} \right]$	(15)
Measurement of residual stress from the deflection of static strain gage, δ . L_{sb} , L_{ib} and L_{tb} are the lengths of the slope, indicator and the test beam respectively.	$\sigma_r = \frac{2}{3} \frac{E}{1-\nu} \frac{L_{sb}}{L_{ib} L_{tb}} \delta$	(16)
Stress gradient as a function of cantilever tip displacement, assuming a linear stress distribution.	$\frac{d\sigma_r}{dh} = \frac{E}{1-\nu} \frac{2}{L^2} \delta$	(17)

Many previous resonance measurements on MEMS structures have been taken while exciting the structures electrostatically [118]. Standard electrostatic actuation is not a possibility with electrically insulating SU-8 because adding metal layers will alter the measured material properties. Instead of integrating actuators onto the polymer MEMS die, an external excitation source provided an input displacement to the test die at different frequencies. This source was chosen to be a piezo-electric crystal, which can provide a displacement ranging from 1-100's of nm depending on input voltage. This crystal is used to oscillate an individual test die back and forth in the direction of the highest degree of compliance in-plane for the resonating test structures. A Trek model PZD700 high voltage, high frequency amplifier [119] was used to power the piezo-electric crystal with appropriate amplitudes and frequencies. Despite the system completion near the end of the fabrication work, it is very useful for testing polymer MEMS material properties for a variety of structural materials and thicknesses. The basic system is shown below in Figure 5.3.

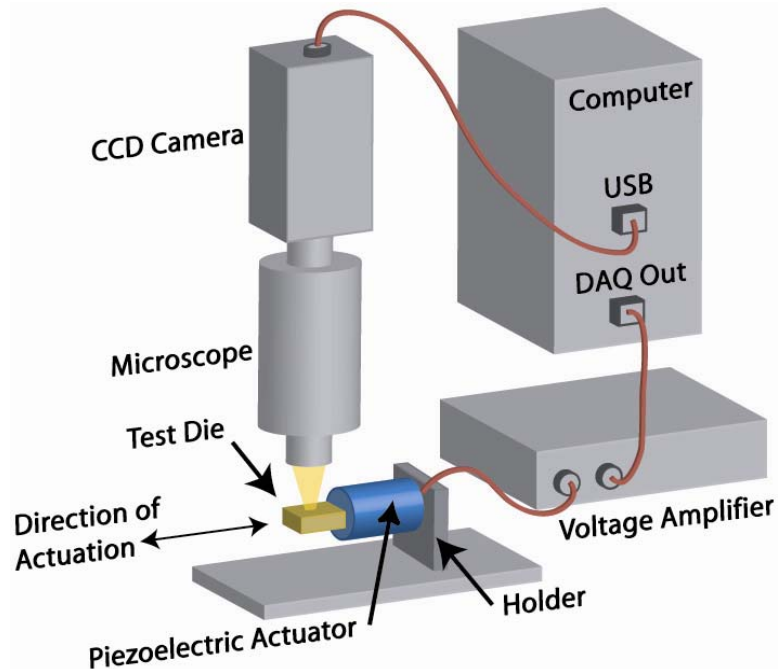


Figure 5.3: Schematic of the mechanical characterization die test system. This image is used with permission from [120]. The resonating test structures are observed through the microscope and each image corresponds to a specific input frequency.

A piezoelectric actuator oscillates the test die under an optical microscope system which takes pictures of the device's response at each input frequency. The amplitude of die vibration is below the optical threshold of the microscope system, avoiding any blurring of non-resonating structures. A vision analysis script was written to measure the device dimensions as fabricated [120] and to correct for any feature size swelling or structural deformations. The equations used to determine the material properties based on resonance are highly sensitive to the beam dimensions in-plane, so an accurate measurement of the fabricated dimensions is an integral part of this system. After images were taken at each frequency, another image analysis script finds the point at which individual devices experience their peak amplitude. Because the analysis is completed on an image that may show the response of several different devices, multiple structures can be analyzed using a single frequency sweep. By doing so, larger sample sizes can be

examined, which increase the confidence in the measured values. Figure 5.4 shows an example of several structures being oscillated at the same time using an external vibration source. No visual motion of the substrate can be detected, and Q factors for devices resonating in air have been as high as 50, resulting in large amplitudes and accurate measurements. An example of fixed-fixed SU-8 beams resonating at approximately 25 kHz is shown in Figure 5.4, demonstrating that non-resonating features are in focus despite substrate motion.

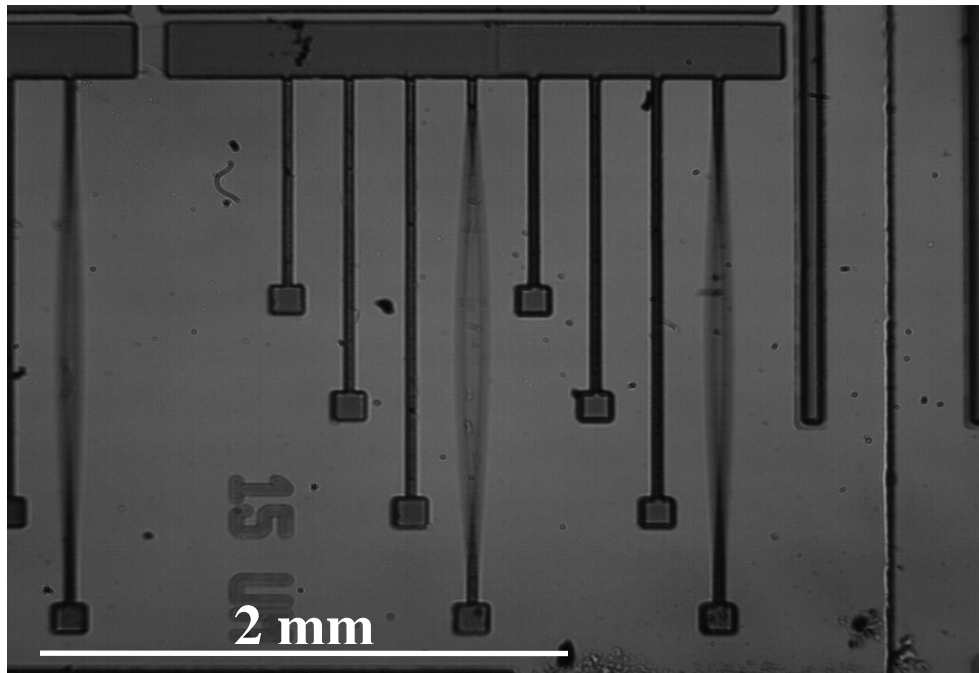


Figure 5.4: Fixed-fixed bars resonating at approximately 25 kHz.

Using this particular test die and measurement system allows changes to the basic polymer MEMS process to be quickly characterized for fabrication quality. To characterize and optimize new SU-8 thicknesses in this process, the following procedure should be used:

1. Fabricate a Cr/Au coated wafer as normal, and spin on polystyrene in the desired thickness.

2. Pattern photoresist with anchor features, and then expose the whole wafer through a blank Mylar sheet to induce surface roughness in the photoresist. This method reduces stiction, increases visibility of transparent polymers.
3. Develop photoresist, and RIE the wafer until the anchors clear and the photoresist is removed. Remove gold from anchors and rinse and dry wafer.
4. Based on the data sheets provided by Microchem, spin on SU-8 at the appropriate speed to achieve the desired thickness. Fine-tuning of spin-coating steps will be required later once feedback on actual thickness is obtained. Pre-bakes should be at least double the manufacturer's recommended time for the specific thickness to remove as much solvent as possible.
5. Align test structures mask, and expose row of die to different doses. The average dose should be close to that recommended in the manufacturer's data sheets for the SU-8 thickness and substrate used. Use long ramping bakes up and down with at least 20 minutes hold at the PEB temperature. Baking steps should be kept at the same length as the final intended process.
6. After PEB is complete, develop the wafer as normal and leave for at least a day to ensure all solvents are removed from the SU-8.

7. Examine the wafer and determine which exposure dose has resulted in the minimum curvature. This dose is the optimal value for the mechanical structures.
8. For the optimal dose, use the test die to determine the minimum resolvable feature size, Young's modulus, tensile stress, and other properties.

Full details on this die and test system can be found in [120], and will be of greater importance as the number of researchers using polymer MEMS technology increases. Future processing will benefit greatly from the rapid feedback on device and material performance which will result in greater quality control of future fabrication runs.

5.4 Thermal actuators

5.4.1 Background

Most MEMS processes are designed to connect electrical signals to devices for powering sensors or actuators. This work was used to fabricate MEMS actuators to demonstrate active structures in a polymer MEMS process. The physical properties of SU-8 make it a very good thermal actuator material for large displacements at low temperatures. A very common active device fabricated in most MEMS processes is the thermal actuator. SU-8 as a structural material has shown great potential to be a superior option for thermal actuation in comparison to silicon based designs. The purpose of this section is to demonstrate the operation of several styles of SU-8 thermal actuator. No direct comparisons are made, owing to the different thicknesses and designs tested, but general operation characteristics and potential failure modes are identified. Deflection

and force versus power is measured for several individual actuators to demonstrate the performance of different designs. Error bars indicate the range of uncertainty in the force or displacement measurements due to the accuracy of the vision builder software.

Although SU-8 thermal actuators have been described previously in the literature [60-62], few attempts have been made to characterize their behaviour as thoroughly as those fabricated in silicon. Previously reported actuators were based on either bi-morph designs [60], or hot/cold thermal actuators [61, 62]. The performance of these actuators cannot be directly compared with the work presented here because processes, scales, and methods of operation are different. The success of the basic SU-8 process developed for this work allowed the fabrication of multiple actuator designs on the same die. Detailed operational characteristics were collected. Two major styles of thermal actuator were fabricated initially: the hot/cold arm thermal actuator [11] and the chevron thermal actuator [11]. Examining the performance of these actuator styles in SU-8 revealed that modifications were necessary to improve performance. A third type of actuator developed for use with SU-8 was designed that combined features of both the hot/cold and chevron thermal actuators. This style of actuator is known as the hybrid thermal actuator [121].

5.4.2 SU-8 hot/cold arm thermal actuators

The hot/cold arm thermal actuator is an asymmetric loop, with a thin arm and a wide arm. When voltage is applied across the loop, current passes through both arms in series, with the thinner arm heating up more due to its higher resistance. The thin arm will expand more than the thick arm, and the actuator geometry then amplifies this

expansion into an arcing motion of the actuator, pivoting approximately around the flexure on the cold arm.

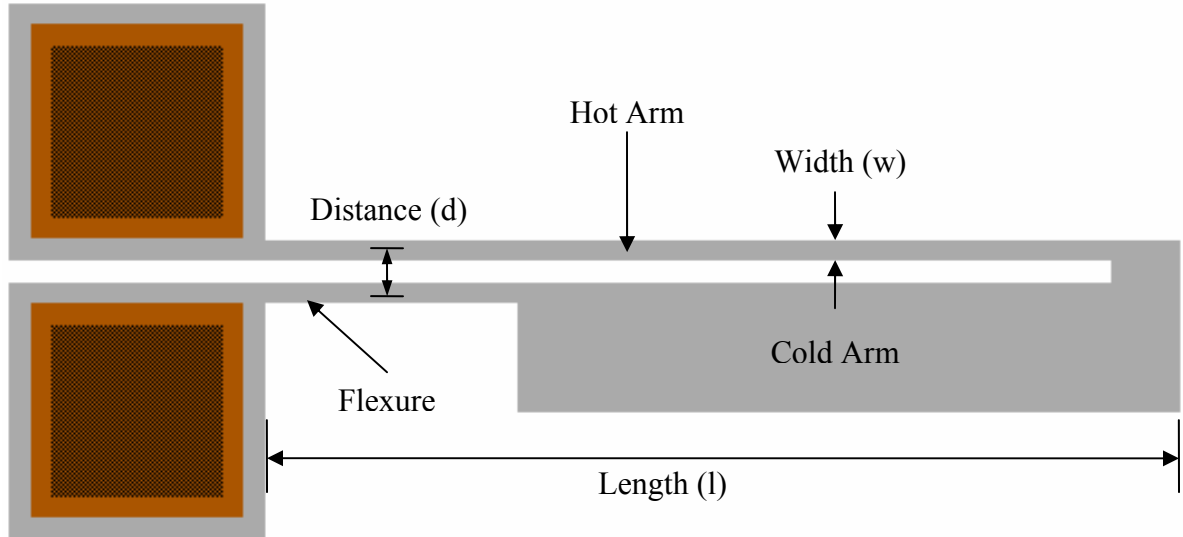


Figure 5.5: Hot/cold thermal actuator layout in L-Edit showing geometric properties.

Hot/cold arm thermal actuators were used by both Nguyen [61] and Chronis [62] in their work with SU-8 microgrippers. The overall design is robust and works well, but it can show significant out-of-plane deflection due to thermal bi-morph effects between the SU-8 and metal layers. These results were also observed in this work when the actuators were given larger input power. Despite this out-of-plane motion, the in-plane deflections can be very large and are approximately linear with input power. Figure 5.6 shows an example of a typical deflection versus power curve for a 1 mm long SU-8 hot/cold thermal actuator powered through direct wirebonding.

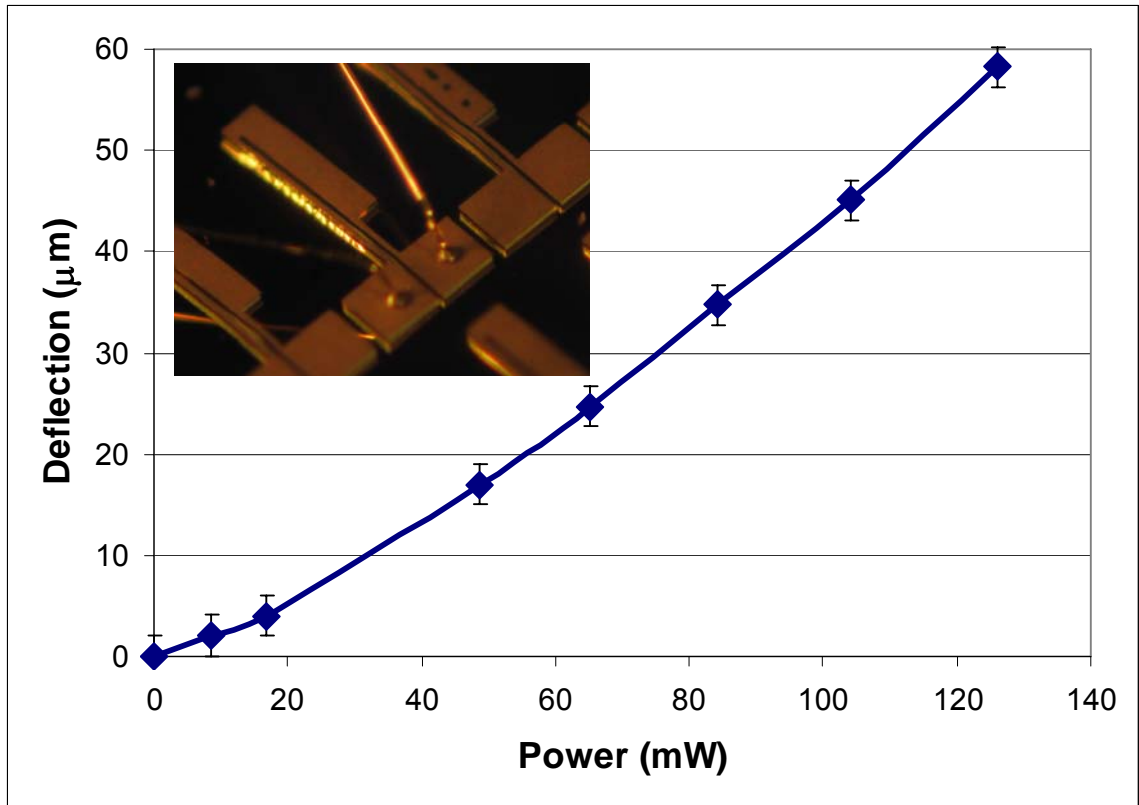


Figure 5.6: Performance of a wirebonded SU-8 hot/cold arm thermal actuator as deflection versus input power. Actuator is 1 mm long and 40 μm thick with a 20 μm wide hot arm [110].

The geometric amplification of the actuator is approximately defined by the actuator length divided by the distance between the hot and cold arms (l/d) [114]. For this particular design, the amplification ratio is approximately 25. In the measurements listed above, only deflection in the initial direction of motion was measured. At higher deflections, significant angular motion occurs at the actuator tip. While this is not likely to be a problem for most single actuator applications, the angular component of motion makes this particular design difficult to connect in parallel, where higher forces might be desirable. In cases where significant force and linear motion is desired, chevron thermal actuators have proven to be a better choice [114].

5.4.3 SU-8 chevron thermal actuators

To the author's knowledge, the paper describing this polymer MEMS process was the first to show a chevron style thermal actuator fabricated using SU-8 [77]. These actuators are significantly different from the hot/cold actuator in that they only require an absolute temperature difference between them and the substrate to operate properly. In addition, they are fixed on either side by anchors, theoretically eliminating much of the out-of-plane motion common to SU-8 hot/cold arm thermal actuators. Other researchers have already published data on their improved performance for high force applications [114], and their fabrication in SU-8 was hoped to lead to very high force actuators with highly efficient mechanical amplifiers integrated for large deflections. Early fabrication results produced relatively low aspect ratio actuators due to the large minimum features of the masks and relatively thin layers. Images of these early chevron actuators are shown in Figure 5.7.

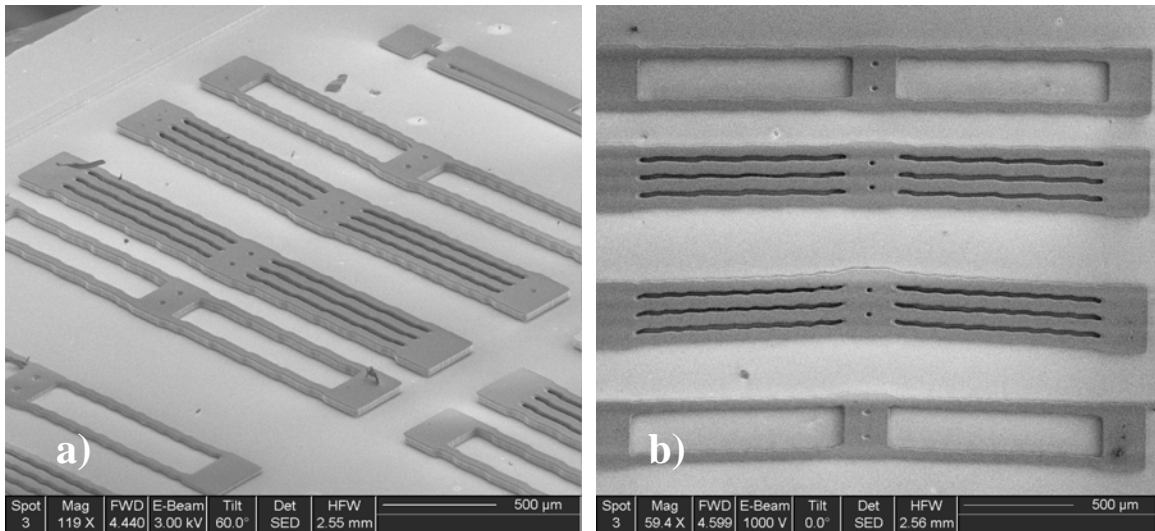


Figure 5.7: SEM images of chevron thermal actuators fabricated in an early version of the polymer MEMS process [89]. Raster scanning effects from the low quality masks can be seen on the arms in a) and b). The actuators have very little electrical resistance due to the large number of wide arms in parallel.

On this particular die, actuator thickness, geometric amplification, and the number of arms were varied to determine their effect on performance. The geometric amplification of the chevron actuator is equal to $1/\theta$ when θ (measured in radians) is small [11] (Figure 5.8). Unfortunately, the thinnest actuators had low aspect ratio arms, which often caused bucking out-of-plane prior to significant in-plane deflection. Thicker actuators worked more reliably, but those actuators with the highest geometric amplifications showed more deviations from expected behaviours. The thick actuators with a geometric amplification of 10 worked most reliably in early trials, and these became the base for all subsequent chevron thermal actuator designs.

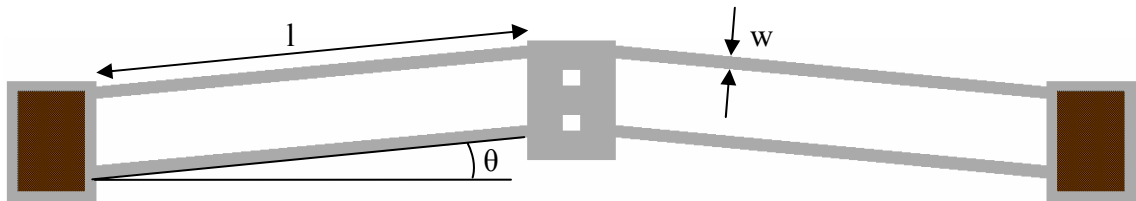


Figure 5.8: Chevron thermal actuator layout in L-Edit and geometric properties.

For these early chevron thermal actuators, linear motion was achieved and little out-of-plane motion was observed in most cases, but the large numbers of wide arms caused significant problems with reliability [77]. The greatest issue was the large current required to power these actuators. For the chevron actuators with four arms, the actuator resistance was low enough that contact resistance between the microprobes delivering power and the thin metal surface became a significant source of power loss. The result was that at higher input powers, actuators would frequently fail by gold melting/electromigration at the point of contact between the actuator and the microprobes. This failure mode was unexpected, but for future SU-8 actuator designs,

the number of arms was minimized to avoid excessively low actuator resistance. For the SU-8 chevron actuators with two arms, a different failure mode was observed. This failure occurred by driving the actuator with too much power, and showed similar characteristics to silicon actuators when powered to excess. Figure 5.9 shows the hysteresis curve of an SU-8 chevron thermal actuator with two 1 mm long hot arms, 40 μm thick, with a designed geometric advantage of 10X.

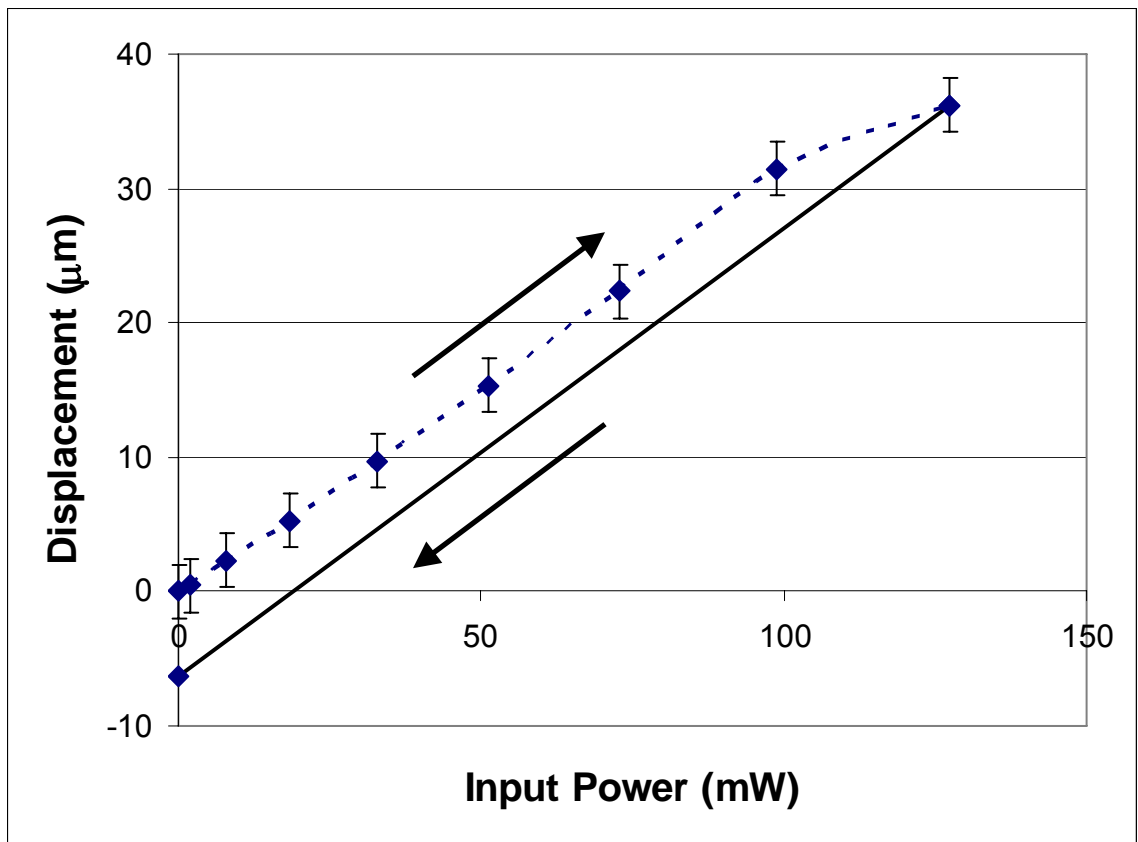


Figure 5.9: Displacement versus power for an SU-8 chevron thermal actuator. Hysteresis occurs after plastic deformation of the SU-8 due to overpowering, resulting in a negative deflection.

When SU-8 is heated to a high temperature or strained outside its elastic range, plastic deformation can occur. Plastic deformation occurs more readily at, or close to, the glass transition temperature. For the actuator described in Figure 5.9, this transition occurred at input powers greater than 100 mW. This input power is very high relative to

most MEMS devices, but is actually lower than the input power required for some smaller silicon thermal actuator designs [114]. In this case, an SU-8 thermal actuator with a volume several orders of magnitude greater than the silicon thermal actuator described in [114] can deflect 10 times greater distances with less input power. By this standard, SU-8 chevron thermal actuators appear to be a superior option for large displacements at low temperatures. Unfortunately, many of the factors that improve static performance of SU-8 thermal actuators also result in poorer dynamic performance. Traditionally, MEMS thermal actuators have very small thermal time constants due to their small mass, or heat capacitance. For hot/cold arm or chevron thermal actuators, the thermal time constant is usually the limiting factor for the maximum frequency of operation [11]. The thermal time constant of a chevron actuator is dependent on the actuator geometry, volume, heat capacitance, and the thermal conductivity of the actuator material and its surroundings. With respect to SU-8 thermal actuators, their low thermal conductivity and relatively high volumes compared to silicon actuators result in very long thermal time constants that greatly limit the maximum actuation rate. In order to measure this effect on the actuator design described in Figure 5.9, the same laser probe microscope used by [11] to determine dynamic performance of silicon thermal actuators was used to measure the SU-8 devices. Measurements in both the time and frequency domain were made and are shown in Figure 5.10 and Figure 5.11.

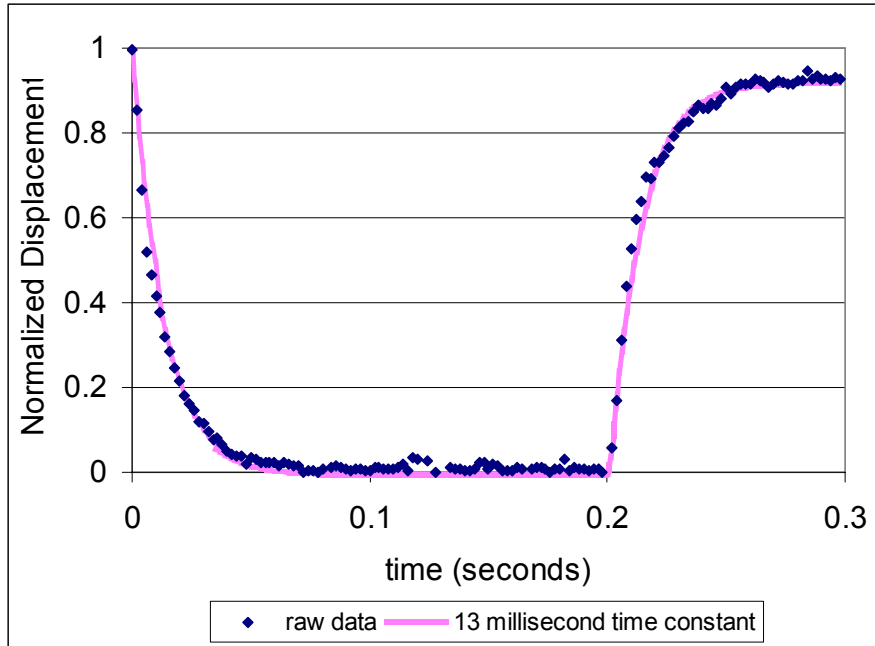


Figure 5.10: Time response of the chevron thermal actuator design described in Figure 5.9. A time constant of 13 ms has been fit to the raw data [89].

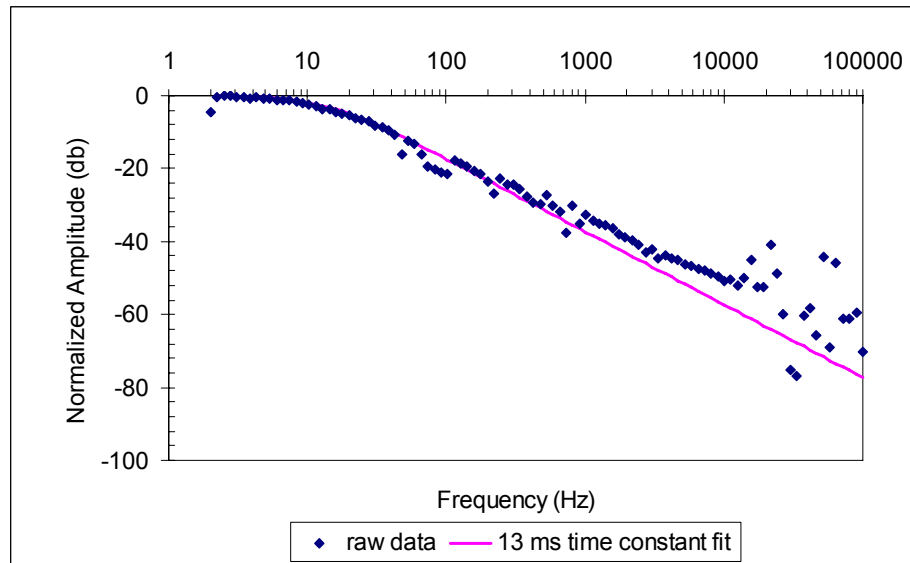


Figure 5.11: Frequency response of the chevron thermal actuator design described in Figure 5.9 [89].

The time constant fit to this data was two orders of magnitude greater than the silicon thermal actuator described in [11]. No mechanical resonance could be conclusively found in the frequency response of this actuator due to the low signal to

noise ratio at higher frequencies with this measurement system. The very low contrast between the gold surface of the actuator and the gold substrate greatly limited the use of this frequency measurement system, but, in the future, an RIE activation/roughening step would be able to enhance measurement accuracy.

5.4.4 SU-8 hybrid thermal actuators

The SU-8 structures fabricated with higher aspect ratios demonstrated significant weaknesses in the traditional chevron actuator designs due to the effect of residual tensile stress in the SU-8. Early work with these actuators resulted in aspect ratios of approximately 1:1 for most devices tested, and the raster scanning effect of the early masks prevented good understanding of the effective geometric advantage of the fabricated actuators. When higher quality masks became available during later work, series of chevron thermal actuators were fabricated with fewer arms and narrower beams, so that the high currents that caused contact failure between the micro-probes and the gold surface would be reduced. These high aspect ratio chevron actuators were actually far less robust than anticipated and demonstrated how the high tensile stress in SU-8 could negatively affect designs.

With narrower hot arms ($< 30 \mu\text{m}$), the flexibility of the chevron thermal actuators increased, and the deformation in fabricated structures due to the tensile stress in SU-8 was clearly visible. While most structures did not appear to fabricate significantly different from their designed dimensions, devices like chevron actuators, which are designed to amplify dimensional changes between two fixed anchors, exhibited large negative deflections from their ‘neutral’ positions. An extreme example is shown in Figure 5.12, where a series of high aspect ratio chevron actuators are fabricated in a 180

μm thick SU-8 layer. Significant warping of structures can be seen, with the narrow structures not even fully exposed down to the polystyrene layer. This results in their twisting out-of-plane during fabrication.

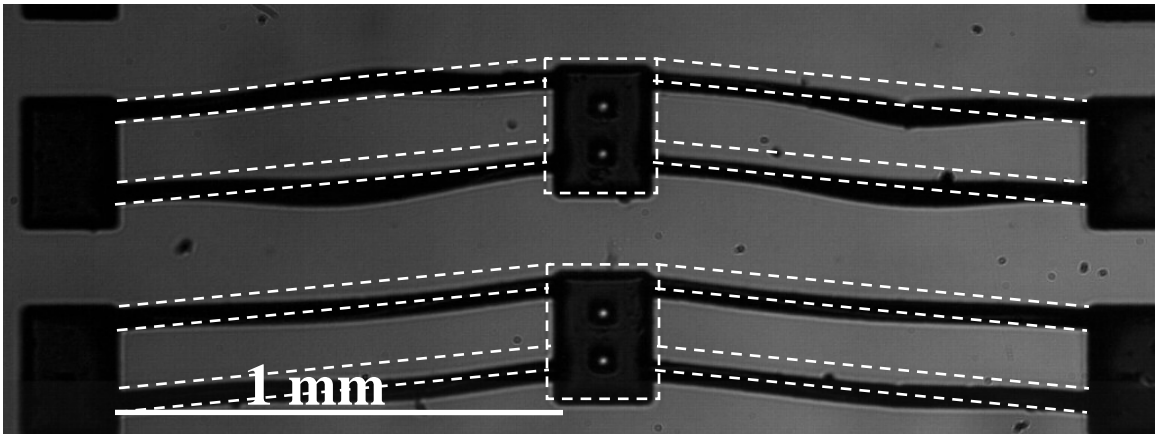


Figure 5.12: Under exposed and highly stressed chevron thermal actuators fabricated in a $180\ \mu\text{m}$ thick SU-8 layer. Tensile stress is amplified by the actuator geometry and results in a negative initial deflection compared to the designed position (shown in outline).

With such significant initial negative deflections, high aspect ratio SU-8 chevron actuators are unpredictable and not as useful. The initial geometric amplification is now larger than the designed value, but the structure must be heated significantly to move back to its designed neutral position. The extreme deformation from tensile stress is not seen in hot-cold thermal actuators because the anchors are located on one side of the actuator, allowing it to shrink freely in its longest dimension. In order to create a more predictable chevron performance, a combination of the two basic thermal actuator designs was required.

The problem with the chevron thermal actuator is the location of the anchors, which do not allow the actuator to shrink freely in its longest dimension. To solve this issue, a folded suspension was added to the chevron actuator to create what was termed a

hybrid thermal actuator. Figure 5.13 shows L-Edit layouts and images of fabricated hybrid thermal actuators.

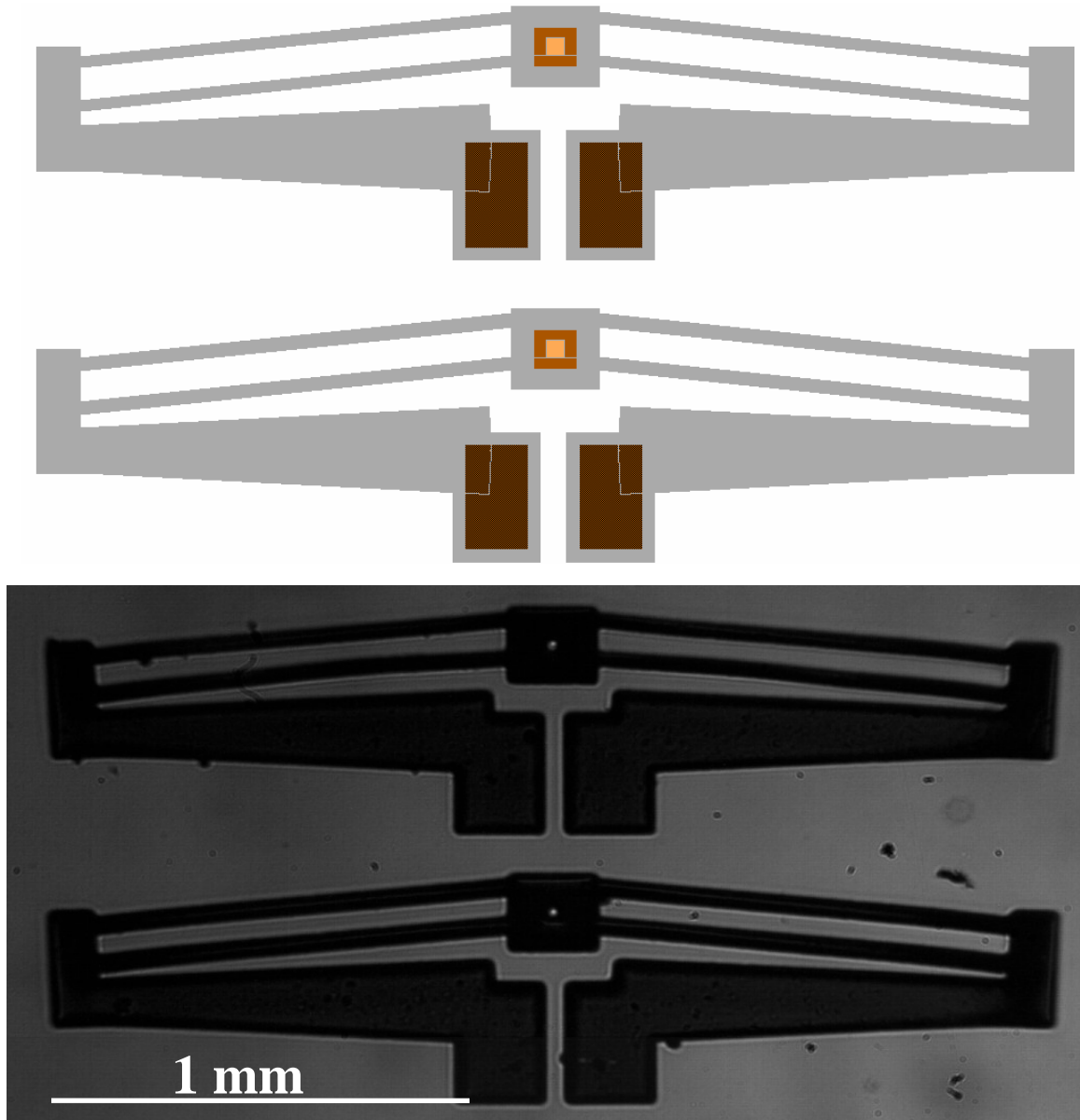


Figure 5.13: L-Edit layouts and images of hybrid thermal actuators fabricated in 180 μm thick SU-8. The folded suspension shrinks with the hot-arms, but constrains the hot arms during actuation. Full shrinkage compensation is not achieved with these actuators due to the anchor spacing.

In the hybrid thermal actuator design, the anchors are located as close to the centre of the actuator as possible, with wide, stiff bars extending out to contain the

chevron thermal actuator. The wide bars are free to shrink at the same rate as the chevron, yet are stiff enough to constrain the expansion of the chevron actuator during operation. Current passes through these wide bars in series with the chevron section, but their resistance is lower, and, therefore, they act like the cold arms in the hot/cold arm thermal actuator. For this reason, these actuators have been named hybrid thermal actuators. The efficiency of the actuators shown in Figure 5.13 is actually fairly poor due to a design oversight. The ratio of electrical resistance between the hot arms and the support bars should be as high as possible, but in these designs, up to 30% of input power may be dissipated in the support bars. The power loss in the wide arms reduces the expansion difference required for actuation. A hybrid actuator was compared with a chevron actuator designed with the same initial dimensions, geometric amplification, and fabricated thicknesses on the same die, and the following results were achieved for deflection versus input power. The error in deflection measurements is approximately $\pm 0.5 \mu\text{m}$.

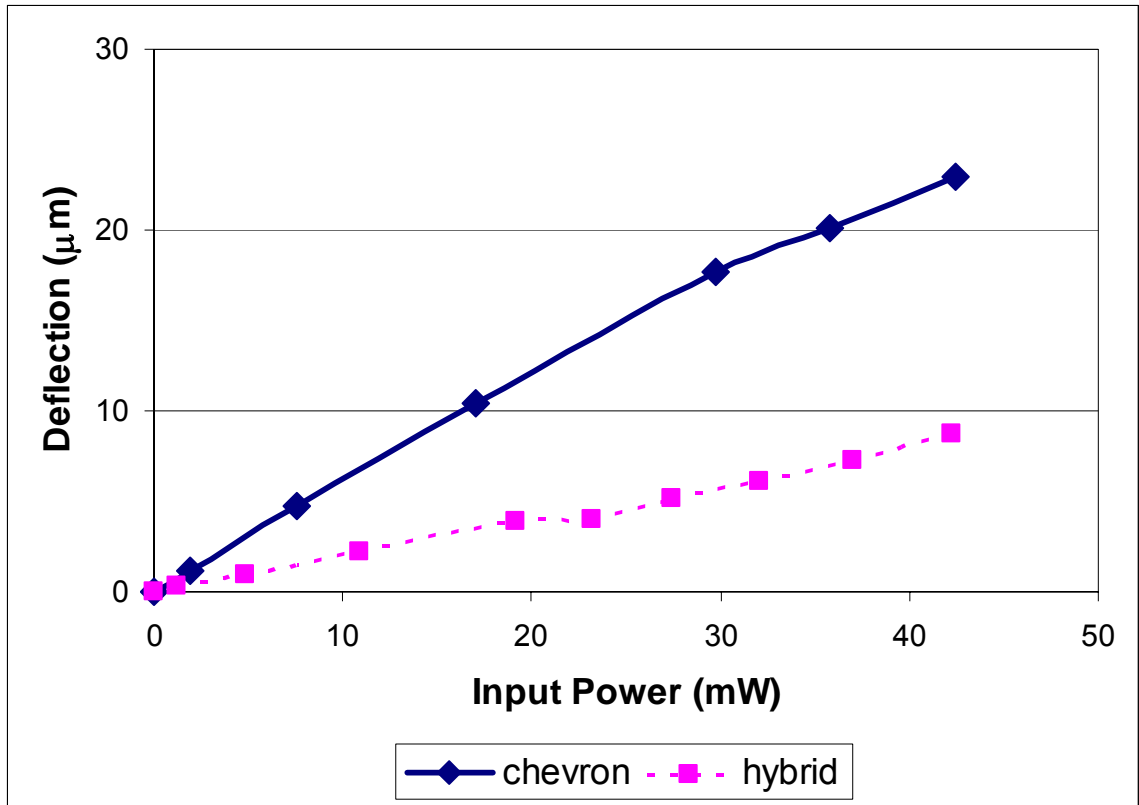


Figure 5.14: Deflection versus input power for chevron and hybrid thermal actuators that are 120 μm thick with 1 mm long hot arms and a designed geometric advantage of 10.

In comparison to a hybrid thermal actuator designed with the same geometric advantage, Figure 5.14 shows that the chevron thermal actuator demonstrates superior performance for deflection versus input power. This decrease in performance is primarily due to the resistance losses in the cold arm of the hybrid thermal actuator and the increased geometric advantage of the initially deflected chevron actuators as fabricated. If the ratio of cold arm resistance to hot arm resistance was higher, and the difference in initial geometric advantage was corrected for, most of the difference in performance would disappear [121].

Several hybrid thermal actuators were fabricated with the same dimensions to determine the effect of thickness on actuator performance. The performance of two

chevron thermal actuators with 30 μm wide hot arms, 1 mm hot arm lengths, and different thicknesses are shown in Figure 5.15.

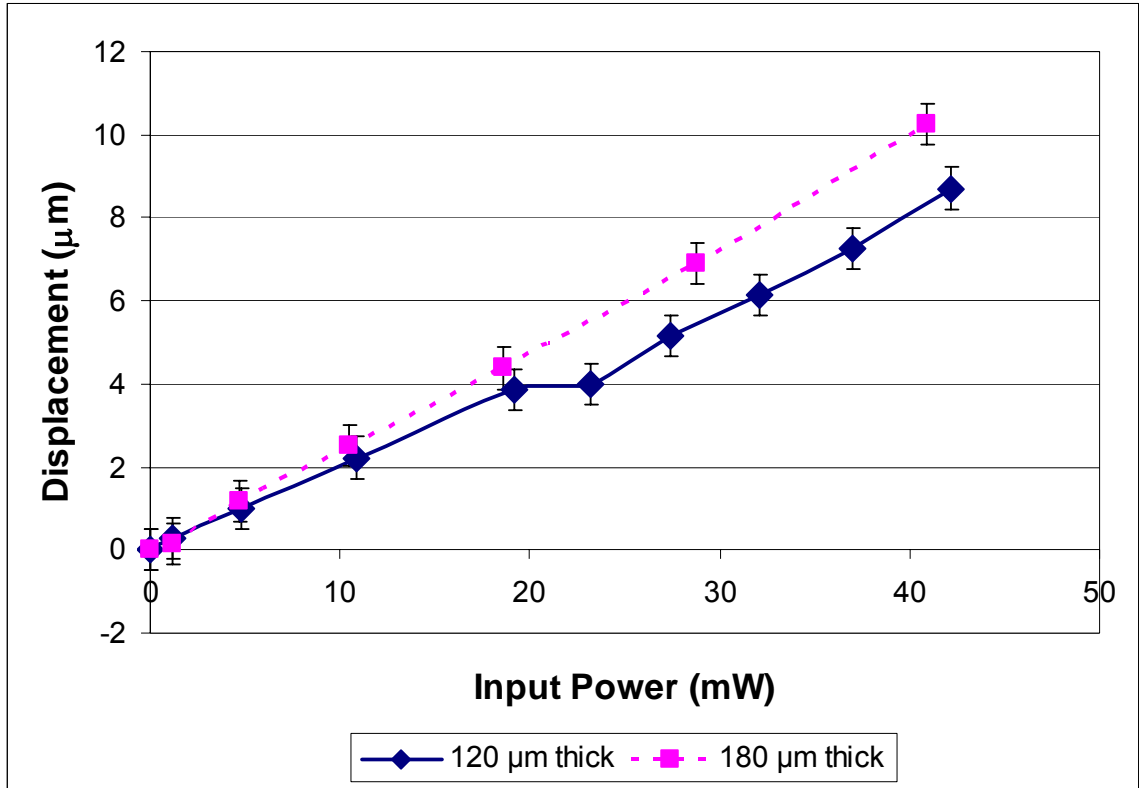


Figure 5.15: Hybrid thermal actuator performance with identical designs fabricated with different thicknesses on the same wafer.

The results show that the thicker SU-8 hybrid actuators show more deflection for a given input power than the thinner structures. This result is also seen with chevron and hot/cold thermal actuators. The exact cause of the kink in the data for the 120 μm thick actuator is unknown, but the slope of deflection versus input power is already lower than that of the 180 μm thick actuator. The effect of reduced heat loss to the substrate from the metal resistor dominates over the extra power required to heat the greater volume of SU-8. Although these thicker structures deflect more for a given input power, they are also likely to have extremely long time constants from both the increased thermal mass, and the increased thermal isolation. If large displacement and static force is required,

larger and thicker SU-8 thermal actuators show improved performance over their smaller counterparts.

5.4.5 SU-8 thermal actuator force output

The low temperature operation of SU-8 thermal actuators ($< 100\text{ }^{\circ}\text{C}$) makes them attractive for low power operations, and are potentially better than silicon thermal actuators for underwater applications [22]. The displacements that they can provide are much greater than a typical silicon thermal actuator with the same input power, but their efficiency is unclear unless the force output could be measured. Earlier work with measuring the work output of thermal actuators had measured the force versus displacement of the actuators for different input powers [114]. Therefore, the work output of the actuator versus a given input power was then used as a figure of merit for efficiency. Technically, thermal actuators are nearly zero percent efficient because they require constant input power to hold a static deflection where zero work is performed, but this measurement ignores the work performed during the initial motion. To determine the relative performance of SU-8 actuators, a similar experimental setup used in [114] was constructed using the same linear stages that were used for the bond pull tests with an acupuncture needle of known stiffness. Three different types of thermal actuator were tested for their force versus deflection, and the experimental results are listed in Figure 5.16, Figure 5.17 and Figure 5.18. The error bars represent the uncertainty of measurement in both displacement and force with the camera resolution and magnification used, and assumes visual accuracy to ± 1 pixel.

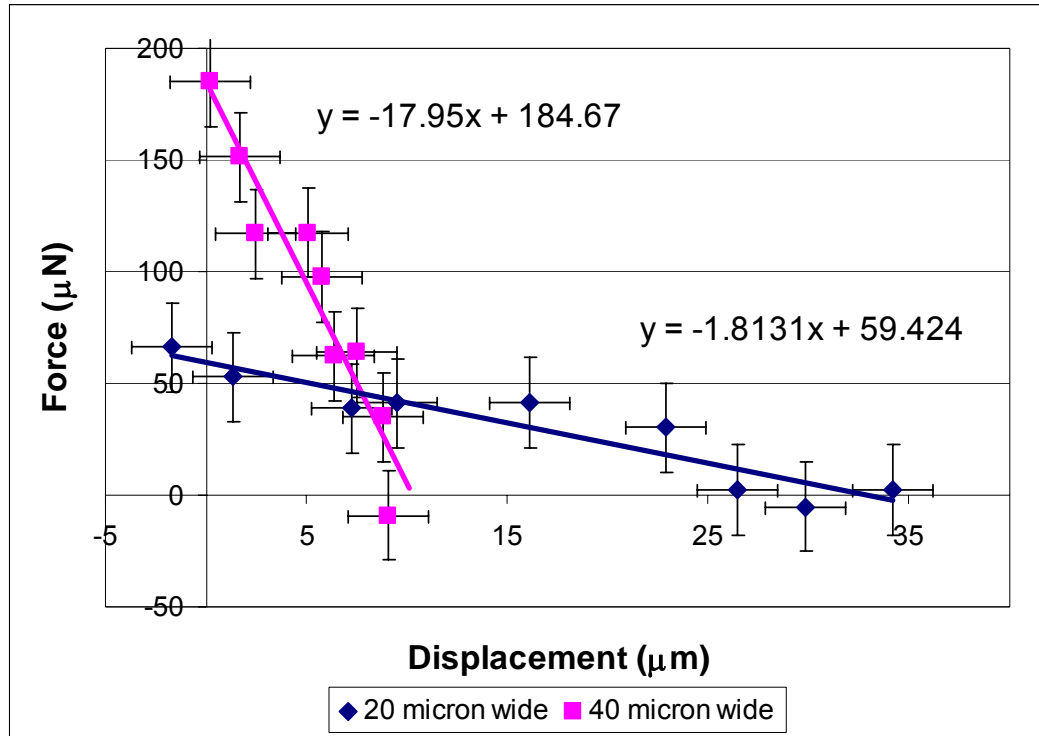


Figure 5.16: Force versus displacement of two different hot/cold thermal actuator designs with different hot arm widths [122]. Input power is 69.4 and 64.35 mW for the 20 and 40 μm wide designs, respectively.

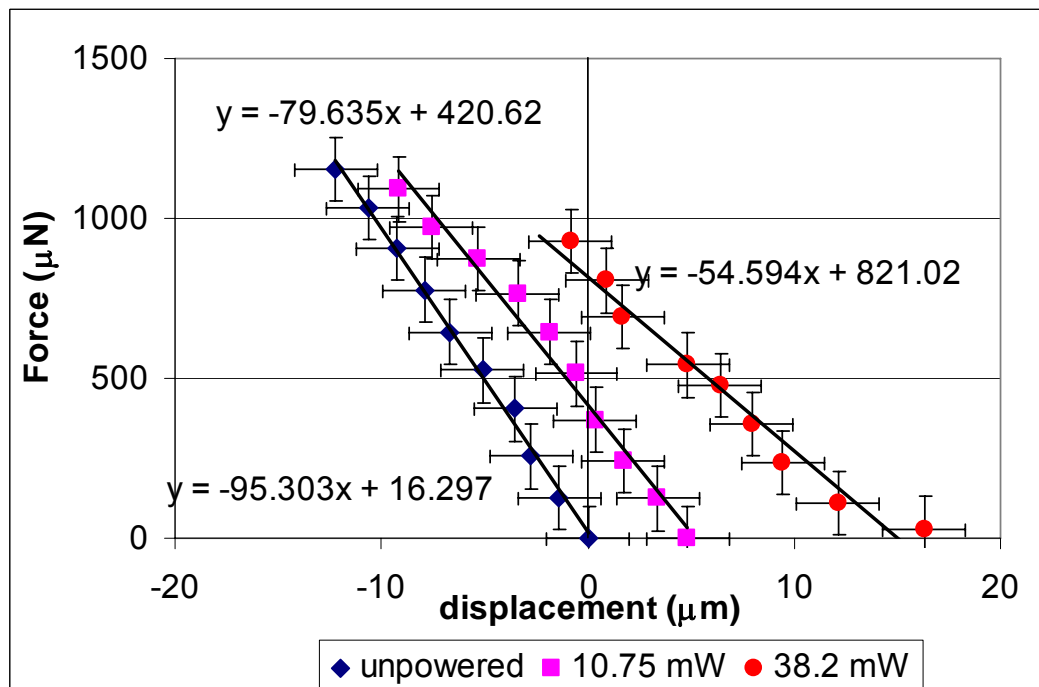


Figure 5.17: Force versus displacement of a chevron thermal actuator at different input powers. The actuator is 40 μm thick with two 40 μm wide hot arms, each 1 mm long with a designed geometric advantage of 10.

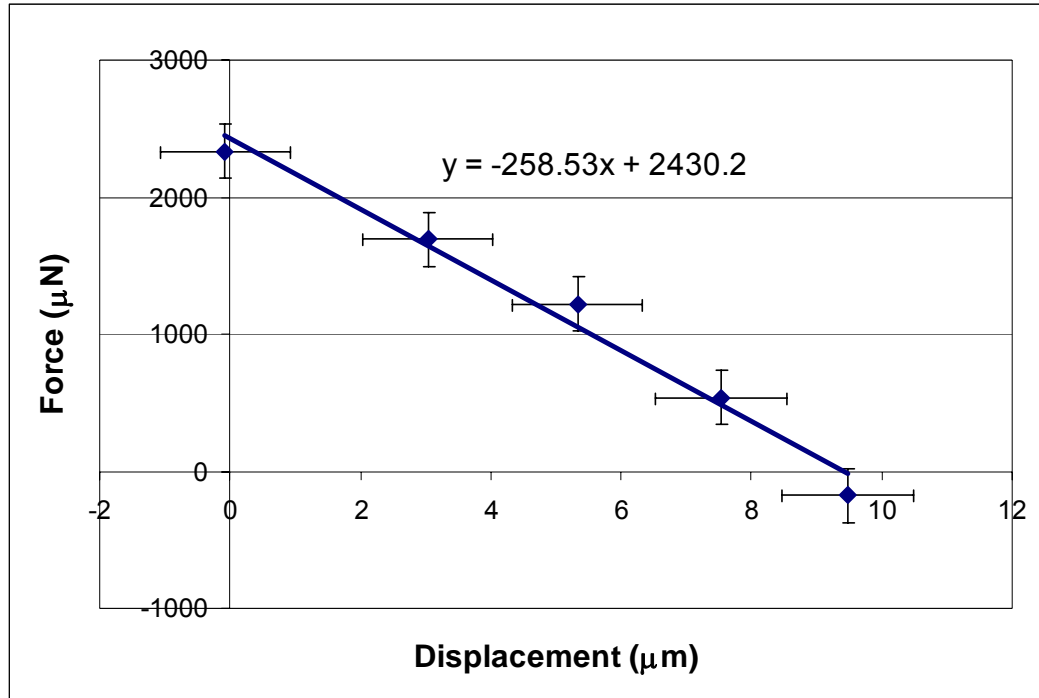


Figure 5.18: Force versus displacement of a hybrid thermal actuator with an input power of 33.24 mW [122]. The actuator is 180 μm thick with two 20 μm wide hot arms, each 1 mm long with a designed geometric advantage of 10.

The slope of force output versus displacement of SU-8 thermal actuators is approximately equal to their unpowered stiffness, but this value can change with temperature, large displacement and actuator type. The stiffness of SU-8 thermal actuators may be reduced at very high input powers, where the SU-8 softens with increased temperatures [111]. At high displacements, SU-8 thermal actuators can also change their geometric advantage enough to affect the stiffness, but this effect can make actuators stiffer or softer depending on geometry [114]. In the case of chevron thermal actuators, the initial tensile stress in the unpowered position will alter the stiffness predicted by the designed geometry.

5.5 Untethered polymer scratch drive actuators

During the course of this doctoral work, an opportunity arose to participate in the first ever Nanogram competition as part of the international Robocup competition held in Atlanta Georgia in 2007 [123]. The nanogram competition was based on the first ever untethered electrostatic actuator that could move around on a specially prepared electrode array [124] that powered the robot through capacitive coupling. This particular method of power delivery to microscopic actuators, without requiring direct electrical connection, opened up new possibilities for creating microscale robots that can be operated over large distances without being attached to the substrate. A proposal was sent out to different universities by one of the authors of [124] to participate in developing new micro-scale robots that could move on this playing field and potentially manipulate objects, in a microscale analogue to playing soccer. This particular challenge was an excellent opportunity to demonstrate the polymer MEMS technology, in order to show its use for electrostatic actuators. A modification of the basic polymer MEMS process was developed for this specific application, that demonstrates the general flexibility of this process in modifying layer thicknesses for a wide variety of applications.

5.5.1 Robocup nanogram competition

The untethered actuator demonstrated by [124] was based on the standard silicon scratch drive actuator, or SDA [125]. In this device, a thin plate of an electrically conducting material, usually silicon, flexes up and down with the application of a high electrical potential between the plate and the substrate. A bushing located at the front of the scratch drive actuator contacts the substrate first, and the flexing of the plate pushes this bushing forward at higher voltages. When the voltage is removed, the restoring

spring force on the plate straightens the actuator while the bushing stays in the same location. Figure 5.19 shows that when the plate flexes down and up with each voltage cycle the actuator steps forward by a few nanometres. Repeating cycles of voltage cause the plate to crawl forward like an inchworm [125].

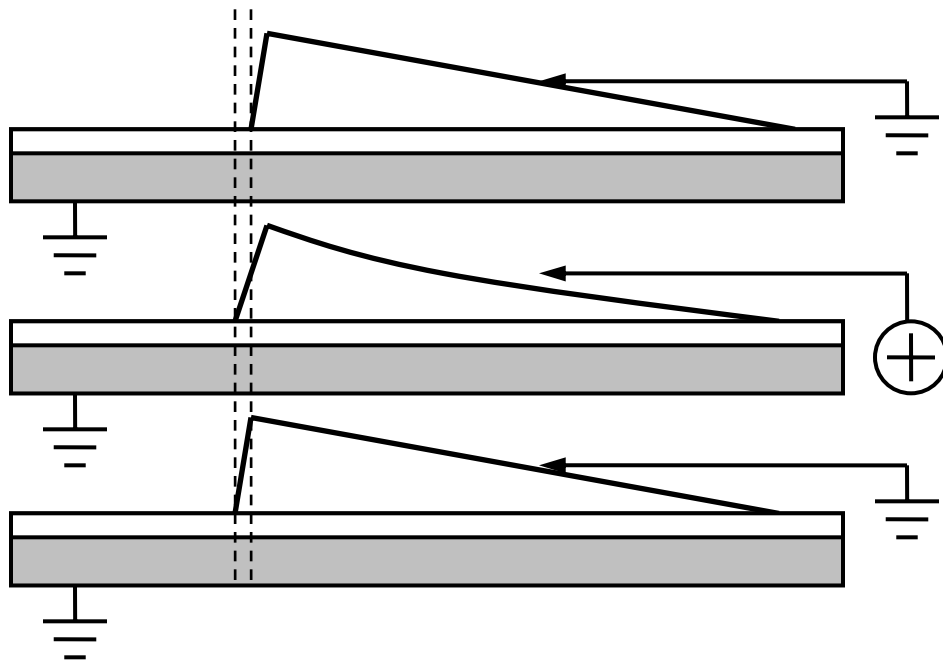


Figure 5.19 Schematic of scratch drive actuator motion.

If a polymer scratch drive can be made with the same dimensions, and if a very thin metal layer is used for electrical conductivity, it should be able to operate at much lower voltages due to its lower stiffness. Also, polymer fabrication allows for much thicker bushings than are possible with the PolyMUMPs process used in the earlier silicon versions [1], which should increase the step size of the actuator. Increasing the step size would have increased the speed of the scratch drive actuator for a given input frequency, and one criterion in the Robocup Nanogram competition was to be as fast as possible. Using the basic concepts of scratch drive actuators, it was determined that different SU-8 actuators based on this design could be fabricated and used in the

competition to demonstrate that the polymer MEMS process could fabricate low voltage and speedy actuators.

A new version of the basic polymer MEMS process was developed specifically to produce thinner polymer structures. It used a 2 μm thick polystyrene sacrificial layer to avoid large radial streaks during spin coating and SU-8 2005 or 2002 for structural layers. The process was designed to make actuators that would have the metal layer in close proximity to the insulated electrodes. This required that scratch drives be fabricated upside down, blanket coated with metal, then flipped upside-down when placed on the playing fields. Aluminum deposition after release was chosen to induce compressive stress on the SU-8 surface, where the thinner structures would bend away from the playing field once flipped upside down. This method was designed to make different actuator sections operate at different threshold voltages [124]. Making dimples in the thinner sacrificial layer would be difficult, so only anchors were produced in the polystyrene layer. The POLY0 mask that normally produced dimples was used, instead, to define a first thin structural layer, with POLY1 and POLY2 defining two other thicknesses. Figure 5.20 shows a schematic of a basic, untethered polymer scratch drive robot a maximum thickness of 15 μm . The fabrication procedure for these designs is listed in Appendix B.

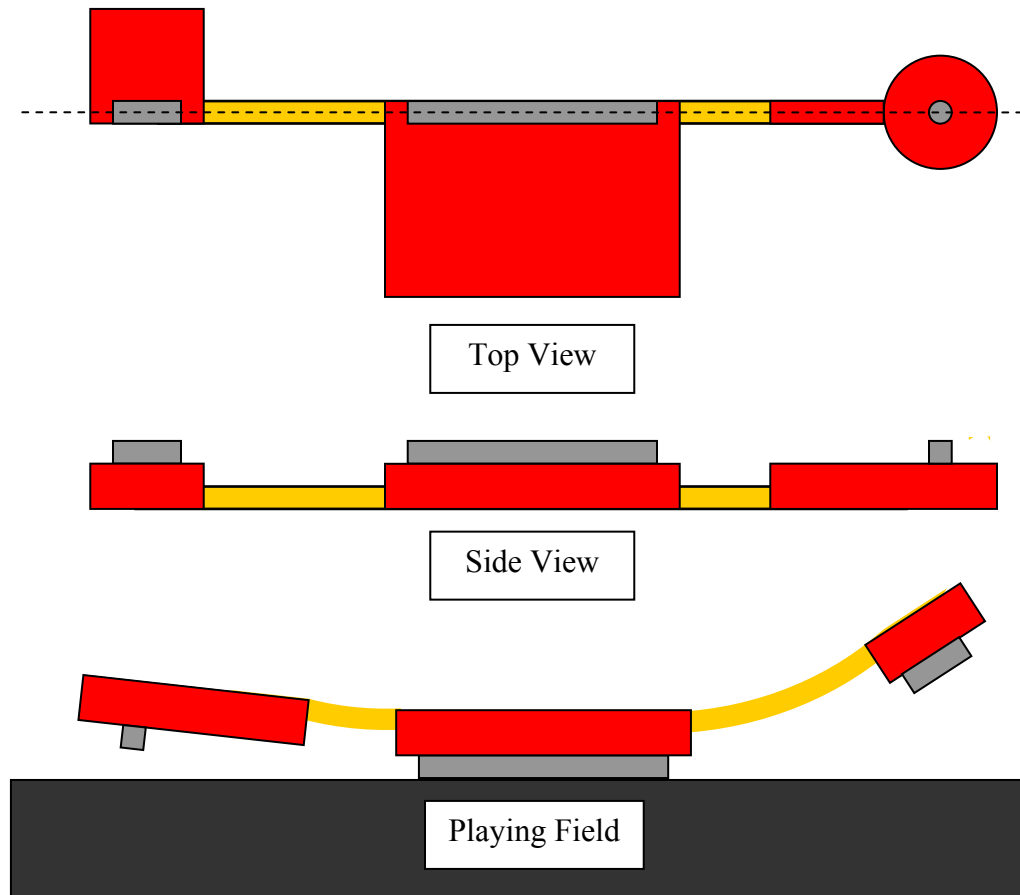


Figure 5.20: Basic untethered polymer scratchdrive robot structure. Structural thicknesses are designed to be 5, 10 and 15 μm .

The natural waviness of the polystyrene due the effect of cyclopentanone is enhanced by the higher solvent content in the SU-8 formulations used. A much greater degree of a “cracked” appearance occurs in very thin polystyrene layers exposed to the cyclopentanone but this rough underside is not transferred to the top surface of SU-8 structures. Each ridge is between 100 and 200 nm in thickness, and behaves as a dimple for this process variation, allowing stiction problems to be minimized without a separate dimple patterning step. Figure 5.21 shows the bottom surface of an SU-8 nanobot design that demonstrates an extremely high density of these ridges.

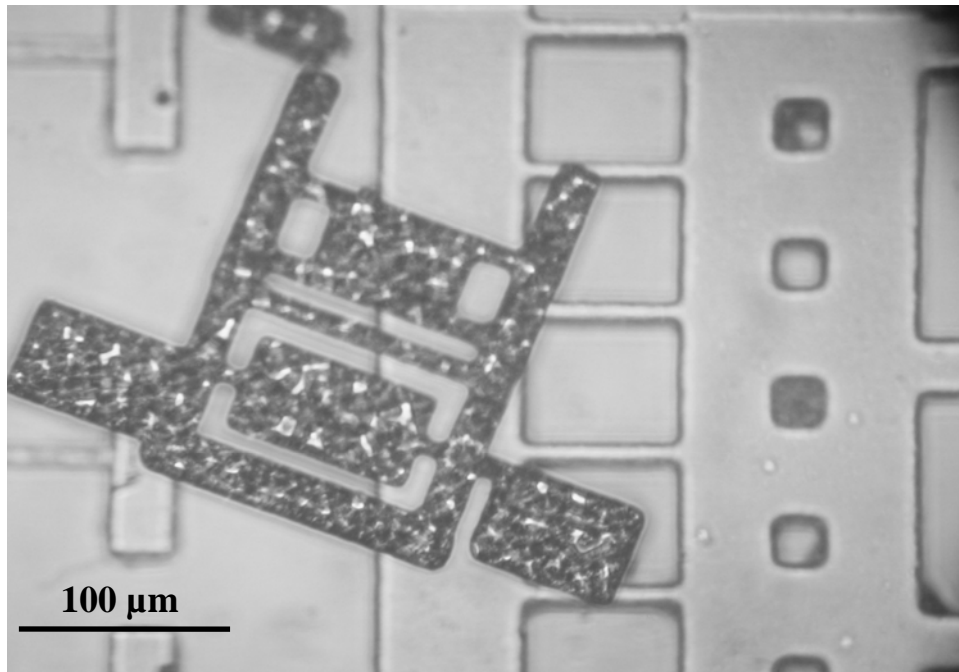


Figure 5.21: Photograph of the underside of a chrome coated polymer scratch drive actuator that has broken off after metal deposition. Waviness of the bottom surface is up to 200 nm.

The nanogram robot designs fabricated for the Robocup competition were the smallest and most complicated structures fabricated during the work with this process. These structures demonstrate that acceptable results can be achieved with Mylar masks. They represented three distinct structural thicknesses on a very thin polystyrene sacrificial layer with a total device dimension on the same scale as polysilicon based scratch drive actuators. From end to end, these robots are one order of magnitude smaller than the cantilevers fabricated in section 4.2. The nanobots were handled on a breakaway tether, which was removed and flipped upside down through the use of two needles. The basic handling and flipping procedure is shown below in Figure 5.22.

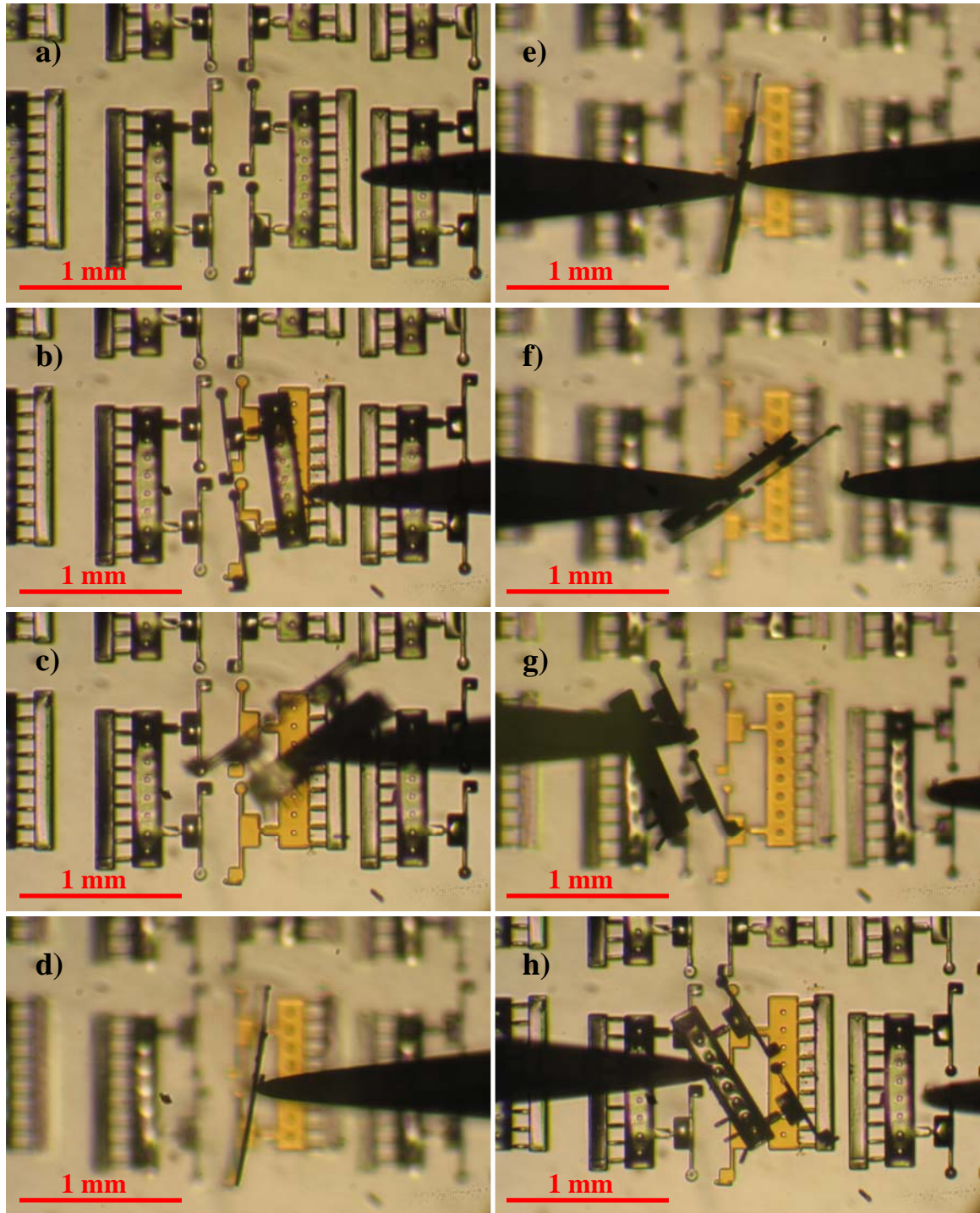


Figure 5.22: Removal and flipping procedure of SU-8 nanobots. Acupuncture needles attached to microprobes remove (b), and manipulate robots. Spinning the needle (d), rotates the robots out-of-plane, where they can be transferred to another needle (e), prior to being rotated into the upside down position (g), and placed on the substrate (h).

Transferring the robots is made easier by the fact that the needles adhere better to SU-8 than the aluminum, which allows for quick transfer between needles. Significant operator skill was initially required, but eventually this task can be completed within seconds with practice. Nanobots are transferred in this manner to the playing fields, based on those detailed in [124], provided by the competition organizers, where the varying amounts of out-of-plane curvature can be seen in Figure 5.23.

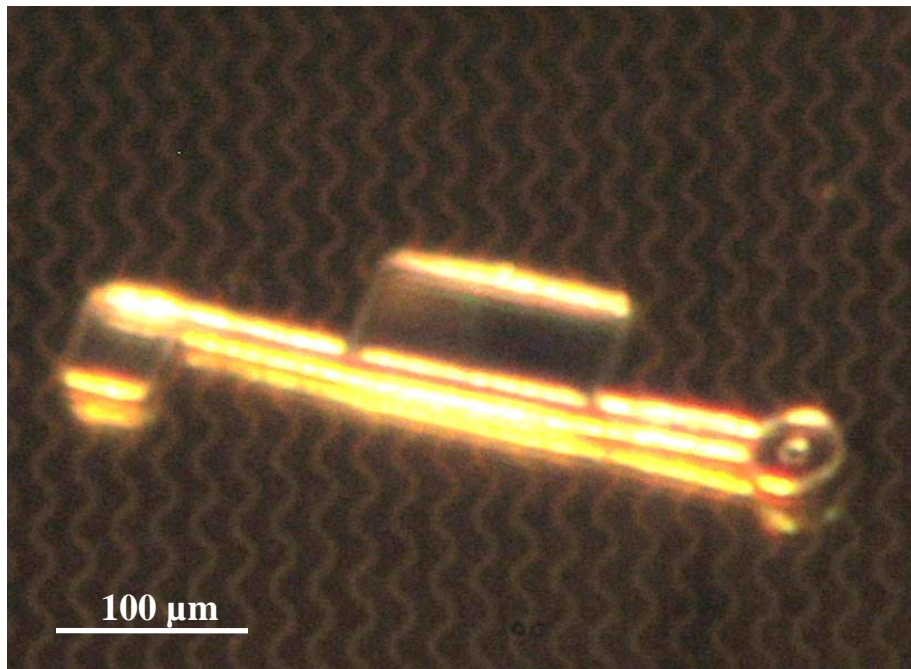


Figure 5.23: Optical image of an SU-8 nanobot on a playing field, demonstrating curvature away from the field due to the compressively stressed aluminum coating.

The initial polymer nanobots were tested, as were polysilicon designs on the playing fields, but reliability was very low. Environmental conditions have a very large effect on the reliability of scratch drive actuators, and neither the initial SU-8 or polysilicon nanobots worked correctly. The very high voltages required to run the nanobots (>150 V) caused significant substrate charging, which resulted in device stiction. In addition, the reliability of the playing fields decreased with the amount of

time they were exposed to the environment due to dust contamination and surface effects due to high relative humidity.

It was discovered accidentally that the nanobot devices would work inverted to their designed operating orientation and at lower voltages. This was unexpected, but it occurs because the stiffness of the actuators has been reduced dramatically, with a very compliant spring holding the main plate suspended above the playing field.

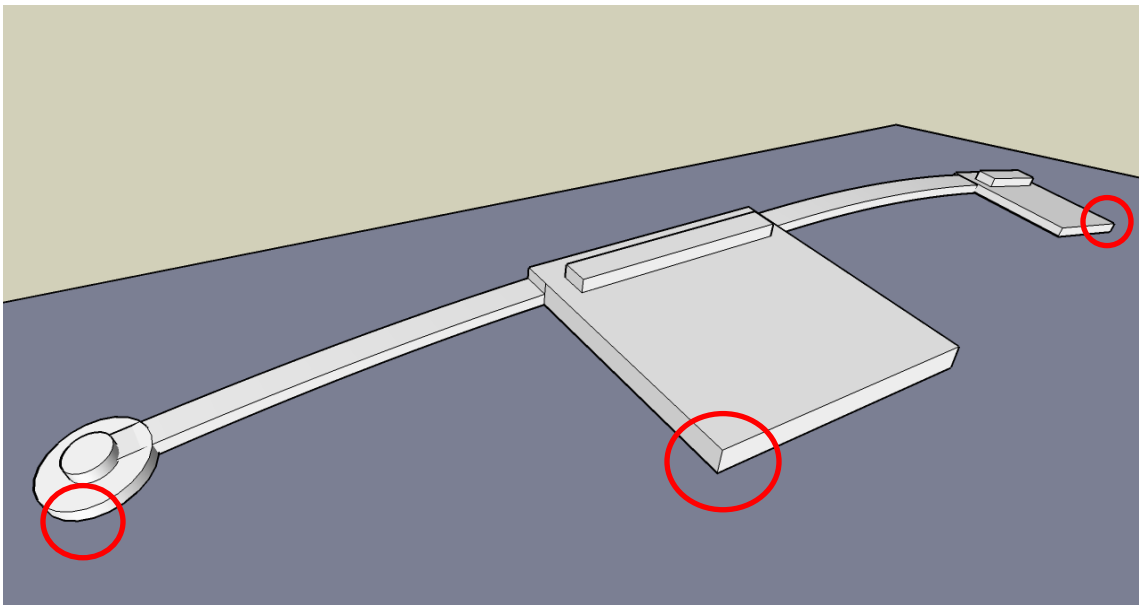


Figure 5.24: Exaggerated schematic of tripod balancing of upside down nanobot design. Areas of contact are circled.

This tri-pod motion has been previously described for thermally activated systems [126] where the actuation mechanism only bent a single arm of a symmetrical design. Our results indicated that an asymmetrically designed structure could move in a preferential motion with a uniform actuation force towards the substrate. Control was extremely difficult for the original scratch drive designs operating in this manner, but motion reliability was much greater. The reliability was experimentally determined to be better because lower voltages caused less charging, and less of the actuator surface was in

direct contact with the substrate during operation. Based on this discovery, a buckled-beam nanobot (Figure 5.25) was created that would make use of this actuation mechanism.

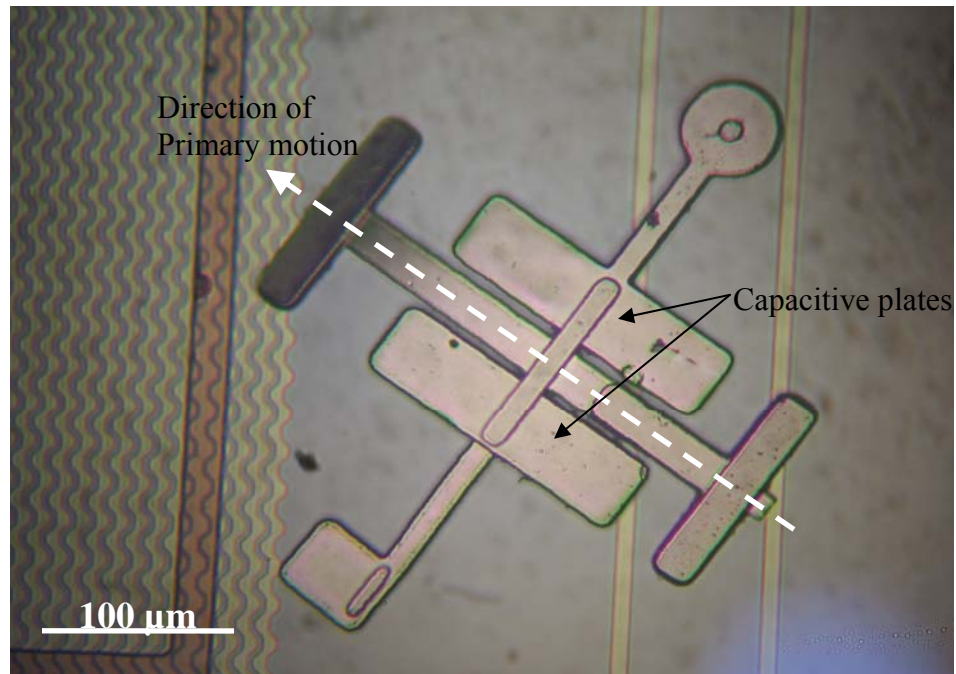


Figure 5.25: Buckled beam nanobot design. This particular structure operates with the SU-8 in contact with the substrate and the top aluminum surface causes negative curvature.

The robot shown above is balanced mainly along its primary axis and is designed to move in the direction shown. The plates on either side of the centre beam increase the capacitance and force of the actuator, while not contributing significantly to the actuator stiffness so that the input voltage can be reduced. The partial tether on the back end prevented reliable linear motion of this particular design, and the device tended to spin, rather than translate smoothly. A 30% duty cycle square wave input resulted in spinning motion, while introducing a DC offset to the pulses caused a more linear motion. Because this project was for a competition rather than academic publication, no quantitative data on the performance of these actuators was collected. However, the

basic project concept and practical lessons learned were taken and combined into a special topics undergraduate course based on this process for nine undergraduate students to compete in future trials. A few of the devices fabricated using this process for the special topics course are shown in Figure 5.26.

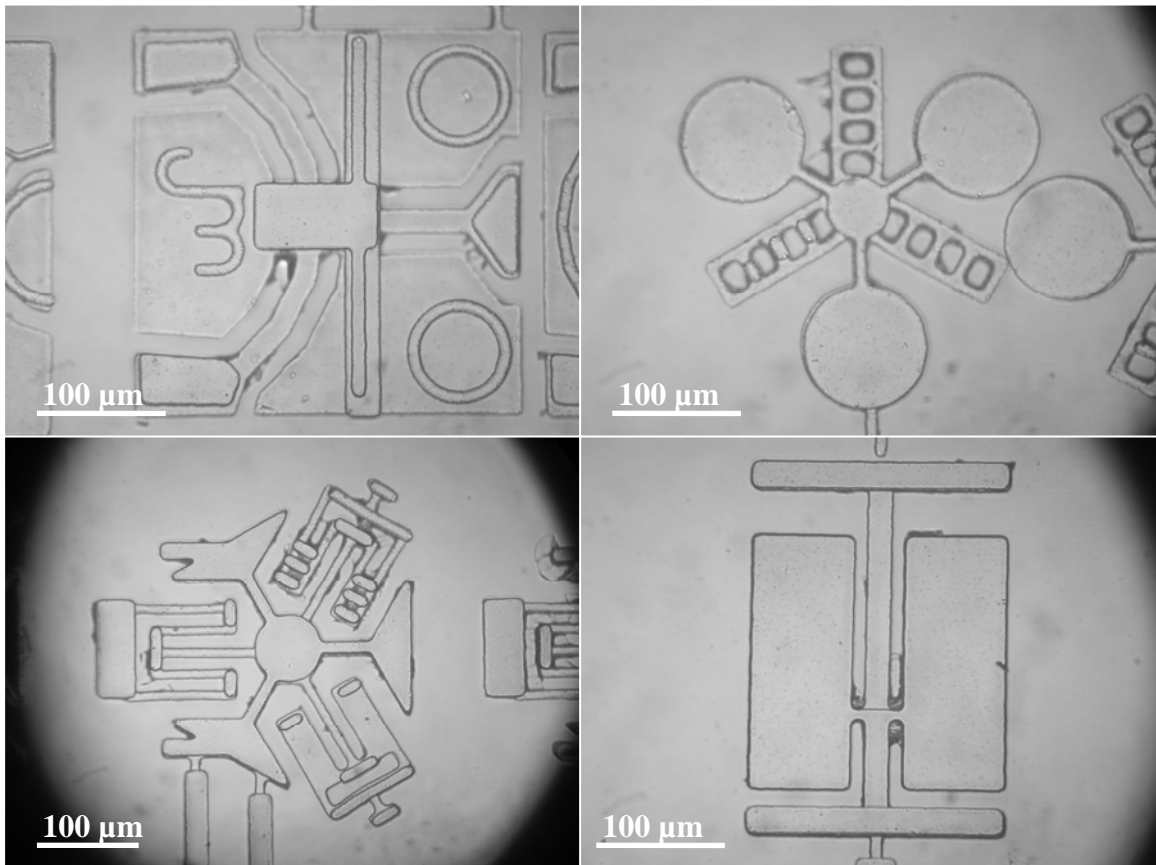


Figure 5.26: Selection of special topics course nanobot designs.

The Robocup competition experience was a great opportunity to push this process to its limits, and fully used all the experience gained in the development of the multi-user polymer MEMS process. Electrostatic actuators were fabricated using a polymer core, representing an opportunity to further reduce the required voltages necessary for electrostatic operation. The development of a successful undergraduate special topics course around this process has also demonstrated the great potential for polymer MEMS

technologies to be used as an educational tool. For rapid prototyping and low cost development, this process confirms its usefulness as a multi-user process.

6 CONTRIBUTIONS

The development of the world's first multi-user polymer MEMS process has yielded a low cost rapid prototyping system. The result of this work has been the publication of three journal articles and four conference papers that are either directly or indirectly related to the process developed for this thesis. A short summary of these academic articles follows; moreover, several other journal publications are in preparation based on some of the conference papers previously published.

1. **D. Sameoto**, S. H. Tsang, M. Parameswaran "Polymer MEMS processing for multi-user applications", *Sensors and Actuators A*, Vol. 134, pp. 457-464, 2007

This article was the first to describe the general concept and processing steps towards creating a multi-user MEMS process. It was submitted to *Sensors and Actuators* within a year of developing the basic steps and accepted a month later. Publication in a specific volume was delayed by nearly a year due to backlog in the journal submission process, leading to a publication date listed as 2007. This work was the first to identify how SU-8 could be used as a structural layer for robust MEMS processing that provided similar capabilities to silicon-on-insulator structures, with respect to layer thicknesses and potential aspect ratios. All processing steps occurred at temperatures below 100 °C, making this entire process thermally compatible with previously processed CMOS or other MEMS, while the developers and solvents used would leave any inorganic materials intact during the final release. This paper was the first to identify that SU-8 curvature could be controlled, but the exact behavior was detailed in later work. In addition, the first dynamic characterization of an SU-8 thermal actuator was performed to

demonstrate the capabilities of a specific common MEMS device. Many compliant structures fabricated and tested in this process were highlighted, including the out-of-plane compliant assembly mechanism [37, 101], focusing on its potential use for micro-optics and thermal isolation platforms.

2. **D. Sameoto**, S. H. Tsang, I. G. Foulds, S. W. Lee, M. Parameswaran “Control of the out of-plane curvature in SU-8 compliant microstructures by exposure dose and baking times”, *Journal of Micromechanics and Microengineering*, Vol. 17, pp. 1093-1098, 2007.

This work was a follow-up to the observations in the earlier publication describing the development of the multi-user polymer MEMS process. Curvature in SU-8 compliant structures had been observed by many researchers in prior publications, but no systematic attempt to characterize or understand this behavior had been made. Attempting to compare direct results between papers was often impossible because of the wide variety of processing conditions, device sizes, and operation. Curvature of SU-8 cantilevers is also a serious issue for papers that use exposure dose control to fabricate compliant structures in a single layer of SU-8, but only some papers describe this issue in any detail [100].

SU-8 cantilevers were fabricated using a variety of baking times and exposure doses to observe their curvature after release. The results revealed that the curvature of SU-8 structures can be controlled, and most devices have an optimal exposure dose for low curvature parts for almost any baking times. This work demonstrated for the first time that curvature and the corresponding internal stress gradients in SU-8 are a parameter than can be optimized and potentially controlled to a great extent for novel applications. This work laid the groundwork for new compliant SU-8 structures designed for self-assembly of out-of-plane microstructures, and the work should be of great

interest to all process designers interested in working with SU-8 and similar crosslinking polymers.

3. **D. Sameoto**, S. W. Lee, M. Parameswaran, “Wirebonding characterization and optimization of thick film SU-8 MEMS structures and actuators”, presented at Transducers 2007, Lyon, France June 2007

This conference paper was the first article to comprehensively investigate the failure modes when wirebonding onto electrodes on top of SU-8 structures. It also examined how the wirebond yield and strength can be improved through process modifications. The results revealed that wirebonder settings had a relatively minor effect on yield and strength, but that the glass transition temperature and the surface energy of the polymer were critical to achieve good bonds. Increasing the glass transition temperature of SU-8 through a hardbaking step allows higher bonder temperatures to be used before SU-8 softens and viscoelastic effects dominate during the bonding step. A surface activation step can dramatically increase the SU-8 surface energy, which will result in much higher metal adhesion and is necessary because the delamination of metal from SU-8 is the primary failure mode of most ball bonds. Our results were improved by the dramatic roughening caused by redeposition of sputtered gold during the reactive ion etch step, but at very high activation times, this effect is detrimental to bond strength. Ultimately, a combination of surface roughening, and a separate surface activation step, may achieve even higher bond strengths on thin SU-8. However, the low Young's modulus of SU-8 will dominate bond behaviour on thicker structures.

4. S. H. Tsang, **D. Sameoto**, I. G. Foulds, R. W. Johnstone, and M. Parameswaran “Automated assembly of hingeless 90 degree out-of-plane microstructures”, *Journal of Micromechanics and Microengineering*, Vol. 17, pp. 1314-1325, 2007.

This journal article was selected as one of the featured papers on the JMM website for its unique contribution to the MEMS field. The out-of-plane compliant

structure was partially developed using the polymer MEMS process and the final design was completed in only three process iterations within a few months. Sample structures fabricated using the polymer MEMS process include the basic thermal isolation platform, fractal antenna cores, and inductors. The basic compliant mechanism was also successfully transferred to a PolyMUMPs run and shown that it can be made to work for a variety of scales and materials. An SU-8 out-of-plane compliant mechanism was successfully assembled and disassembled over 200 times using an automatic system, which demonstrates the robustness of both the mechanical design and the polymer MEMS process.

5. **D. Sameoto**, M. Hamidi, M. Parameswaran “Characterization of work and power efficiency of micromachined polymer thermal actuators”, presented at the Canadian Conference on Computer and Electrical Engineering 2007, Vancouver, BC April 2007

The examination of a variety of very thick, high aspect ratio SU-8 thermal actuators was completed with respect to their output displacements and forces in order to obtain a general measurement of actuator efficiency is obtained. The results revealed a very favorable comparison between SU-8 thermal actuators and their silicon counterparts due to higher thermal expansion coefficients and lower thermal conductivities. The failures of high aspect ratio chevron thermal actuators were revealed and a new actuator style that compensates for the high tensile stress in SU-8 structures was designed and tested. Results reveal that significant improvements can be made to the hybrid thermal actuator, but that linear motion can be achieved without the significant negative deflections observed in the chevron thermal actuators.

6. **D. Sameoto**, A. H. Ma, M. Parameswaran, A. Leung “Assembly and characterization of buckled cantilever platforms for thermal isolation in a polymer

micromachining process”, presented at the Canadian Conference on Computer and Electrical Engineering, Vancouver, BC April 2007

This paper describes a new assembly mechanism for thermal isolation platforms that only requires a single degree of freedom motion that can be delivered by a wirebonder tip. The buckled cantilevers were prototyped in the polymer MEMS process and are used to determine the maximum distance from the substrate they can assemble a platform. Their basic geometry once that deflection is reached was also determined. Platforms can be placed at different lengths on the bucked cantilever to achieve assembly at angles tangent to the beam, resulting in the assembly of multi-axes sensors using a single motion. Different anchor and clip designs were also introduced to improve device stability and ease of assembly. This project took less than two weeks to complete from original concept to fabricated devices, proving that the idea could work. Variations on the basic design have been successfully fabricated in both polyimide and polysilicon [127] since the original publication.

7. **D. Sameoto**, C. Plesa, M. Parameswaran “Integrated testing of polymer MEMS material properties”, to be presented at the Solid State Sensors, Actuators and Microsystems Workshop, Hilton Head Island, SC, June 1-5 2008.

This work describes the integration of a polymer MEMS test die designed originally using the polymer MEMS technology developed in this thesis, combined with a novel chip level actuation mechanism. This system is the first to specifically address challenges in testing polymer MEMS properties, including feature size variations due to thicker layers, observing transparent materials and actuating insulating materials at high frequencies. The work presented at Hilton Head uses a polyimide based sacrificial layer, to make the general system more applicable to testing other polymers, but otherwise uses similar processing techniques. Measuring the resonant frequencies of different SU-8 test

structures excited by a piezoelectric actuator that moves a full chip in-plane allows Young's modulus to be extracted. Out-of-plane structures described previously [37], are combined with cantilevers to measure curvature in the same manner as [82]. In addition, sidewall angle can be measured using these structures, and automated vision assistance scripts automatically compensate for the fabricated device geometry when extracting Young's modulus from resonant frequencies. Wide, low aspect ratio structures demonstrate the best reliability during fabrication and testing, and this work demonstrates that resonating low aspect ratio structures in-plane can produce superior data, and repeatability with this test system. Future work will include improved static test structures and improved piezoelectric actuator performance to collect data on a wider range of material properties.

CONCLUSIONS

The objective of this work was to develop a multi-user polymer micromachining process that could duplicate many of the types of devices used in silicon surface micromachining processes. The technology developed for this thesis has proved capable of serving that purpose, with compliant structures, electrothermal, and electrostatic actuators all being designed, fabricated, and tested using the polymer MEMS process. While the use of silicon and metals for structural layers in MEMS processes has been well established, the use of polymers in MEMS has been somewhat delayed by the general problems in choosing acceptable sacrificial materials and developing processing steps for maximum reliability. Creating a multi-user polymer MEMS process required that many new fabrication issues had to be characterized and explained. Significant challenges involved in developing a reliable polymer MEMS process have been overcome, including choosing appropriate sacrificial polymers, aligning two polymers with matching indices of refraction and reducing stiction in a wet release step. Many researchers have successfully used the rapid prototyping of polymer MEMS structures at Simon Fraser University to complete a variety of projects. Using polymer structural and sacrificial layers allows this process to be one of the lowest temperature MEMS processes available, giving this technology the potential for direct fabrication on top of electronics wafers for fully integrated MEMS and integrated circuits. The use of all spin-coated layers makes the basic process easy to modify if different layer thicknesses are required, allowing great flexibility for fabricating a wide variety of structures. By

keeping processing steps simple, fabrication of polymer MEMS prototypes can be completed in less than 24 hours with minimal equipment time. Using polystyrene as a sacrificial layer reduces costs significantly, and the methods for patterning this polymer can be modified to be compatible with many organic sacrificial layers. Creating a polymer MEMS process that consistently gives high yields with reliable fabrication steps provided a foundation to make several important discoveries making the SU-8 processing more reliable and useful.

Through the development of the polymer MEMS process, two important processing issues have been examined and solved. The first is the behaviour of compliant structures with processing conditions, and the second is determining a reliable method for wirebonding onto SU-8 structures. The work presented here was the first to thoroughly investigate the curvature of SU-8 structures and determine that this curvature could be varied and minimized for nearly any processing conditions. The very large sample size, more than 20 processed wafers, of SU-8 structures fabricated in a standardized process allowed the direct comparison of curvature for identical structures fabricated with different exposure doses and baking times. When SU-8 compliant parts exhibit negative curvature, it negatively affects performance of all types of structures due to contract with the substrate in undesired locations. Positive curvature of SU-8 structures is only a significant problem when structures are very large, due to the maximum positive curvature condition limited by the thermal gradients. The thesis work demonstrates that longer exposures and longer post exposure bakes are required compared with the manufacturer's recommended values in order to fabricate mechanically stable, low curvature SU-8 parts. The prediction of curvature cannot be

presently done with accuracy due to a lack of empirical data on the exact crosslinking reaction, but in the future, modelling and predicting curvature and stress gradient within SU-8 for any thermal history should be possible. Wirebonding onto SU-8 reliably is challenging, but the experiments performed using this process demonstrate that it can be greatly improved with minor processing steps. The work presented in this thesis shows that the major failure mode of wirebonds to SU-8 is metal delamination, but that this problem can be solved with an appropriate surface activation step. Surprisingly, the effect of the gold-coated substrate actually improves metal adhesion to SU-8 through the micro-roughening effect. Future optimization may improve bond yield further, but should be left to commercial wirebonding equipment and tests to increase accuracy and yield. Ultimately, the difficulties of bonding onto thin layers on top of soft substrates will require stiff electroplated bond pads, as in most multi-chip modules; however the work presented here demonstrates that SU-8 could eventually be a reliable material for use with existing packaging technologies.

The negative tone photoresist SU-8 has been used extensively for MEMS applications over the last 10 years, but it has never been used as ambitiously as this project has allowed. Most SU-8 MEMS structures described in the literature have been fabricated in novel processes, which had made comparisons of results between different papers very difficult. The lack of standardized processing steps in the literature has limited the ability of researchers to directly compare results or truly understand the behaviour of this commonly used polymer. Most academic papers have focused on the fabrication of individual devices, and only characterized these structures from a narrow perspective. This work was not designed to fabricate any one specific device, but to

examine and solve the basic issues in creating reliable MEMS processes based on polymers. The creation of a reliable MEMS process allowed many thousands of individual SU-8 compliant structures to be fabricated in a short period of time, in order to examine their performance for a wide variety of processing conditions. It is quite possible that more compliant SU-8 structures have been fabricated at Simon Fraser University over the last three years than at any other institution worldwide, providing unprecedented insights into the behaviour and performance of SU-8 as a mechanical material. Silicon will continue to be the dominant MEMS material in the future, but polymer MEMS can serve a valuable purpose for low cost, rapid prototyping.

APPENDICES

A. A solvent free lift-off method to pattern metal on SU-8

The patterning of metal on SU-8 in this process was difficult for two reasons; polystyrene cannot be selectively removed independent of the SU-8 development, and uncrosslinked SU-8 can crosslink or reflow during metal deposition. The exposure of SU-8 during the sputtering process is a more serious issue, because the crosslinking reaction can be initiated during metal deposition, regardless of sacrificial material. Early experiments revealed that several microns of Shipley 1827 photoresist would effectively block UV during a typical metal deposition to prevent the photoinitiation of SU-8. Shipley photoresist could be removed independently from uncrosslinked SU-8 by development in 25% TMAH, which, as a base, does not initiate SU-8 crosslinking. The basic processing steps for this lift-off method are shown below.

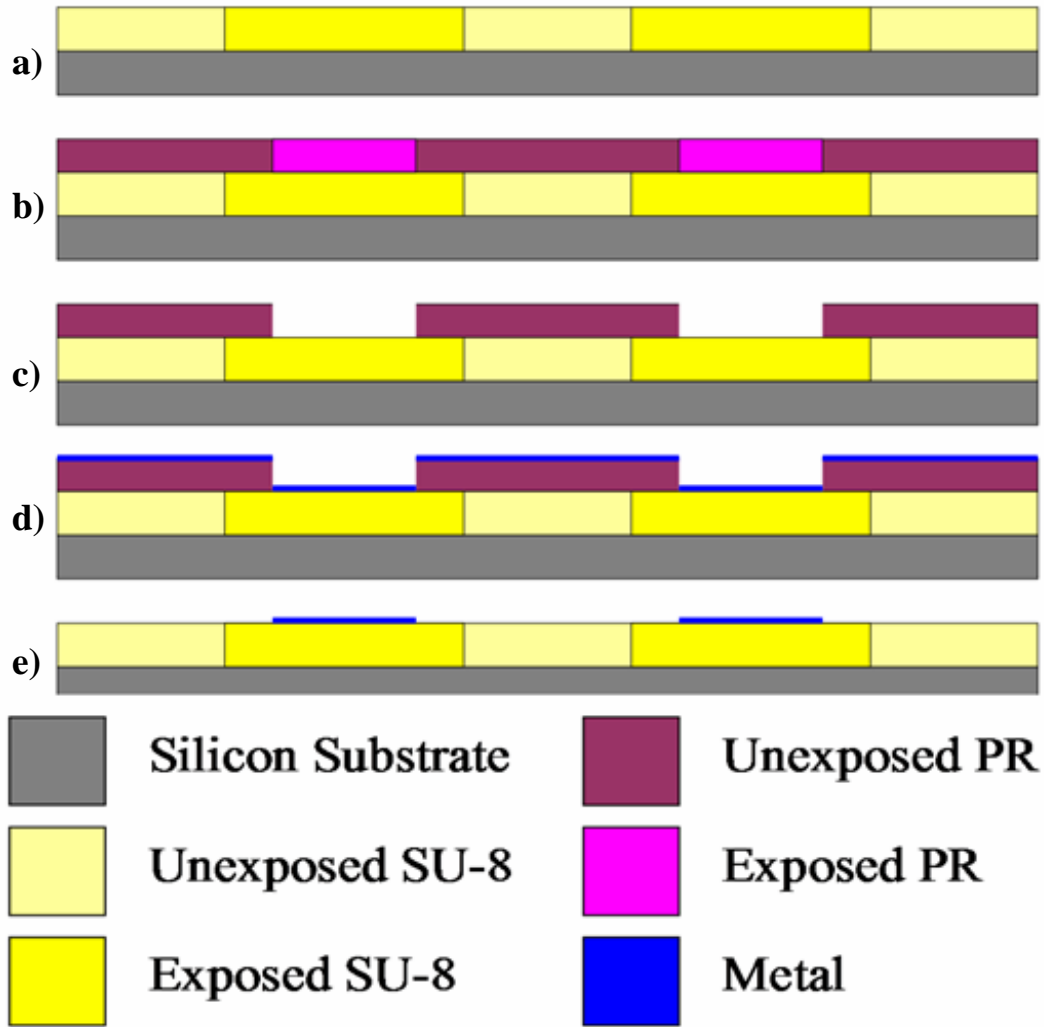


Figure A.1: Basic process steps for using a positive tone photoresist on patterned (but undeveloped) SU-8 structures. a) SU-8 is exposed and baked, but not developed; b)-c) a highly absorbing photoresist like Shipley 1827 is deposited on top of the SU-8 and exposed and developed; d) metal is deposited on photoresist layer; e) Photoresist is removed with TMAH, lifting off metal.

This basic procedure was successful at both preventing SU-8 from crosslinking during metal deposition, and lifting off metal from SU-8, but the photoresist solvent (PGMEA) would partially dissolve uncrosslinked SU-8 during spin coating, resulting in significant material intermixing. In order to develop a method of patterning metal on crosslinked SU-8 without developing the uncrosslinked material or having problems with

solvent intermixing, a solvent-free method of applying photoresist was required. Basic process steps are shown below:

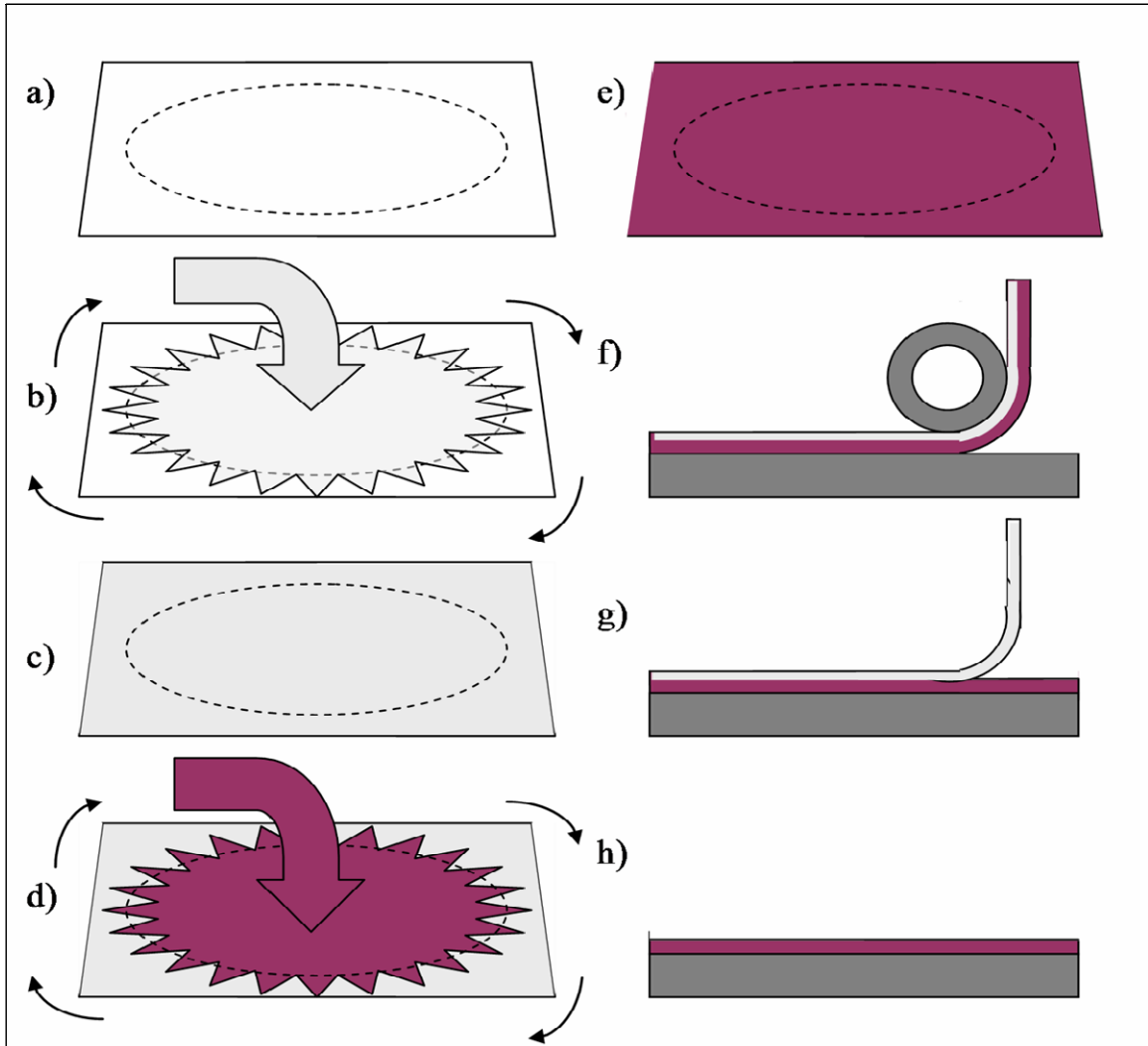


Figure A.2: Basic process steps to convert a liquid photoresist into a dry, laminatable layer.

a) A polytetrafluoroethylene (PFTE) sheet is cut in a 10x10 cm square and placed on a spin coater

b-c) A thin release layer ($\sim 3\text{-}5\ \mu\text{m}$) of polystyrene is spun coat onto the PFTE and left to dry naturally ($\sim 1\ \text{min}$), which results in a stressed, porous layer.

d-e) Shipley 1827 photoresist is spun onto the polystyrene release layer and baked at low temperature (~ 50 °C), which drives out solvent, but keeps the glass transition temperature (T_g) of the photoresist low and prevents relaxation of the polystyrene.

f) The PFTE layer is laminated onto the MEMS wafer at temperatures above the T_g of the dry photoresist.

g) The photoresist/polystyrene polystyrene is removed from the PFTE once the wafer is cooled. Adhesive tape is placed over the whole wafer and the polystyrene is removed from the photoresist layer at approximately 50 °C.

h) Photoresist is baked and then exposed.

Using this method, liquid photoresist can be transferred as a dry layer, and different thicknesses, compositions or substrates may be used in this method. The PFTE sheets have extremely low surface energy, allowing all polystyrene films to be removed as a single layer. Polystyrene will wet the PFTE only during the initial spin-coating, but, because the toluene dries completely before the spinning stops, a polystyrene film can be spun on in a stable configuration. In contrast, photoresists, and SU-8 will all dewet from the PFTE prior to drying, leaving beads of material on the PFTE if an underlying polystyrene layer is not used. By creating the underlying polystyrene sheet, many different polymers may be spun onto the PFTE for later removal.

The lamination of the dry photoresist layer onto substrates has been the biggest challenge due to the quality of the laminating equipment used. All early efforts used a GBC HeatSeal 100 business card laminator, which can laminate 10 cm wide substrates. A thermocouple monitored the internal temperature of the laminator, and when the

desired temperature was reached, the laminator was switched to cool operating mode and the wafer and photoresist were run through it. The laminator cools very slowly, so this method is a crude way of laminating at a constant desired temperature without requiring commercial quality equipment. A carrier pouch was made with acetate and tape and the whole setup was fed through as shown in Figure A.3:

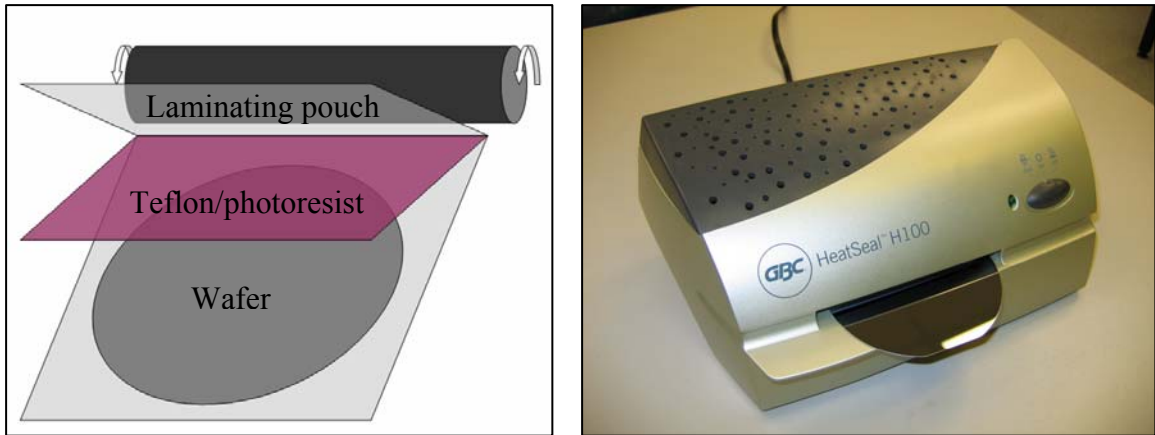


Figure A.3: Schematic of laminating pouch and image of HeatSeal laminator with a 4" wafer for scale. Laminating pouch is made of acetate or Mylar.

The major failure mode using this technique is air bubbles being trapped between the photoresist and the SU-8. The Teflon sheets used were too thick to properly conform to the SU-8 surface and the very thin photoresist did not have time to reflow properly for the temperatures and pressures and lamination speeds used. Because not all these parameters could be controlled by the operator, further work remains using better quality laminators, thicker photoresist layers, and thinner PFTE sheets. Despite some of these problems, several successful demonstrations of the basic concept were completed, and an example of one structure is shown in Figure A.4:

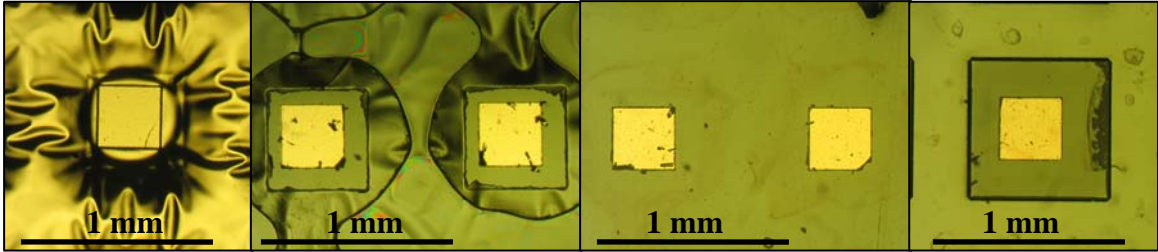


Figure A.4: Sequence of metal deposition, lift-off, encapsulation and development of embedded gold electrode in SU-8.

In Figure A.4, from left to right: Cr/Au sputter deposited on a photoresist layer on top of exposed but undeveloped SU-8 showing significant reflow due to elevated temperatures. Gold electrodes on crosslinked SU-8 after photoresist removal (reflowed uncrosslinked SU-8 clearly visible). Second SU-8 layer spun coat on electrodes for planarization. Development of uncrosslinked SU-8, leaving a Cr/Au square inside an SU-8 post. The deposition temperature was very high in this instance, but, because the SU-8 can still be developed at the end, this method proves that the photoresist blocks enough UV light to be an effective protection for future metal depositions. The deposition rate should be altered in the future to reduce the maximum temperature and will prevent as much reflow in the future. In this manner, multiple levels of embedded electrodes may be fabricated within polymer structures for sensing and actuator applications.

This work is to the author's knowledge, the first to convert positive tone photoresists, like Shipely 1827, into dry laminatable layers for solvent free processing with other polymers. Future work on this topic will deal with optimizing layer thicknesses and lamination temperatures for better coverage on polymer surfaces, exposure and baking experiments to determine the minimum baking times and temperatures for acceptable pattern transfer with laminated Shipley photoresist, and metal

deposition experiments to determine an optimal deposition rate that minimizes reflow of uncrosslinked SU-8, and still demonstrates acceptable adhesion.

B. Process recipe for three level SU-8 nanobots

1. Start with a wafer coated with 50 nm Cr/50 nm Au.
2. Spin coat thin PS on wafer at 3000 rpm/30 sec (3000/30).
3. Bake one minute on a hot plate at 150 °C, no ramps up or down (this densifies the PS and makes it slightly more resistant to the SU-8 solvents. (It may make the surface look wavier but it is worth it). Scratch off a small patch (~1x1 mm) of PS at the bottom of the wafer to check thickness in the profilometer. Hopefully this will be about 2-2.5 μm . Record the actual data. If the layer is really thin (<1 μm), strip in toluene and spin at lower speeds.
4. Spin coat thick PR at 1500/30.
5. 15 minute bake at 100 °C.
6. Anchor expose 90 sec.
7. Develop 3 minutes in MF-319 (PR should be approximately 6.2 μm thick).
8. RIE 30 minutes at 40 sccm O₂, 5 sccm CF₄, 60 mtorr setting (probably 100 mtorr actual) at 150W. Check to see that centre is clear because the centre etches slower.
9. Check layer thickness with profilometer (should be greater than 4 μm)
10. Blanket expose wafer for 90 seconds and develop 2 min in MF-319.
11. Check layer thickness again with profilometer to see if is approximately the same as original PS.
12. Gold etch for 30 seconds, rinse, dry.

13. Bake for 5 minutes at 120C.
14. Spin coat SU-8 2005 for 5 sec @ 1000 rpm, then quickly ramp up to 4000 rpm and spin for 30 sec.
15. Bake on a hotplate 20-95 °C at 300 °C/hr hold 10 min then natural cool.
16. Align and expose POLY0 layer for 40 seconds.
17. PEB 20-95 °C at 300 °C/hr, hold 20 minutes and then natural cool
18. Spin on SU-8 2005 for 5 sec @ 1000 rpm, then quickly ramp up to 4000 rpm and spin for 30 sec.
19. Bake 20-95 °C at 300 °C/hr, hold 10 minutes then natural cool.
20. Expose POLY1 for 40 sec.
21. PEB 20-95 °C at 300 °C/hr, hold 20 minutes then natural cool.
22. Spin on SU-8 2005 5 sec at 1000 rpm then quick ramp to 4000/30.
23. Bake 20-95 °C at 300 °C/hr, hold 20 minutes then natural cool.
24. Expose POLY2 for 40 seconds.
25. PEB 20-95 °C at 300 °C/hr, hold 30 minutes then natural cool.
26. Nick the wafer on the back side so that you can break it into quarters (just in case development doesn't go well).
27. Develop each quarter wafer for approximately 15 sec in SU-8 developer with ultrasonics (or until you see the PS start to peel/float off gold). Carefully remove the quarter wafer and place in toluene for very gentle hand agitation (slight rocking back and forth) for 1.5-2 minutes.
28. Rinse gently in toluene for 30 sec- 1 minute with the glass beakers. Pour fresh toluene in the bucket of other toluene for development of other quarter wafers.

29. IPA rinse for 1 minute, N₂ dry upside down. Inspect the quarter wafer for alignment/stiction/broken devices.
30. Wait one day then sputter metal to induce curvature. Aluminum will produce negative curvature, while chrome provides positive curvature. Use the pop-up structures to determine the exact curvature and determine if it meets expectations.

REFERENCE LIST

- [1] http://www.memscap.com/en_mumps.html, "Polymumps," MEMSCAP, 2007.
- [2] http://www.memx.com/NSF_Summit_VII.htm, "SUMMiT Process," MEMX, 2003.
- [3] J. J. Allen, *Micro Electro Mechanical System Design*. Boca Raton, FL: CRC Press, 2005.
- [4] H. Guckel, D. W. Burns, T. H. A. C., D. W. DeRoo, and C. R. Rutigliano, "Mechanical properties of fine grained polysilicon - the repeatability issue," *Solid State Sensors, Actuators and Microsystems Workshop (Hilton Head, SC, June 1988)*, pp. 96-99, 1988.
- [5] W. A. Brantley, "Calculated elastic constants for stress problems associated with semiconductor devices," *Journal of Applied Physics*, vol. 44, pp. 534-535, 1973.
- [6] K. Sato, M. Shikida, T. Yoshioka, T. Ando, and T. Kawabata, "Micro tensile-test of silicon film having different crystallographic orientations," *Proceedings of TRANSDUCERS 1997*, vol. 1, pp. 595-598, 1997.
- [7] W. N. Sharpe, B. Yuan, R. Vaidyanathan, and R. L. Edwards, "Measurements of Young's modulus, Poisson's ratio and tensile strength of polysilicon," presented at Tenth Annual International Workshop on Micro Electro Mechanical Systems, Nagoya, Japan, 1997.
- [8] J. J. Wortman and R. A. Evans, "Young's modulus, shear modulus and poisson's ration in silicon and germanium," *Journal of Applied Physics*, vol. 36, pp. 153-156, 1965.
- [9] K. E. Petersen, "Silicon as a Mechanical Material," *Proceedings of the IEEE*, vol. 70, pp. 420-457, 1982.
- [10] D. Yan, A. Kharjepour, and R. Mansour, "Design and modeling of a MEMS bidirectional vertical thermal actuator," *J. Micromech. Microeng.*, vol. 14, pp. 841-850, 2004.
- [11] R. Hickey, D. Sameoto, T. Hubbard, and M. Kujath, "Time and Frequency response of two-arm micromachined thermal actuators," *J. Micromech. Microeng.*, vol. 13, pp. 40-46, 2003.
- [12] C.-J. Kim, A. P. Pisano, and R. S. Muller, "Silicon-Processed Overhanging Microgripper," *Journal of Microelectromechanical Systems*, vol. 1, pp. 31-36, 1992.

- [13] J. Chae, H. Kulah, and K. Najafi, "A monolithic three-axis micro-g micromachined silicon capacitive accelerometer," *Journal of Microelectromechanical Systems*, vol. 14, pp. 235-242, 2005.
- [14] R. Zengerle, S. Kluge, M. Richter, and A. Richter, "A bidirectional silicon micropump," presented at MEMS '95, Amsterdam, The Netherlands, 1995.
- [15] S. H. Tsang, D. Sameoto, and M. Parameswaran, "A free-space tunable beam expander designed for automated assembly," presented at the Canadian Conference on Electrical and Computer Engineering, Vancouver, Canada, 2007.
- [16] R. Kakkad, J. Smith, W. S. Lau, S. J. Fonash, and R. Kerns, "Crystallized Si films by low-temperature rapid thermal annealing of amorphous silicon," *Journal of Applied Physics*, vol. 65, pp. 2069-2072, 1989.
- [17] J. M. Bustillo, G. K. Fedder, C. T.-C. Nguyen, and R. T. Howe, "Process technology for the modular integration of CMOS and polysilicon microstructures," *Microsystem Technologies*, vol. 1, pp. 30-41, 1994.
- [18] S. M. Spearing, "Materials issues in microelectromechanical systems (MEMS)," *Acta Mater*, vol. 48, pp. 179-196, 2000.
- [19] H. Fettig, J. Wylde, T. Hubbard, and M. Kujath, "Simulation, dynamic testing and design of micromachined flexible joints," *J. Micromech. Microeng.*, vol. 11, pp. 209-216, 2001.
- [20] http://www.cmc.ca/about/fab_schedule.html, "Canadian Microelectronics Corporation list of fabrication technologies," 2007.
- [21] R. W. Johnstone, D. Sameoto, and M. Parameswaran, "Non-uniform residual stresses for parallel assembly of out-of-plane surface-micromachined structures," *Journal of Micromechanics and Microengineering*, vol. 16, pp. N17-N22, 2006.
- [22] D. Sameoto, M. Kujath, and T. Hubbard, "Operation of electrothermal and electrostatic MUMPs microactuators underwater," *J. Micromech. Microeng.*, vol. 14, pp. 1359-1366, 2004.
- [23] N. Ellerington, T. Hubbard, and M. Kujath, "Electro-kinetic movement of micro-objects in fluids using microelectromechanical system electrode arrays," *Journal of Vacuum Science and Technology A: Vacuum, Surfaces, and Films*, vol. 22, pp. 831-836, 2004.
- [24] E. H. Klaassen, K. E. Petersen, J. M. Noworolski, J. Logan, N. I. Maluf, J. Brown, C. Storment, W. McCully, and G. T. A. Kovacs, "Silicon fusion bonding and deep reactive ion etching a new technology for microstructures," presented at TRANSDUCERS '95, Stockholm, Sweden, 1995.
- [25] A. Neukermans and R. Ramaswami, "MEMS technology for optical networking applications," *Communications Magazine, IEEE*, vol. 39, pp. 62-69, 2001.
- [26] W. C. Tang, T.-C. H. Nguyen, and R. T. Howe, "Electrostatic-comb drive of lateral polysilicon resonators," presented at Micro Electro Mechanical Systems, 1989, Proceedings, 'An Investigation of Micro Structures, Sensors, Actuators, Machines and Robots'. IEEE, Salt Lake City, UT, 1989.

- [27] http://www.memscap.com/en_mumps.html, "SOIMUMPs," MEMSCAP, 2007.
- [28] <http://www.micalyne.com/capabilities/products/micragem.htm>, "MicraGEM Process Description," Micalyne, 2007.
- [29] D. J. Bell, T. J. Lu, N. A. Fleck, and S. M. Spearing, "MEMS actuators and sensors: observations on their performance and selection for purpose," *J. Micromech. Microeng.*, vol. 15, pp. S153-S164, 2005.
- [30] http://www.microchem.com/products/pdf/SU-82000DataSheet2000_5thru2015Ver4.pdf, "SU-8 2000.5-2015 data sheet," MicroChem Corp, 2007.
- [31] <http://www.microchem.com>, "MicroChem Homepage," MicroChem Corporation, 2007.
- [32] R. W. Johnstone, S.-H. Tsang, I. G. Folds, S.-W. Lee, D. Sameoto, and M. Parameswaran, "Fabrication of an inexpensive cleanroom module for microsystem testing," *J. Micromech. Microeng.*, vol. 17, pp. N47-N51, 2007.
- [33] www.torreypinesscientific.com, "Torrey Pines Scientific Homepage," 2007.
- [34] www.fineline-imaging.com, "Fineline Imaging Company Website," 2007.
- [35] J. Ge and J. K. Kivilahti, "Effects of surface treatments on the adhesion of Cu and Cr/Cu metallizations to a multifunctional photoresist," *Journal of Applied Physics*, vol. 92, pp. 3007-3015, 2002.
- [36] G. G. Harman, *Wirebonding in Microelectronics, Materials, Processes, Reliability and Yield*. Second ed. New York: McGraw Hill, 1997.
- [37] S.-H. Tsang, D. Sameoto, I. G. Foulds, R. W. Johnstone, and M. Parameswaran, "Automated assembly of hingeless 90° out-of-plane microstructures," *J. Micromech. Microeng.*, vol. 17, pp. 1314-1325, 2007.
- [38] D. Sameoto, A. H. Ma, M. Parameswaran, and A. M. Leung, "Assembly and characterization of buckled cantilever platforms for thermal isolation in a polymer micromachining process," presented at the Canadian Conference on Electrical and Computer Engineering, Vancouver, Canada, 2007.
- [39] http://www.ni.com/pdf/products/us/vbai_datasheet.pdf, "NI Vision Builder for Automated Inspection data sheet," 2007.
- [40] <http://www.microchem.com/products/pdf/SU-82000DataSheet2025thru2075Ver4.pdf>, "SU-8 2025-2075 data sheet," MicroChem Corp, 2007.
- [41] R. Yang and W. Wang, "A numerical and experimental study on gap compensation and wavelength selection in UV-lithography of ultra-high aspect ratio SU-8 microstructures," *Sensors and Actuators B*, vol. 110, pp. 279-288, 2005.
- [42] H. Lorenz, M. Despont, N. Fahrni, N. LaBianca, and P. Renaud, "SU-8: a low-cost negative resist for MEMS," *J. Micromech. Microeng.*, vol. 7, pp. 121-124, 1997.

- [43] J. R. Thorpe, D. P. Steenson, and R. E. Miles, "High frequency transmission line using micromachined polymer dielectric," *Electronics Letters*, vol. 34, pp. 1237-1238, 1998.
- [44] R. Feng and R. J. Farris, "Influence of processing conditions on the thermal and mechanical properties of SU8 negative photoresist coatings," *Journal of Micromechanics and Microengineering*, vol. 13, pp. 80-88, 2003.
- [45] H. Yu, O. Balogun, B. Li, T. W. Murray, and X. Zhang, "Building embedded microchannels using single layered SU-8, and determining Young's modulus using a laser acoustic technique," *J. Micromech. Microeng.*, vol. 14, pp. 1576-1584, 2004.
- [46] H. Lorenz, M. Laudon, and P. Renaud, "Mechanical characterization of a new high-aspect ratio near UV photoresist," *Microelectronic Engineering*, vol. 41-42, pp. 371-374, 1998.
- [47] Y. J. Chuang, F. G. Tseng, and W.-K. Kim, "Reduction of diffraction effect of UV exposure on SU-8 negative thick photoresist by air gap elimination," presented at HARMST 2001, Baden Baden, Germany, 2001.
- [48] B. Bilenberg, T. Nielsen, B. Clausen, and A. Kristensen, "PMMA to SU-8 bonding for polymer based lab-on-a-chip systems with integrated optics," *J. Micromech. Microeng.*, vol. 14, pp. 814-818, 2004.
- [49] S. Arscott, F. Garet, P. Mounaix, L. Duvillaret, J.-L. Coutaz, and D. Lippens, "Terahertz time-domain spectroscopy of films fabrication from SU-8," *Electronics Letters*, vol. 35, pp. 243-244, 1999.
- [50] S. Jiguet, A. Bertsch, H. Hofmann, and P. Renaud, "SU8-Silver Photosensitive Nanocomposite," *Advanced Engineering Materials*, vol. 6, pp. 719-724, 2004.
- [51] S. Jiguet, A. Bertsch, M. Judelewicz, H. Hofmann, and P. Renaud, "SU-8 nanocomposite photoresist with low stress properties for microfabrication applications," *Microelectronic Engineering*, vol. 83, pp. 1966-1970, 2006.
- [52] E. W. Becker, W. Ehrfield, P. Haggmann, A. Maner, and D. Münchmeyer, "Fabrication of microstructures with high aspect ratios and great structural heights by synchrotron radiation lithography, galvanofarming, and plastic moulding (LIGA process)," *Microelectronic Engineering*, vol. 4, pp. 35 - 5, 1986.
- [53] L. Jian, Y. M. Desta, J. Goettert, M. Bednarzik, B. Loechel, J. Yoonyoung, G. Aigeldinger, V. Singh, G. Ahrens, G. Gruetzner, R. Ruhmann, and R. Degen, "SU-8 based deep x-ray lithography/LIGA," *Proc. SPIE*, vol. 4979, pp. 394-401, 2003.
- [54] L. J. Guerin, M. Bossel, M. Demierre, S. Calmes, and P. Renaud, "Simple and low cost fabrication of embedded micro-channels by using a new thick-film photoplastic," presented at Solid State Sensors and Actuators, 1997. TRANSDUCERS '97 Chicago., 1997 International Conference on, 1997.

- [55] B.-H. Jo, L. M. VanLerberghe, K. M. Motsegood, and D. J. Beebe, "Three-dimensional micro-channel fabrication in polydimethylsiloxane (PDMS) elastomer," *Journal of Microelectromechanical Systems*, vol. 9, pp. 76-81, 2000.
- [56] V. Seidemann, S. Butefisch, and S. Buttgenbach, "Fabrication and investigation of in-plane compliant SU8 structures for MEMS and their application to micro valves and micro grippers," *Sensors and Actuators A*, vol. 97-98, pp. 457-461, 2002.
- [57] V. Seidemann, J. Rabe, M. Feldmann, and S. Buttgenbach, "SU8-micromechanical structures with in situ fabricated movable parts," *Microsystem Technologies*, vol. 8, pp. 348-350, 2002.
- [58] S. Butefisch, V. Seidemann, and S. Buttgenbach, "A new micro-pneumatic actuator for micromechanical systems," presented at TRANSDUCERS '01 EUROSENSORS XV, Munich, Germany, 2001.
- [59] I. Roch, P. Bidaud, D. Collard, and L. Buchaillot, "Fabrication and characterization of an SU-8 gripper actuated by a shape memory alloy thin film," *Journal of Micromechanics and Microengineering*, vol. 13, pp. 330-336, 2003.
- [60] B. Kim, D. Collard, M. Lagouge, F. Conseil, B. Legrand, and L. Buchaillot, "Thermally actuated probe arrays for manipulation and characterization of individual bio-cell," presented at TRANSDUCERS, Solid-State Sensors, Actuators and Microsystems, 12th International Conference on, Boston, USA, 2003.
- [61] N.-T. Nguyen, S.-S. Ho, and C. L.-N. Low, "A polymeric microgripper with integrated thermal actuators," *Journal of Micromechanics and Microengineering*, vol. 14, pp. 969-974, 2004.
- [62] N. Chronis and L. P. Lee, "Electrothermally Activated SU-8 Microgripper for Single Cell Manipulation," *Journal of Microelectromechanical Systems*, vol. 14, pp. 857 - 863, 2005.
- [63] A. Johansson, M. Calleja, P. A. Rasmussen, and A. Boisen, "SU-8 cantilever sensor system with integrated readout," *Sensors and Actuators A*, vol. 123-124, pp. 111-115, 2005.
- [64] J. El-Ali, I. R. Perch-Nielsen, C. R. Poulsen, D. D. Bang, P. Telleman, and A. Wolff, "Simulation and experimental validation of a SU-8 based PCR thermocycler chip with integrated heaters and temperature sensor," *Sensors and Actuators A*, vol. 110, pp. 3-10, 2003.
- [65] S. J. Jeong and W. Wang, "Microaccelerometers using cured SU-8 as structural material," presented at MEMS/MOEMS Components and Their Applications, San Jose, CA, USA, 2004.
- [66] W. Dai, K. Lian, and W. Wang, "A quantitative study on the adhesion property of cured SU-8 on various metallic surfaces," *Microsystem Technologies*, vol. 11, pp. 526-534, 2005.

- [67] M. Calleja, J. Tamayo, A. Johansson, P. Rasmussen, L. Lechuga, and A. Boisen, "Polymeric Cantilever arrays for biosensing applications," *Sensor Letters*, vol. 1, pp. 1-5, 2003.
- [68] P. B. Chu, J. T. Chen, R. Yeh, G. Lin, J. C. P. Huang, B. A. Warneke, and S. J. Pister, "Controlled pulse-etching with xenon difluoride," presented at Solid State Sensors and Actuators, 1997. TRANSDUCERS '97 Chicago., 1997 International Conference on, 1997.
- [69] A. H. Ma, S. H. Tsang, M. Parameswaran, and A. M. Leung, "Spin-on glass as a sacrificial layer for patterned metalization of compliant SU-8 microstructures," presented at CCECE 2007, Vancouver, BC, pp. 288-291.
- [70] H. C. Song, M. C. Oh, S. W. Ahn, W. H. Steier, H. R. Fetterman, and C. Zhang, "Flexible low-voltage electro-optic polymer modulators," *Applied Physics Letters*, vol. 82, pp. 4432-4434, 2003.
- [71] M. Nordstrom, A. Johansson, E. S. Nogueron, B. Clausen, M. Calleia, and A. Boisen, "Investigation of the bond strength between the photo-sensitive polymer SU-8 and gold," *Microelectronic Engineering*, vol. 79-79, pp. 152-157, 2005.
- [72] I.-h. Song and P. K. Ajmera, "Use of a photoresist sacrificial layer with SU-8 electroplating mould in MEMS fabrication," *J. Micromech. Microeng.*, vol. 13, pp. 816-821, 2003.
- [73] C. Chung and M. Allen, "Uncrosslinked SU-8 as a Sacrificial Material," *J. Micromech. Microeng.*, vol. 15, pp. N1-N5, 2005.
- [74] C. Fu, C. Hung, and H. Huang, "A novel and simple fabrication method of embedded SU-8 micro channels by direct UV lithography," presented at International MEMS Conference 2006, Singapore, 2006.
- [75] M. Gaudet, J.-C. Camart, L. Buchaillet, and S. Arscott, "Variation of absorption coefficient and determination of critical dose of SU-8 at 365 nm," *Applied Physics Letters*, vol. 88, pp. 024107, 2006.
- [76] C. Luo, A. Govindaraju, J. Garra, T. Schneider, R. White, J. Currie, and M. Paranjape, "Releasing SU-8 structures using polystyrene as a sacrificial material," *Sensors and Actuators A*, vol. 114, pp. 123-128, 2004.
- [77] D. Sameoto, S. H. Tsang, and M. Parameswaran, "Polymer MEMS processing for multi-user applications," *Sensors and Actuators A*, vol. 134, pp. 457-464, 2007.
- [78] S. Metz, S. Jiguet, A. Bertsch, and P. Renaud, "Polyimide and SU-8 microfluidic devices manufactured by heat-depolymerizable sacrificial material technique," *Lab on a Chip*, vol. 4, pp. 114-120, 2004.
- [79] V. Linder, B. D. Gates, D. Ryan, B. A. Parviz, and G. M. Whitesides, "Water-soluble sacrificial layers for surface micromachining," *Small*, vol. 1, pp. 730-736, 2005.
- [80] I. G. Foulds and M. Parameswaran, "A planar self-sacrificial multilayer SU-8 based MEMS process utilizing a UV-blocking layer for the creation of freely moving parts," *J. Micromech. Microeng.*, vol. 16, pp. 2109-2115, 2006.

- [81] Z. Huang, W. Hong, and Z. Suo, "Evolution of wrinkles in hard films on soft substrates," *Physical Review E*, vol. 70, pp. 030601-1 - 030601-4, 2004.
- [82] D. Sameoto, S. H. Tsang, I. G. Foulds, S.-W. Lee, and M. Parameswaran, "Control of the out-of-plane curvature in SU-8 compliant microstructures by exposure dose and baking times," *Journal of Micromechanics and Microengineering*, vol. 17, pp. 1093-1098, 2007.
- [83] D. Hall, P. Underhill, and J. Torkelson, "Spin Coating Thin and Ultrathin Polymer Films," *Polymer Engineering and Science*, vol. 38, pp. 2039-2045, 1998.
- [84] L. J. Guo, "Recent Progress in Nanoimprint Technology and its Applications," *Journal of Physics D: Applied Physics*, vol. 37, pp. R123-R141, 2004.
- [85] C. E. Carraher, *Seymour/Carraher's Polymer Chemistry*, 7th ed. Boca Raton, FL, USA: CRC Press, 2008.
- [86] C.-Y. Chao and L. J. Guo, "Polymer microring resonators fabricated by nanoimprint technique," *Journal of Vacuum Science and Technology B: Microelectronics and Nanometer Structures*, vol. 20, pp. 2862-2866, 2002.
- [87] Y. Tu, G. Chapman, J. Dykes, D. Poon, C. Choo, and J. Peng, "Calibrating grayscale direct write bimetallic photomasks to create 3D photoresist structures," *Proc. SPIE*, vol. 5567, pp. 245-256, 2004.
- [88] M. Geoghegan, C. Wang, N. Rehse, and R. Magerle, "Thin polymer films on chemically patterned, corrugated substrates," *Journal of Physics: Condensed Matter*, vol. 17, pp. S389-402, 2005.
- [89] Reprinted from *Sensors and Actuators A*, vol. 134, D. Sameoto, S. H. Tsang, M. Parameswaran, Polymer MEMS processing for multi-user applications, pp. 457-464. Copyright (2007), with permission from Elsevier.
- [90] B. Eyre, J. Blosiu, and D. Wilberg, "Taguchi optimization for the processing of EPON SU-8 resist," presented at IEEE MEMS '98, 1998.
- [91] J. Zhang, K. L. Tan, G. D. Hong, L. J. Yang, and H. Q. Gong, "Polymerization optimization of SU-8 photoresist and its applications in microfluidic systems and MEMS," *J. Micromech. Microeng.*, vol. 11, pp. 20-26, 2001.
- [92] Y. J. Chuang, F. G. Tseng, and W. K. Lin, "Reduction of diffraction effect of UV exposure on SU-8 negative thick photoresist by air gap elimination," *Microsystem Technologies*, vol. 8, pp. 308-313, 2002.
- [93] C. M. Waits, A. Modafe, and R. Ghodssi, "Investigation of gray-scale technology for large area 3D silicon MEMS structures," *J. Micromech. Microeng.*, vol. 13, pp. 170-177, 2003.
- [94] J.-B. Bureau, B. Legrand, D. Collard, and L. Buchaillet, "3D self-assembling of SU-8 microstructures on silicon by plasma induced compressive stress," presented at Transducers '05, Seoul, South Korea, 2005.

- [95] C. K. Chung and Y. Z. Hong, "Surface modification of SU-8 photoresist for shrinkage improvement in a monolithic MEMS microstructure," *J. Micromech. Microeng.*, vol. 17, pp. 207-212, 2007.
- [96] S. J. Lee, W. Shi, P. Maciel, and S. W. Cha, "Top-edge profile control for SU-8 structural photoresist," presented at University/Government/Industry Microelectronics Symposium, 2003. Proceedings of the 15th Biennial, 2003.
- [97] D. Bachmann, B. Schoberle, S. Kuhne, and Y. Leiner, "Fabrication and characterization of folded SU-8 suspensions for MEMS applications," *Sensors and Actuators A*, vol. 130-131, pp. 379-386, 2006.
- [98] D. Haefliger, O. Hansen, and A. Boisen, "Self-Positioning of Polymer Membranes Driven by Thermomechanically Induced Plastic Deformation," *Advanced Materials*, vol. 18, pp. 238-241, 2006.
- [99] A. Hartley, R. Miles, N. Dimitrakopoulos, and R. D. Pollard, "SU-8 Beams and Membranes," presented at 1st EMRS DTC Technical Conference, Edinburgh, 2004.
- [100] F. Ceyskens and R. Puers, "Creating multi-layered structures with freestanding parts in SU-8," *Journal of Micromechanics and Microengineering*, vol. 16, pp. S19-S23, 2006.
- [101] S.-H. Tsang, D. Sameoto, I. G. Foulds, A. M. Leung, and M. Parameswaran, "Wirebonder assembly of hingeless 90 degree out-of-plane microstructures," presented at Solid State Sensors and Actuators Workshop, Hilton Head Island, SC, USA, 2006.
- [102] Reprinted from *Journal of Micromechanics and Microengineering*, vol. 17, D. Sameoto, S.-H. Tsang, I. G. Foulds, S.-W. Lee and M. Parameswaran, Control of the out-of-plane curvature in SU-8 compliant microstructures by exposure dose and baking times, pp. 1093-1098. Copyright (2007), with permission from IOP publishing. <http://www.iop.org/EJ/abstract/0960-1317/17/5/032/>.
- [103] K. K. Seet, V. Mizeikis, S. Juodkazis, and H. Misawa, "Spiral three-dimensional photonic crystals for telecommunications spectral range," *Applied Physics A*, vol. 82, pp. 683-688, 2005.
- [104] A. Moroni, J. Mijovic, E. M. Pearce, and C. C. Foun, "Cure kinetics of epoxy resins and aromatic diamines," *Journal of Applied Polymer Science*, vol. 32, pp. 3761-3773, 1986.
- [105] T. A. Anhoj, A. M. Jorgensen, D. A. Zauner, and J. Hubner, "The effect of soft bake temperature on the polymerization of SU-8 photoresist," *J. Micromech. Microeng.*, vol. 16, pp. 1819-1824, 2006.
- [106] D. Sameoto, S.-W. Lee, and M. Parameswaran, "Wirebonding characterization and optimization on thick film SU-8 MEMS structures and actuators," presented at Transducers 2007, Lyon, France, 2007.

- [107] N. Chronis and L. P. Lee, "Polymer MEMS-based microgripper for single cell manipulation," presented at Micro Electro Mechanical Systems, 2004. 17th IEEE International Conference on. (MEMS), 2004.
- [108] A. Johansson, J. Janting, P. Schultz, K. Hoppe, I. N. Hansen, and A. Boisen, "SU-8 cantilever chip interconnection," *J. Micromech. Microeng.*, vol. 16, pp. 314-319, 2006.
- [109] R. Ulrich, M. Wasef, J.-h. Im, P. Garrou, and D. Scheck, "Thermosonic gold wirebonding to electrolessly-metallized copper bondpads over benzocyclobutene," *The International Journal of Microcircuits and Electronic Packaging*, vol. 22, pp. 190-195, 1999.
- [110] Copyright 2007 IEEE. Reprinted from the proceedings of TRANSDUCERS 2007, Wirebonding characterization and optimization on thick film SU-8 MEMS structures and actuators, D. Sameoto, S.-W. Lee, M. Parameswaran, pp. 2055-2058.
- [111] T. Namazu, S. Inoue, K. Takio, T. Fujita, K. Maenaka, and K. Koterazawa, "Visco-elastic properties of micron-thick SU-8 polymers measured by two different types of uniaxial tensile tests," presented at MEMS 2005, Miami, FL, 2005.
- [112] H. Nabesawa, T. Hitobo, S. Wakabayashi, T. Ashaji, T. Abe, I. Nakatani, and M. Seki, "Polymer surface morphology control for microfluidic devices," presented at Transducers 07, Lyon, France, 2007.
- [113] H. Jansen, M. d. Boer, Johannes, Burger, R. Legtenberg, and M. Elwenspoek, "The black silicon method II: The effect of mask material and loading on the reactive ion etching of deep silicon trenches," *Microelectronic Engineering*, vol. 27, pp. 475-480, 1995.
- [114] Y. J. Lai, J. MacDonald, M. Kujath, and T. Hubbard, "Force, Deflection and Power Measurements of Toggled Micro Thermal Motors," *J. Micromech. Microeng.*, vol. 14, pp. 49-56, 2004.
- [115] D. Sameoto, C. Plesa, and M. Parameswaran, "MEMS material property measurement using an all optical system and an external vibration source," presented at Texpo 2007, Ottawa, Ontario, October 17-18, 2007.
- [116] V. T. Srikar and S. M. Spearing, "A critical review of microscale mechanical testing methods used in the design of microelectromechanical systems," *Experimental Mechanics*, vol. 43, pp. 238-247, 2003.
- [117] L. Lin, A. P. Pisano, and R. T. Howe, "A micro strain gauge with mechanical amplifier," *Journal of Microelectromechanical Systems*, vol. 6, pp. 313-321, 1997.
- [118] K. E. Petersen and C. R. Guarnieri, "Young's modulus measurements of thin films using micromechanics," *Journal of Applied Physics*, vol. 50, pp. 6761-6766, 1979.

- [119] <http://www.trekinc.com/products/PZD700.asp>, "Trek Model PZD700 Data sheet," Trek, 2007.
- [120] C. Plesa, "Development of a polymer MEMS characterization system," Undergraduate Report, School of Engineering Science, Simon Fraser University, Burnaby 2007.
- [121] D. Sameoto, M. Hamidi, and M. Parameswaran, "Characterization of work and power efficiency of micromachined polymer thermal actuators," presented at the Canadian Conference on Electrical and Computer Engineering, Vancouver, Canada, 2007.
- [122] Copyright 2007 IEEE. Reprinted from the proceedings of CCECE 2007, Characterization of work and power efficiency of micromachined polymer thermal actuators, D. Sameoto, M. Hamidi, M. Parameswaran, pp. 1441-1444.
- [123] <http://www.robocup-us.org/>, "Robocup 2007 Homepage," 2007.
- [124] B. R. Donald, C. G. Levey, C. D. McGray, I. Paprony, and D. Rus, "An untethered, electrostatic, globally controllable MEMS micro-robot," *Journal of Microelectromechanical Systems*, vol. 15, pp. 1-15, 2006.
- [125] T. Akiyama, D. Collard, and T. Fujita, "Scratch drive actuator with mechanical links for self-assembly of three-dimensional MEMS," *Journal of Microelectromechanical Systems*, vol. 6, pp. 10-17, 1997.
- [126] O. J. Sul, M. R. Falvo, R. M. Taylor, S. Washburn, and R. Superfine, "Thermally actuated untethered impact-driven locomotive microdevices," *Applied Physics Letters*, vol. 89, pp. 2035121-3, 2006.
- [127] R. W. Johnstone, A. H. Ma, D. Sameoto, M. Parameswaran, and A. M. Leung, "Buckled cantilevers for out-of-plane platforms," *J. Micromech. Microeng.*, vol. 18, pp. 045024 (1-7), 2008.